DISSERTATION

INFLUENCE OF TERRAIN ON THE CHARACTERISTICS AND LIFE CYCLE OF CONVECTION OBSERVED IN SUBTROPICAL SOUTH AMERICA

Submitted by

Marquette N. Rocque

Department of Atmospheric Science

In partial fulfillment of the requirements

For the Degree of Doctor of Philosophy

Colorado State University

Fort Collins, Colorado

Summer 2023

Doctoral Committee:

Advisor: Kristen L. Rasmussen

Russ S. Schumacher
Steven D. Miller
V. Chandrasekar

ABSTRACT

INFLUENCE OF TERRAIN ON THE CHARACTERISTICS AND LIFE CYLCE OF CONVECTION OBSERVED IN SUBTROPICAL SOUTH AMERICA

Subtropical South America (SSA) is a hotspot for deep, intense convection that often grows upscale into large mesoscale convective systems (MCSs) overnight. The local terrain, including the Andes and a secondary feature known as the Sierras de Córdoba (SDC) are hypothesized to play a major role in the initiation, development, and evolution of convection in the region. Some satellite studies have investigated this role, but storm-scale and life cycle characteristics of these MCSs have not been studied in depth due to the lack of high-resolution, ground-based instruments in the region. However, in 2018-2019, several research-quality platforms were deployed to Córdoba, Argentina as part of the Remote sensing of Electrification, Lightning, And Mesoscale/microscale Processes with Adaptive Ground Observations (RELAMPAGO) and the Cloud, Aerosol, and Complex Terrain Interactions (CACTI) field campaigns. The data collected during these campaigns is used in the studies presented in this dissertation to investigate how the Andes and SDC contribute to convection initiation and rapid upscale growth under varying synoptic conditions. Determining why convection is so unique in SSA may provide insight into characteristics of other storms around the world.

The first two studies in the dissertation evaluate how the Andes and SDC modulate the large-scale environment and storm-scale characteristics under strong vs. weak synoptic forcing. High resolution, convection-permitting simulations in which the terrain is modified are designed to investigate synoptic (Chapter 2) and mesoscale (Chapter 3) processes related to the development of two severe mesoscale convective systems (MCSs) observed during RELAMPAGO-CACTI. Results from the simulations are also compared with radar observations to determine how well the model performs. Under strong synoptic forcing, when the Andes are reduced by 50%, the lee cyclone that develops is weaker, the South American Low-level Jet (SALLJ) is weaker and shallower, and the MCS that develops is weaker and moves quickly off the terrain. When the SDC are removed, there are no substantial changes to the large-scale environment. However, there is no back-building signature of deep convection, likely because cold pools are no longer blocked by the SDC. Under weak synoptic forcing, there are no significant changes to the large-scale environment, even when the Andes are halved. Similar to the strongly forced case though, when the SDC are removed, there are fewer deep convective cores toward the west. In both cases, the model tends to overestimate convection compared to observations. These studies show that the terrain plays varying roles in the evolution of convection in SSA.

The third and fourth studies use ground-based lightning observations from RELAMPAGO-CACTI to better understand the electrical and microphysical characteristics of these intense storms. Three-dimensional storm structures are identified in the radar data and lightning flashes are matched with these storm modes to evaluate how lightning varies throughout the convective life cycle (Chapter 4). Results show that lightning flashes associated with deep convective cores are most common along the higher terrain of the SDC and occur in the afternoon hours. They also tend to be the smallest in size. Flashes associated with wide convective cores occur more frequently along the eastern edge of the SDC and are observed around midnight local time. Stratiform flashes are found most frequently in the early morning hours about 50-100 km east of the SDC, and they tend to be the largest in area and occur lower within the cloud. These distributions highlight the life cycle of systems, which initiate along the SDC and grow upscale as they move towards the plains overnight.

Flash rates are then related to microphysical properties such as graupel mass and ice water path (Chapter 5). The first lightning flash rate parameterizations are developed for storms in SSA. We find these storms have considerably more graupel associated with them compared to storms in the U.S. These new parameterizations are tested on the simulated strongly forced MCS, and results agree well with observed flash rates. If parameterizations based on U.S. storms had been used instead, the flash rates would have been overestimated by up to a factor of 8. This work, in conjunction with other studies in this dissertation, highlights just how different storms in SSA are compared to the U.S.

ACKNOWLEDGEMENTS

I would first like to thank my advisor, Dr. Kristen Rasmussen, for accepting me into her group three years ago and supporting me throughout this research. It has been a pleasure learning from her, and I always look forward to our conversations. I am also thankful she allowed me to participate in several field campaigns while I was a Ph.D. student, which have been some of the most memorable experiences of my career thus far.

I would also like to thank my committee members: Dr. Russ Schumacher, Dr. Steven Miller, and Dr. Chandra. Their feedback and discussions have been very helpful in preparing this dissertation. Additionally, I would like to thank the RELAMPAGO orographic team including Dr. Angela Rowe, Dr. Lynn McMurdie, Stacy Brodzik, Clayton Sasaki, Daniel Veloso-Águila, and Anthony Bernal Ayala. It has been great collaborating with them, and our biweekly meetings have always been full of interesting discussions.

Many others have assisted me in my Ph.D. studies which I am very grateful for. Dr. Wiebke Deierling and Dr. Rachel Albrecht have been especially supportive of my lightning work, a subject that I was not very familiar with coming into this research. Others that have helped me along the way include Dr. Brenda Dolan, Dr. Lulin Xue, Kyle Hilburn, and Ivan Arias Hernandez. I will also always be grateful to Dr. Steven Rutledge who invited me to join the department five years ago and taught me so much during my M.S.

I would also like to thank the members of the Rasmussen group that I have had the privilege of working with, both past and present. Additionally, I would like to thank the entire faculty and staff of the Department of Atmospheric Science at Colorado State University for their support.

Finally, I would like to thank my friends and family who have encouraged me to pursue my dreams of higher education. Particular thanks goes to Allix Coon for continuing to be my best friend as we struggle through grad school together half way across the country from one another. Thanks also to my partner, Thomas Zeleskey, for listing to me complain about grad school, for helping me choose colors for my figures and posters, for helping me format this dissertation, and most importantly, for supporting me and loving me unconditionally. Finally, thanks to my parents and my sister Jacqi for always being interested in what I do.

This research was supported by NSF grants AGS-1661657 and AGS-2146709, DOE grant DE-SC0022056, and a NASA FINESST Fellowship (NASA grant 80NSSC21K1618).

TABLE OF CONTENTS

LIST OF TABLES

LIST OF FIGURES

CHAPTER 1

Introduction

1.1 Motivation

Global convection has many effects on the earth system. Convection is important in the radiation and energy budget as different clouds and the height at which they occur can have either heating or cooling effects on the atmosphere (Hartmann et al. 2001; Trenberth et al. 2009; Zhou et al. 2016). Convection is also important in the global water cycle. Mesoscale convective systems (MCSs), in particular, contribute a significant amount (up to 95%) to precipitation around the world (Fritsch et al. 1986; Nesbitt et al. 2006; Rasmussen et al. 2016). Additionally, deep convection transports mass, heat, and aerosols vertically through the lower atmosphere that can have local and global impacts (Houze 1973, 2004; Ervens 2015). Finally, convection can be associated with severe weather including large hail, damaging winds, tornadoes, flash and slow-rise flooding, and lightning, all of which can be detrimental to the region of impact (Cecil and Blankenship 2012; Rasmussen et al. 2014; Bruick et al. 2019; Nesbitt et al. 2021).

Several global satellite studies have examined where and when deep convection most frequently occurs. An early study by Zipser et al. (2006) used data from the first spaceborne precipitation radar onboard the Tropical Rainfall Measuring Mission (TRMM) satellite to identify hotspots in deep, intense convection in the tropics and subtropics. Using proxies such as minimum brightness temperatures, maximum 40-dBZ echo top heights, and lightning flash rates, they found a maximum in deep convection downstream of the Andes in subtropical South America (SSA). These storms are observed in all seasons, but more frequently occur during the austral spring and summer months. Subsequent studies using TRMM have shown that extreme three-dimensional storm modes including deep convective cores (DCCs; 40-dBZ echoes > 10 km MSL), wide convective cores (WCCs; 40-dBZ echoes > 1,000 km^2), and broad stratiform regions (BSRS; stratiform echo > 50,000 km^2) are prevalent in this region and are associated with the life cycle of MCSs (Romatschke and Houze 2010, 2013; Rasmussen and Houze 2011, 2016; Houze et al. 2015; Rasmussen et al. 2014, 2016).

Based on these satellite studies and a set of terrain-modification simulations, Rasmussen and Houze (2016) developed a conceptual model for storm development in SSA. Warm, moist air is advected south from the Amazon via the South American low-level jet (SALLJ; Vera et al. 2006). Strong upper-level flow subsides in the lee of the Andes, creating a capping inversion above this moist air. A lee cyclone also develops to the east as a result of the upper-level flow crossing the Andes. This lee cyclone enhances the north-south pressure gradient force, which strengthens the SALLJ. Ageostrophic winds from the upper-level wave passing over the southern Andes converge with the SALLJ near a secondary mountain feature known as the Sierras de Córdoba (SDC). This convergence of air masses, along with mechanical lifting caused by the SDC, initiates convection, which often rapidly grows upscale into MCSs that move off the terrain overnight.

Although a significant amount of new information had been learned by these satellite studies, mesoscale processes and the evolution of convective characteristics of individual storms were not able to be investigated in depth due to the polar-orbiting nature of TRMM and the lack of ground-based observations in the region. This was a primary motivator for the Remote sensing of Electrification, Lightning, And Mesoscale/microscale Processes with Adaptive Ground Observations (RELAMPAGO; Nesbitt et al. 2021) field campaign and the Cloud, Aerosol, and Complex Terrain Interactions (CACTI; Varble et al. 2021) field campaign, which took place in the austral spring and summer of 2018-2019. Several ground-based platforms including radars, soundings, surface stations, and a lightning mapping array were deployed for these projects by a number of institutions, which provided high spatial and temporal resolution data to investigate storm scale processes. Some recent studies have used this data to examine the environments that support deep convection (Nelson et al. 2021; Schumacher et al. 2021; Piersante et al. 2021), variations in the SALLJ related to synoptic patterns (Sasaki et al. 2022), and lightning characteristics of severe storms (Lang et al. 2020; Medina et al. 2022a, b).

Most studies of convection in SSA have shown that MCSs preferentially form under strong synoptic conditions (Rasmussen and Houze 2011, 2016; Bruick et al. 2019; Piersante et al. 2021), and the terrain in the region, including the Andes and the SDC, play a major role in the initiation and development of convection. However, based on observations from RELAMPAGO and CACTI, we know large MCSs also form under weak synoptic forcing. Thus, research presented in this dissertation analyzes the importance of the topography on MCS development under both strong and weak synoptic forcing. Storm-scale, electrical, and microphysical characteristics of convection are analyzed in detail for strongly and weakly forced MCSs. This work extends the work of previous satellite studies by using high resolution, ground-based observations from RELAMPAGO and CACTI, and results from this work have the potential to improve forecasts and simulations of severe weather in SSA.

1.2 Dissertation outline

To better understand why and how deep convection forms in SSA, this research uses observations from the RELAMPAGO field campaign and high-resolution simulations to examine how the large-scale environment, mesoscale processes, microphysics, and electrical characteristics of storms are influenced by the Andes and the SDC. In particular, two case studies of severe MCSs from RELAMPAGO are analyzed in depth to determine what makes these storms unique compared to other areas of the world.

Chapter 2 (Rocque and Rasmussen 2022)[1] presents results from several terrain-modification simulations performed over SSA, which provide insights into how the Andes and the SDC influence the large-scale environment and MCSs that develop under strong and weak synoptic forcing. Under strong synoptic forcing, the Andes produce a strong lee cyclone and enhance the SALLJ that allows for convection to rapidly develop and remain tied to the terrain. Under weak synoptic forcing, the Andes and SDC do not have a strong influence on the large scale environment, and mesoscale processes dominate the MCS development.

Chapter 3 (Rocque, Rasmussen, and Rowe 2023)[2] examines the role of the SDC on the convective development of two case studies from RELAMPAGO using C-band radar data and high-resolution simulations. In general, the simulations tend to overestimate deep convection and underestimate stratiform precipitation compared to radar observations. Removing the SDC results in less back-building of deep convection toward the west. Further analysis suggests that cold pools are more dispersed and shallower when the SDC are removed, and the impact of cold pools on the convective life cycle is more important under weak synoptic forcing.

Chapter 4 (Rocque, Rasmussen, Deierling, Albrecht, and Medina 2023, in prep)[3] uses ground- and satellite-based observations of lightning to better understand the electrical characteristics of storms in SSA. Ground-based lightning observations are matched with extreme three-dimensional storm structures to find that convective flashes occur most frequently along the SDC around 10 km and are smaller compared to stratiform flashes which occur most frequently

---

[1] The research presented in Chapter 2 has been presented in *Monthly Weather Review* as Rocque and Rasmussen (2022).

[2] The results presented in Chapter 3 have been submitted to *Monthly Weather Review* and are under review.

[3] The results presented in Chapter 4 will be submitted to *a peer-reviewed journal* in spring 2023.

50-100 km east of the SDC. Microphysical analysis using radar also indicate lightning flash rates are closely related to graupel and hail mass and volume, ice water path, and 35-dBZ volume.

Chapter 5 (Rocque, Deierling, and Rasmussen 2023, in prep)[4] develops a set of lightning parameterizations for storms in SSA using ground-based observations from RELAMPAGO. Linear regressions between storm total lightning parameters (graupel and hail mass, graupel and hail volume, ice water path, and 35-dBZ volume) and lightning flash rates are calculated, and these parameterizations are applied to a high-resolution model simulation. This is the first set of lightning parameterizations developed for use in SSA.

---

[4] The results presented in Chapter 5 will be submitted to *Geophysical Research Letters* in spring 2023.

CHAPTER 2

The Impact of Topography on the Environment and Life Cycle of Weakly and Strongly Forced MCSs during RELAMPAGO[5]

2.1 Introduction

Global satellite studies have shown that some of the most intense deep convection occurs in the vicinity of large mountain ranges including the Rockies, Himalayas, and Andes (Zipser et al. 2006; Houze et al. 2015). It is hypothesized that these mountain ranges modulate the flow and environment in such a way that creates favorable conditions for the frequent development of mesoscale convective systems (MCSs). MCSs play an important role in the water and energy cycles through their influence on the radiation budget, and their vertical transport of latent heat and momentum (Houze 2004). Thus, better understanding the environments in which they form in around the world will aid in their representation in numerical weather forecasts and climate models.

In the past decade, specific focus has been given to subtropical South America (SSA) where Tropical Rainfall Measuring Mission (TRMM; Kummerow et al. 1998) satellite studies have shown a high frequency of deep convection with high lightning flash rates in all seasons, but especially in the spring and summer months (Zipser et al. 2006; Nesbitt et al. 2006; Romatschke and Houze 2010; Rasmussen and Houze 2011; Houze et al. 2015; Rasmussen et al. 2014, 2016). Nesbitt et al. (2006) found that MCSs contribute about 90% to the total rainfall in the La Plata

---

[5] This chapter has been published by the American Meteorological Society in *Monthly Weather Review*: Rocque, M. N., and K. L. Rasmussen, 2022: The Impact of Topography on the Environment and Life Cycle of Weakly and Strongly Forced MCSs during RELAMPAGO. *Mon. Wea. Rev.*, **150**, 2317–2338. © American Meteorological Society. Used with permission.

basin in SSA, while other regions around the world including the Sahel, Congo basin, and the Great Plains of the U.S. have MCS rainfall contributions greater than 70%. Rasmussen et al. (2016) similarly found that nearly 95% of the warm-season rainfall over the eastern plains of Argentina comes from MCSs, and Liu and Zipser (2013) showed that the largest and strongest convective lines occur over central Africa, the southeast U.S., and Argentina. These large MCSs in SSA are often associated with severe weather including flooding, large hail, and tornadoes (Rasmussen and Houze 2011; Rasmussen et al. 2014; Bruick et al. 2019).

Using observations from TRMM and several model simulations, Rasmussen and Houze (2016; hereafter RH16) investigated the impact of terrain on MCSs in SSA. They performed a variety of terrain-modification experiments that involved both reducing the height of the Andes and increasing the height of the southern Andes. They found that lowering the Andes resulted in a weaker South American Low-Level Jet (SALLJ; Vera et al. 2006; Sasaki et al. 2022), less convective available potential energy (CAPE) and convective inhibition (CIN), and more widespread convection that moved faster towards the east. Increasing the southern Andes resulted in a stronger SALLJ, more CAPE and CIN, and convection that was located further south. These results were used to develop a conceptual model of the important environmental conditions that support the production of large convective events in SSA (RH16). Warm, moist air transported from the Amazon basin to SSA along the SALLJ is capped by dry midlevel flow subsiding off the Andes. The northerly SALLJ then collides with southerly ageostrophic flow from the mid-latitudes near the north-south oriented Sierras de Córdoba (SDC) mountain range in western Argentina where deep convection is often initiated. Due to the extreme height of the Andes, CAPE and CIN are enhanced downstream of the topography compared to shorter mountain ranges. These conditions create a favorable environment for deep convection and rapid upscale growth which is focused along the topography.

Subsequent studies have followed this conceptual model and shown that some of the most intense convective features and severe weather are associated with these strong synoptic conditions including a deep upper-level trough, strong lee cyclogenesis, and an enhanced SALLJ. Piersante et al. (2021) analyzed 16 years of wide convective cores (40 dBZ echoes > 1000 km^2; WCCs) identified by TRMM and found that large (>90% percentile) WCCs occurred under stronger synoptic conditions during the spring compared to summer. Additionally, small (<10% percentile) WCCs occurred under quiescent synoptic flow in the summer. They suggested that the poleward and westward shift in upper-level troughs and jet streaks allowed convection to focus along the SDC in the summer, helping to explain the westward shift in WCC rainfall observed by Rasmussen et al. (2016). In terms of severe weather, Bruick et al. (2019) found that systems with a high probability of hail occurred under more anomalous synoptic conditions.

Unfortunately, due to the polar-orbiting nature of TRMM and the lack of ground-based radar observations in SSA until 2015, the complete life cycle of MCSs and how they evolve within the large-scale flow has not been studied in great detail. This was a primary motivation for the Remote sensing of Electrification, Lightning, And Mesoscale/microscale Processes with Adaptive Ground Observations (RELAMPAGO; Nesbitt et al. 2021) field campaign, which took place near Córdoba, Argentina in late 2018 – early 2019. Several studies have used resulting datasets from RELAMPAGO and the Córdoba radar to investigate how intense convective events are related to the large-scale flow in SSA. A recent study by Sasaki et al. (2022) used sounding observations from RELAMPAGO to analyze the relationship between SALLJ events and convection in the region and found that longer duration jets were often more elevated, associated with large precipitation events, and driven by the synoptic flow, where lee cyclogenesis intensifies the north-south pressure gradient force downstream of the Andes. Shorter duration jets were controlled by the diurnal cycle (Holton 1967) and boundary layer processes such as the inertial oscillation (Blackadar 1957), more similar to jets in the U.S. Great Plains (Du and Rotunno 2014; Shapiro et al. 2016).

Using two years of data from the Córdoba radar, Mulholland et al. (2018) produced one of the first studies on the convective life cycle within the SSA region. They found the majority of convective events near the SDC were multicellular in nature, initiated over the highest terrain of the southern SDC, and often rapidly grew upscale directly downstream of the SDC in as little as three hours. These events were associated with deep upper-level troughs, a strong SALLJ, and enhanced CAPE and CIN, further supporting RH16's conceptual model. Further studies by Mulholland et al. (2019, 2020) looked at varying the height of the SDC and the resulting changes to the environment and convective development/evolution. Results from their case study analysis (Mulholland et al. 2019), as well as idealized simulations (Mulholland et al. 2020), show that increasing the SDC height increases vertical wind shear, reduces CAPE, leads to convection initiating earlier, and causes enhanced blocking of cold pools. The deepest cold pools and fastest transition from supercell to MCS occurred in the control run, suggesting the SDC are at a unique height for intense and rapid upscale growth (Mulholland et al. 2019). However, the influence of the synoptic environment was not considered, especially in the idealized simulations. Interestingly, Parker (2021) has recently shown that nocturnal MCSs in the U.S. Great Plains can have a considerable self-organizing component in which the evolution of the MCS is dependent on its own environment and prior evolution. They find the synoptic scale provides a favorable environment for MCS initiation, but mesoscale dynamics associated with the MCS such as cold pool processes ultimately control the MCS life cycle.

As mentioned, there are a lot of ingredients that come together to create a favorable environment for MCS development in SSA (RH16). It is known that the Andes and SDC play a major role in modulating the environment, but there has been little research on terrain influences on the environment and convection under different (particularly weak) synoptic conditions associated with the development and upscale growth of MCSs in the region. Several of the studies mentioned above have shown that large MCSs, often associated with severe weather, tend to occur under strong synoptic conditions in the spring, yet results from RELAMPAGO demonstrate that MCSs occur under a range of synoptic environments in SSA. Thus, the main objective of this study is to explore how the Andes and SDC impact the environment and convective development under strong and weak synoptic conditions in SSA.

2.2 Methodology

2.2.1 Model

The impact of the Andes and the SDC on convective growth is analyzed using a set of five terrain-modification experiments. The Weather Research and Forecasting (WRF; Skamarock et al. 2008) Model version 4.2 was run to simulate two cases from the RELAMPAGO field campaign. The first is an upscale growth MCS case that occurred on 13-14 December 2018 (IOP17) and resulted in large hail, significant lightning activity, and flooding. This case featured a deep upper-level trough and strong SALLJ and will be referred to as the strongly forced case. The second case is an upscale growth MCS event that occurred on 25-26 January 2019 and again resulted in significant severe weather associated with very deep convective cells with 40-dBZ echo tops greater than 20 km (Schumacher et al. 2021, Nesbitt et al. 2021). A small upper-level shortwave trough passed through the mid-latitudes but the flow across the Córdoba region was weakly zonal. Hence, this case will be referred to as the weakly forced case and provides a nice contrast to the strongly forced case. Both cases were initialized about 24 hours before convection associated with the event of interest initiated (1800 UTC 12 December 2018 for the strongly forced case and 1800 UTC 24 January 2019 for the weakly forced case) and run for 54 hours using three nested domains of 27, 9, and 3 km centered around Córdoba, Argentina (Fig. 2.1). ERA5 reanalysis data (Copernicus Climate Change Service 2017) was used to force the simulations every hour. The Thompson aerosol-aware microphysics scheme (Thompson and Eidhammer 2014) was used as it best represents both the convective and stratiform components of MCSs in SSA (RH16). Both sets of simulations used the following physics parameterizations: Rapid Radiative Transfer Model (RRTM) longwave radiation (Mlawer et al. 1997), Dudhia shortwave radiation (Dudhia 1989), Kain-Fritsch cumulus convection in the 27- and 9-km domains (none in the 3-km domain; Kain and Fritsch 1993), Monin-Obukhov surface layer scheme, Noah land surface model (Chen and Dudhia 2001), and the Yonsei University (YSU) planetary boundary layer (PBL) scheme (Hong et al. 2006).

The first simulation run for each case was the control (CTRL), in which the terrain in each domain was not altered. In the second simulation, the SDC were removed from each domain (noSDC; Fig. 2.2a). This was accomplished by creating several boxes over the SDC, setting the values inside each box to the average height of the terrain downstream of the SDC (60-100 meters), and then using a 9-point smoothing function around the edge of the boxes to eliminate any sharp gradients in terrain that would have been produced. This was performed on each domain prior to running metgrid.exe, and the SDC-modification box domains are shown in Table 2.1. The third

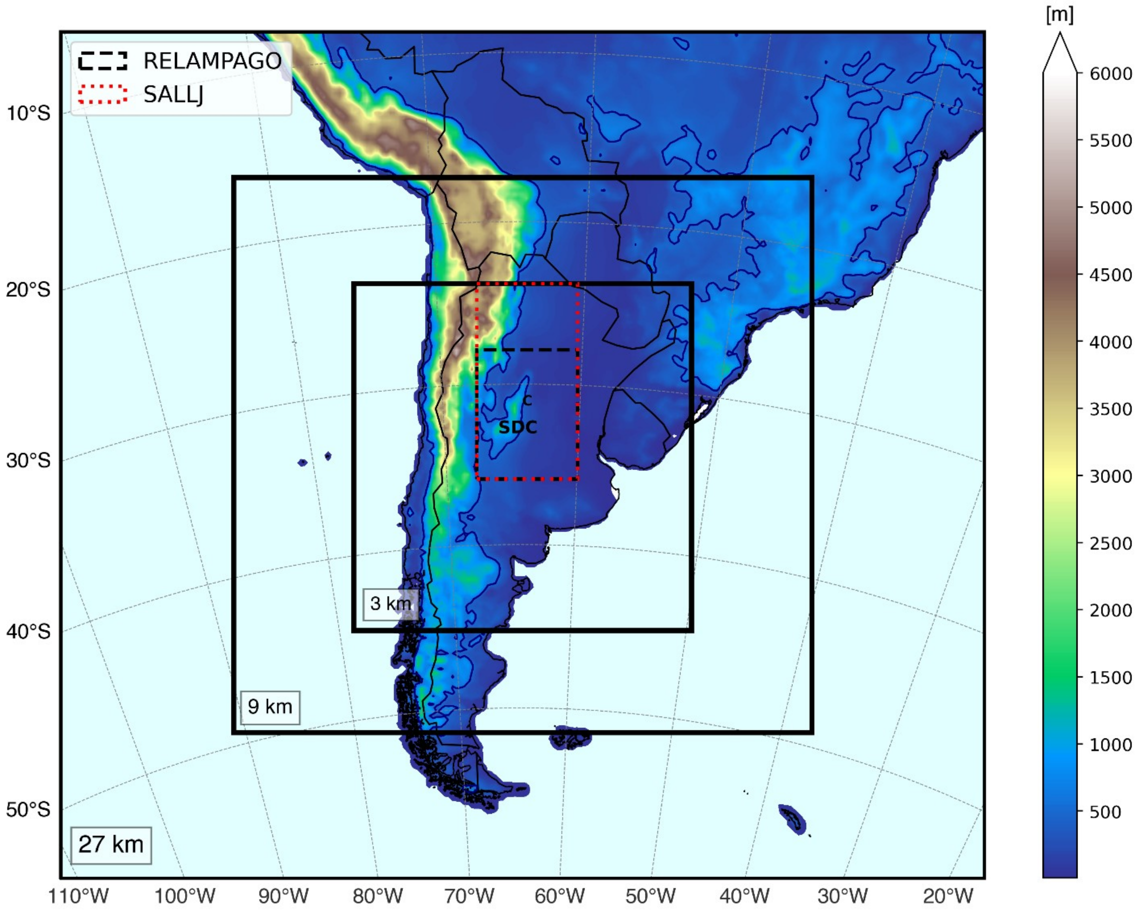

Figure 2.1: 27-, 9-, and 3-km domains used in the WRF simulations. The SALLJ domain (red dotted box) and RELAMPAGO domain (black dashed box) are used for Hovmöller averaging. CTRL topography is shaded with the 500 m terrain contour in navy and the 'C' representing Córdoba.

Table 2.1: Summary of WRF domains and where SDC-modification boxes were placed within each domain. The last column is the height set within the terrain-modification box (approximately the height downstream of the SDC).

name	resolution	grid points	box 1	box 2	box 3	height
d01	27 km	238 x 218	[111:121, 105:131]	n/a	n/a	60 m
d02	9 km	446 x 428	[214:240, 204:282]	[207:224, 207:263]	[198:216, 203:243]	100 m
d03	3 km	782 x 803	[370:435, 357:610]	[343:379, 356:559]	[316:345, 356:491]	100 m

and fourth simulations involved reducing the height of the Andes by 50% and either keeping the SDC at the same height (lAndes; Fig. 2.2b) or removing them (lAndes_noSDC; Fig. 2.2c). Similar smoothing functions were applied near the modifications to create a more gradual slope. These experiments were designed to investigate how the height of the Andes impacts convective growth and synoptic to mesoscale flow features, and this terrain height more closely resembles the height of the Rockies in North America. For the final simulation, the terrain was completely removed across each domain (noTer; Fig. 2.2d). Results from this simulation highlight the important impact of the Andes, Andean foothills, and SDC on the development of intense MCSs in SSA. RH16 used this same methodology to modify terrain in their study (both the Andes and SDC modification), thus the current methodology is consistent with prior research.

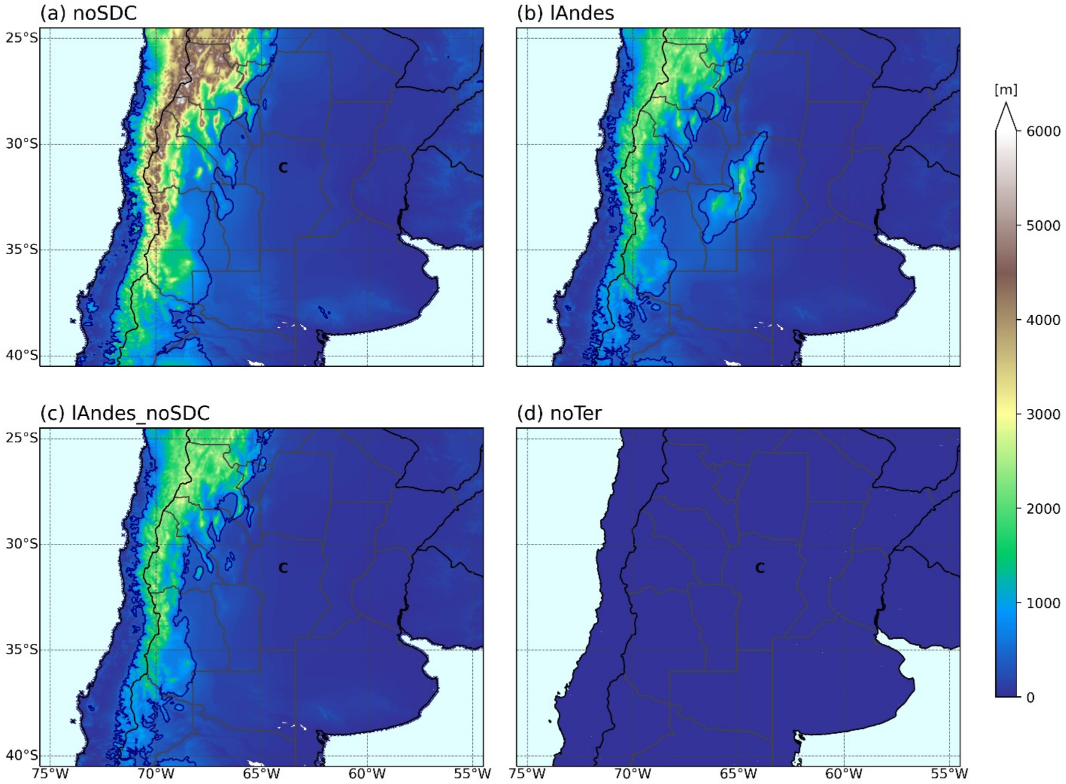

Figure 2.2: Topography from the a) noSDC, b) lAndes, c) lAndes_noSDC, and d) noTer 3-km WRF simulations with the 500 m terrain contour shown in navy and the ‘C’ representing Córdoba.

2.2.2 GOES-16

Data from the *Geostationary Operational Environmental Satellite* (*GOES-16*) Advanced Baseline Imager (ABI; Schmit et al. 2017) was used to see how well the simulations captured the events. Here we use the Channel 14 11.2 μm band (infrared longwave window) to look at cloud top brightness temperatures.

2.2.3 ERA5

ERA5 reanalysis data (Copernicus Climate Change Service 2017), which has 0.25° x 0.25° resolution, 37 vertical grid levels, and hourly temporal resolution, was also used to examine the synoptic set-up of the two cases. Relative vorticity at 500 hPa, specific humidity at 850 hPa, and geopotential height and winds at both 500 and 850 hPa were analyzed across South America. Additionally, to look at the climatology of moisture in the region, the average monthly 850 hPa specific humidity was calculated for December and January from 1978-2018.

2.3 13-14 December 2018: Strongly forced case

2.3.1 Overview

An intense MCS rapidly developed on the east side of the Andes in SSA during the RELAMPAGO field campaign from 13-14 December 2018 and was associated with strong synoptic forcing including a high-amplitude, slow-moving 500 hPa trough, strong lee cyclogenesis, and an enhanced low-level jet (Fig. 2.3). At 0000 UTC on 13 December, an upper-level trough was located at 85°W off the coast of Chile (Fig. 2.3a). Enhanced moisture (>12 g kg^{-1}) was funneled along the eastern edge of the Andes from the Amazon to about 35°S at 850 hPa by the SALLJ (Fig. 2.3b). Over the next 24 hours, the 500 hPa trough deepened as it approached the Andes, with the 552 dm height contour extending to around 38°S (Fig. 2.3c). Strong relative vorticity advection occurred downstream of the trough associated with both shear and curvature vorticity (Fig. 2.3c). At 850 hPa, the SALLJ increased in strength to 18 m s^{-1} which advected specific humidity values of 10 g kg^{-1} to nearly 40°S (Fig. 2.3d). By 15 December, the 500 and 850 hPa troughs had moved over the Atlantic and the greatest moisture was concentrated north of the SDC and within the trough to the east (Figs. 2.3e, f).

Convective cells initiated around 1800 UTC 13 December on the southern end of the SDC and about three hours later off the higher terrain of the foothills to the north. After 0000 UTC on 14 December, deep cells had developed south of Córdoba and over the southern SDC. These cells quickly grew into a strong convective line which remained tied to the Andes and SDC through 0600 UTC. A comparison between *GOES-16* infrared brightness temperatures and outgoing longwave radiation from the 3-km CTRL run shows weaker convection was present over the eastern plains of Argentina from a previous system at 1200 UTC on 13 December (Figs. 2.4a, b). Six hours later, convection initiated in similar locations near the SDC (Figs. 2.4c, d). The CTRL run is more aggressive in developing convection along the cold front to the south (Figs. 2.4c-f), but by 0600 UTC when the MCS reached peak maturity, the convective structures are quite similar (Figs. 2.4g, h). Therefore, we reason that the simulations provide valuable insight into the interactions between the topography and convective growth in the region.

2.3.2 Synoptic scale

Under strong synoptic conditions the Andes act as a barrier to the upper-level flow (RH16). Figure 2.5a shows the progression of the 500 hPa trough in the CTRL run in a time-longitude (Hovmöller) format. 500 hPa geopotential heights are averaged across the 3-km domain latitude

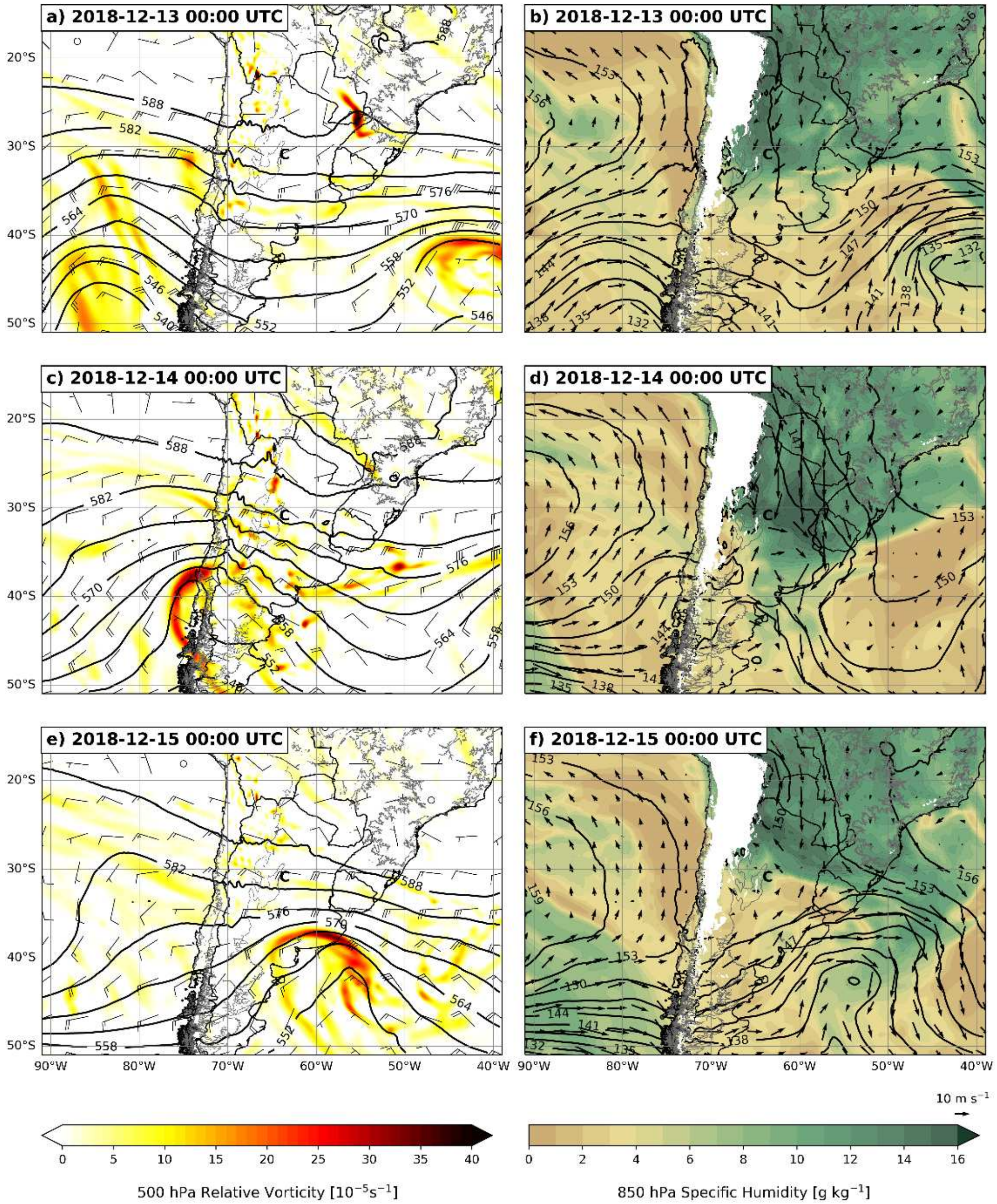

Figure 2.3: 500 hPa geopotential heights (contoured; dm), relative vorticity (shaded; 10^{-5} s^{-1}), and winds (barbs; m s^{-1} where a half barb = 5 m s^{-1} and a full barb is 10 m s^{-1}) on the left and 850 hPa geopotential heights (contoured; dm), specific humidity (shaded; g kg^{-1}), and winds (arrows; m s^{-1}) on the right from ERA5 reanalysis starting at 0000 UTC 13 December 2018 and stepping through every 24 hours. The 500 m terrain contour is shown in grey and the 'C' represents Córdoba.

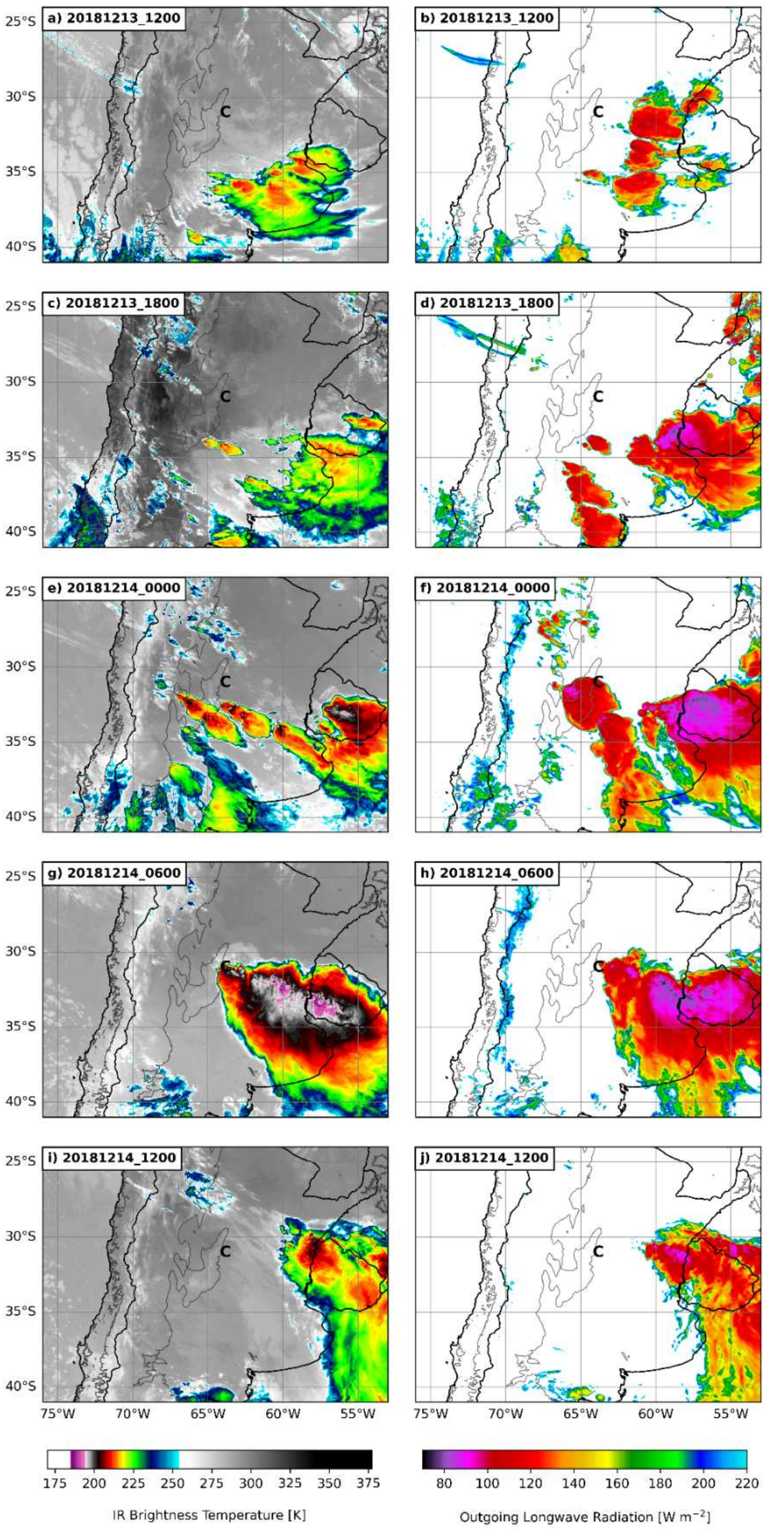

Figure 2.4: Comparison between *GOES-16* Channel 14 IR brightness temperatures (left; K) and outgoing longwave radiation from the 3-km CTRL run (right; W m^{-2}) starting at 1200 UTC 13 December 2018 and stepping through every 6 hours. The 500 m terrain contour is shown in grey and the 'C' represents Córdoba.

band (23-45°S; Fig. 2.1) to examine the evolution of the upper-level flow in the subtropics that directly impacted the life cycle of the MCS. The trough is strongest on the west side of the Andes around 0900 UTC on 13 December at 5565 m (Fig. 2.5a). As the trough approaches the Andes, it significantly weakens. When the Andes are reduced by half, the upper-level trough is at least 20 m (on average) deeper than the trough in the CTRL simulation (Fig. 2.5b), and at least 40 m deeper when the terrain is removed completely (Fig. 2.5c). In the presence of the full Andes, the trough is sheared apart, but when the Andes are reduced or removed, the upper-level flow remains intact and strong.

A lee cyclone develops downstream of the Andes in the CTRL run as a result of the strong upper-level trough and potential vorticity conservation, which is clearly visible at 1800 UTC on 13 December, where the 1410 and 1425 m 850 hPa geopotential height contours are located near the SDC (Fig. 2.6a). There is a weaker signature of a lee cyclone when the Andes are reduced (Fig. 2.6b), but the main baroclinic system to the south is at least 30 m deeper. When the terrain is reduced/removed, the mechanism for producing a lee cyclone is also reduced/removed, so the only low pressure is associated directly with the upper-level trough in the mid-latitudes (Figs. 2.6b, c). There is a small shortwave visible in the noTer geopotential heights which could be a forcing for new convection, but the mechanism for its production is not clear (Fig. 2.6c). The evolution of the 850 hPa geopotential heights averaged across the SALLJ domain (Fig. 2.1) in a Hovmöller format also highlights the development of the lee cyclone in the CTRL run (Fig. 2.7a). Geopotential heights are lowest between 1800-0000 UTC and the minimum of 1390 m extends just east of the SDC. At this time, convection initiates along the Andean foothills around 66.5°W and propagates east. When the Andes are halved, geopotential heights are at least 30 m greater between 1800-0000 UTC in the western part of the domain indicating a weaker cyclone, and there is little-to-no

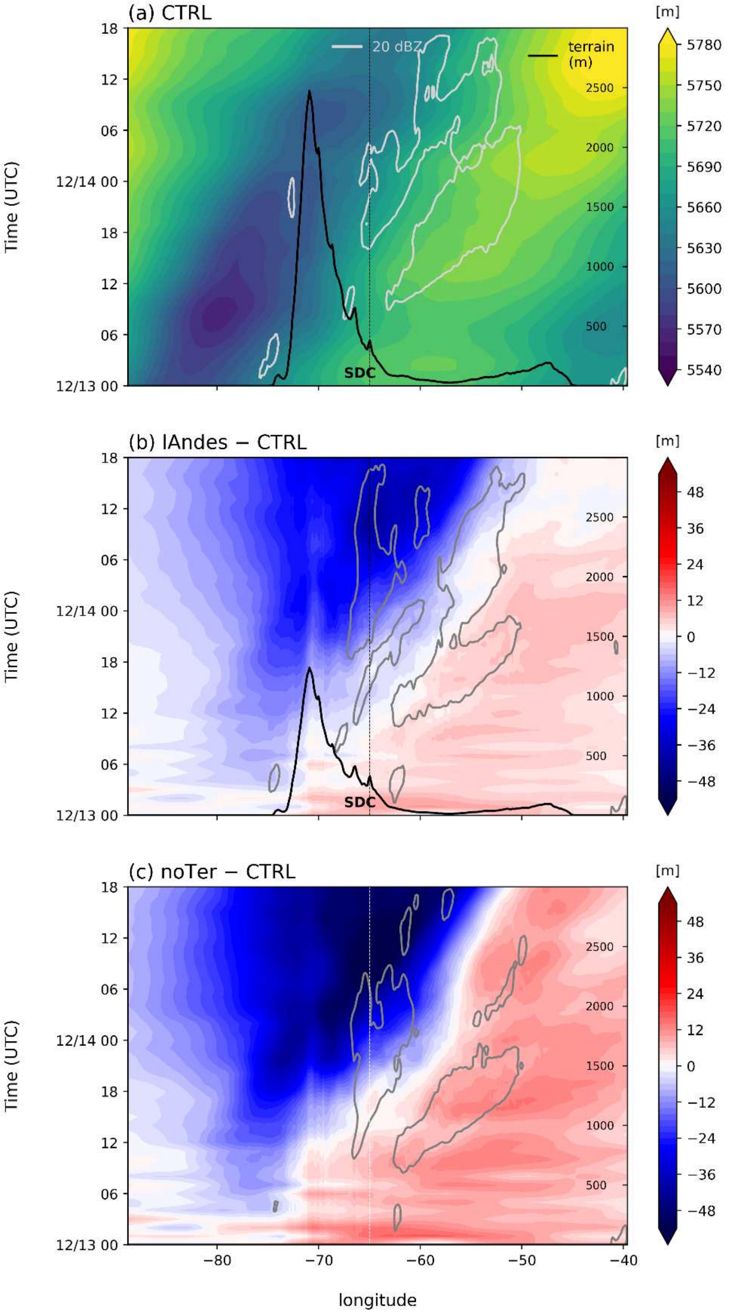

Figure 2.5: Hovmöllers of a) CTRL 500 hPa heights (shaded; m) and 20-dBZ composite reflectivity (grey contour; dBZ) from the 9-km domain averaged across the 3-km domain latitude band, b) lAndes – CTRL, c) noTer – CTRL. Longitude ranges from about 90-40°W and times are shown from 0000 UTC 13 December to 1800 UTC 14 December. Average terrain profile is shown in the black contour. The location of the SDC near 65°W is shown as a dashed black line in panels (a-b) and where the SDC would be is shown in a dashed white line in panel (c).

convection in this region (Fig. 2.7b). The cyclone is even weaker when the Andes are removed, with 850 hPa heights at least 60 m greater than the CTRL (Fig. 2.7c), again highlighting the impact of terrain height on lee cyclogenesis and convective development. RH16 similarly found that reducing the height of the Andes by 50% led to a significant increase in 850 hPa geopotential heights and weaker lee cyclogenesis close to the Andean foothills.

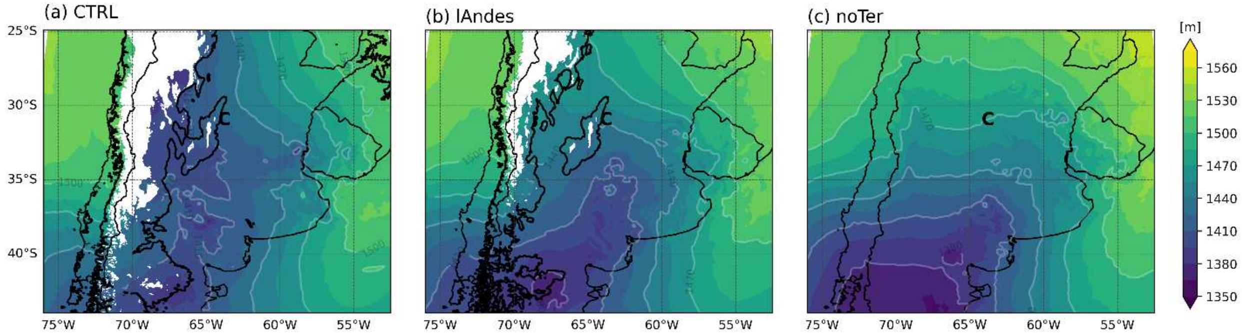

Figure 2.6: 850 hPa heights (m) from 1800 UTC on 13 December for a) CTRL, b) lAndes, and c) noTer simulations shown across the 3-km domain. The 500 m terrain contour is shown in black and the 'C' represents Córdoba.

The movement of air parcels at different levels is also analyzed to better understand how the Andes impact the low-, mid-, and upper-level flow. Backward trajectories starting from 0000 UTC on 14 December at a location north of the SDC (63.5°W, 28.6°S) are shown in Figure 2.8. These trajectories were computed every 10 minutes in the Read/Interpolate/Plot (RIP) program maintained by the National Center for Atmospheric Research (NCAR). Locations near Córdoba and Villa Yacanto within the SDC were also analyzed, but the influence of the SDC made results more difficult to interpret. This northern location was chosen because it is near the center of the SALLJ domain yet about 100 km north of the SDC. At 500 hPa, the trajectories of air parcels in each simulation are quite similar (Fig. 2.8a). The 500 hPa flow in the CTRL simulation (red) is slower than in the lAndes (blue) and noTer (yellow) runs, though. At 1200 UTC on 13 December, the 500 hPa parcels are located off the Chilean coast around 71°W in the lAndes and noTer runs,

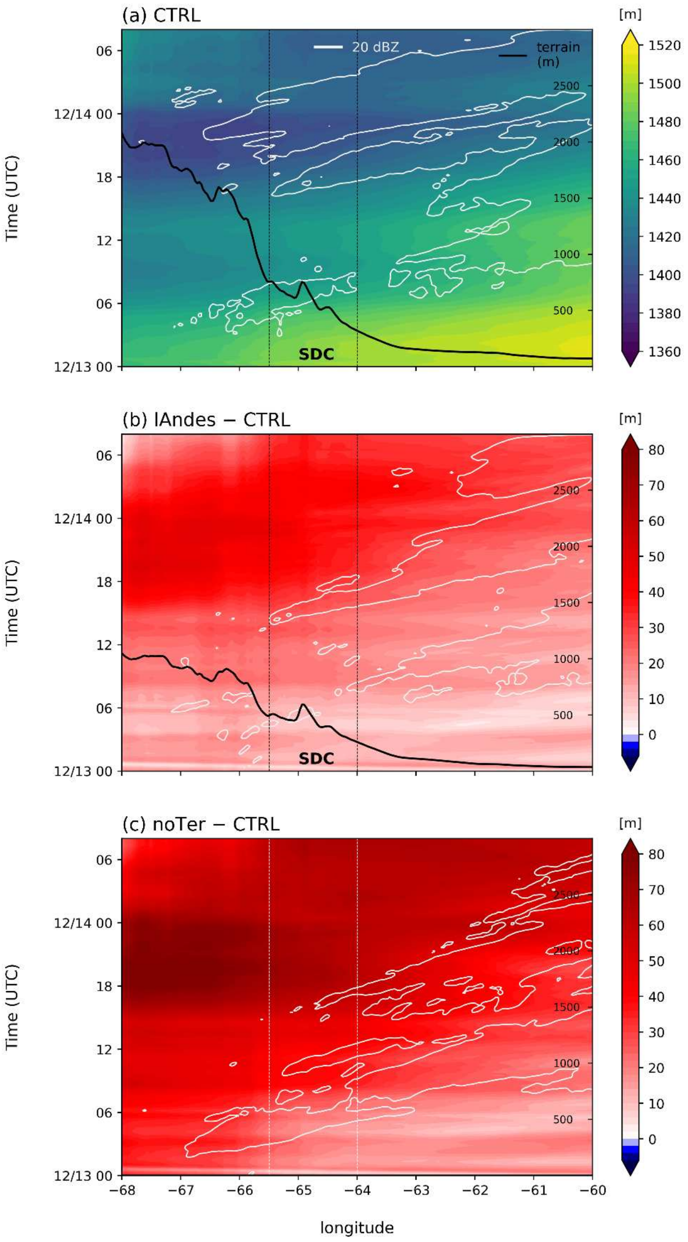

Figure 2.7: Hovmöllers of a) CTRL 850 hPa heights (shaded; m) from the 3-km domain averaged across the SALLJ domain and 20-dBZ composite reflectivity (grey contour; dBZ) from the 3-km domain averaged across the RELAMPAGO domain, b) lAndes – CTRL, c) noTer – CTRL. Longitude ranges from about 68-60°W and times are shown from 0000 UTC 13 December to 0800 UTC 14 December. Average terrain profile from the 3-km domain averaged across the SALLJ domain is shown in the black contour. The location of the SDC is shown within the dashed black lines in panels (a-b) and where the SDC would be is shown in dashed white lines in panel (c).

while the CTRL 500 hPa parcel is over the high terrain of the Andes (4400 m) near 69°W. There is not much vertical motion along the parcel trajectories as they all remained around 500 hPa (Fig.

2.8d). At 700 hPa, the trajectories are more unique for each terrain modification experiment. The flow in the CTRL run originates over the eastern Andes (3100 m) at around 600 hPa and descends off the terrain to the southeast (Figs. 2.8b, e). As the height of the Andes decreases in each modification, the trajectories become more westerly and faster (Fig. 2.8b). There is also not much vertical motion with the lAndes and noTer 700 hPa parcels (Fig. 2.8e). Finally, at 850 hPa, the CTRL and lAndes runs both highlight the presence of the SALLJ (Fig. 2.8c). The average speed of the jet in the CTRL run is 17 m s^{-1} while it is about 10 m s^{-1} in the lAndes run and has a more easterly component. There is no SALLJ signature in the noTer run because the SALLJ is partially driven by sloping terrain. Instead, the flow is weaker and generally from the west, demonstrating the clear role of the Andes in the low-level jet dynamics associated with the SALLJ (Vera et al. 2006; Insel et al. 2010; Sasaki et al. 2022).

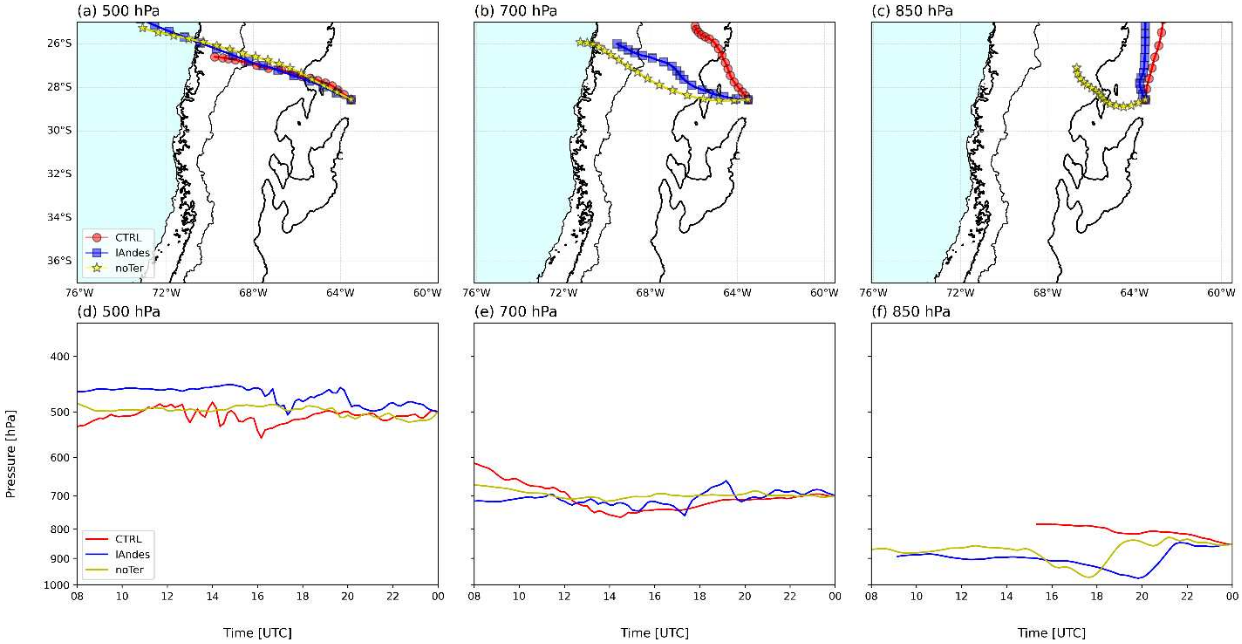

Figure 2.8: Back-trajectories calculated from 0000 UTC on 14 December every 10 minutes using RIP. Parcel locations (a-c) and time series of parcel pressures (d-f; hPa) at 500 hPa (left), 700 hPa (middle), and 850 hPa (right) for the CTRL (red), lAndes (blue), and noTer (yellow) simulations. Markers in panels (a-c) represent each hour, the 500 m terrain contour is shown in black, and the 'C' represents Córdoba.

Results from this analysis show how the Andes impact the synoptic environment in SSA. In the full-Andes simulations, the 500-hPa trough is strongest over the Chilean coast before becoming sheared apart by the Andes. A strong lee cyclone develops on the east side of the Andes in the subtropics which coincides with convection initiation. A strong SALLJ is present, which is likely strengthened by the north-south pressure gradient force induced by the lee cyclone. When the Andes are reduced by 50%, the upper-level trough crosses the Andes without being sheared apart, the resulting lee cyclone is significantly weaker, and the SALLJ, although still present, is nearly twice as slow as in the full-Andes case. When the Andes are removed completely, the upper-level trough steadily moves across southern South America, there is no lee cyclogenesis, and there is no low-level jet signature, consistent with previous studies on SALLJ dynamics (Marengo et al. 2004; Vera et al. 2006; Insel et al. 2010; Sasaki et al. 2022). The SALLJ characteristics will be further explored in the following section.

2.3.3 SALLJ

Two major components of the SALLJ are analyzed here: meridional flow and moisture. Although there is no cohesive hypothesis for moisture advection associated with the SALLJ in SSA like there is in the U.S., several studies have shown that at least 20% of the moisture associated with warm-season precipitation over the La Plata basin in SSA comes from the southern Amazon via the SALLJ (Dirmeyer et al. 2009; Martinez and Dominguez 2014; Sasaki et al. 2022). Differences between the SALLJ across terrain-modification experiments are more closely examined with Hovmöller plots of 850 hPa meridional winds and specific humidity. The evolution of meridional winds across the SALLJ domain in the full Andes runs shows two maxima in northerly winds at 850 hPa at around -20 m s^{-1} (Figs. 2.9a, b). Both maxima extend from the eastern edge of the SDC to the eastern edge of the domain (60°W). The first occurs around 1300 UTC on 13 December and has some convection associated with it, although mostly to the east of the SDC. The second maximum is connected to the large MCS event and is visible at 0000-0300 UTC on 14 December. These results agree with Sasaki et al. (2022) who identified a low-level jet in consecutive soundings from Córdoba and Villa de María del Río Seco (~175 km NNE of Córdoba) from 0000 UTC 13 December to 0600 UTC 14 December. After 0000 UTC, there is southerly flow over the higher terrain in both CTRL and noSDC cases. Some convection develops in this flow in the CTRL run but convection is mostly cut off in this transition zone in the noSDC run. In the lower Andes cases, the secondary northerly wind maximum disappears and winds across the entire domain are generally ~4-5 m s^{-1} weaker (Figs. 2.9c, d). No convection develops in the southerly flow. Once again, when the terrain is removed there is a single northerly wind maximum earlier in the period at 1200 UTC associated with convection to the east (Fig. 2.9e).

To put this event into context of the climatology, anomalies of specific humidity are calculated using the ERA5 December monthly means from 1978-2018 over the SALLJ domain. The average 850 hPa specific humidity value across the domain during December is 8.9 g kg^{-1}. This value is subtracted from the specific humidity values calculated in each WRF experiment to examine anomalous moisture in each simulation. In the CTRL run, the specific humidity anomaly is maximized at 8.1 g kg^{-1} around 1800 UTC directly downstream of the SDC and remains present until 0000 UTC (Fig. 2.10a). Convection initiates over the higher terrain of the Andes while this high moisture anomaly is present in the immediate lee of the Andes. When the SDC are removed, the moisture anomaly maximum is slightly weaker (~7.6 g kg^{-1}) and shorter lived compared to the CTRL (Fig. 2.10b). Convection initiates further west along the Andes foothills in the noSDC case, but there is no evidence of repeated initiation later in the time period. When the Andes are reduced

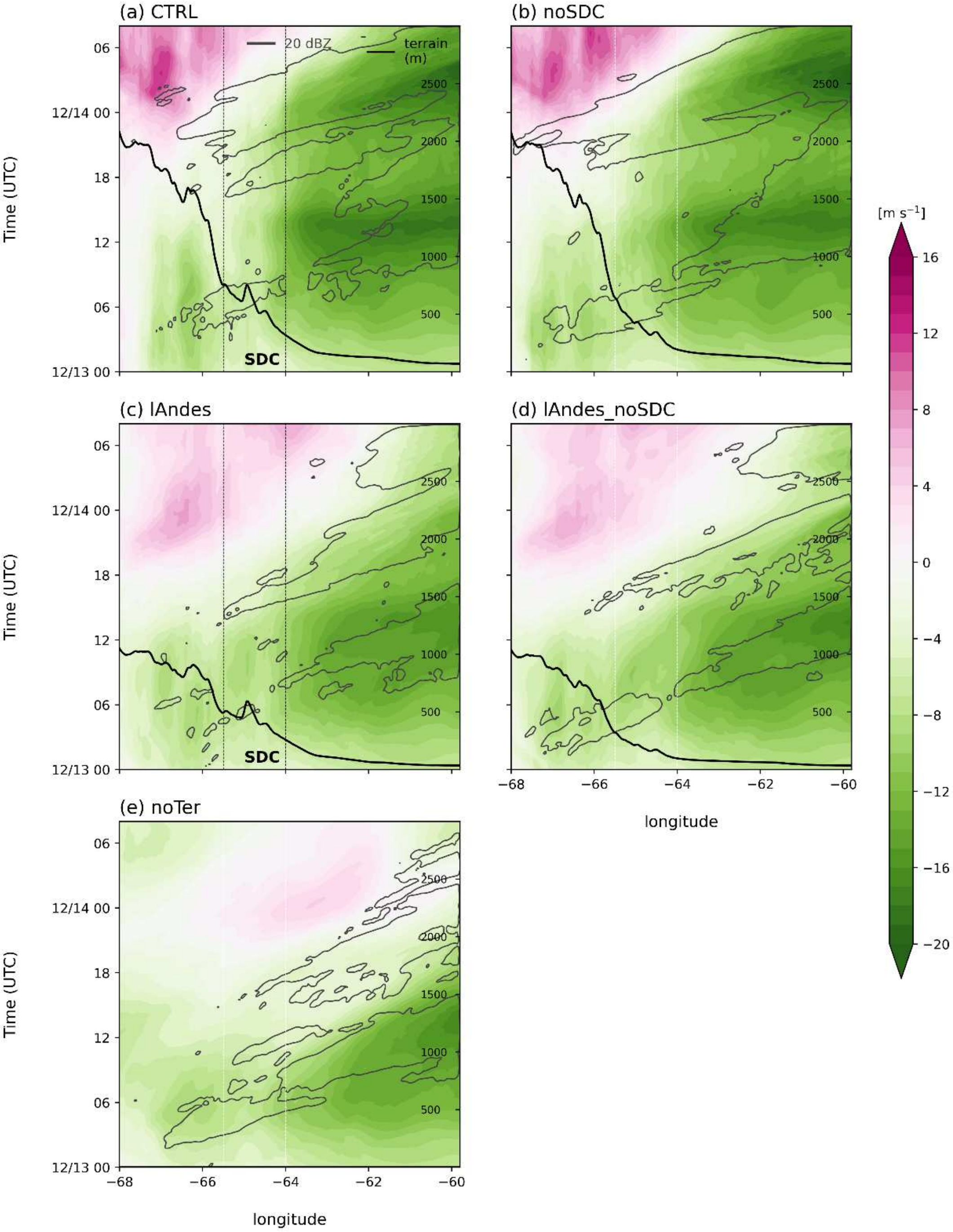

Figure 2.9: Hovmöllers of 850 hPa meridional winds (shaded; m s^{-1}) from the 3-km domain averaged across the SALLJ domain and 20-dBZ composite reflectivity (grey contour; dBZ) from the 3-km domain averaged across the RELAMPAGO domain. a) CTRL, b) noSDC, c) lAndes, d) lAndes_noSDC, and e) noTer simulations. Longitude ranges from about 68-60°W and times are shown from 0000 UTC 13 December to 0800 UTC 14 December. Average terrain profile from the 3-km domain averaged across the SALLJ domain is shown in the black contour. The location of the SDC is shown within the dashed black lines in panels (a,c) and where the SDC would be is shown in dashed white lines in panels (b,d,e).

by 50%, there is no longer a moisture maximum along the foothills (Figs. 2.10c, d). Instead, specific humidity is maximized east of 64°W. Anomalously dry air begins to enter the domain around 1800 UTC and remains over the Andes through the end of the period. This dry air likely inhibits convection from developing off the Andes and corresponds to the shift in winds (Figs. 2.9c, d). There are few differences between the lAndes and lAndes_noSDC runs, suggesting that the Andes have a larger impact than the SDC on convective development in this case, as was also shown in RH16. When the terrain is removed completely, dry air quickly spreads east, and any convection that does develop is confined to anomalously moist regions only (Fig. 2.10e).

These results are also visible when looking at a map of 850 hPa specific humidity and winds at 2100 UTC on 13 December (Fig. 2.11). In the full Andes runs (CTRL and noSDC), the greatest moisture (>15 g kg^{-1}) is confined to the eastern edge of the Andes and downstream of the SDC region north of 33°S (Figs. 2.11a, b). Winds are strong from the north northeast at around 15 m s^{-1} in both simulations. There are very slight differences between the two, with moisture extending further south in the CTRL run and winds about 5 m s^{-1} stronger directly downstream of the SDC compared to the noSDC run. When the Andes are halved, dry air (<6 g kg^{-1}) is concentrated over and to the west of the SDC (Figs. 2.11c, d). Vertical cross sections of specific humidity taken south of Córdoba also show the environment between the Andes and SDC from the surface to near 4 km is 8-10 g kg^{-1} drier when the Andes are reduced compared to when the Andes are kept at full height (not shown). At 850 hPa, the greatest moisture in the lower-Andes runs is not directly downstream of the foothills but is further north and east compared to the full Andes runs (Figs. 2.11c, d). Winds throughout the domain have a more westerly component, especially in the drier air over the SDC, and are about 5 m s^{-1} weaker north of the SDC. Once again, there are much smaller differences between the lAndes and lAndes_noSDC runs compared

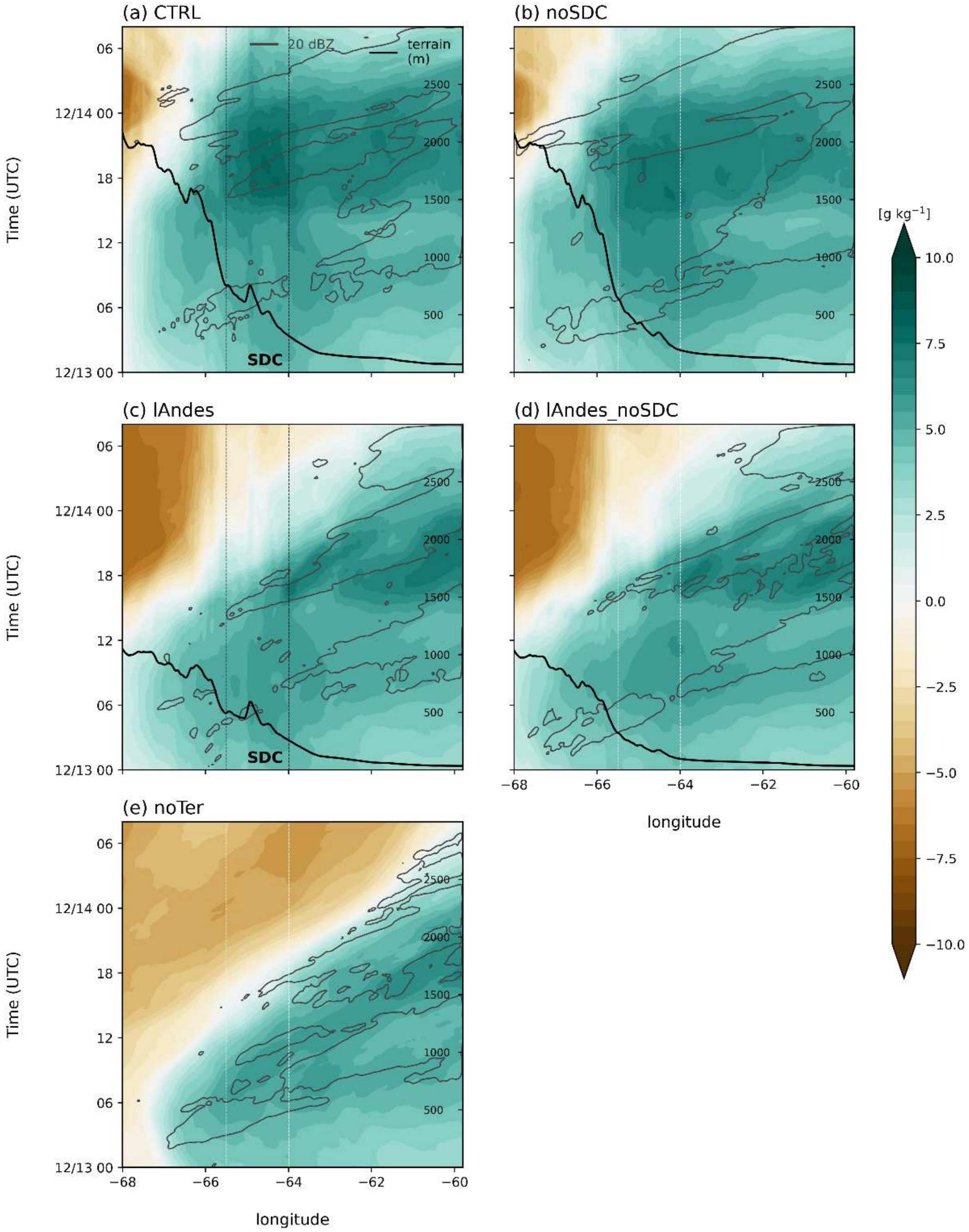

Figure 2.10: Hovmöllers of 850 hPa specific humidity anomalies (shaded; g kg^{-1}) from the 3-km domain averaged across the SALLJ domain and 20-dBZ composite reflectivity (grey contour; dBZ) from the 3-km domain averaged across the RELAMPAGO domain. Anomalies were calculated from monthly mean ERA5 reanalysis data from 1978-2018. a) CTRL, b) noSDC, c) lAndes, d) lAndes_noSDC, and e) noTer simulations. Longitude ranges from about 68-60°W and times are shown from 0000 UTC 13 December to 0800 UTC 14 December. Average terrain profile from the 3-km domain averaged across the SALLJ domain is shown in the black contour. The location of the SDC is shown within the dashed black lines in panels (a,c) and where the SDC would be is shown in dashed white lines in panels (b,d,e).

to the full Andes and reduced Andes runs suggesting the Andes play a larger role in the convective development compared to the SDC. In the noTer run, winds are completely from the west across the entire domain and drier air has advanced even further east to 63-64°W (Fig. 2.11e).

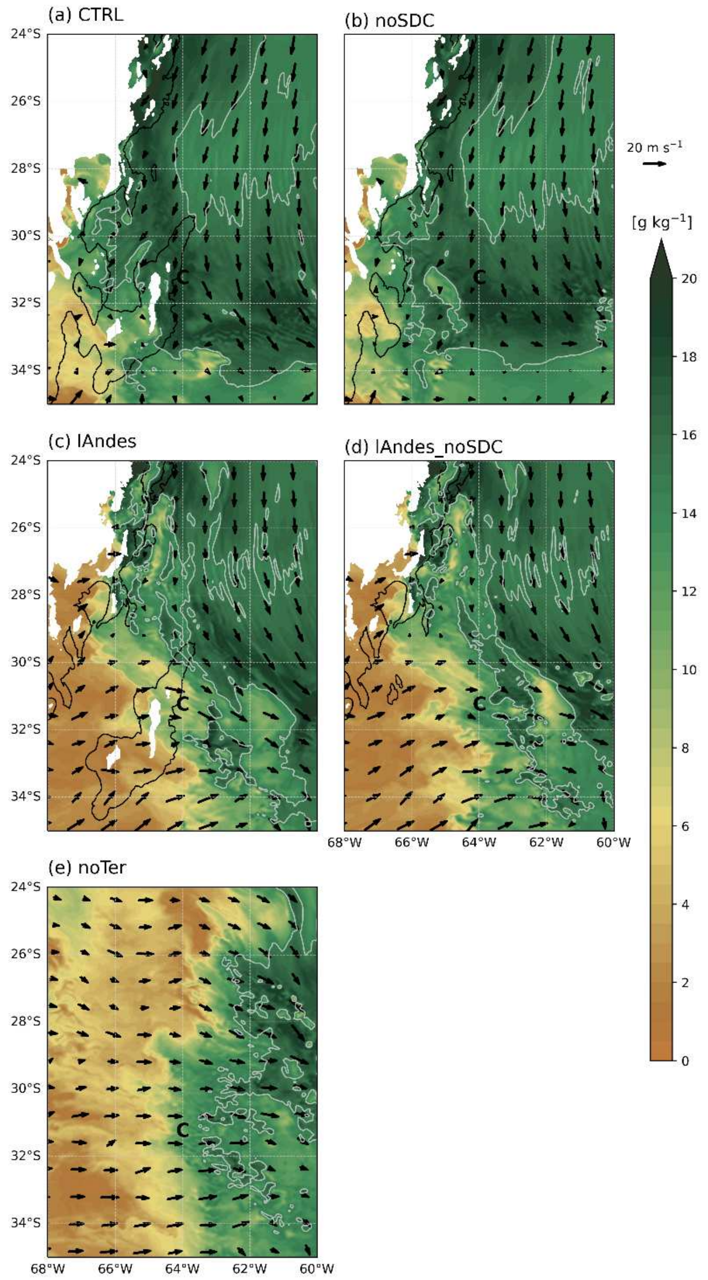

Figure 2.11: 850 hPa specific humidity (shaded; g kg^{-1}) and winds (arrows; m s^{-1}) from the 3-km domain at 2100 UTC 13 December 2018, shown across the SALLJ domain. a) CTRL, b) noSDC, c) lAndes, d) lAndes_noSDC, and e) noTer simulations. The 15 g kg^{-1} contour is shown in grey. The 500 m terrain contour is shown in black and the 'C' represents Córdoba.

Results from this analysis highlight the relative importance of the Andes and SDC on the SALLJ. The greatest differences in low-level meridional winds and moisture are seen when the Andes are reduced or removed compared to when the SDC are removed. In the full-Andes cases, two maxima in northerly winds are identified over the plains which coincide with convective development. The largest moisture anomaly occurs along the SDC longitude towards the beginning of the second northerly wind maximum. In the half-Andes cases, only one wind maximum is identified in the morning hours over the plains. The winds are 5 m s^{-1} weaker across the domain and dry air surges in from the west several hours earlier compared to the full-Andes cases which prevents convection from developing over the foothills in the afternoon and evening. When the Andes are completely removed there is no low-level jet signature and dry air restricts convective development to the eastern portion of the domain. These results suggest the unique height of the Andes is essential in the maintenance of the SALLJ and MCS development under strong synoptic conditions.

2.3.4 MCS evolution

The detailed convective characteristics of the MCSs for each experiment will be analyzed in future work. However, a summary of the MCS development in each of the simulations is shown in Figure 2.12. At 2100 UTC on 13 December, convection is beginning to develop over the southern SDC in the CTRL run and over the Andean foothills (Fig. 2.12a). Additionally, there is a larger system that persisted the entire day over Uruguay and the eastern edge of Argentina near Buenos Aires. At this time, the lee cyclone has reached its lowest pressure (Fig. 2.7a). About 2-3 hours earlier, 850 hPa moisture is maximized over the SDC (Fig. 2.10a) and northerly winds are beginning to increase further east (Fig. 2.9a). In the noSDC run, convection initiation occurs over the Andes at about the same time, and the large system to the east is also present (Fig. 2.12b). Six hours later, convection has grown upscale into a large linear feature that is oriented northwest to southeast and extends from about 66°W to the Atlantic Ocean in both the CTRL and noSDC runs (Figs. 2.12f, g). The MCS slowly moves to the northeast, and by 0600 UTC is still a strong linear system that has just passed over Córdoba (Figs. 2.12k, l). Interestingly, more rain falls across the RELAMPAGO domain when the SDC are removed compared to the CTRL (noSDC rain accumulation is 104.6% of CTRL; Table 2.2). Given the environmental similarities between the two simulations and the strength of the synoptic flow, it is not surprising that both full-Andes cases produce a strong MCS.

When comparing the full-Andes runs to the half-Andes runs, some significant differences stand out. Weaker convection initiates over the southern SDC around 1600 UTC in the lAndes case and there is no development off the Andean foothills like in the CTRL. The primary forcing for convection in the half-Andes runs is the cold front rather than topography. At 2100 UTC, both lAndes and lAndes_noSDC cases have a smaller linear system already well into the domain (Figs. 2.12c, d). There are no isolated features over the Andes at this time like there are in the full-Andes simulations (Figs. 2.12a, b). At 0300 UTC, the line has already passed Córdoba in both half-Andes runs (Figs. 2.12h, i). The lAndes MCS is narrower and does not extend as far east as the CTRL and noSDC MCSs. The lAndes_noSDC MCS is not nearly as intense as either the lAndes or full-Andes MCSs at this time. However, three hours later there seems to be some reinvigoration, and the convective lines between the lower-Andes cases are more similar (Figs. 2.12m, n). Accumulated rain across the RELAMPAGO domain in the lAndes run is about 56% of the CTRL run, while it is 67% of the CTRL in the lAndes_noSDC run (Table 2.2). When the Andes are reduced by 50%, rainfall is also reduced by nearly 50%. Similar to the full-Andes cases, when the

SDC are removed, accumulated rain increases. The noTer simulation does not end up producing an MCS in the overnight hours, and there is weaker isolated convection scattered across the eastern portion of the domain (Figs. 2.12e, j, o). Accumulated rainfall is about 46% of the CTRL which corresponds well with the drier air observed in Figs. 2.10e and 2.11e.

Table 2.2: Accumulated rainfall from the 3-km domain (mm) summed across the RELAMPAGO domain from 1500 UTC 13 December to 0800 UTC 14 December (top) and from 1500 UTC 25 January to 1800 UTC 26 January (bottom). The percentage of the CTRL is shown in parentheses.

run	CTRL	noSDC	lAndes	lAndes_noSDC	noTer
December	855029	894666 (104.6%)	476990 (55.8%)	573149 (67.0%)	394887 (46.2%)
January	1864352	1384152 (74.2%)	1721603 (92.3%)	1183450 (63.5%)	856166 (45.9%)

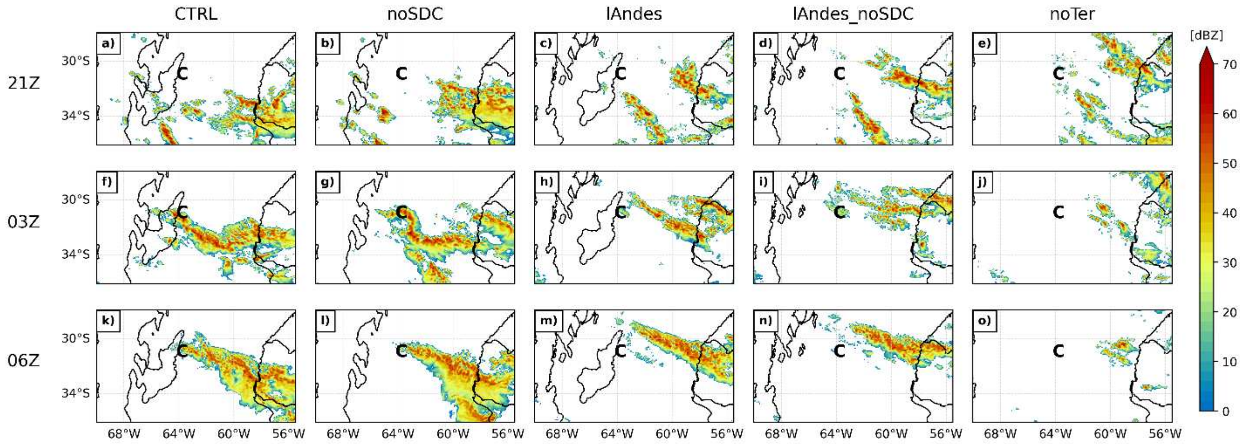

Figure 2.12: Reflectivity at 3 km MSL for each simulation (column) at 2100 UTC 13 December and 0300 and 0600 UTC on 14 December. The 500 m terrain contour is shown in black and the ‘C’ represents Córdoba.

In all of the terrain-modification experiments, an MCS develops due to the passage of a cold front associated with strong synoptic forcing. However, the timing, location, and intensity of the MCS differs significantly between runs. In the full-Andes runs, the MCS reaches peak intensity around 0300 UTC 14 December (midnight local time). When the Andes are reduced by 50%, the resulting MCSs move faster to the east and are smaller and weaker than the full-Andes MCSs.

Additionally, the accumulated rainfall is greater when the SDC are removed. One hypothesis for this is the SDC may interfere with the cold front structure and progression under strong synoptic forcing. Plots of equivalent potential temperature show a more cohesive cold front when the SDC are removed (not shown) supporting this hypothesis, but these perspectives will be explored in future work.

2.4 25-26 January 2019: Weakly forced case

2.4.1 Overview

In order to more carefully understand the interactions between the synoptic flow and terrain in SSA, a second set of terrain-modification simulations was conducted on the 25-26 January 2019 case. This was another intense upscale growth case that featured convective echo tops greater than 20 km in height and had the greatest number of lightning flashes captured by the lightning mapping array network during RELAMPAGO (Schumacher et al. 2021; Nesbitt et al. 2021; Lang et al. 2020). This case was chosen because it was not strongly synoptically forced like the December case. A shortwave trough passed over the southern Andes at around 45°S while the flow over Córdoba was weakly zonal at 500 hPa (Fig. 2.13a). There was a significant amount of moisture within the region which was funneled south by the SALLJ and maximized at 18 g kg^{-1} over the SDC (Fig. 2.13b). Specific humidity values greater than 10 g kg^{-1} were seen as far south as 48°S and appeared to wrap around the high pressure over the Atlantic. Unlike the strongly forced case, the MCS that formed remained tied to the SDC for an extended period of time, and the WRF CTRL simulation did a reasonable job of capturing the intense convection and life cycle of upscale growth in the region (Figs. 2.13c, d).

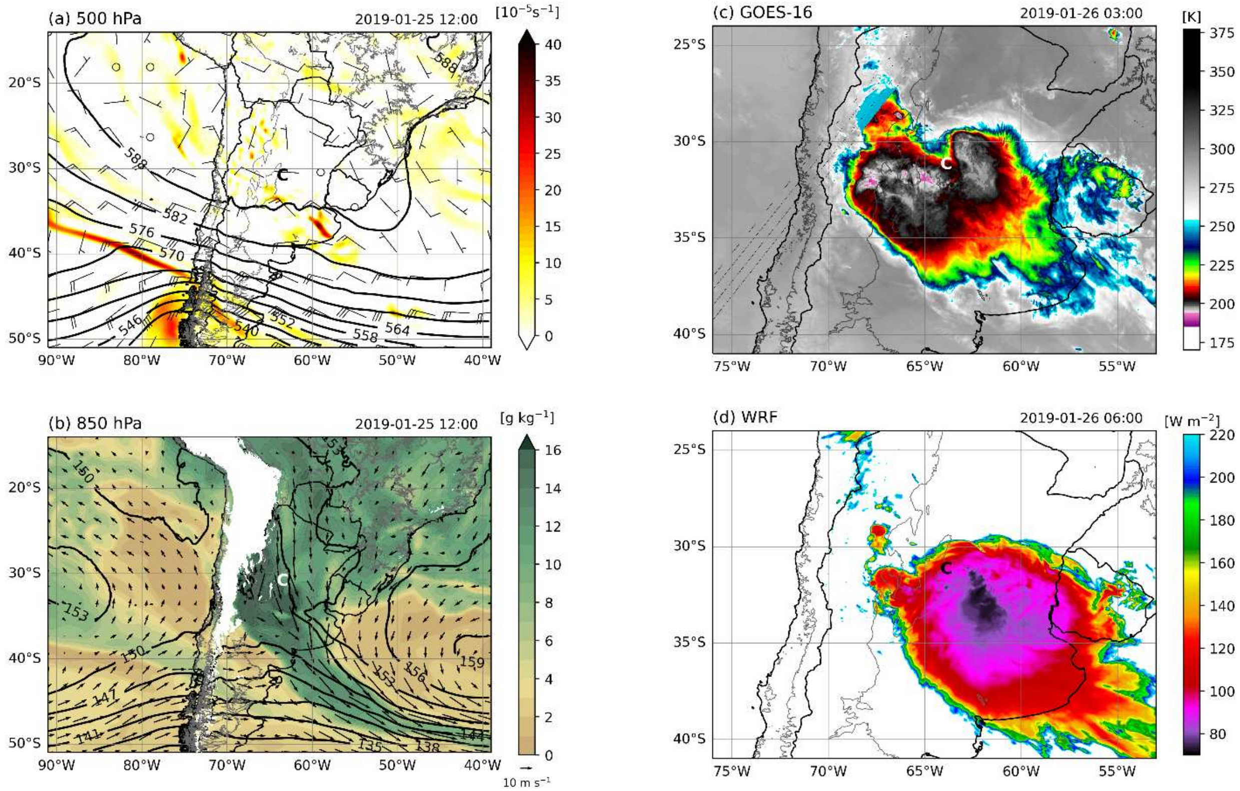

Figure 2.13: a) 500 hPa geopotential heights (contoured; dm), relative vorticity (shaded; 10^{-5} s^{-1}), and winds (barbs; m s^{-1} where a half barb = 5 m s^{-1} and a full barb is 10 m s^{-1}) from ERA5 reanalysis at 1200 UTC 25 January 2019, b) 850 hPa geopotential heights (contoured; dm), specific humidity (shaded; g kg^{-1}), and winds (arrows; m s^{-1}) from ERA5 reanalysis at 1200 UTC 25 January 2019, c) *GOES-16* Channel 14 IR brightness temperatures (K) at 0300 UTC 26 January 2019, and d) outgoing longwave radiation (W m^{-2}) from the 3-km CTRL simulation at 0600 UTC 26 January 2019. The 500 m terrain contour is shown in grey and the 'C' represents Córdoba.

2.4.2 Synoptic scale and SALLJ

Hovmöller plots of 500 and 850 hPa heights clearly show that the synoptic activity was much weaker compared to the strongly forced case (Fig. 2.14). The minimum average 500 hPa geopotential height of 5672 m is achieved just west of the Andes between 0600-1200 UTC on 25 January (Fig. 2.14a). This is about 100 m higher than the trough on 13 December. Interestingly, when the Andes are reduced and removed, the 500 hPa shortwave does not strengthen like in December (Figs. 2.14b, c). At 850 hPa, lee cyclogenesis is visible in the CTRL run between 1800-0000 UTC over the higher terrain of the Andes, but again this is not as strong as the strongly forced case and the minimum geopotential height achieved is 1452 m (about 60 m higher than the December lee cyclone). Convection also starts to develop when the lee cyclone is maximized. Unlike the strongly forced case, there is a secondary peak in convection that is tied to the terrain between the Andes and SDC. This back-building component is not as visible when the Andes are lowered and is not present at all when the terrain is removed. Similar to the strongly forced case, geopotential heights in the lAndes and noTer simulations are higher than the CTRL, highlighting the influence of the terrain on the development of the lee cyclone in a weak synoptic forcing case.

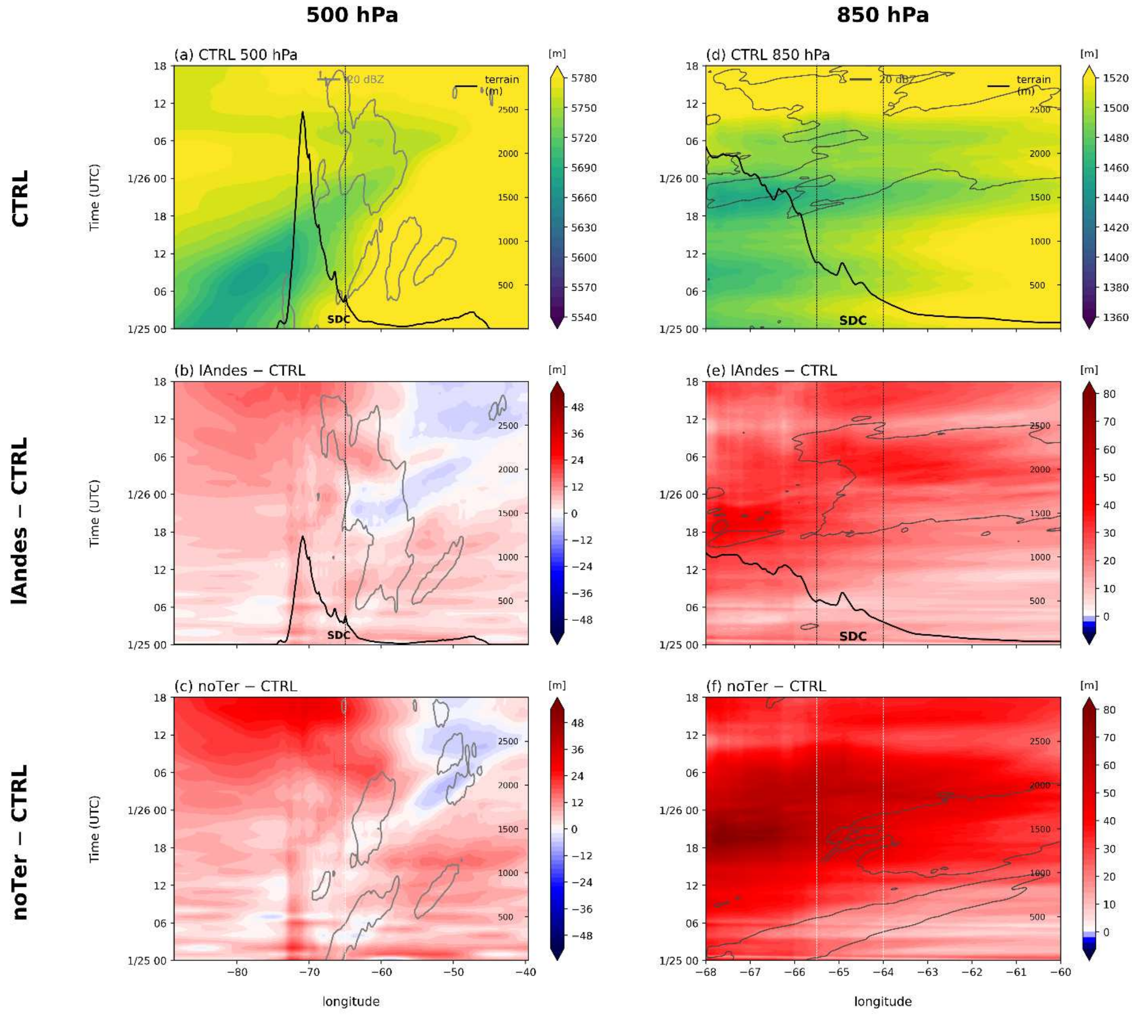

Figure 2.14: a-c) as in Fig. 2.5 and d-f) as in Fig. 2.7 but for the weakly forced case. Longitude ranges from about 90-40°W for (a-c) and about 68-60°W for (d-f) and times are shown from 0000 UTC 25 January to 1800 UTC 26 January.

The strength of the 850 hPa jet is also analyzed across terrain-modification runs for the weakly forced case. There is a single maximum in northerly winds located just east of 64°W, downstream of the SDC (Fig. 2.15). The strongest northerly flow occurs between 0000-1500 UTC on 25 January, where winds reach a maximum magnitude of 18-20 m s^{-1} (on average) at 0900 UTC for all runs. This area of enhanced northerlies (>10 m s^{-1} magnitude) extends further east and west when the SDC are removed and when the Andes are removed (Figs. 2.15b, d, e). This timing agrees with Sasaki et al. (2022) who show shorter duration jets are driven more by boundary layer processes and the diurnal cycle. Weak southerly flow is observed in the CTRL and noSDC runs over the higher terrain starting around 0000 UTC on 26 January (Figs. 2.15a, b). This flow is about 5 m s^{-1} weaker than the southerly flow in the strongly forced case. There are few differences between the CTRL and noSDC wind patterns near the higher terrain. Interestingly, the back-building convection visible in the CTRL run develops in southerly flow and this back-building component is not visible when the SDC are removed.

Moisture anomalies are also calculated for this case using the January monthly means from ERA5. The average 850 hPa specific humidity across the domain during January is 9.7 g kg^{-1}, about 1 g kg^{-1} moister than December. Hovmöller plots of 850 hPa specific moisture anomalies show increased moisture over the higher terrain early in the period from 0000-1800 UTC on 25 January (Fig. 2.16). These values are maximized in the CTRL and noSDC cases at 7.5 and 7.7 g kg^{-1}, respectively (Figs. 2.16a, b). They are about 0.5 g kg^{-1} weaker when the Andes are halved, but the moisture patterns are similar between the full-Andes and half-Andes runs (Figs. 2.16c, d), unlike in the strongly forced case (Fig. 2.10). Vertical cross sections of specific humidity averaged south of Córdoba at 2100 UTC on 25 January show moisture is present as high as 8 km above ground, which is about 3 km deeper than moisture available in December (not shown). The region

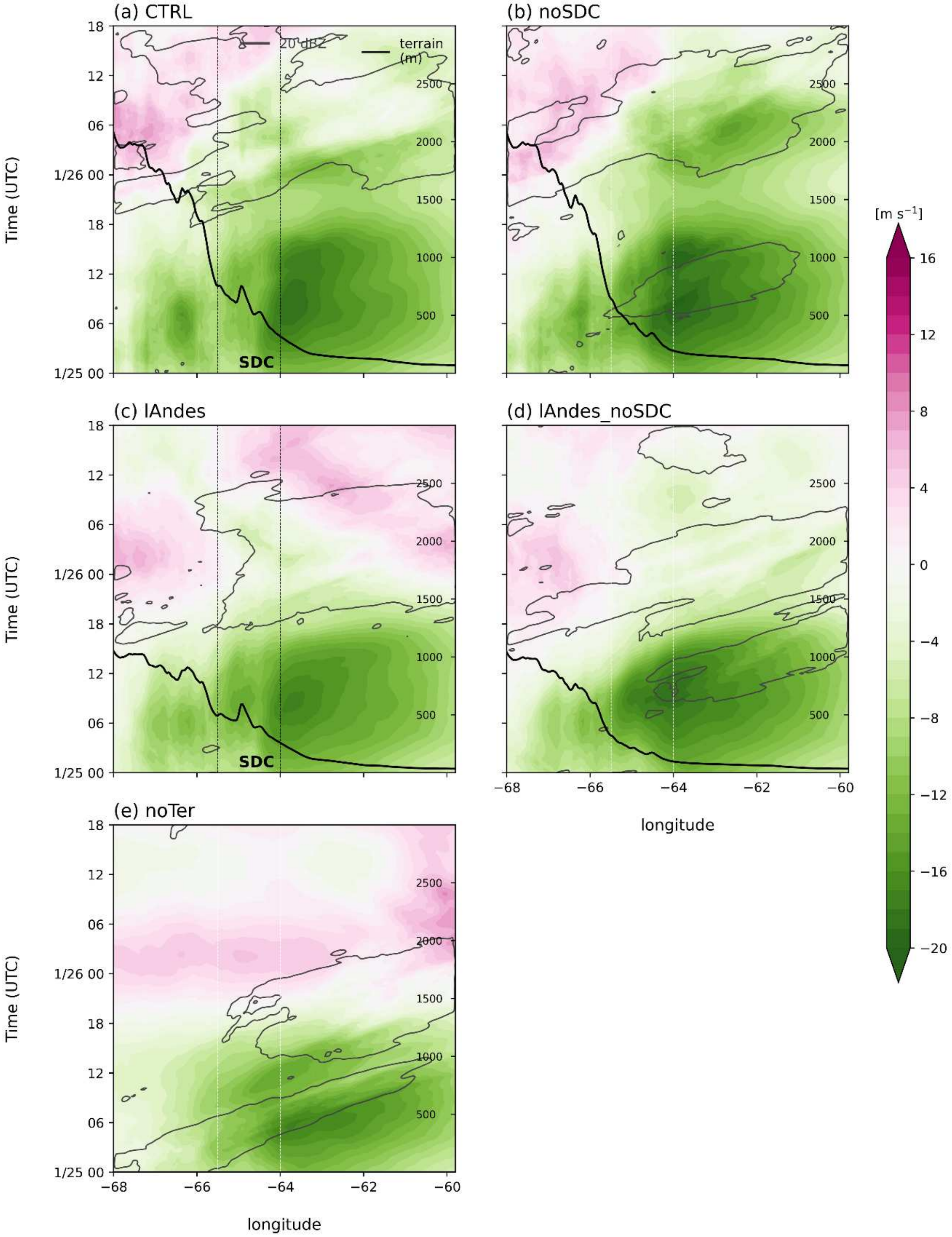

Figure 2.15: As in Fig. 2.9 but for the weakly forced case. Times are shown from 0000 UTC 25 January to 1800 UTC 26 January.

between the Andes and SDC in the CTRL simulation has equivalent potential temperature values about 10 K warmer than the strongly forced CTRL. Additionally, specific humidity values greater than 20 g kg^{-1} extend more than 500 km downstream of the SDC at the surface in the weakly forced runs, while the moisture maximum is only 100 km wide in the strongly forced runs and is not directly connected to the SDC.

Convection generally starts to develop at the end of the high-moisture period to the west of the SDC in each simulation around 1800 UTC on 25 January. Moisture is only 1-2 g kg^{-1} higher than normal over the eastern plains across all the simulations, possibly explaining why the convection was more focused on the terrain in this case compared to the strongly forced case with more widespread moisture anomalies east of the SDC. The atmosphere tends to dry out during and after the convection, especially right downstream of the SDC in the CTRL and lAndes runs (Figs. 2.16a, c). In fact, at 1200 UTC on 26 January, moisture anomalies are 2-4 g kg^{-1} lower in the CTRL and lAndes runs compared to the noSDC and lAndes_noSDC runs at 64°W (Figs. 2.16a-d). When the Andes are removed, moisture anomalies are generally weaker to the east compared to when the Andes are present, and there is slightly drier air (~2 g kg^{-1} less than normal) present over the western domain (Fig. 2.16e). There is no convective development later in the period since there is no terrain to help initiate convection.

Results from this weakly forced case analysis provide an important contrast to those from the strongly forced case. First, the upper-level flow was significantly weaker than in the strongly forced case, and 500 and 850 hPa heights increased when the Andes were reduced/removed. A lee cyclone still developed in the evening hours with the full-Andes but it was not as deep as in the strongly forced case. The SALLJ was also present in this weakly forced case, but it was located further west and a single maximum in northerly winds was identified in the morning hours,

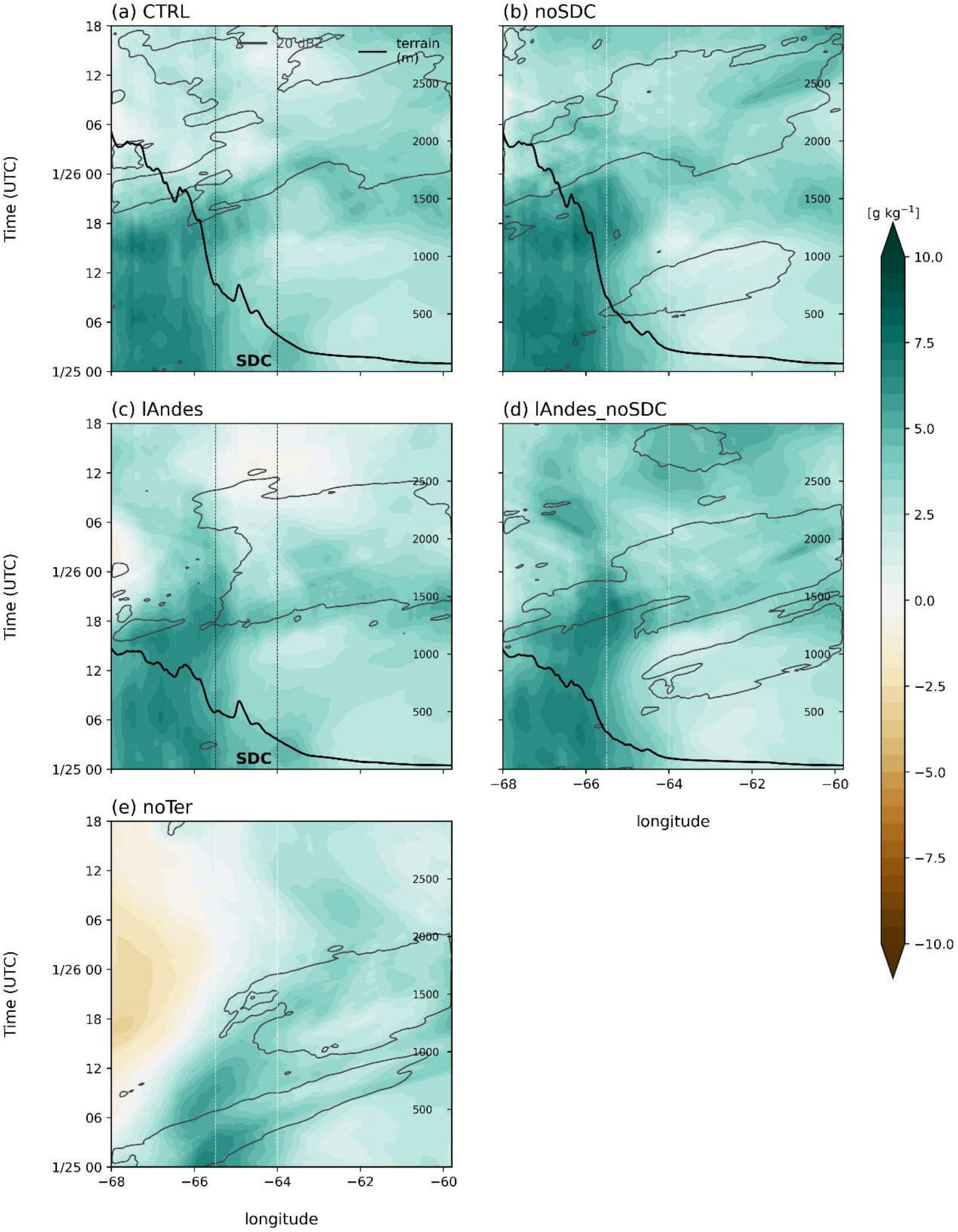

Figure 2.16: As in Fig. 2.10 but for the weakly forced case. Times are shown from 0000 UTC 25 January to 1800 UTC 26 January.

consistent with shorter duration jets identified in Sasaki et al. (2022). The jet strength was weaker when the Andes were reduced, but the location and timing was similar to the full-Andes. The greatest moisture anomalies were concentrated to the west of the SDC in the full-Andes and half-Andes runs, and there was no intrusion of dry air like in the strongly forced case. The environments with full-Andes and half-Andes were much more similar than the strongly forced case, but the timing and location of convection was considerably different across runs.

2.4.3 MCS evolution

The life cycle of the storm is shown at three times in Figure 2.17. At 2100 UTC on 25 January, convection initiates over the Andes and the southern SDC in the CTRL run (Fig. 2.17a). Similar initiation over the Andes is seen in the noSDC case, but the secondary convection around 66°W is not visible (Fig. 2.17b). Six hours later, a large convective line develops in the CTRL run that stretches from the SDC to the Atlantic (Fig. 2.17f). In the noSDC run, the convective line remains tied to the Andean foothills but does not extend as far east as the Atlantic (Fig. 2.17g). At 1500 UTC on 26 January, there is significant precipitation northwest of Córdoba between the foothills and the SDC in the CTRL run (Fig. 2.17k). At 3 km MSL, the intensity is generally less than 40 dBZ. This back-building and direct connection to the SDC is removed when the SDC are removed and weaker convection is visible across the eastern plains (Fig. 2.17l). The accumulated rainfall across the RELAMPAGO domain is less in the noSDC run compared to the CTRL (74% of CTRL; Table 2.2), with the largest differences occurring between 00-06 UTC 26 January (not shown).

When the Andes are reduced by 50%, a convective line still forms when the SDC are present (Fig. 2.17c). This line is within the domain at 2100 UTC, suggesting that convective initiation begins earlier when the Andes are reduced and moves eastward faster. At 0300 UTC, the line is positioned just south of Córdoba, but is oriented more zonally compared to the MCS in the CTRL run (Fig. 2.17h). At 1500 UTC, weak back-building in the northwest portion of the domain is visible, although not as intense as in the CTRL run (Fig. 2.17m). This signature is also visible in the Hovmöller plots, and the total rainfall summed across the RELAMPAGO domain for the lAndes case is second highest (92% of the CTRL; Table 2.2). When the Andes are reduced and SDC are removed, a convective line does not develop (Figs. 2.17d, i, n). Isolated convection downstream of the Andes is visible at 2100 UTC (Fig. 2.17d), and a weaker, un-organized system is present at 0300 UTC (Fig. 2.17i). Only isolated convection remains at 1500 UTC (Fig. 2.17n), and the accumulated rainfall is 63.5% of the CTRL. These results are similar for when the terrain is completely removed (Figs. 2.17e, j, o). A smaller system still develops but is likely driven by the diurnal sea-breeze and a weaker baroclinic trough.

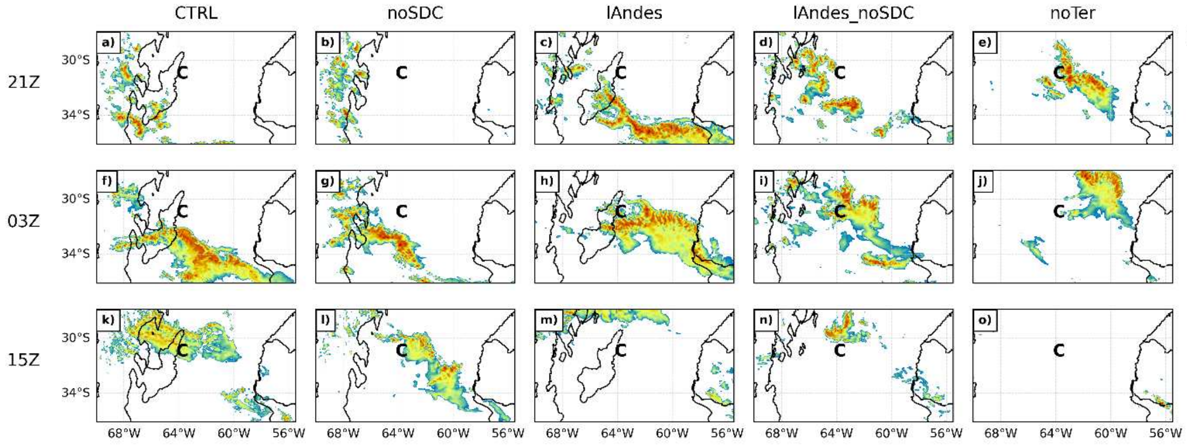

Figure 2.17: As in Fig. 2.12 but for the weakly forced case. Times displayed are 2100 UTC on 25 January and 0300 and 1500 UTC on 26 January.

Similar to the strongly forced case, convection develops in each terrain modification experiment but the location, timing, and intensity of the convection varies significantly. A robust MCS develops in the CTRL and lAndes simulations that produces similar amounts of rainfall.

There is a strong sign of back-building in these runs. When the SDC are removed, the rain accumulation is reduced by nearly 25% and there is no strong connection to the topography. These results contrast with those from the strongly forced case where the height of the Andes appeared to play a more important role in the MCS evolution compared to the SDC. The environments under the weakly forced case for the full-Andes and half-Andes runs were similar, despite producing different MCSs, suggesting the SDC may be more important in convective development under weak synoptic conditions.

2.5 Discussion

Two RELAMPAGO cases in December 2018 and January 2019 were chosen since they both produced a large MCS that resulted in severe weather, flooding, and extreme lightning flash rates, but the synoptic forcing supporting convective development and upscale growth was significantly different between the two. A strong synoptic trough passed over the Andes during the December case which led to the development of a robust lee cyclone in the Córdoba region. During the January case, however, a weak shortwave passed through the mid-latitudes with zonal flow over the Córdoba region that resulted in a weaker lee cyclone. In the simulations, when the Andes are reduced by 50% for the strongly forced case, the upper-level trough is able to cross the southern Andes without being sheared apart. A lee cyclone also develops downstream, but it is not as intense as when the Andes are at full height. The impact of reducing the Andes during the weakly forced case is a slightly weaker shortwave trough aloft and a weaker lee cyclone as well.

In terms of the SALLJ, two northerly wind maxima at 850 hPa are observed in the CTRL and noSDC runs for the strongly forced case that occur over the eastern plains. When the Andes are reduced, these wind maxima are also reduced in magnitude. In the weakly forced case, however, a single northerly wind maximum is observed directly downstream of the SDC in all terrain-modification experiments in the overnight/morning hours. Meridional wind patterns are similar across experiments in the weakly forced case. Although the weakly forced case was not included in the sounding analysis by Sasaki et al. (2022), we hypothesize this event would fit into their 'shorter duration jet' classification. To further explore the impact of terrain on the SALLJ under strong and weak synoptic environments, the meridional flow was averaged across the northern half of the SALLJ domain at different heights (Fig. 2.18). Under strong synoptic forcing, the jet in the full-Andes runs has a broad maximum of 10 m s^{-1} which stretches from ~900-775 hPa (Fig. 2.18a). When the Andes are halved though, the depth of the jet is smaller, reaching a maximum of about 7.5 m s^{-1} around 850-825 hPa. There is no clear jet signature in the noTer run, consistent with the Hovmöller plots and the ingredients necessary for a SALLJ (i.e. sloping terrain). These results agree well with Sasaki et al. (2022) who show that long duration jets are often deeper and occur under stronger synoptic flow. The height of the Andes appears to control the depth of the jet, and this may explain why jets in the U.S. are often shallower, consistent with the lower height of the Rockies. Under weak synoptic forcing, the depth of the jet does not change between full-Andes and half-Andes runs (Fig. 2.18b). The maximum is achieved around 900-850 hPa and is 2-4 m s^{-1} weaker than the strongly forced case. These jets are driven by boundary layer processes rather than the synoptic flow.

Regarding the moisture associated with the SALLJ, higher values of specific humidity are observed at 850 hPa during the weakly forced case compared to the strongly forced case. However, taking climatology into context, the strongly forced case has higher anomalous moisture values compared to the weakly forced case. In addition to differences in moisture, the locations of the moisture maxima are different between the two cases. In December, the moisture maximum is

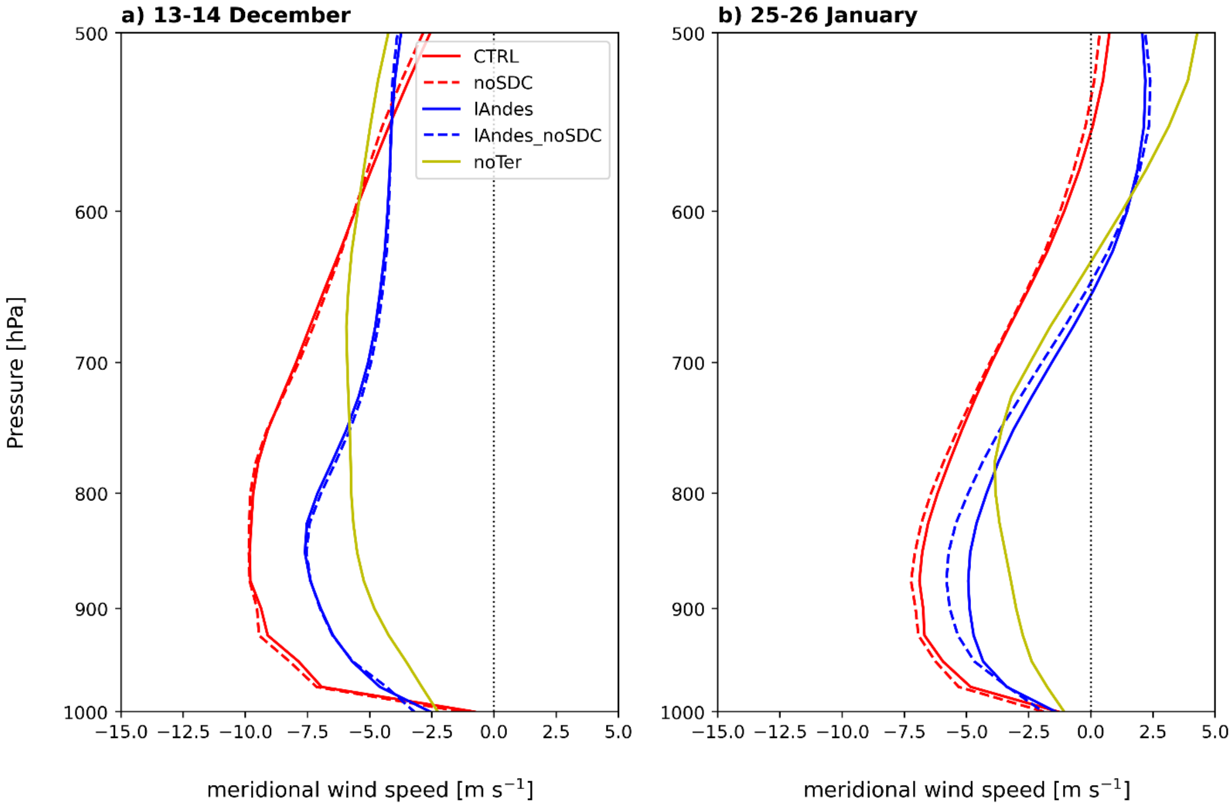

Figure 2.18: Vertical profiles of meridional wind speed averaged across the northern SALLJ domain (north of 30°S) and across times a) 0000 UTC 13 December to 0800 UTC 14 December and b) 0000 UTC 25 January to 1800 UTC 26 January. CTRL (red), lAndes (blue), and noTer (yellow) simulations.

concentrated downstream of the SDC, whereas it is further west over the higher terrain of the Andes during January. This agrees with Rasmussen et al. (2014) who showed a shift in moisture and convection to the west during the summer months. When the Andes are reduced during the strongly forced case, anomalously dry air is concentrated over the mountains later in the period which prevents convection from developing over the terrain. However, during the weakly forced case when the Andes are reduced, the moisture patterns are quite similar to when the Andes are at full height.

The broad convective patterns analyzed are also fairly different between the two cases. In the strongly forced case, a large MCS develops in each terrain-modification experiment simply due to the strong synoptic forcing and low-level convergence associated with the robust lee cyclone interacting with the northerly SALLJ (RH16; Piersante et al. 2021). The position and intensity of the MCS are similar between the CTRL and noSDC runs suggesting the SDC do not have a large impact on the overall structure of the system. The accumulated rainfall is also highest in the CTRL and noSDC runs during December. When the SDC are removed, rainfall actually increases during the strongly forced case. In this case, the SDC may interfere with the passing cold front which could reduce precipitation. In the weakly forced case, however, the most rain falls in the CTRL and lAndes runs. Both simulations have convection redevelop between the Andes and SDC which does not occur when the SDC are removed. This once again highlights the importance of the SDC in forcing convection under weak synoptic conditions. In both December and January cases, convection tends to move off the terrain faster when the Andes are reduced. Additionally, when the terrain is removed, a single system develops, moves towards the east, and dissipates, as one might expect an idealized MCS to do. These results all suggest that under strong synoptic conditions, the height of the Andes plays a larger role in modulating the environment and the evolution of the MCS compared to under weaker synoptic conditions when the SDC act to enhance convective development and keep the MCS tied to the terrain.

2.6 Conclusions

Two RELAMPAGO cases of upscale growth are studied using terrain modification WRF simulations to investigate how the convective development and synoptic-scale environmental conditions varied in strongly and weakly forced synoptic environments. Five experiments were run on the 13-14 December 2018 case, which exhibited a deep upper-level trough and strong lee cyclogenesis, and another five simulations were run on the 25-26 January 2019 case, which exhibited a weak shortwave trough pass over the Andes in the midlatitudes. Each case study had a CTRL simulation where the terrain was not modified, a noSDC run where the SDC were removed, a lAndes run where the Andes were reduced by 50% and SDC were kept at the same height, a lAndes_noSDC run where the Andes were halved and SDC were removed, and a noTer run in which terrain was reduced to 0 m across the domains. Analyses of the terrain modification simulations for both cases led to the following general conclusions:

1) Under strong synoptic flow, the height of the Andes, rather than the SDC, has a greater impact on the environment and convective growth associated with MCSs. A large MCS develops in all scenarios simply due to synoptic forcing, but the environment and SALLJ are significantly altered when the Andes are reduced.
2) Under weak synoptic flow, the SDC have a more direct impact in forcing convection and the environment is more similar for different terrain modification runs. Mesoscale and orographic processes are likely more important in forcing convection in these cases, including diurnal heating and mountain flow patterns.
3) The Andes are a unique height which allows systems to rapidly grow upscale while remaining tied to the terrain. The SDC are a secondary feature which aid in convection initiation and redevelopment, especially under weaker synoptic flow, which leads to prolonged convective events in the Córdoba region.

These results generally focused on large-scale changes to the environment and convection. Future work will use ground-based observations from RELAMPAGO and the Cloud, Aerosol, and

Complex Terrain Interactions (CACTI) field campaign and 1-km grid spacing WRF simulations of the CTRL and select terrain-modification experiments to evaluate the frequency, intensity, and structure of convective features produced during the strongly and weakly forced cases. Specific focus will be on how the SDC alter the intensity and location of updrafts within the system, how the terrain impacts the development and propagation of cold pools, and the role of the SDC in producing high lightning flash counts in the Córdoba region. This study, in junction with future work, provides a better insight into what drives intense convection in this region of the world.

CHAPTER 3

Influence of the Sierras de Córdoba on the Convective Characteristics of Weakly and Strongly Forced MCSs from RELAMPAGO

3.1 Introduction

Satellite studies have shown that intense, deep convection occurs downstream of mountain ranges around the globe, including the Andes in subtropical South America (SSA; Zipser et al. 2006; Houze et al. 2015). Convection in SSA is known to grow upscale into large mesoscale convective systems (MCSs) capable of producing hazardous weather in the form of large hail, frequent lightning, and significant flooding (Zipser et al. 2006; Cecil and Blankenship 2012; Rasmussen et al. 2014; Bruick et al. 2019), which can be detrimental to the agriculture and infrastructure of the region. These MCSs also play an important role in the energy and water cycles (Houze 2004). Up to 95% of the warm season rainfall that falls over the La Plata basin downstream of the Andes can be attributed to MCSs (Nesbitt et al. 2006; Rasmussen et al. 2016).

Previous research has shown that MCSs in SSA typically form under strong synoptic conditions, where a deep trough aloft induces lee cyclogenesis downstream of the Andes (Romatschke and Houze 2010; Rasmussen and Houze 2011, 2016). The development of the lee cyclone strengthens the north-south pressure gradient force, accelerating the South American Low-Level Jet (SALLJ; Vera et al. 2006; Sasaki et al. 2022) and advecting moisture from the Amazon into SSA. The Sierras de Córdoba (SDC), a smaller mountain range east of the Andes, are in a prime location where the northerly SALLJ and southerly ageostrophic flow meet (Rasmussen and Houze 2016). Deep convection often initiates along the SDC in the afternoon/evening and can persist throughout the night (Rasmussen et al. 2014).

Using 16 years of Tropical Rainfall Measuring Mission (TRMM; Kummerow et al. 1998) data, Piersante et al. (2021) found that large wide convective cores (40 dBZ echoes > 1,000 km^2; WCCs) embedded in MCSs typically occur under strong synoptic conditions characterized by a slow moving upper-level trough and an enhanced SALLJ. Smaller WCCs tend to occur under weaker synoptic conditions. Bruick et al. (2019) similarly found that hail is more likely to occur in the presence of strong synoptic forcing, and storms that produce hail are deeper and wider (up to 15,000 km^2 larger).

Due to the lack of ground-based observations in the region, most of the climatology studies of convection in SSA were conducted using polar-orbiting satellite data, which only provide snapshots of storms. To more accurately study the life cycle of MCSs in the region, several ground-based instruments including radars, surface stations, and radiosondes were deployed during the Remote sensing of Electrification, Lightning, And Mesoscale/microscale Processes with Adaptive Ground Observations (RELAMPAGO; Nesbitt et al. 2021) field campaign in the austral spring/summer of 2018-2019. Several studies utilizing radar data from the Servico Meteorólogico Nacional in Argentina and RELAMPAGO data have explored the development and evolution of convection. Mulholland et al. (2018) produced one of the first ground-based radar climatologies of convective features over the SDC and found the majority of events were multicellular in nature and rapidly grew upscale along the topography in only a few hours. MCS events often occurred under strong synoptic conditions including deep upper-level troughs and strong SALLJs. Using satellite observations and a convection-permitting simulation, Zhang et al. (2021) similarly showed MCSs that rapidly grew upscale were associated with stronger upper- and low-level jets. Mulholland et al. (2019, 2020) specifically looked at the transition of supercells to MCSs in real-data and idealized models and explored how the SDC influence upscale growth of MCSs. They found the SDC have both direct and indirect effects on the convective life cycle including by blocking cold pools and modulating the local environment. Singh et al. (2022) also investigated the role of the SDC in convection initiation with varying low-level wind profiles. Under most of their regimes, the northerly flow splits around the SDC and creates a convergence line over the southern ridge of the SDC where convection is initiated and moves off to the east. Notably, these idealized studies did not evaluate the importance of the strength of synoptic scale forcing on the development of convection and life cycle evolution.

To better understand how the topography of SSA influences the environment and growth of MCSs under varying synoptic conditions, Rocque and Rasmussen (2022) analyzed two cases from RELAMPAGO that occurred under strong and weak synoptic forcing. The strongly forced case occurred on 13-14 December 2018 and was associated with a deep upper-level trough, enhanced SALLJ, and the passage of a cold front, while the weakly forced case occurred on 25-26 January 2019 under weak zonal flow aloft and a short-lived SALLJ. Through a series of terrain-modification experiments, the authors showed that under strong synoptic forcing, the SDC have little impact on the modulation of the environment and MCSs in the simulations. The Andes, in contrast, play an important role in the strength and depth of the SALLJ and intensity of the lee cyclone. By reducing the height of the Andes by 50%, the authors found that the resulting MCS was weaker and quickly moved off to the east compared to when the Andes were at full height, agreeing with similar terrain-modification experiments from Rasmussen and Houze (2016). Contrastingly, under weak synoptic forcing the SDC play a more important role in the development and evolution of the MCS. Interestingly, the large-scale environment was not significantly modulated when the SDC terrain was modified. However, there were differences in the MCS rainfall totals, especially when the SDC were removed where precipitation was reduced by about

25%. Rocque and Rasmussen (2022) did not further investigate how the SDC influence the convective characteristics or life cycle of MCSs in SSA, nor did they utilize ground-based observations to validate the simulated MCSs. Thus, the current study seeks to answer several outstanding questions from prior work using radar observations and high-resolution simulations from the same two RELAMPAGO cases including:

1) Can the life cycle of three-dimensional storm features associated with MCSs in SSA (as observed by radar) be accurately represented in high-resolution simulations under strong and weak synoptic forcing?

2) How do the SDC influence the intensity and location of storm features and precipitation under strong and weak synoptic forcing?

3) Can cold pools in the vicinity of the SDC explain differences in precipitation when the large-scale environment does not significantly change when the SDC are removed?

Answering these questions will provide a clearer picture of the key synoptic through mesoscale processes that contribute to the formation and growth of intense MCSs in SSA in strong and weak synoptic environments.

3.2 Data and Methodology

3.2.1 Observations

3.2.1.1 Radar

The primary observations used in this study are from the Colorado State University (CSU) C-band radar (CHIVO) that was located about 20 km south of Córdoba, Argentina near the town of Lozada during RELAMPAGO (Arias et al. 2019). CHIVO is a dual-polarization radar, so in addition to fields such as reflectivity and Doppler velocity, dual-polarization parameters including differential reflectivity (ZDR), correlation coefficient, and specific differential phase are also retrieved. CHIVO was deployed from 10 November 2018 to 31 January 2019, operating during precipitation events including the two cases of interest, 13-14 December 2018 and 25-26 January 2019. The radar operated in several different scanning modes including 360° plan position indicators (PPIs), 135° sector scans (SEC), and range height indicators (RHIs), with the user-selected mode depending on the location and intensity of convection within the domain.

After the data were collected, several quality-control (QC) tests were applied to improve data quality and remove any non-meteorological echo. An azimuthal correction, attenuation correction, and ZDR-bias correction were each applied to the dataset. Additionally, a second QC algorithm was developed by the author to filter out clutter and second trip echo. The standard deviation of differential phase was calculated in areas of low reflectivity (<10 dBZ), and regions that exceeded 20° were masked. Additionally, normalized coherent power was smoothed, and regions that were below 0.25 were masked. Finally, a despeckling filter was applied that required at least 4 contiguous gates of good data along each ray. Once the data was QCed, PPIs and SECs were interpolated to a 1 km x 1 km x 0.5 km grid with a horizontal range of 150 km and 44 vertical levels between 0.5 and 22 km. A fuzzy logic hydrometeor identification (HID) algorithm developed by Dolan et al. (2013) for C-band was applied to the interpolated dataset.

3.2.1.2 Soundings

In addition to the radar observations, eight soundings were analyzed and compared with profiles from the simulations. Soundings used in this study are from the Ingeniero Aeronáutico Ambrosio L. V. Taravella International Airport in Córdoba, Argentina located at 31.30°S, 64.21°W. Four soundings representing the pre-convective environment were analyzed for the 13-

14 December 2018 and 25-26 January 2019 cases. Mixed-layer convective available potential energy (MLCAPE) and convective inhibition (MLCIN) were calculated using the MetPy python package (May et al. 2022). Virtual temperature was used in the calculations, as was a 100 hPa mixed layer depth. Additional parameters including total precipitable water, and 0-1 km, 0-3 km, 0-6 km, and 6-12 km vertical wind shear were also calculated using MetPy.

3.2.2 Model experimental design

The Weather Research and Forecasting (WRF; Skamarock et al. 2008) Model version 4.2 was used to simulate the strongly and weakly forced MCS cases from RELAMPAGO. The model set-up is detailed in Rocque and Rasmussen (2022), but a summary is provided here. Three nested domains with 27-, 9-, and 3-km horizontal grid spacing were set up over SSA, centered roughly around Córdoba, Argentina. These domains were forced hourly with ERA5 reanalysis data (Copernicus Climate Change Service 2017), which has 0.25° x 0.25° resolution and 37 vertical grid levels. The physics schemes that were used are as follows: Rapid Radiative Transfer Model (RRTM) longwave radiation (Mlawer et al. 1997), Dudhia shortwave radiation (Dudhia 1989), Kain–Fritsch cumulus convection in the 27- and 9-km domains (none in the 3-km domain; Kain and Fritsch 1993), Monin–Obukhov surface layer scheme, Noah land surface model (Chen and Dudhia 2001), and the Yonsei University (YSU) planetary boundary layer (PBL) scheme (Hong et al. 2006). Additionally, the Thompson aerosol-aware microphysics scheme was used (Thompson and Eidhammer 2014). These parameterizations were used in the University of Illinois Urbana-Champaign (UIUC) real-time WRF simulations that were run during RELAMPAGO and have recently been shown to best represent convection in the SDC region (Casaretto et al. 2022).

A few sensitivity tests were also completed to ensure the best representation of the MCSs was achieved. First, the number of vertical levels was changed from 54 to 81. Sensitivity tests completed by Kelly (2022) show that increasing the number of vertical levels in WRF improves the representation of convection near the terrain in SSA. Additionally, the initialization time of each simulation was tested for both 12 and 24 hours before convection initiated in the region. As a result of this sensitivity test, the simulations for both cases that were initialized 12 hours prior to convection initiation most closely resembled the radar observations. For the strongly forced case, simulations were initialized at 0600 UTC on 13 December. For the weakly forced case, simulations were initialized at 0500 UTC on 25 January. Increasing the number of vertical levels and reducing the model spin-up time resulted in improved simulations, particularly in the timing and location of convection compared to radar observations.

In addition to these domains, a fourth 1-km domain was also created for this study to analyze the convective characteristics of the MCSs. This 1-km domain was initialized using NDOWN, in which the 3-km WRF domain acts as the forcing for the nested 1-km domain. The strongly forced 1-km simulation was initialized at 2000 UTC on 13 December (2 hours after convection had initiated along the southern SDC) and run through 0800 UTC on 14 December with output every 10 minutes. This time frame captured the initiation of the MCS along the SDC and the rapid upscale growth and movement of the MCS to the east. The weakly forced 1-km simulation was initialized at 1600 UTC on 25 January (1 hour before convection initiated within the CHIVO domain) and run through 1800 UTC on 26 January, also with output every 10 minutes. This time frame similarly captured the initiation, upscale growth, and dissipation of the MCS along the SDC.

In addition to analyzing how well the model captured the initiation and development of convection for these cases, the overarching goal of the study is to determine the role of the SDC on the MCS life cycle under varying synoptic conditions. To examine this aspect, an additional simulation was run for each case in which the SDC were removed from the domain. This terrain-modification technique followed that of Rocque and Rasmussen (2022) and Rasmussen and Houze (2016) in which several boxes were placed over the SDC and the terrain inside the boxes was reduced to the height of the plains (~150 m). A 9-point smoothing function was then applied to the modified regions to remove any artificially-produced sharp gradients in the topography which could influence the meteorology. This process was repeated for each domain several times, and the location of the terrain-modification boxes for each pass in the 1-km domain is shown in Table 3.1 (see Rocque and Rasmussen 2022 for outer domain modifications). These runs were called the noSDC runs and the comparison with the control (CTRL) topography from the 1-km run can be seen in Figure 3.1.

Table 3.1: Summary of where SDC-modification boxes were placed within the 1-km domain of size 701 x 895 grid points. The last column is the height set within the terrain-modification box (approximately the height downstream of the SDC).

pass	box 1	box 2	box 3	box 4	height
1	[257:427, 119:760]	[177:258, 119:627]	[112:178, 69:433]	[77:178, 69:237]	150 m
2	[77:167, 345:415]	[91:167, 210:346]	n/a	n/a	400 m
3	[135:192, 412:515]	n/a	n/a	n/a	150 m

3.2.3 Precipitation feature identification

A precipitation feature (PF) identification algorithm was used to compare convective characteristics across observations and model simulations for each case. The PF identification

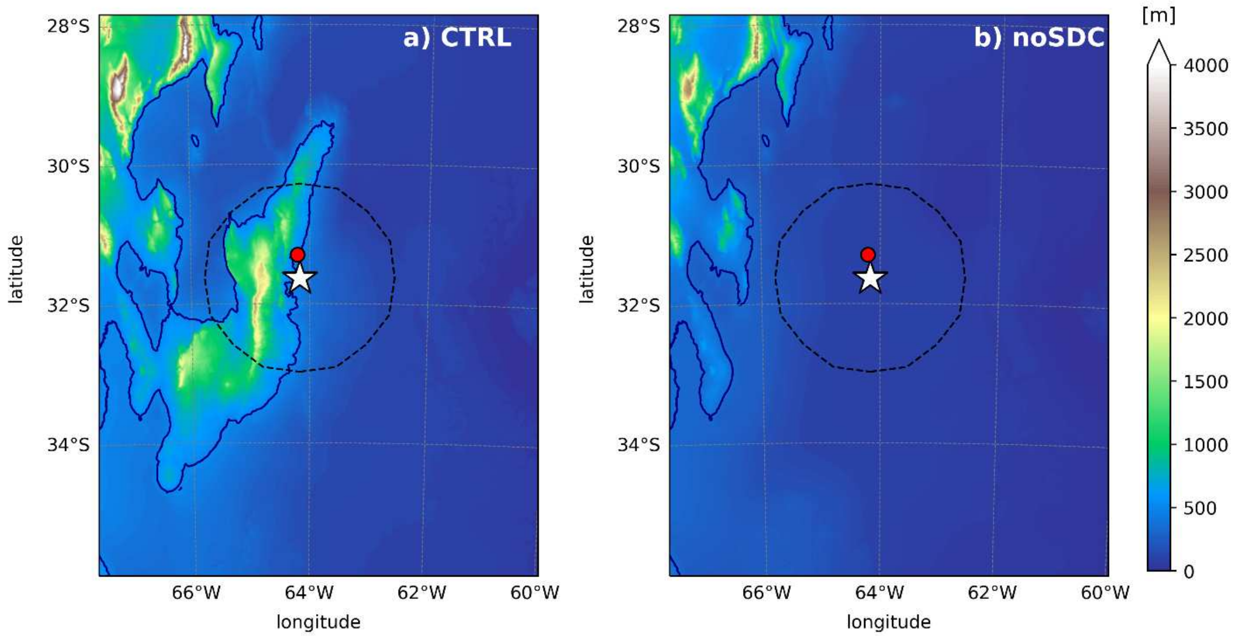

Figure 3.1: 1-km WRF domains for a) CTRL and b) noSDC runs. Terrain is shaded with the 500 m contour shown in navy. The dashed circle represents the CHIVO domain, with the white star being the center. The Córdoba sounding location is indicated by the red circle.

algorithm was based off an algorithm previously used in a tropical radar analysis by Rocque and Rutledge (2021), and several others used in past TRMM studies (Nesbitt et al. 2000, 2006; Liu et al. 2008; Liu and Zipser 2013). The algorithm works by fitting ellipses to features identified in the given dataset and computing statistics associated with that ellipse. A few sensitivity tests were performed to determine the appropriate thresholds for PF identification including minimum reflectivity and vertical levels. In this work, PFs are defined by having composite reflectivity greater than 0 dBZ between 3 and 5 km above mean sea level (MSL). This height range was chosen due to the data quality of the CHIVO dataset. Below 3 km, clutter from the SDC was still present in the final product, and the PF algorithm would have identified this clutter as convective pixels. Additionally, the radar is significantly blocked at low levels to the west due to the SDC. The upper bound of 5 km was the approximate height of the melting level. A composite between these two levels was chosen rather than a single level to retrieve a better representation of the MCSs (Fig.

3.2a). Some of the statistical output from the algorithm include PF locations, areas, convective/stratiform areas, rain rates, and echo top heights. In order to calculate convective/stratiform areas, the Steiner et al. (1995) algorithm was applied. Additionally, the rain rates were computed using a Z-R relationship used in the Dual-Polarization Radar Operational Processing System (DROPS2.0; Chen et al. 2017) developed at CSU based on continental MCSs: $R(Z_h) = 0.02Z_h^{0.657}$.

In addition to PFs, the algorithm was also developed to identify three-dimensional storm features. Deep convective cores (DCCs), wide convective cores (WCCs), deep and wide convective cores (DWCCs), and broad stratiform regions (BSRs) were identified based on the strong-intensity threshold definitions outlined in Houze et al. (2015) and used in numerous other studies of spaceborne and ground-based convective systems (Houze et al. 2007; Romatschke and Houze 2010; Rasmussen and Houze 2011, 2016; Zuluaga and Houze 2013). DCCs have 40-dBZ echoes greater than 10 km MSL, WCCs have 40-dBZ areas greater than 1000 km^2, and DWCCs have both 1000 km^2 40-dBZ areas and 10 km MSL 40-dBZ echoes (Fig. 3.2b). These convective features also only have convective pixels associated with them (as defined by the Steiner et al. (1995) algorithm; Fig. 3.2c). The BSR definition used in this work was modified compared to the traditional BSR definition to adjust for the smaller radar domain compared to TRMM domain. Here, BSRs have stratiform areas greater than 10,000 km^2 (compared to 50,000 km^2 in TRMM studies). Statistics are also output for each storm mode including locations and areas. An example of the PF identification algorithm results is shown in Figure 3.2 for 0330 UTC during the 25-26 January 2019 case from CHIVO.

This algorithm was also adapted to work with the model simulations. In order to directly compare results across observations and simulations, a radar forward model operator called Cloud

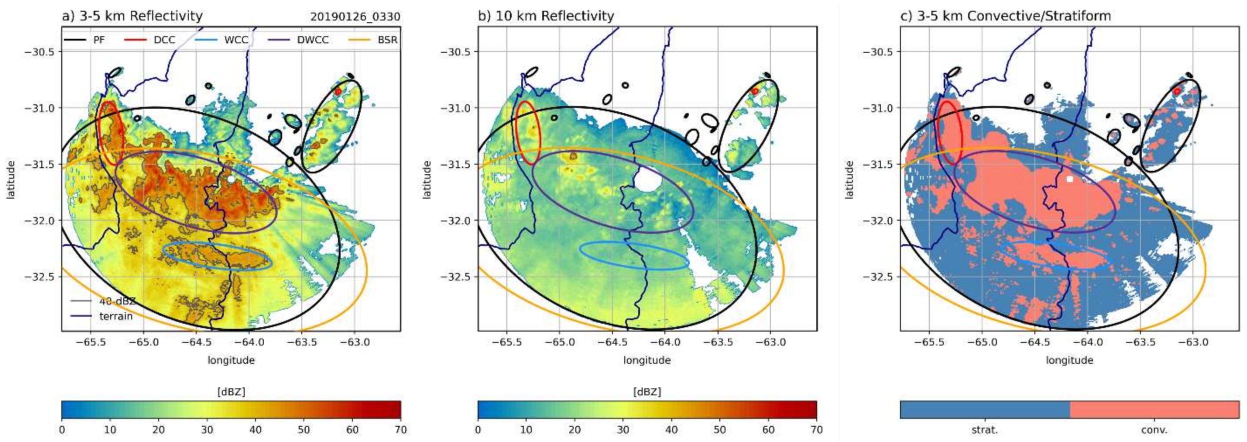

Figure 3.2: a) Composite reflectivity between 3 and 5 km, b) reflectivity at 10 km, and c) composite convective/stratiform partitioning between 3 and 5 km applied to CHIVO at 0330 UTC on 26 January 2019. The 40-dBZ contour is shown in grey in panels (a-b) and the 500 m terrain contour is shown in navy in each panel. Storm modes are identified in colored ellipses as follows: PF (black), DCC (red), WCC (blue), DWCC (purple), BSR (gold).

Resolving Model Radar Simulator (CR-SIM; Oue et al. 2020) was used to calculate C-band reflectivity and other dual-polarization parameters from the model. The resulting reflectivity was then interpolated to the same vertical levels as CHIVO (0.5-22 km) using the python module wrf-python (Ladwig 2017). The Steiner et al. (1995) algorithm was applied to the interpolated reflectivity, and the PF and storm mode identification algorithm was run on the simulations, centered on the same domain as CHIVO.

3.3 13-14 December 2018: Strongly forced case

3.3.1 Overview

The intense MCS that developed during 13-14 December 2018 was characterized by strong synoptic flow and a strong, long-lived SALLJ (Rocque and Rasmussen 2022). A deep 500-hPa trough was located off the coast of Chile around 40°S at 1200 UTC (0900 LT) on 13 December which produced strong cyclonic vorticity advection downstream into southern Argentina. The passage of the upper-level trough helped to produce a strong lee cyclone downstream of the Andes and SDC, which maximized between 18 and 00 UTC (1500-2100 LT). The development of the lee cyclone enhanced the north-south pressure gradient force, which played a role in the intensification and deepening of the SALLJ (Rocque and Rasmussen 2022; Sasaki et al. 2022). The SALLJ brought enhanced moisture at 850 hPa as far south as 40°S between 2100 and 0000 UTC (1800-2100 LT). Convection initiated over the southern SDC around 18 UTC (1500 LT), and farther north along the foothills at 2100 UTC (1800 LT). The first echoes identified within the CHIVO domain occurred just before 2300 UTC (2000 LT), after which convection quickly grew upscale into a large MCS by 0300 UTC (0000 LT; Rocque and Rasmussen 2022).

Comparisons of the upper-level flow, SALLJ, surface cold front, and cloud shields between observations and the CTRL at 0300 UTC on 14 December are shown in Figure 3.3. The location of the 500-hPa trough and strength of the upper-level flow are comparable between ERA5 and WRF (Figs. 3.3a, b). The strength of the SALLJ is also similar between ERA5 and WRF, but WRF appears to be slightly moister at 850 hPa (Figs. 3.3c, d). The development of the lee cyclone is also visible in WRF, consistent with Rocque and Rasmussen (2022). At the surface, the cold front appears to be farther south at 0300 UTC in the model compared to ERA5 (Figs. 3.3e, f). This results in warmer temperatures near Córdoba in WRF. Despite these differences, the MCS cloud shields are quite similar in the model and satellite observations (Figs. 3.3g, h). Even the locations of deep convection align well. Thus, we are confident in exploring characteristics of the MCS in more detail.

An overview of the MCS event is shown in a time-longitude (Hovmöller) diagram of reflectivity for CHIVO and the CTRL and noSDC runs in Figure 3.4. Convection is present downstream of the SDC in CHIVO observations at around 2300 UTC (Fig. 3.4a). At 0100 UTC,

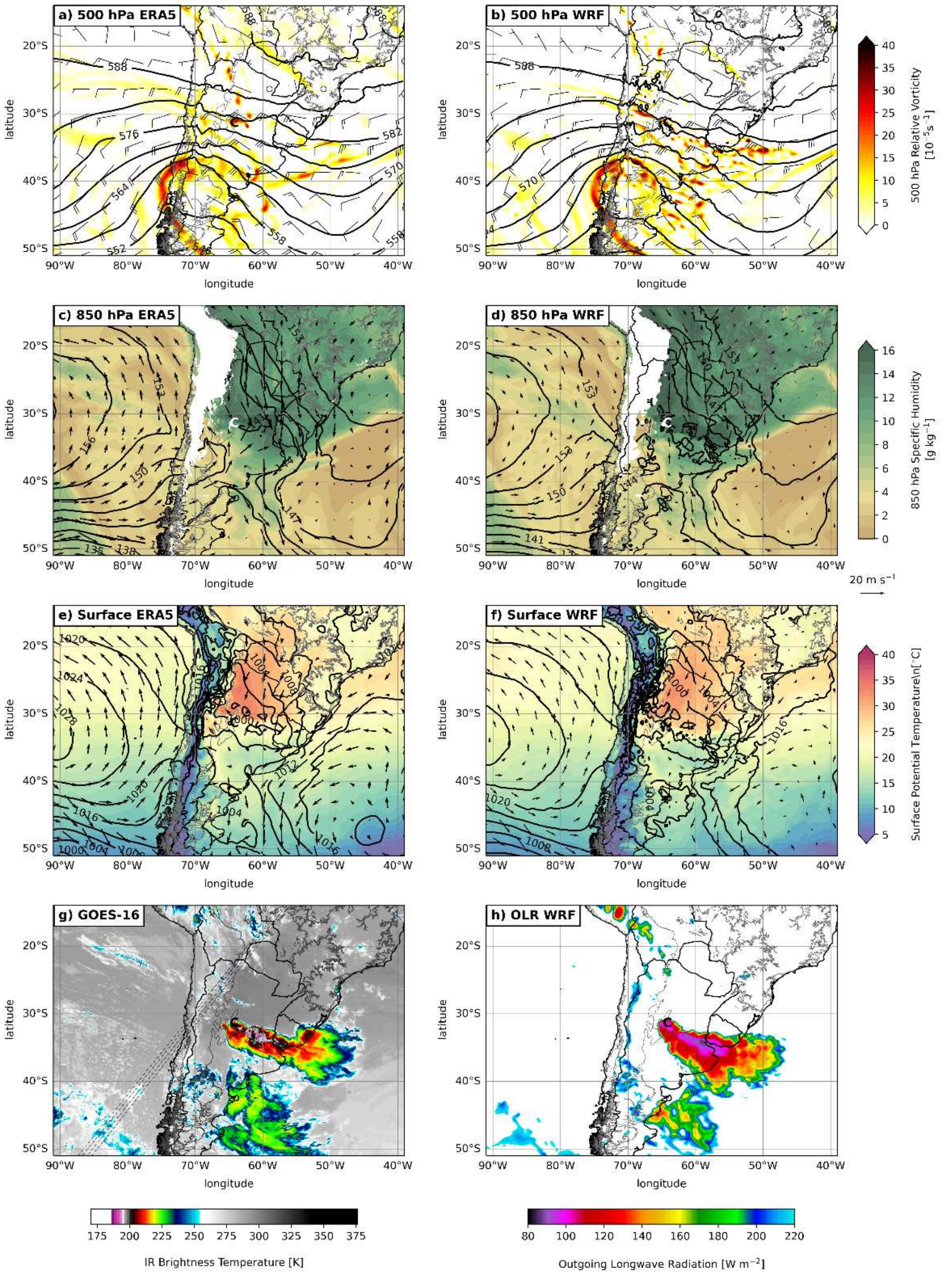

Figure 3.3: (a-b) 500-hPa geopotential heights (contoured; dam), relative vorticity (shaded; 10^{-5} s^{-1}), and winds (barbs; m s^{-1}, where a half barb is 5 m s^{-1} and a full barb is 10 m s^{-1}), (c-d) 850-hPa geopotential heights (contoured; dam), specific humidity (shaded; g kg^{-1}), and winds (arrows; m s^{-1}), (e-f) mean sea level pressure (contoured; hPa), potential temperature at the surface (shaded; °C), and 10-m winds (arrows; m s^{-1}), (g) GOES-16 channel-14 infrared brightness temperatures (K) and (h) outgoing longwave radiation (W m^{-2}) at 0300 UTC on 14 December 2018. Right panels are from ERA5 or GOES-16, while left panels are from the CTRL run. The 500-m terrain contour is shown in gray, and the "C" represents Córdoba.

the main system enters the domain from the southwest, with convection remaining intense over the SDC for several hours. Redevelopment of convection is seen over and downstream of the SDC beginning around 0300 UTC which persists until the MCS exits the domain around 0800 UTC. It is important to note that the CHIVO radar is blocked at low levels west of the SDC terrain and we only show data above 3 km. Hovmöllers of reflectivity observed by the second-generation C-band Scanning Atmospheric Radiation Measurement (ARM) Precipitation Radar (CSAPR2), located about 100 km southwest of CHIVO with less blockage to the west at low levels, do show some convection along and west of 65°W between 2300-0030 UTC (not shown). In the CTRL run, there is some convection that enters the domain from the southwest just after 2200 UTC that is not observed by the radars (Fig. 3.4b). However, the main convective event enters the domain around 0100 UTC, similar to the observations. Enhanced reflectivity is observed along the SDC in both CHIVO and the CTRL run after about 0400 UTC, consistent with a back-building signature. Results from the noSDC run show convection initiates at a similar time as in the CTRL run, around 2200 UTC (Fig. 3.4c). The intensities of reflectivity are not as strong over the western portion of the domain compared to the CTRL run. However, the overall structures are fairly similar.

3.3.2 MCS characteristics and life cycle

Previous satellite studies have shown that MCSs in SSA typically initiate with DCCs over the terrain to the west (Rasmussen and Houze 2011, 2016; Rasmussen et al. 2014). These features then grow upscale to WCCs farther east over the La Plata basin, and finally transition to BSRs over eastern Argentina and the Atlantic Ocean. Whether ground-based radar observations and convection-permitting simulations capture a similar life cycle evolution has not been determined. We first investigate where and when storm modes are identified in the observations and model

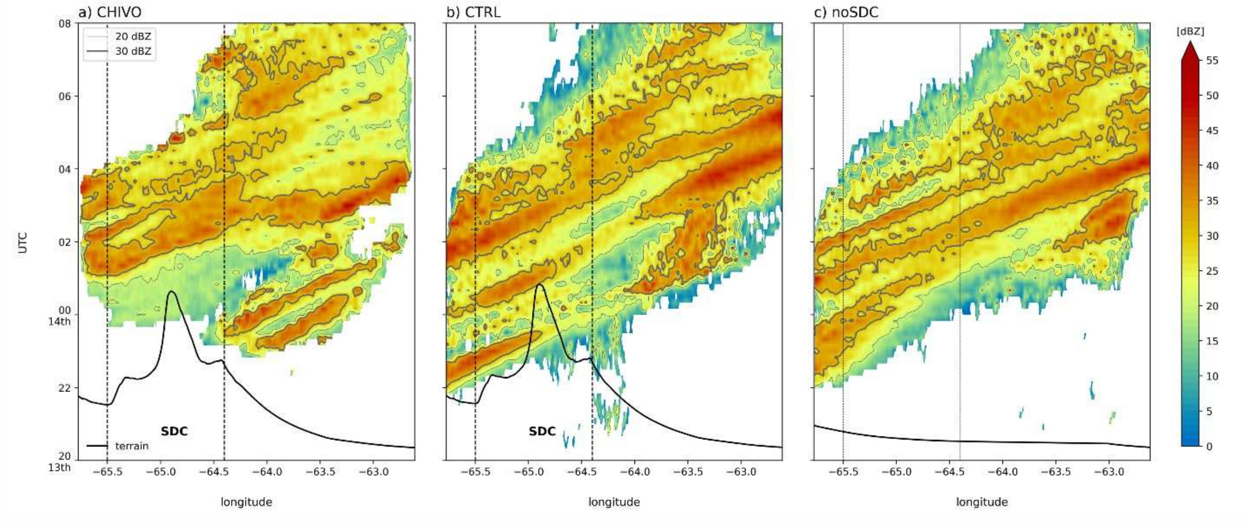

Figure 3.4: Hovmöllers of 3-5 km composite reflectivity averaged across the CHIVO domain for a) CHIVO, b) CTRL, and c) noSDC runs from 2000 UTC on 13 December to 0800 UTC on 14 December. The terrain profile is shown in black, the 20-dBZ contour is in the thin grey line and 30-dBZ in the thicker grey line. Vertical dashed lines in panels (a) and (b) indicate the longitude range of the SDC. C-band reflectivity was calculated using CR-SIM for the WRF simulations in (b) and (c).

(Fig. 3.5). In the observations, DCCs are seen across the domain, and they occur throughout the time period (Fig. 3.5a). They are first identified within a smaller PF at 0000 UTC in the southeast portion of the domain, downstream of the SDC. DCCs are then associated with the northeastward progression of the main PF (Fig. 3.4a), and evidence of redevelopment can be seen with DCCs located over the SDC later around 0600-0800 UTC. On average, DCCs are about 70 km^2 larger over the SDC compared to over the plains (Table 3.2). In the CTRL simulation, several smaller DCCs are first seen in the southern portion of the domain around 2200-0000 UTC (Fig. 3.5b). They are then scattered across the domain as the MCS moves towards the northeast, consistent with observations. However, the DCCs simulated in the CTRL run are generally about 40 km^2 larger over the SDC compared to those identified by the radar (Table 3.2). DCCs simulated in the noSDC run are similarly scattered across the domain as they move toward the northeast with the larger system (Fig. 3.5c). However, as shown in the Hovmöller (Fig. 3.4c), there is not as much redevelopment of convection over the western portion of the domain. DCCs also tend to be smaller on average over the western portion of the domain compared to the observations and CTRL (Table 3.2).

As the MCS matures, DWCCs are identified in radar observations between 0200-0500 UTC, primarily along the edge of the SDC (Fig. 3.5d). This corresponds to the most intense activity observed in the Hovmöller (Fig. 3.4a). DWCCs are slightly larger over the western portion of the domain compared to the eastern portion (Table 3.2). In the CTRL, DWCCs are more widespread across the domain compared to the observations and are about 2000 km^2 larger on average (Fig. 3.5e; Table 3.2). There are also a few DWCCs identified early in the MCS life cycle on 13 December. DWCCs in the noSDC run are found at similar times compared to the CTRL, but they are smaller on average (Fig. 3.5f; Table 3.2). The track of the noSDC DWCCs earlier in the MCS is more perpendicular to the Andes, and the back-building signature is not evident. Interestingly, the only WCCs identified during this event also had a deep component (i.e., DWCCs) in both the observations and simulations.

The final components of the MCS life cycle are BSRs. In the observations, BSRs occurred on the southeast side of the main PF from about 0300 to 0600 UTC (Fig. 3.5g). Winds aloft at this time are from the northwest which may explain why BSRs are offset from the main MCS track. The lack of BSRs at the very end of the event is due to the system exiting the domain to the east, so the 10,000 km^2 threshold is not met at those times. BSRs over the SDC are twice the size of those over the plains on average at about 22,000 km^2 (Table 3.2). In the CTRL simulation, BSRs are identified in similar locations as in observations, but they occur in the middle of the MCS event and are infrequent (Fig. 3.5h). Additionally, they are half the size of BSRs identified in observations (Table 3.2). This is consistent with past studies that have shown microphysics

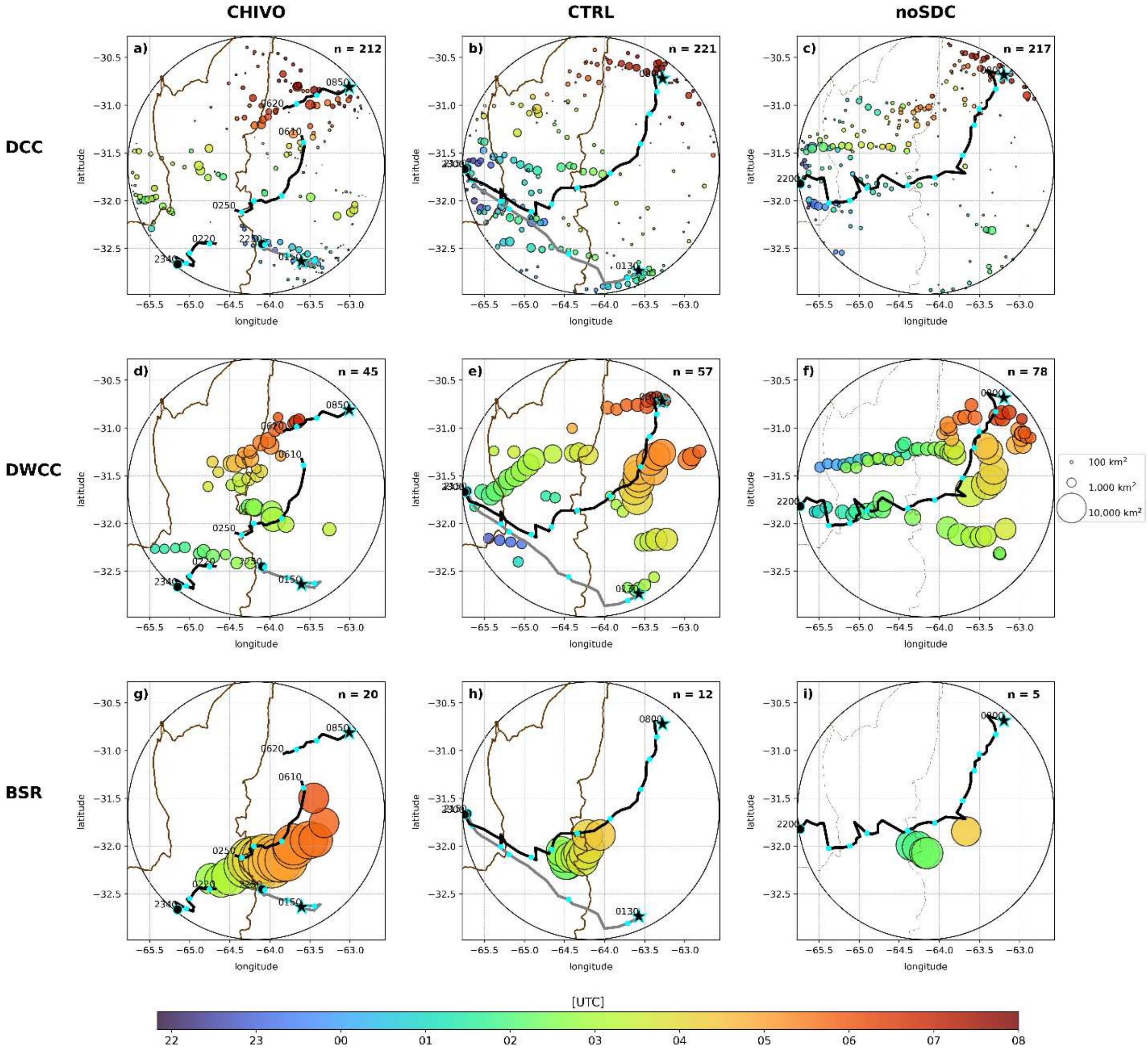

Figure 3.5: Location of storm modes identified in the CHIVO radar observations (left column), WRF 1-km CTRL simulation (middle column), and WRF 1-km noSDC simulation (right column) for the 13-14 December 2018 case. DCCs are shown in the top row, DWCCs in the middle, and BSRs in the bottom, with marker sizes corresponding to feature areas. Colors represent the timing of the feature with blues occurring towards the beginning of the event and reds towards the end. The track of the main PF is shown in black with secondary PFs shown in grey. The start of the PF is marked by a large, cyan-outlined circle, the end of the PF is marked by a cyan-outlined star, and each hour is represented by a cyan dot along the track with select times labeled. The number of features identified is in the top right corner. The 500-m terrain contour is shown in brown, and the radar volume is indicated by the large circle.

schemes in WRF often significantly underestimate stratiform precipitation (Morrison et al. 2009; Han et al. 2019). In the noSDC simulations, only 5 BSRs are identified (Fig. 3.5i). They occur relatively early in the time period (around 0200 UTC) and are quite smaller than those identified in the radar (Table 3.2). The implications of these results will now be explored from a precipitation intensity and duration perspective.

Table 3.2: Average storm mode area (km^2) computed over the mountains domain (west of 63.5°W) and plains domain (east of 63.5°W) for the 13-14 December 2018 case.

	CHIVO		**CTRL**		**noSDC**	
	mountains	**plains**	**mountains**	**plains**	**mountains**	**plains**
DCC	224	152	264	153	194	145
WCC	0	0	0	0	0	0
DWCC	2143	2076	3729	4414	2576	4105
BSR	22040	11444	11508	0	10854	0

To determine how precipitation intensity and duration varies with MCS life cycle and how the SDC may influence these characteristics, time series of PF-averaged rain rate, rain volume, and storm mode areas are shown in Figure 3.6 for the observations and simulations. The rain rate from CHIVO has three local maxima (Fig. 3.6a). The first occurs around 2330 UTC which is when DCCs start to develop over the SDC. Here the mean rain rate is about 3.5 mm hr^{-1}. Rain rate begins to increase again around 0100 UTC and reaches a peak near 0300 UTC at 10 mm hr^{-1}, when the convective area is increasing most rapidly, and DWCCs are the largest (Fig. 3.6b). The rain volume is also maximized at this time near 8 x 10^7 kg s^{-1}. After 0300 UTC, BSRs are identified, which reduces the average rain rate and rain volume. A third peak in rain rate occurs between 0600-0700 UTC when BSRs have left the domain but DCCs and some DWCCs are still present. The rain volume continues to decrease steadily due to the decreasing area associated with the MCS leaving the domain.

In the CTRL run, rain rates and rain volume generally increase from 2200 UTC to 0400-0500 UTC where they peak at around 12 mm hr^{-1} and 12 x 10^{7} kg s^{-1}, respectively (Fig. 3.6c). DCC areas are largest in the beginning, while DWCCs increase in size until around 0430 UTC (Fig. 3.6d). Although the total PF size is similar between the observations and CTRL, there is nearly twice as much convective area in the CTRL compared to CHIVO (while there is nearly half as much stratiform area). DWCCs begin to decrease in size after 0500 UTC, and as such the rain rate and rain volume also begin to decrease.

In the noSDC run, rain rates and rain volumes increase from 2200 UTC to 0300-0400 UTC (about an hour earlier compared to the CTRL; Fig. 3.6e). The peak magnitudes of rain rate are similar between the two simulations, though. The peak in rain rate corresponds to the maximum in DWCC area, and the lack of BSRs compared to CHIVO is clear (Fig. 3.6f). Convective and stratiform areas are also similar in the noSDC and CTRL simulations. The removal of the SDC does not appear to have altered the intensity of the precipitation much, which may not be surprising given the intensity of the synoptic flow and the favorable environment for MCS development.

The PF and storm mode analyses provided here highlight important similarities and differences between the observations and simulations with and without the SDC. In all scenarios, a strong MCS develops and moves through the domain with widespread DCCs. DWCCs are identified in the middle of the event in CHIVO and are concentrated along the SDC. In contrast, DWCCs in the simulations are more prevalent and widespread compared to observations and are much larger compared to observations. Larger DWCCs in the simulations lead to an enhancement in rain volume. Additionally, the simulations significantly underestimate the amount of stratiform precipitation compared to the observations. Few BSRs are identified in the CTRL and noSDC runs that are significantly smaller compared to those identified in CHIVO. This overestimation of

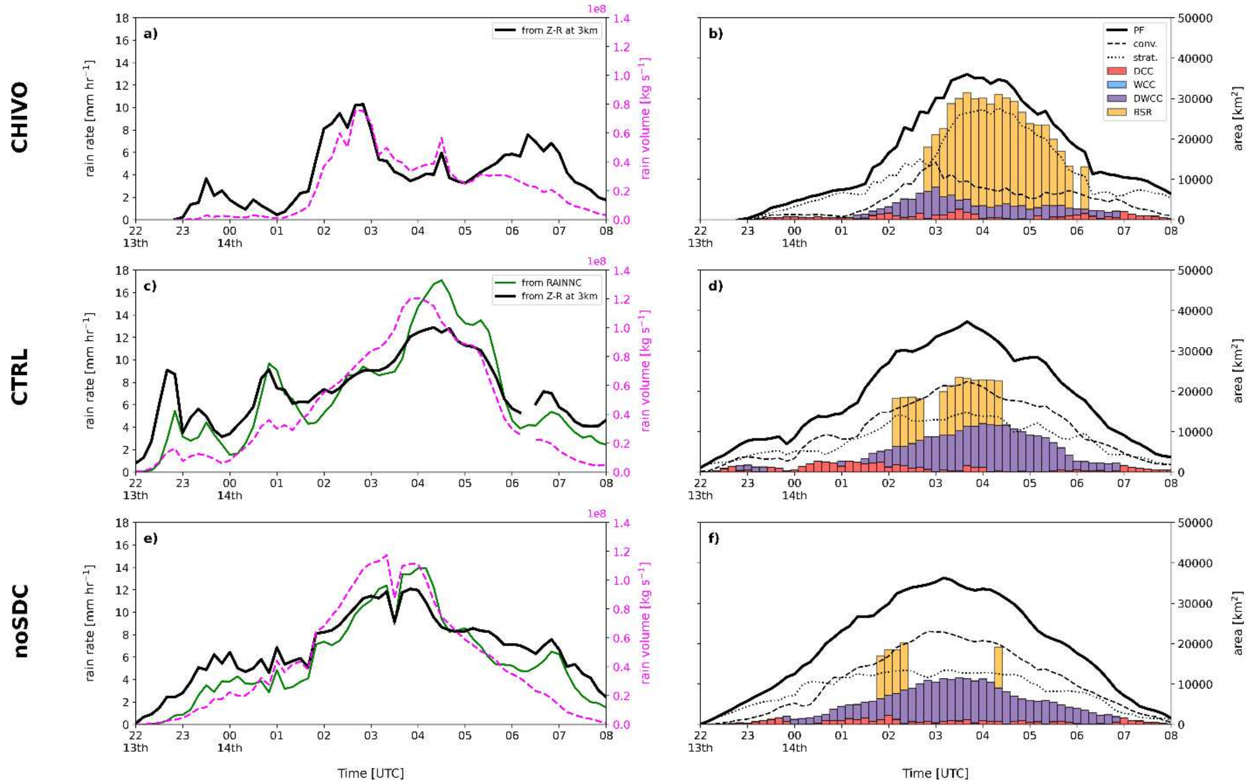

Figure 3.6: Time series of PF statistics calculated from the (a-b) CHIVO radar observations, (c-d) WRF 1-km CTRL simulation, and (e-f) WRF 1-km noSDC simulation for the 13-14 December 2018 case. The left panels show the PF-averaged rain rate calculated using a Z-R relationship at 3-km (mm hr^{-1}; black) and rain volume (kg s^{-1}; dashed magenta). Rain rate was also derived from the RAINNC parameter in the WRF simulations and plotted in green in (c) and (e). The right panels show PF area (solid; km^2), PF convective area (dashed; km^2), PF stratiform area (dotted; km^2) and storm mode areas (DCC: red, WCC: blue, DWCC: purple, BSR: gold; km^2).

convection and underestimation of stratiform is a known issue with WRF, as mentioned above. Some of these results are consistent with the findings of Rasmussen and Houze (2016), although the direct comparison to ground-based radar observations provides new and important information in determining model fidelity in reproducing mesoscale storm structures in SSA. The mesoscale processes behind these differences in storm intensity and how they are influenced by the SDC will now be explored.

3.3.3 Convective environment

Favorable thermodynamic conditions are critical for convection initiation and development. MLCAPE and MLCIN are two quantities that can be used to determine whether an environment is able to support convection. Previous research by Mulholland et al. (2019) has suggested that the SDC can modulate the environment and alter MLCAPE and MLCIN, leading to differences in the timing, location, and intensity of supercell and MCS development. In addition to thermodynamics, vertical wind shear is also important in the formation and organization of convection. Mulholland et al. (2019) also showed that decreases in idealized SDC terrain height resulted in decreases in low-level and deep-layer vertical wind shear which led to small supercell updrafts. Here we explore how the convective environments vary in observations and the topographic sensitivity experiments under strong synoptic forcing. As with the observations, sounding parameters including MLCAPE, MLCIN, total precipitable water, and vertical wind shear across different layers were calculated using the MetPy package for the CTRL and noSDC runs. A few point soundings were generated from the CTRL and noSDC runs at the Córdoba airport early in the event to see how well they compared with observations (Fig. 3.7).

At 1500 UTC (1200 LT), there is a strong inversion around 800 hPa in the observed sounding (Fig. 3.7a). Winds shift from north northeasterly to westerly above the inversion, and there is considerable dry air aloft. In the CTRL and noSDC runs, a similar profile is seen, although the inversion is about 50 hPa higher. Additionally, the profile in the simulations is not as dry as the observed profile. This results in total precipitable water being higher in the simulations compared to observations (Table 3.3). MLCAPE and MLCIN are also slightly underestimated in the models at this time, as is the 0-3 km, 0-6 km and 6-12 km shear. 3 hours later, the surface warms considerably and the lower atmosphere becomes more mixed (Fig. 3.7b). WRF does a better job of capturing the moisture profile aloft (total precipitable water is now only 1-2 mm off; Table 3.3), but the low levels are moister and cooler than the observations. MLCAPE is about 500 J kg^{-1} greater in the simulations compared to observations (Table 3.3). Vertical wind shear at different levels is similar between observations and WRF, though.

At 2100 UTC (1800 LT), an even deeper mixed layer is observed, as is the SALLJ (Fig. 3.7c). Dry air is still prevalent aloft, resulting in even lower total precipitable water around 32 mm (Table 3.3). As in the previous time, CTRL and noSDC profiles are cooler and moister at the surface. MLCAPE is more than 2000 J kg^{-1} greater in the simulations, and MLCIN is at least 100 J kg^{-1} less than observed MLCIN (Table 3.3). Winds also have a more easterly component compared to observations. 0-3 km shear and 6-12 km shear are notably greater in the model runs compared to observations. At 0000 UTC (about 1-2 hours before convection), the profiles still show extremely dry air aloft (Fig. 3.7d). Low-level winds now have a westerly component, and the low-level shear is weak (< 5 m s^{-1}). Low-level winds in the simulations still have an easterly component, and surface dewpoints are about 5°C higher than observations. This results in large MLCAPE values (more than 2000 J kg^{-1} greater than observations; Table 3.3).

In general, WRF does a reasonable job at simulating atmospheric profiles compared to observations, and these profiles were greatly improved when the number of vertical levels was increased. When comparing CTRL and noSDC profiles, MLCAPE tends to be larger in the noSDC run compared to the CTRL run (no more than 500 J kg^{-1}, though). Total precipitable water and 6-12 km shear are also slightly larger in the noSDC run. In contrast, MLCIN, 0-3 km shear, and 0-6 km shear are smaller in the noSDC run compared to the CTRL. Some of these results, including the increase in MLCAPE and decrease in low-level shear agree well with previous idealized studies of terrain impacts on the convective environments near the SDC (Mulholland et al. 2019, 2020).

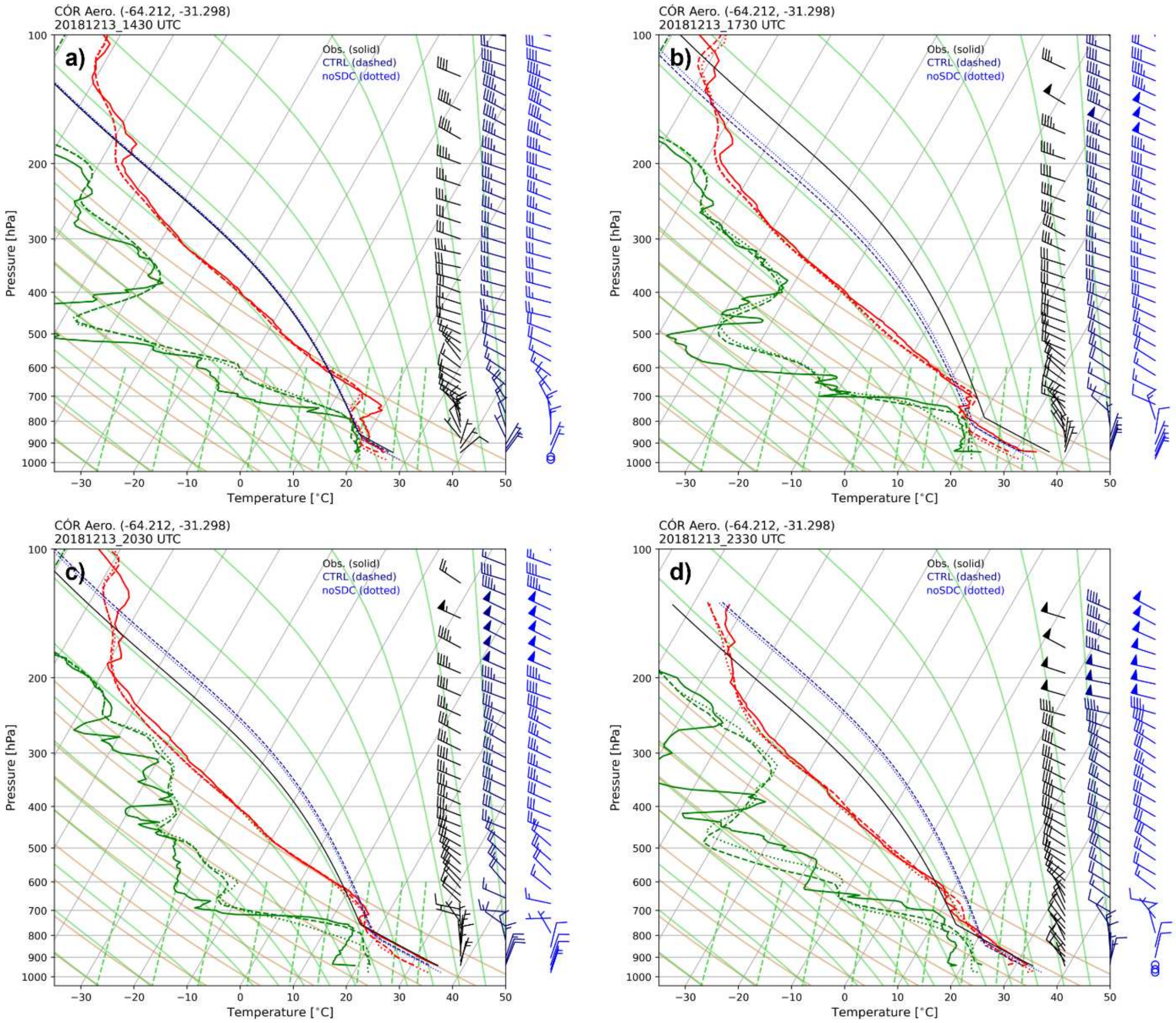

Figure 3.7: Sounding profiles taken at the Córdoba airport at a) 1500 UTC, b) 1800 UTC, c) 2100 UTC, and d) 0000 UTC on 13-14 December 2018, plotted on a skew T-logp diagram. Red lines are the temperature profile, green lines are the dewpoint profile, and black/blue curves are the parcel path (lifted from the surface). Solid lines are from the observed sounding, while dashed (dotted) lines are from the CTRL (noSDC) simulation. Wind barbs are plotted on the right for observations (black), CTRL (navy), and noSDC (blue) profiles, where a half barb is 5 m s^{-1} and a full barb is 10 m s^{-1}.

3.3.4 Cold pools

Despite the similarities in large-scale environments between the CTRL and noSDC (as shown by Rocque and Rasmussen 2022) and the similarities in MLCAPE, MLCIN, and vertical wind shear, some differences in the convective characteristics and precipitation intensity associated with the MCSs were found. One hypothesis to explain these differences is the modification of cold pools by the SDC. A few studies from around the world have shown that cold pools can become trapped in regions of complex terrain which can lead to secondary convective initiation (Xu et al. 2012; Phadtare 2018; Mulholland et al. 2019; Zhang et al. 2022). Additionally, cold pools that descend off terrain can cause a hydraulic jump, which can cause secondary convection downstream of the terrain (Frame and Markowski 2006). Mulholland et al. (2019) showed through idealized simulations that the SDC act to block cold pools, which strengthens and deepens them and leads to secondary initiation.

Table 3.3: Sounding variables calculated at the Córdoba airport for the observed, CTRL, and noSDC profiles at 1500, 1800, 2100, and 0000 UTC 13-14 December 2018. Sounding variables include MLCAPE (J kg^{-1}), MLCIN (J kg^{-1}), total precipitable water (mm), and 0-1, 0-3, 0-6, and 6-12 km vertical wind shear (m s^{-1}).

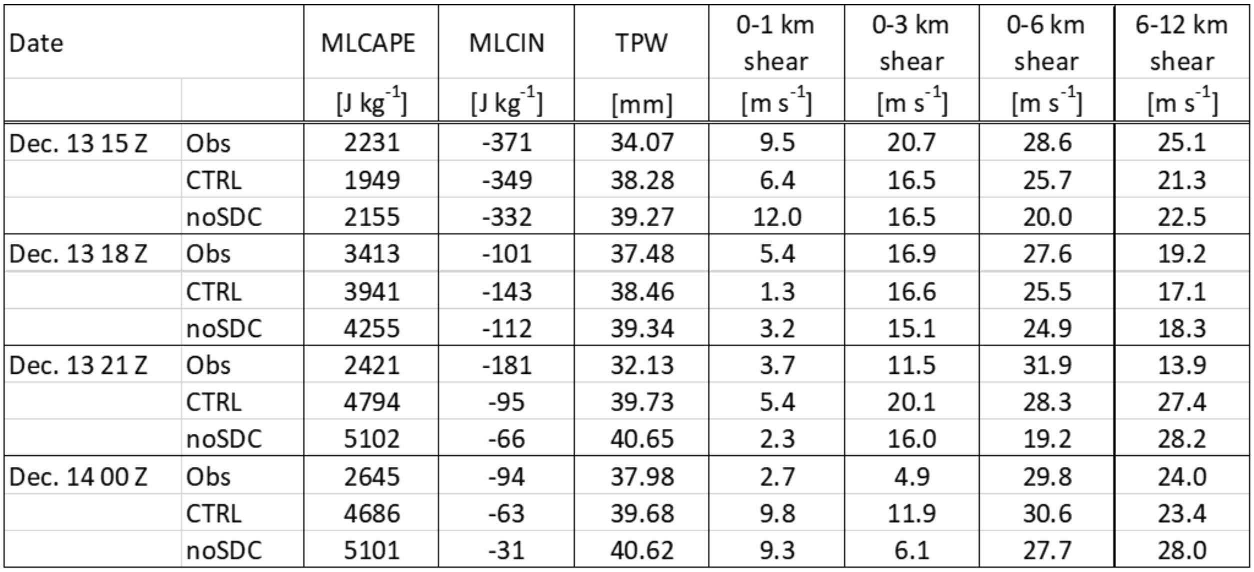

Date		MLCAPE	MLCIN	TPW	0-1 km shear	0-3 km shear	0-6 km shear	6-12 km shear
		[J kg^{-1}]	[J kg^{-1}]	[mm]	[m s^{-1}]	[m s^{-1}]	[m s^{-1}]	[m s^{-1}]
Dec. 13 15 Z	Obs	2231	-371	34.07	9.5	20.7	28.6	25.1
	CTRL	1949	-349	38.28	6.4	16.5	25.7	21.3
	noSDC	2155	-332	39.27	12.0	16.5	20.0	22.5
Dec. 13 18 Z	Obs	3413	-101	37.48	5.4	16.9	27.6	19.2
	CTRL	3941	-143	38.46	1.3	16.6	25.5	17.1
	noSDC	4255	-112	39.34	3.2	15.1	24.9	18.3
Dec. 13 21 Z	Obs	2421	-181	32.13	3.7	11.5	31.9	13.9
	CTRL	4794	-95	39.73	5.4	20.1	28.3	27.4
	noSDC	5102	-66	40.65	2.3	16.0	19.2	28.2
Dec. 14 00 Z	Obs	2645	-94	37.98	2.7	4.9	29.8	24.0
	CTRL	4686	-63	39.68	9.8	11.9	30.6	23.4
	noSDC	5101	-31	40.62	9.3	6.1	27.7	28.0

Here, we investigate cold pool propagation in the context of the SDC to determine if this mechanism can explain the differences in MCS characteristics in this set of simulations under strong synoptic forcing. As in Mulholland et al. (2019), cold pools are defined using thermal buoyancy based on the following equation:

$$B = g\left(\frac{\theta_v - \overline{\theta_v}}{\overline{\theta_v}}\right)$$

where g is gravity (m s^{-2}), θ_v is the virtual potential temperature at a given location and time, and $\overline{\theta_v}$ is the virtual potential temperature averaged across the 1-km domain at the 1-km domain initialization time (2000 UTC 13 December). Figure 3.8 shows thermal buoyancy calculated at the lowest model level across the 1-km domain for the CTRL and noSDC runs at several times. Cold pools are defined as regions of thermal buoyancy $B < 0.2$ m s^{-2} (Verrelle et al. 2015; Mulholland et al. 2019). At 2100 UTC on 13 December there are no cold pools visible across either 1-km domain (Figs. 3.8a, b). There is convection that develops off the Andean foothills in the southern portion of the domain in both CTRL and noSDC runs, and broader convection to the east which appears to be more intense in the CTRL run compared to noSDC. Two hours later, cold pools associated with developing convection are seen in the southern portion of the domain along the foothills in both simulations (Figs. 3.8c, d). Convection is aligned more linearly from west to east in the CTRL run, perpendicular to the SDC. In the noSDC run, though, convection extends from the northwest to southeast. As time progresses, cold pools build along the terrain to the west and convection continues to advance to the north (Figs. 3.8e-h). Cold pools surge farther north along the foothills when the SDC are removed but remain between the SDC and foothills in the CTRL run (Figs. 3.8g-j). Convection is also enhanced over the SDC around 03 UTC, which is also visible in the Hövmoller (Fig. 3.4b).

Even though there are some differences in the location of cold pools in the CTRL and noSDC runs, averaging cold pool perturbations across the domains leads to less than a 0.5 K difference between CTRL and noSDC at any given time during the simulation (not shown). We hypothesize the reason for this small difference is the strong cold front passage that occurs during this time east of the SDC. Maps of virtual potential temperature at 2000, 0000, and 0400 UTC

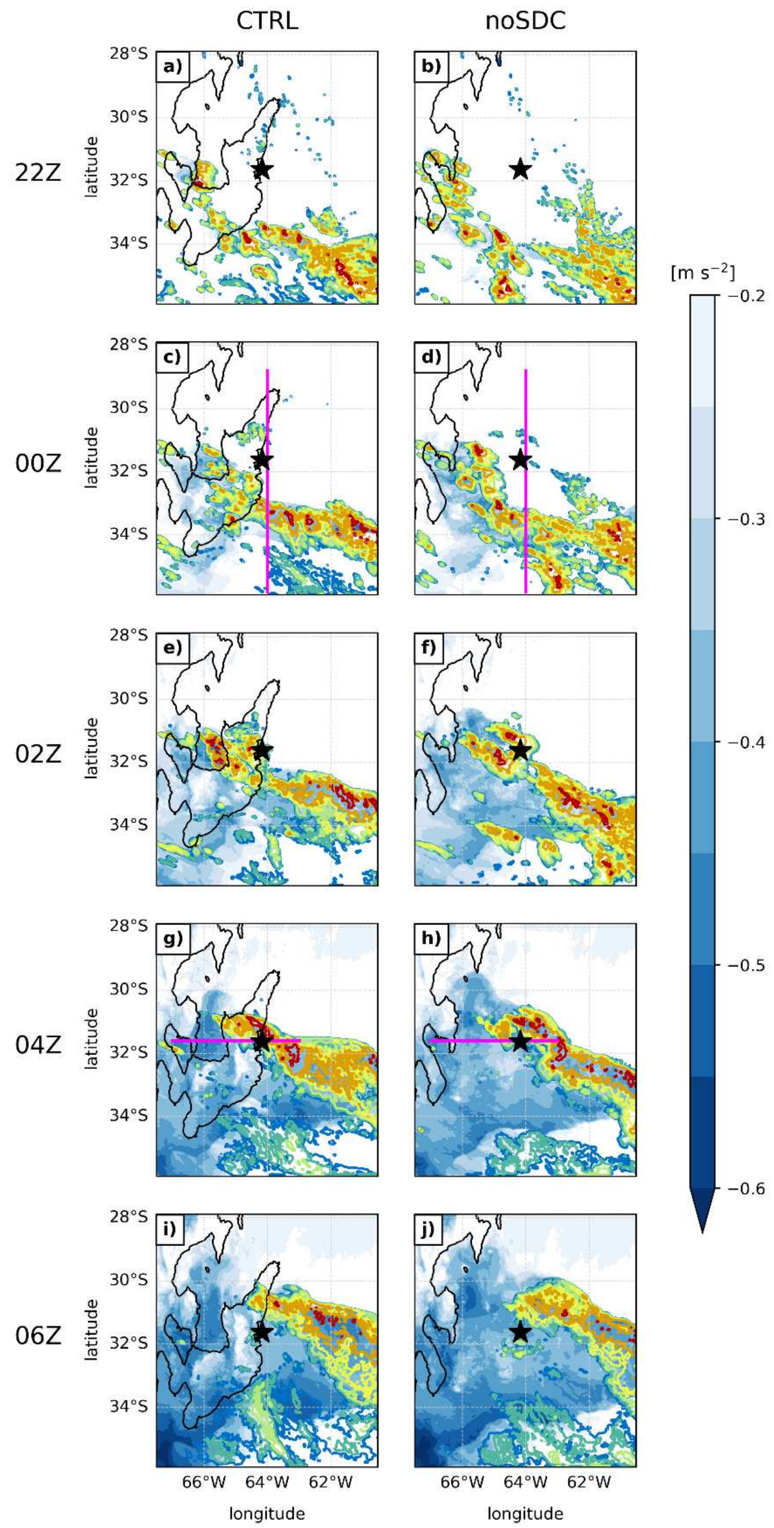

Figure 3.8: Maps of cold pools (B < 0.2 m s^{-2}; shaded) and reflectivity (contoured every 10 dBZ) at the lowest model level for the CTRL (left) and noSDC (right) runs at 2200, 0000, 0200, 0400, and 0600 UTC on 13-14 December 2018. Magenta lines in panels (c), (d), (g), and (h) indicate cross sections shown in Fig. 3.10. The 500 m terrain contour is shown in black and the star represents CHIVO.

show the cold front moving through the region with similar strengths for the CTRL and noSDC runs (Fig. 3.9). The cold front moves more parallel to the long-axis of the SDC in the CTRL run, and so convection that develops along the front is also oriented parallel to the terrain. In the noSDC run, the cold front and associated convection is oriented northwest to southeast. North-south cross sections of the cold front, cold pool, and winds at 0000 UTC show the convergence of warm northerly air and cool southerly air around 33°S (Figs. 3.10a, b). The cold pool is deepest along the leading edge and is about 1 km deep. In the noSDC run, the cold front is located slightly south compared to the CTRL, but there is still a cold pool along the leading edge. However, the cold pool is deepest farther back within the cold front, around 34.4°S. The cold front also appears to be slightly deeper in the noSDC run compared to the CTRL. East-west cross sections taken 4 hours later show cold pools west and east of the SDC (Figs. 3.10c, d). In the CTRL run, the cold pool is deeper west of the SDC, extending to about 1.5 km. However, in the noSDC run, the cold pool is shallower in the western portion of the domain. East of the SDC, cold pools are shallower (generally less than 1 km deep) in the CTRL run. In the noSDC run, cold pools are deeper along the plains rather than to the east. In both simulations, westerlies prevail and generally increase with height.

3.4 25-26 January 2019: Weakly forced case

3.4.1 Overview

Some of the deepest, most intense convective cores recorded during RELAMPAGO were associated with the 25-26 January 2019 MCS (Schumacher et al. 2021; Nesbitt et al. 2021, Feng et al. 2022). This event, in contrast to the 13-14 December case, occurred under weak synoptic conditions (Rocque and Rasmussen 2022). Weak, zonal flow aloft resulted in weak lee

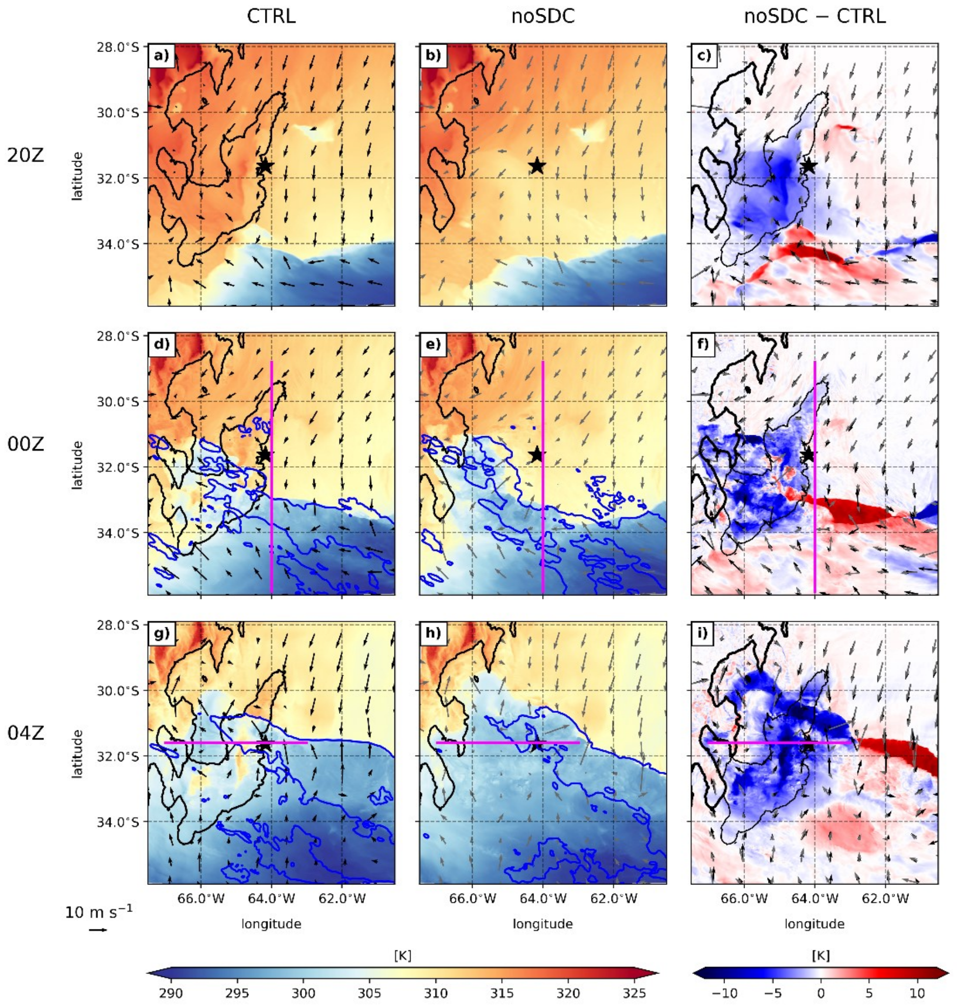

Figure 3.9: Maps of virtual potential temperature (K; shaded), 0-dBZ reflectivity (contoured), and winds (arrow; m s^{-1}) at the lowest model level for the CTRL (left), noSDC (middle), and noSDC – CTRL (right) at 2000, 0000, and 0400 UTC on 13-14 December 2018. Magenta lines in panels (d-i) indicate cross sections shown in Fig. 3.10. The 500 m terrain contour is shown in black and the star represents CHIVO.

cyclogenesis and a short-lived, shallow SALLJ which reached peak magnitudes around 0900 UTC (0600 LT) on 25 January. Anomalously high moisture concentrated over the higher terrain and diurnal heating helped convection initiate over the SDC in the afternoon around 1800 UTC (1500 LT). This convection remained relatively stationary for nearly 24 hours where it grew upscale into a large MCS. Rocque and Rasmussen (2022) suggested under weaker synoptic flow, the SDC play a more important role in convective development and upscale growth, possibly by strengthening

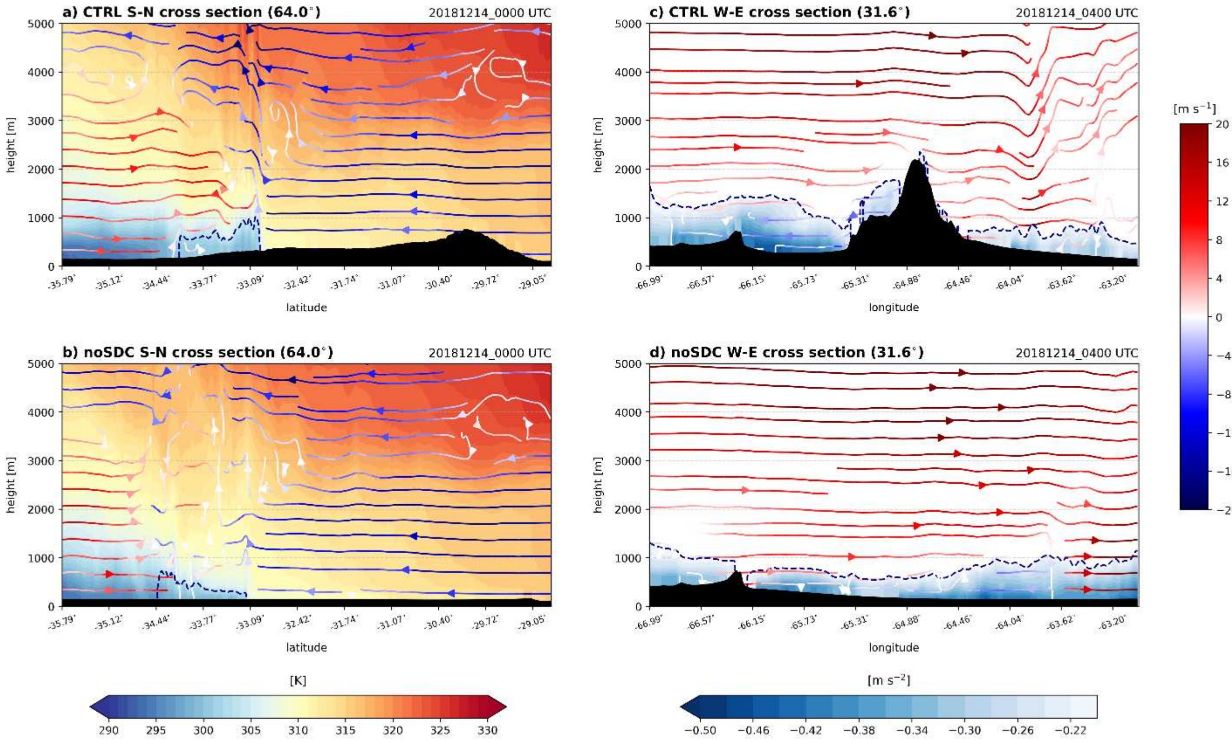

Figure 3.10: a) Cross section of the CTRL run at 0000 UTC on 14 December taken at 64°W from 35.8°S to 28.8°S of virtual potential temperature (shaded; K), in-plane winds (streamlines shaded by magnitude; m s^{-1}), and cold pools (dashed; B = -0.2 m s^{-2}). b) As in (a) but for the noSDC run. c) Cross section of the CTRL run at 0400 UTC on 14 December taken at 31.6°S from 67°W to 63°W of cold pools (shaded; B < -0.2 m s^{-2} and dashed; B = -0.2 m s^{-2}) and in-plane winds (streamlines shaded by magnitude; m s^{-1}). d) As in (c) but for the noSDC run. All cross sections are averaged 10 km perpendicular to the line.

and blocking cold pools. The details surrounding the convective characteristics and environment for this case will be examined further.

Comparisons of the upper-level flow, SALLJ, surface temperature gradient, and cloud shields between observations and the CTRL at 0000 UTC (2100 LT) on 26 January are shown in Figure 3.11. As in the strongly forced case, the upper-level flow is similar between ERA5 and WRF (Figs. 3.11a, b). A small shortwave trough is located around 45°S off the coast of Argentina. The SALLJ is visible in both ERA5 and the CTRL run as well, and an enhanced tail of moisture is shown extending from the SALLJ region to the shortwave trough (Figs. 3.11c, d). At the surface, very warm air (>35°C) is concentrated along the foothills from ~20-30°S in ERA5, and a bit farther south in the model (Figs. 3.11e, f). Mean sea level pressure is also minimized in this region of warm air. A large MCS is visible in satellite imagery at this time over the SDC, with colder cloud tops over the foothills to the west (Fig. 3.11g). Convection is slightly delayed in the model compared to observations, but the location of the modeled MCS three hours later is similar to satellite at 0000 UTC (Fig. 3.11h). The coldest cloud tops in the model are over the plains, though. However, given the weak synoptic forcing associated with this case, the model was still able to produce an MCS in a similar location as observations, even if the timing is slightly off. Thus, we continue to analyze the convective characteristics of the MCS in more detail.

Hovmöllers of composite reflectivity from CHIVO, and the CTRL and noSDC runs for the 25-26 January 2019 case are shown in Figure 3.12. Intense convection located over the SDC is visible in the observations around 1700 UTC (1400 LT; Fig. 3.12a). These convective features move off to the east and by 0000 UTC, a second wave of less intense convection develops over the SDC. This region of higher reflectivity is fairly stationary over the SDC for the next 12 hours. When looking at the model simulations, the intense isolated cells that develop in the afternoon along the SDC in the observations are not present. The CTRL run does show more intense convection developing farther east along the SDC about four hours later around 2200 UTC (Fig. 3.12b). Similar to the observations, there is another round of convection in the CTRL run that remains relatively stationary over the SDC throughout the night. When the SDC are removed, convection does not initiate until 0000-0200 UTC (Fig. 3.12c). Additionally, the redevelopment of convection over the western portion of the domain does not last as long and is not as prominent as the observations and CTRL convection.

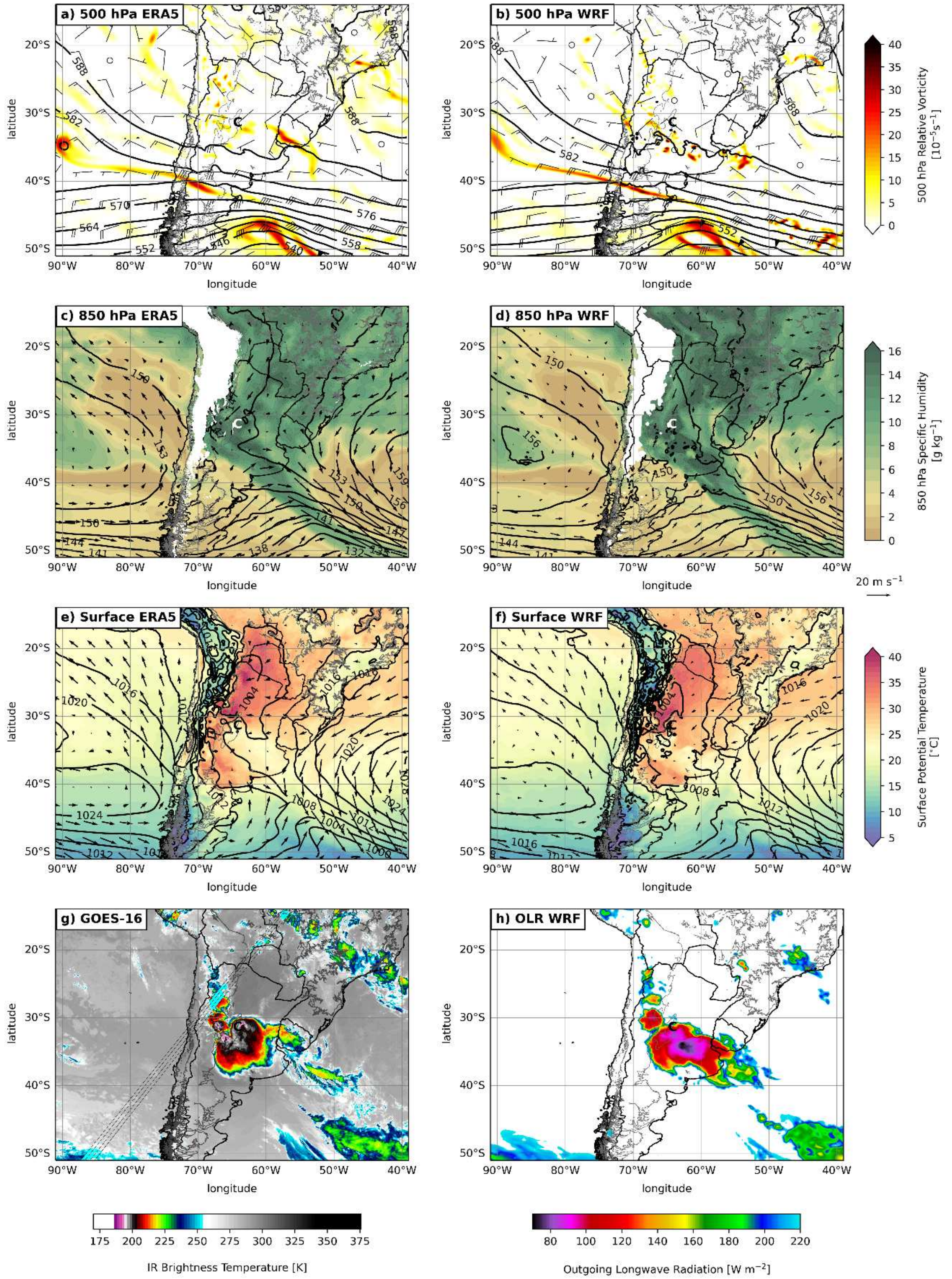

Figure 3.11: As in Fig. 3.3 but for the 25-26 January 2019 weakly forced case. Times shown in panels (a-g) are 0000 UTC on 26 January, while panel (h) is at 0300 UTC on 26 January.

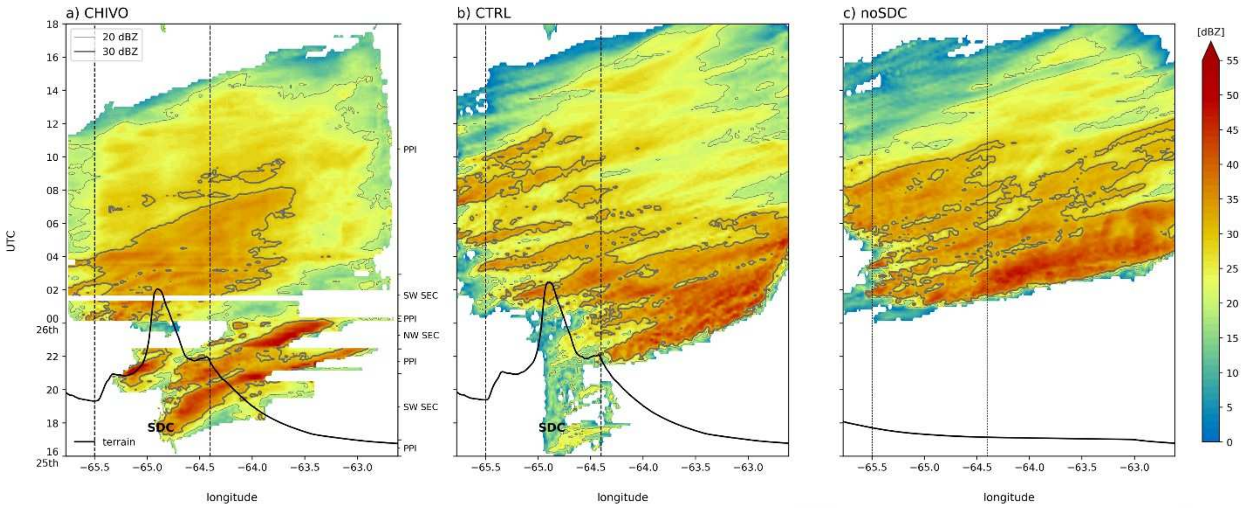

Figure 3.12: As in Fig. 3.4 but for the 25-26 January 2019 case. Time ranges from 1600 UTC on 25 January to 1800 UTC on 26 January. CHIVO scan types are shown on the right axis of panel (a), alternating between SEC and PPI modes.

3.4.2 MCS characteristics and life cycle

As with the strongly forced case, PFs and storm modes were identified and tracked across the runs to investigate the MCS life cycle. The tracking of PFs was more difficult with CHIVO since the scan strategy alternated between SEC and PPI, often with SEC covering different azimuths. After 0300 UTC on 26 January, the radar was scanning in PPI-mode consistently, though. Results from the PF and storm mode analysis show there are some DCCs that occur toward the beginning of the time period associated with the very intense cells that initiated over and moved off the SDC in the afternoon (Fig. 3.13a). There is then secondary development of DCCs farther west around 0100 UTC which moves north. Similar to DCCs in the strongly forced case, DCCs over the western portion of the domain are larger than over the eastern portion (Table 3.4). In the CTRL simulation, DCCs are also mostly concentrated over the SDC, and although there are no deep cells identified in the beginning of the event, there is a clear progression of DCCs to the north over the SDC from about 0200-1200 UTC (Fig. 3.13b). As with the observations, DCCs are larger on average over the SDC compared to over the plains (Table 3.4). In contrast to the observations and CTRL, DCCs that are identified in the noSDC run tend to follow a southwest to northeast path from about 0400-1200 UTC and there is no clear back-building signature to the west (Fig. 3.13c).

DWCCs are identified in the initial cells that move across the domain between 1800-0000 UTC in the observations (Fig. 3.13d). A second set of DWCCs are identified farther west over the SDC which move north between 0000 and 0500 UTC. This pattern is similar to the DCCs. Additionally, DWCCs over the terrain are over 1,000 km^2 larger than those over the plains (Table 3.4). DWCCs in the CTRL once again follow a similar pattern as the observations, although there are more identified (similar to the strongly forced case) and they occur slightly more downstream of the SDC compared to observations (Fig. 3.13e). DWCCs are nearly twice as large over the plains compared to the mountains, but DWCCs over the SDC have similar sizes in the observations and CTRL (Table 3.4). In the noSDC simulation, DWCCs start to occur around 0000 UTC and move toward the north until about 1200 UTC (Fig. 3.13f). As with the DCCs, there is a more easterly component to their movement compared to the CTRL which is more northerly. DWCCs are much larger than those identified in observations and CTRL, though.

These deep features are then followed by a few WCCs which are also concentrated along the edge of the SDC near the center of the domain in the observations (Fig. 3.13g). Only four WCCs are identified in the CTRL near 1000 UTC and there is one WCC identified when the SDC are removed (Figs. 3.13h, i). These WCC areas are also smaller than the observed WCCs (Table 3.4). The lack of wide convection is the model is consistent with the idea that WRF favors deep convection.

The remainder of the event is mostly stratiform and represents the mature and dissipating stages of the MCS. Several BSRs are identified from about 0200 UTC throughout the remainder of the period and move very slowly to the north along the SDC (Fig. 3.13j). As noted by the spacing of the cyan dots in Figs. 3.13a, d, g, j, there is a period from about 0600-1100 UTC when the center of the main PF does not move (the speed of the system is less than 2 m s^{-1}). These features are much larger in size compared to the strongly forced BSRs, nearing 40,000 km^2 on average (Table 3.4). BSRs are similarly identified in the CTRL run and can been seen moving along the SDC to the north (Fig. 3.13k). Unlike the strongly forced case, the model fairly accurately depicts these features, although they tend to occur later in the MCS life cycle compared to observations. BSRs are also identified in the noSDC run and follow a similar track parallel to the foothills of the Andes (Fig. 3.13l). Simulated BSRs are 5000-6000 km^2 smaller on average compared to observed BSRs, though (Table 3.4).

Table 3.4: As in Table 3.2 but for the 25-26 January 2019 case.

	CHIVO		**CTRL**		**noSDC**	
	mountains	**plains**	**mountains**	**plains**	**mountains**	**plains**
DCC	246	212	225	168	257	180
WCC	1918	0	1155	0	1854	0
DWCC	2965	1764	2994	4978	5872	4964
BSR	38779	0	33990	11278	32370	0

Analyses of the rain characteristics in observations and the suite of model simulations are presented to determine how the SDC impact the precipitation intensity and duration throughout the MCS life cycle evolution. Time series of rain rates and PF areas are shown in Figure 3.14. Rain rates in the beginning of the event when intense cells are moving through the CHIVO domain are around 20 mm hr^{-1} (Fig. 3.14a). There are some large variations in the calculated rain rate, mainly

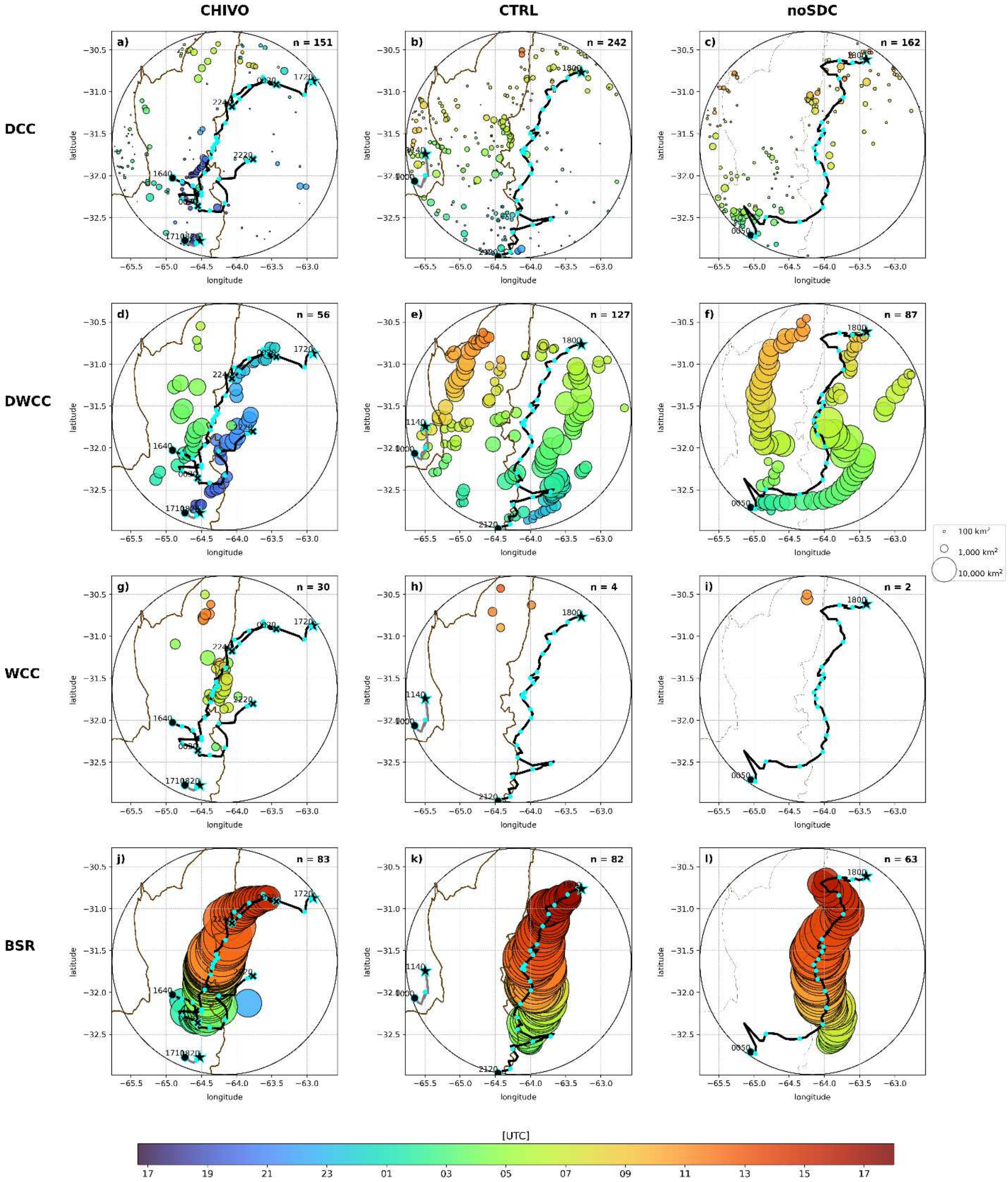

Figure 3.13: As in Fig. 3.5 but for the 25-26 January 2019 case. An additional WCC row was added since there were a few of these features identified, particularly in the radar data (g).

due to the changing scan strategy from SEC to PPI and back to SEC. This period is dominated by DCCs and DWCCs and rain volume is around 3 x 10^7 kg s^{-1} (Figs. 3.14a, b). The second event enters the domain around 0000 UTC with some DCCs and DWCCs (Figs. 3.14a, d). A slightly enhanced rain rate is observed from 0100-0400 UTC when DWCCs are most active. The rain volume also peaks around 0400 UTC near 6 x 10^7 kg s^{-1}, similar to the strongly forced case when rain volumes peaked with DWCC areas. After 0400 UTC, the DWCCs transition to WCCs, which are sporadically identified until 1200 UTC. BSRs are prevalent for the remainder of the MCS, which decreases rain rates and rain volumes (Figs. 3.14a, b).

In the CTRL run, rain rates rapidly increase from 2100-0100 UTC and DCCs and DWCCs are present during this time (Figs. 3.14c, d). After 0100 UTC, rain rates begin to decrease, but rain volume still increases to around 0500 UTC. At 0500 UTC, BSRs are rapidly growing in size, and stratiform area surpasses convective area (Fig. 3.14d). BSRs continue to grow until about 1300 UTC. In the noSDC run, rain rates increase even more rapidly at 0100-0200 UTC and there is not as broad of a peak in rain rates compared to the CTRL. DWCCs continue to grow in size though, as does the rain volume which peaks at 14 x 10^7 kg s^{-1} at 0630 UTC. BSRs are identified later in the morning compared to the CTRL, and they tend to decrease in size faster compared to the CTRL. The most obvious difference between the CTRL and noSDC runs is the timing of convection, which generally occurs later when the terrain is removed.

This analysis provides insight into how the SDC influence convective components of MCSs under weak synoptic conditions. In the observations, deep, very intense cells develop in the afternoon over the SDC and move off the terrain to the northeast. In the early evening hours, a second round of convection enters the domain and remains tied to the SDC for more than 12 hours. The model simulates this second round of convection fairly well but does not capture the intense

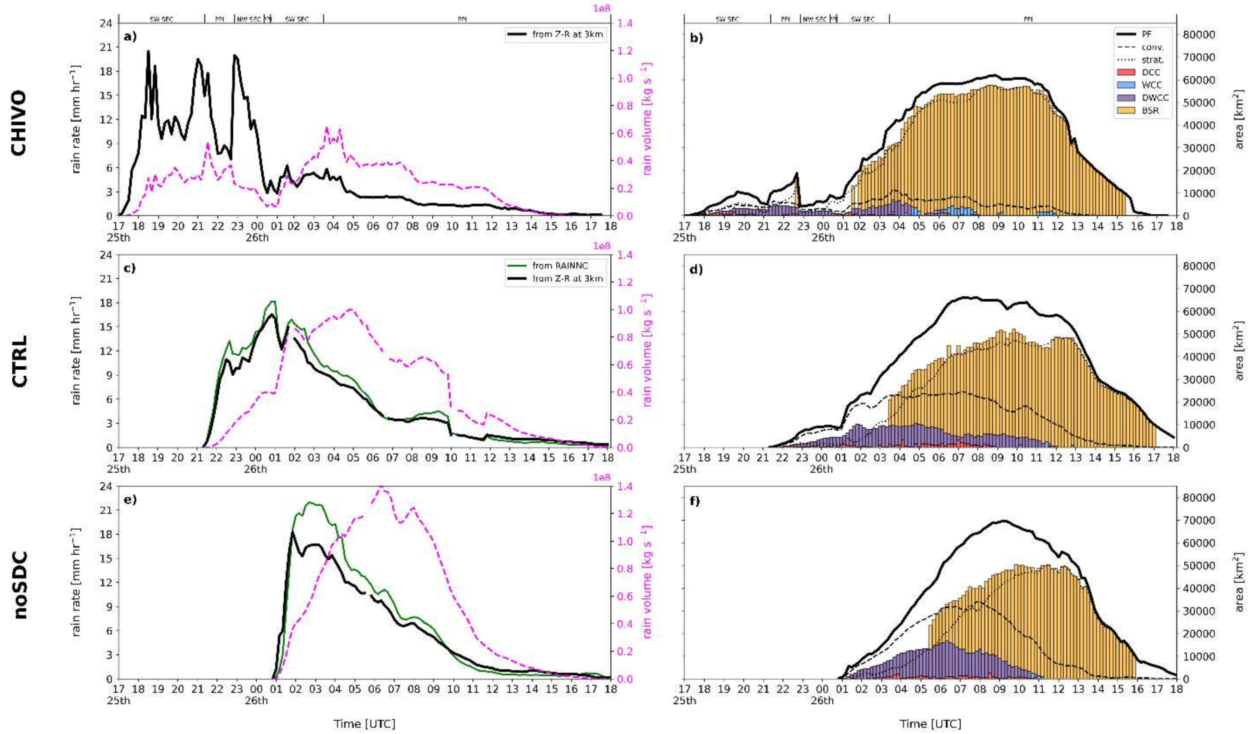

Figure 3.14: As in Fig. 3.6 but for the 25-26 January 2019 case. CHIVO scan types are shown on the top axis of panels (a-b), alternating between SEC and PPI modes.

initial cells along the SDC. Deep convection in the form of DCCs are identified exclusively over the SDC in CHIVO and the CTRL run whereas when the SDC are removed, deep convection is more widespread across the domain. The life cycle of the MCS starts off with DCCs which then grow upscale into DWCCs. Later, WCCs are identified together with BSRs, which are prevalent through the remainder of the event as the system slowly moves to the north. A similar life cycle is seen in the simulations, although only a few WCCs are identified in the CTRL run. Additionally, DWCCs are 1,000-5,000 km^2 larger on average over the eastern portion of the domain in the simulations compared to CHIVO which leads to a significant increase in convective area and rain volume.

3.4.3 Convective environment

To better understand the mechanisms behind MCS intensity differences, the convective environment is analyzed, similar to the strongly forced case. At 1200 UTC (0900 LT), there is an inversion just above the surface and winds are generally from the north in the low levels, consistent with the SALLJ (Fig. 3.15a). The profile is quite moist compared to the strongly forced case, with total precipitable water values around 50 mm (Table 3.5). The moisture profile is similar in the simulations, but there is no temperature inversion in the CTRL run. MLCAPE values are also similar between observations and simulations, but MLCIN is underestimated in the model. Three hours later, winds turn from northeasterly to northwesterly in the low levels and the mid-levels have become moister (Fig. 3.15b). MLCAPE is around 5300 J kg^{-1}, which is one of the highest values recorded during the RELAMPAGO campaign (Schumacher et al. 2021; Table 3.5). The model has a similar profile in the low-levels, but there is increased dry air in the mid-levels which reduces the total precipitable water. 0-6 km vertical wind shear is also smaller in the simulations compared to observations.

In the afternoon at 1800 UTC (1500 LT), the surface has warmed to about 35°C (Fig. 3.15c). Total precipitable water continues to increase, as does MLCAPE (Table 3.5). Winds near the surface have a stronger upslope component, and the 0-3 km vertical wind shear increases to 14.0 m s^{-1}. The simulations are still drier than observations in the mid-levels and the low-level winds are not as easterly. MLCAPE in the CTRL run is about 1000 J kg^{-1} greater than in observations, whereas the MLCAPE in the noSDC run is similar to observations. MLCIN is overestimated in both simulations, though. By 21 UTC, the atmosphere has moistened even more, and winds are 10-15 m s^{-1} from the east near the surface (Fig. 3.15d). 0-3 km and 0-6 km vertical wind shear are particularly high at 17.5 and 24.0 m s^{-1}, respectively. Additionally, MLCAPE is still above 5000 J kg^{-1} and MLCIN has decreased to -40 J kg^{-1}. In the simulations, there is not as strong of an upslope component to the winds as there is in the observations. The low-to-mid levels are still considerably dry compared to observations, which results in total precipitable water values around 50 mm, more than 10 mm less than observations. This enhanced dry air in the simulations could explain why the deep isolated cells do not develop and why convection initiation is delayed. Similar to 18 UTC, MLCAPE is overestimated in the CTRL simulation, but is captured well in the noSDC run.

When comparing CTRL and noSDC profiles, MLCIN and 0-3 km vertical wind shear tend to be larger when the SDC are removed. Other parameters such as MLCAPE and 0-1 km shear are larger in the noSDC run in the morning soundings, but smaller in the afternoon soundings compared to the CTRL. These findings for this case are not consistent with the strongly forced case. Further analysis would be needed to determine if this is a result of the weak synoptic forcing, or if this case is an anomaly. The direct effect of the SDC on thermodynamics and the development of cold pools is now analyzed.

Table 3.5: As in Table 3.3 but for the 25-26 January 2019 case.

Date		MLCAPE	MLCIN	TPW	0-1 km shear	0-3 km shear	0-6 km shear	6-12 km shear
		[J kg^{-1}]	[J kg^{-1}]	[mm]	[m s^{-1}]	[m s^{-1}]	[m s^{-1}]	[m s^{-1}]
Jan. 25 12 Z	Obs	3638	-164	50.12	22.0	5.6	15.0	10.1
	CTRL	3447	-83	50.40	8.9	2.8	10.4	6.3
	noSDC	3865	-150	51.73	17.4	12.1	10.0	6.8
Jan. 25 15 Z	Obs	5297	-125	54.49	9.8	3.5	19.7	6.0
	CTRL	4169	-85	47.80	8.7	4.5	12.0	6.9
	noSDC	4399	-183	49.02	16.3	9.6	11.8	6.8
Jan. 25 18 Z	Obs	5505	-52	56.73	8.7	14.0	21.6	7.3
	CTRL	6427	-76	51.43	9.3	6.0	15.0	7.0
	noSDC	5578	-115	52.65	2.5	9.2	12.0	7.0
Jan. 25 21 Z	Obs	5234	-40	64.00	6.2	17.5	24.0	1.5
	CTRL	6054	-76	51.17	5.2	7.3	13.6	7.1
	noSDC	5261	-131	52.36	4.0	10.4	13.7	9.1

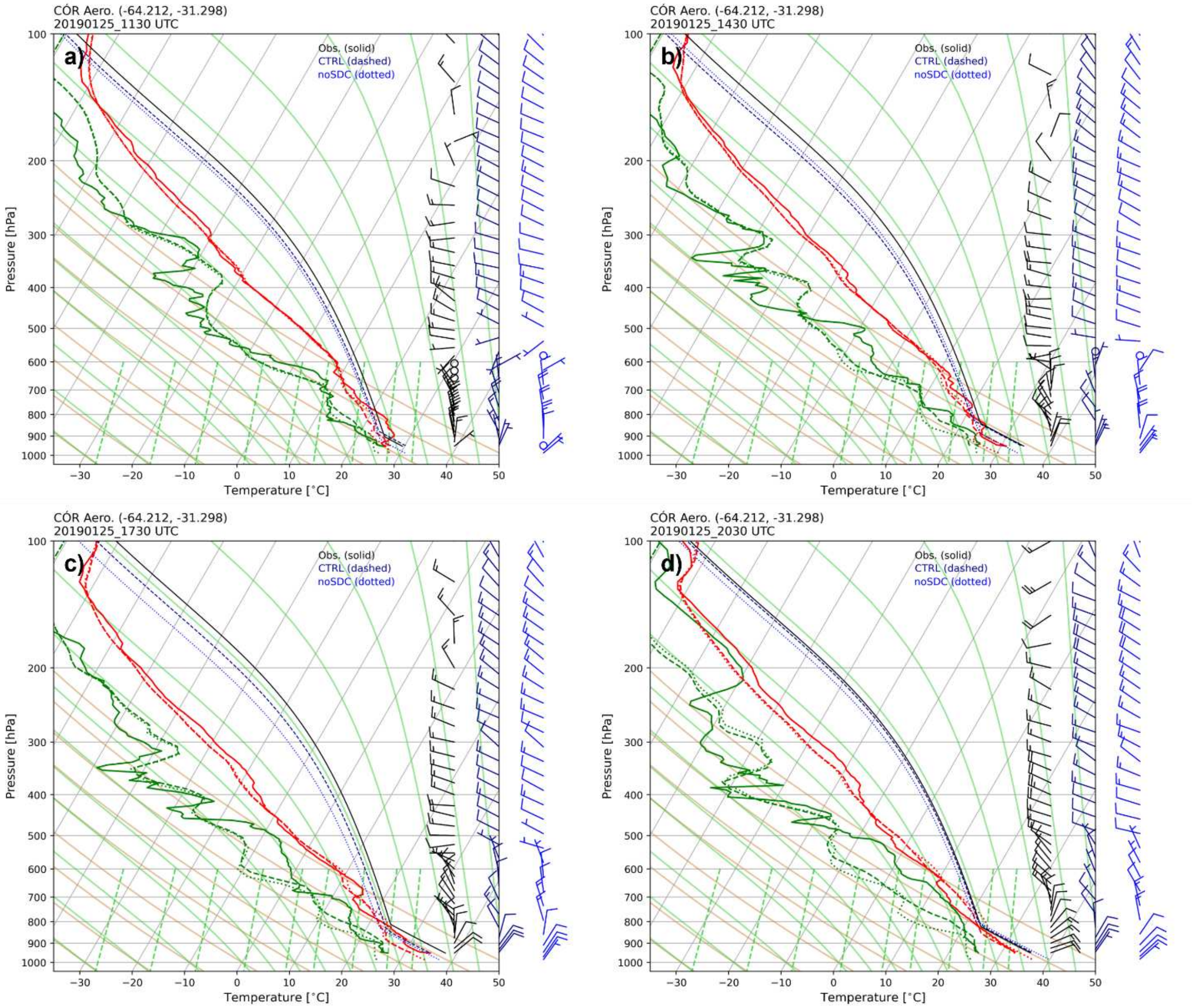

Figure 3.15: As in Fig. 3.7 but for the 25-26 January 2019 case. Sounding times are a) 1200 UTC, b) 1500 UTC, c) 1800 UTC, and d) 2100 UTC on 25 January.

3.4.4 Cold pools

Under weak synoptic conditions, cold pools and their interactions with the SDC seem to play a larger role in precipitation redevelopment. Figure 3.16 shows the development of cold pools throughout the MCS life cycle for the CTRL and noSDC runs. At 2000 UTC, isolated convection has developed along the southern SDC and along the foothills in the CTRL run (Fig. 3.16a).

Convection along the foothills is also visible in the noSDC run at 2000 UTC, but there is no convection around 65°S where the SDC would be (Fig. 3.16b). Four hours later, convection has organized into two cohesive lines along the southern SDC in the CTRL run, with cold air pooling along the foothills (Fig. 3.16c). There is similarly a western line of convection that develops along the foothills in the noSDC run, but there is no convection south of CHIVO in the SDC region (Fig. 3.16d). At 0400 UTC, the lines have merged and bowing convection is visible along the SDC in the CTRL run (Fig. 3.16e). When the SDC are removed, convection does not surge north as rapidly, and convection is strongest over the plains (Fig. 3.16f). Cross sections along 64°W at 0400 UTC show the cold pool in the CTRL run is located slightly to the north compared to the noSDC run, but it is also slightly shallower (Figs. 3.17a, b). Northerly and southerly winds converge at the head of the cold pool in both simulations. Virtual potential temperature shows the cooler air is associated with the cold pools and not a large-scale front like in the strongly forced case. Cross sections across the SDC also at this time show cold pools are strongest along the western side of the SDC (Fig. 3.17c). This is also where deep convection is enhanced (Figs. 3.13b, e). In contrast, when the SDC are removed, cold pools are deep across the plains, coinciding with the most intense convection (Figs. 3.12c, 3.13f, 3.17d).

At 0800 UTC, convection and cold pools are fairly widespread across the domain in the CTRL and noSDC runs (Figs. 3.16g, h). Cross sections across the SDC at this time show the strongest cold pools are trapped between the foothills and SDC in the CTRL run (Fig. 3.17e). Strong upslope flow is observed in the lowest 2 km east of the SDC, and cold pools reach 3-4 km above the surface. There is deep convection observed along and west of the SDC (Figs. 3.13b, e). When the SDC are removed, cold pools are strongest along the foothills to the west (Fig. 3.17f). The average cold pool depth is shallower, especially farther east, and the easterly flow near the surface is also weaker and shallower compared to the CTRL run. Deep convection is spread farther east at this time (Figs. 3.13c, f). At 12 UTC, convection is enhanced along the foothills to the north and the coldest cold pools at the surface are found along the terrain to the west (Figs. 3.16i, j). Four hours later, the majority of the convection has moved north well beyond the CHIVO domain and cold pools at the surface have decreased in strength (Figs. 3.16k, l). These results suggest terrain, including the SDC and the foothills, play an important role in blocking cold pools and reinvigorating convection.

3.5 Discussion

Mesoscale characteristics of two MCSs from RELAMPAGO showed the SDC have varying roles in focusing convection under strong vs. weak synoptic forcing. Under strong synoptic forcing, a strong line of convection develops overnight and moves through the region of study. Observations show deep convection grows upscale rapidly, and many DCCs and DWCCs are identified across the radar domain. The CTRL and noSDC simulations produce significantly more convective echoes compared to observations which are also widespread across the domain. Back-building of deep convection is visible along the SDC in the observations and CTRL, but this characteristic is not as prominent when the terrain is removed. The cold front and associated convection move parallel to the long-axis of the SDC in the CTRL run, but are titled more northwest to southeast when the SDC are removed. Even though the SDC are removed, cold pools are still blocked by the foothills of the Andes to the west, but these cold pools are not as deep as those found between the foothills and SDC in the CTRL run. Under strong synoptic flow, forcing along the cold front appears to be the dominant driver of convection.

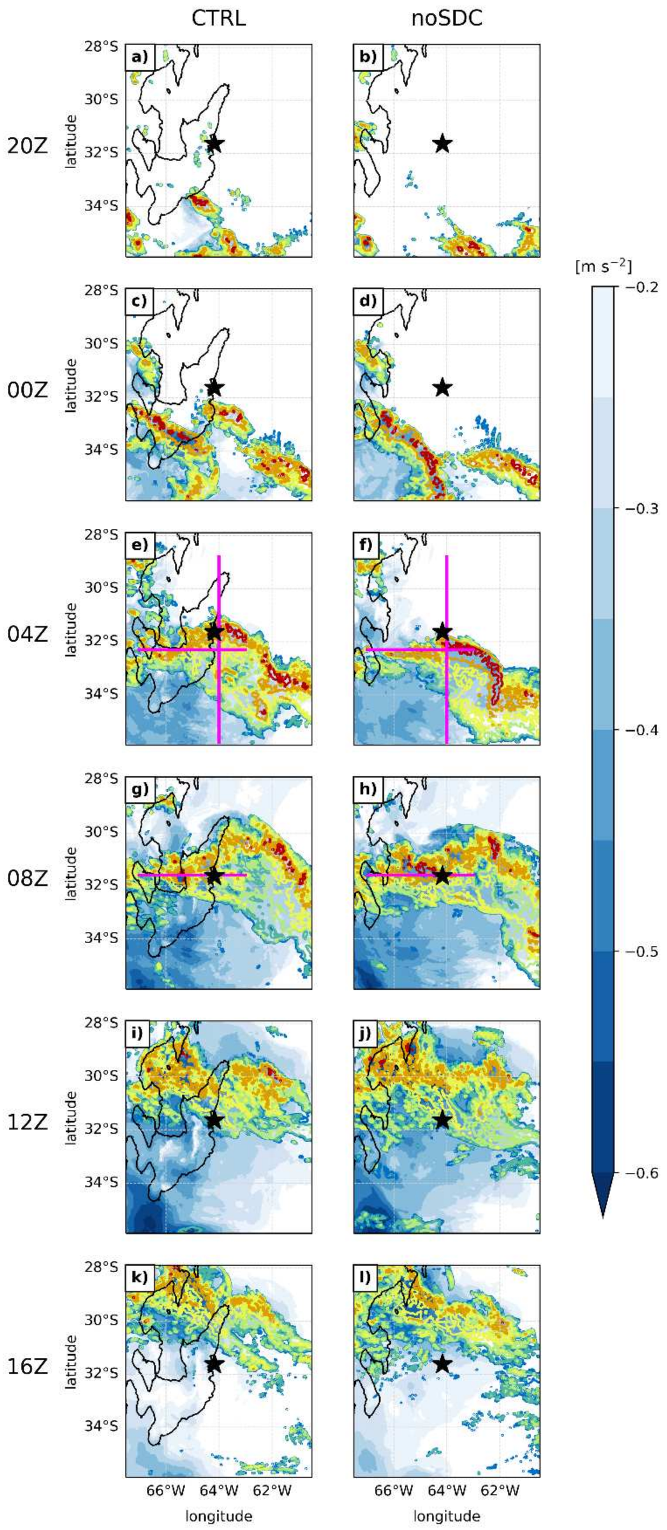

Figure 3.16: As in Fig. 3.8 but for the 25-26 January 2019 case. Times shown are 2000, 0000, 0400, 0800, 1200, and 1600 UTC on 25-26 January 2019. The initial time used to calculate perturbations was 16 UTC on 25 January. Magenta lines in panels (e-h) indicate the cross sections shown in Fig. 3.17.

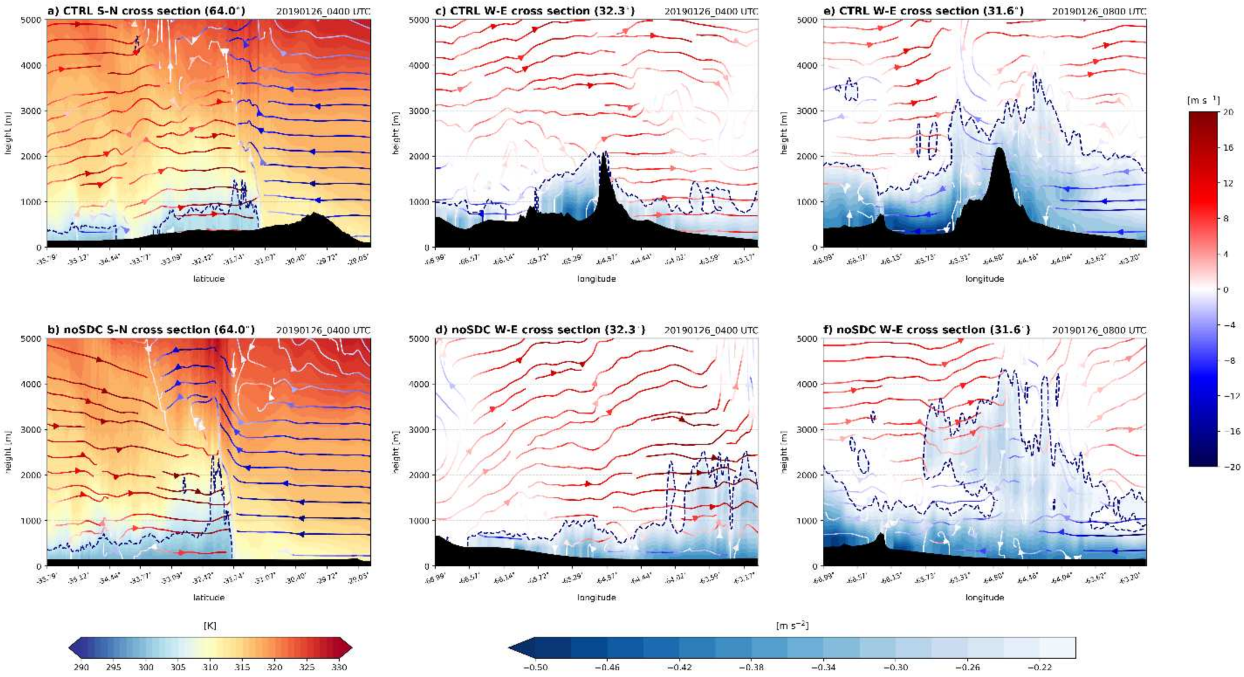

Figure 3.17: a) Cross section of the CTRL run at 0400 UTC on 26 January taken at 64°W from 35.8°S to 28.8°S of virtual potential temperature (shaded; K), in-plane winds (streamlines shaded by magnitude; m s^{-1}), and cold pools (dashed; B = -0.2 m s^{-2}). b) As in (a) but for the noSDC run. c) Cross section of the CTRL run at 0400 UTC on 26 January taken at 32.3°S from 67°W to 63°W of cold pools (shaded; B < -0.2 m s^{-2} and dashed; B = -0.2 m s^{-2}) and in-plane winds (streamlines shaded by magnitude; m s^{-1}). d) As in (c) but for the noSDC run. e) As in (c) but taken across 31.6°S at 0800 UTC and f) as in (e) but for the noSDC run. All cross sections are averaged 10 km perpendicular to the line.

In contrast, under weak synoptic forcing, the SDC act to spatially focus convection. Observations from this MCS event recorded the deepest convective echoes throughout the RELAMPAGO field campaign, with 40-dBZ echo tops reaching above 20 km. These isolated cells occurred in the afternoon and were followed by a secondary round of convection which developed overnight and quickly grew upscale into a large MCS that remained relatively stationary over the SDC. DCCs, DWCCs, and WCCs were confined to the western portion of the domain over the SDC. The majority of the event in the early morning and late morning hours was stratiform which produced the most precipitation between the Andean foothills and the SDC. The CTRL simulation was not able to capture the deep isolated cells in the afternoon well, potentially because the low-to-mid levels were considerably drier than observations. However, the CTRL captured the second round of convection quite well, with the deepest cores remaining over the SDC, and stratiform precipitation occurring throughout the morning along and west of the SDC. DWCCs that were identified were considerably larger on average over the plains than the ones observed by radar, though, leading to much larger rain rates, rain volumes, and deep convective echoes. Interestingly, when the SDC were removed, a strong MCS still developed, likely because the convective environment was favorable for convective development. However, the timing of the convection within the radar domain was 4-5 hours later than in the CTRL and there were fewer deep cores over the western portion of the domain. The cold pool analysis for this case revealed the coldest air was located between the foothills and SDC in the CTRL which allowed for reinvigoration and repeated precipitation over this region. When the SDC were removed, the foothills of the Andes still acted to block cold pools, but they were weaker compared to the CTRL.

To test the importance of cold pools in MCS formation and evolution, additional simulations were conducted where the cooling due to evaporation was turned off. This effectively turns off cold pool production and we can thus evaluate the importance of cold pool-terrain interactions on the development of convection in the region. Figure 3.18 shows surface cold pools and reflectivity from two times for the strongly and weakly forced cases. Under strong synoptic forcing, an MCS still develops when evaporative cooling is turned off (Figs. 3.18a-d). However, the convection enters the radar domain 1-2 hours earlier compared to when evaporative cooling is turned on (not shown). Perhaps the biggest difference is that there is no secondary generation of convection to the west over the terrain. Cross sections of cold pools and winds across the SDC show there are no cold pools generated when evaporative cooling is turned off (Figs. 3.19a-d).

Thus, under strong synoptic forcing, cold pools play a role in the secondary generation of convection near terrain.

Under weak synoptic forcing when evaporative cooling is turned off, a large vortex develops and moves west towards the Andes (Figs. 3.18e-h). Cross sections of cold pools and winds show upslope slow is enhanced when evaporative cooling is turned off (Figs. 3.19e-h). There are no surface cold pools, but there is enhanced cooling aloft. In these regions of cooling aloft, the flow reverses from westerly when evaporative cooling is on, to easterly when it is turned off. The fact that these runs are so different from the CTRL and noSDC runs show that evaporative cooling and cold pools are crucial in the development and evolution of the MCS under weak synoptic forcing.

3.6 Conclusions

Observations from the CHIVO radar were analyzed for two MCS events from RELAMPAGO which occurred under strong and weak synoptic conditions and compared with a 1-km control simulation (CTRL) and a 1-km simulation where the SDC were removed (noSDC). PFs and storm modes including DCCs, WCCs, DWCCs, and BSRs are identified in each dataset and statistics including areas, rain rates, and echo top heights are calculated. The role of the SDC on convective development and thermodynamics including cold pool propagation is determined for the strong- vs. weak-synoptically forced cases. General conclusions from this work are as follows:

1) For the strongly forced system, the role of cold pools and their interaction with the SDC is secondary to forcing from the cold frontal passage. However, blocking of the cold pools by the SDC enhances deep convection over the terrain which is not as prominent when the SDC are removed.

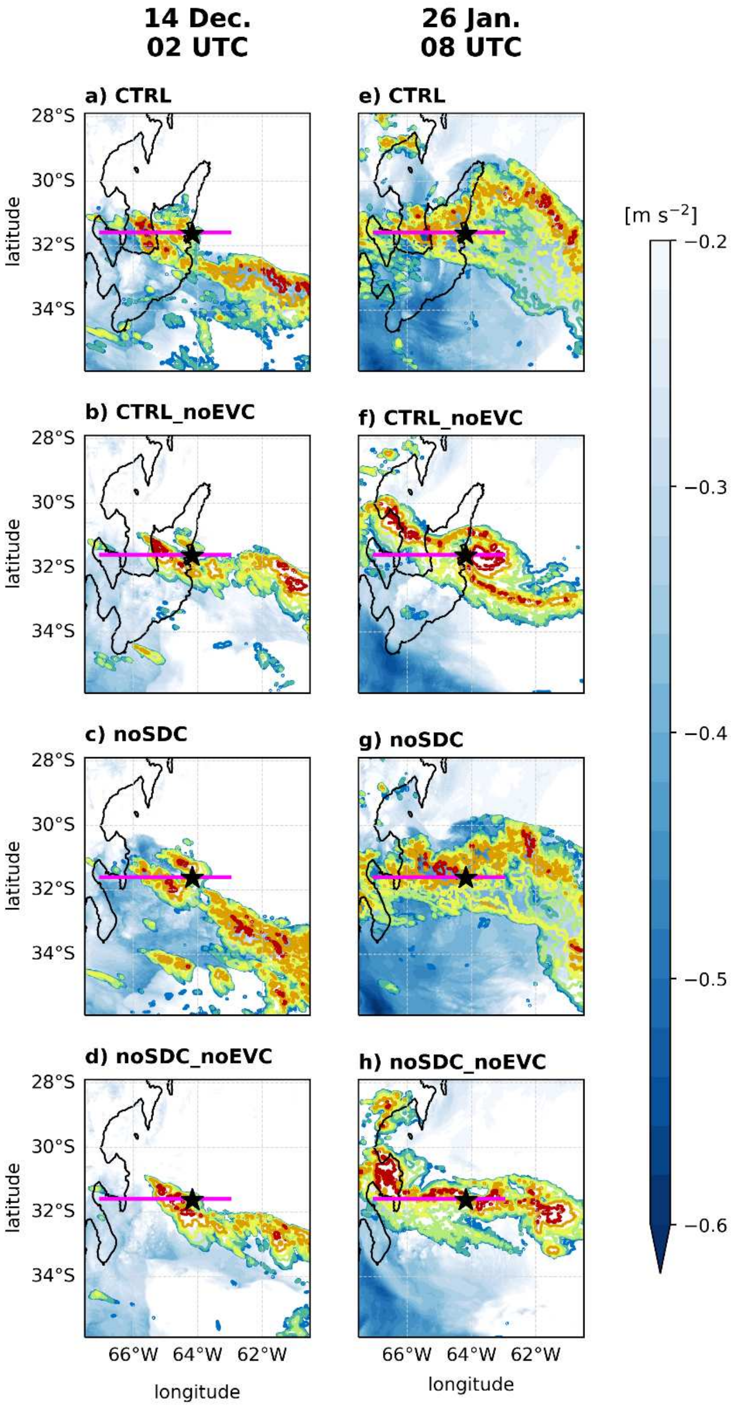

Figure 3.18: As in Figs. 3.8 and 3.16. A comparison of reflectivity and cold pools at the lowest model level between CTRL and noSDC runs with and without evaporative cooling. Left panels are shown at 0200 UTC on 14 December 2018 and right panels are shown at 0800 UTC on 26 January 2019. Panels (a) and (e) are from the CTRL runs, panels (b) and (f) are from the CTRL runs with evaporative cooling turned off (CTRL_noEVC), panels (c) and (g) are from the noSDC runs, and panels (d) and (h) are from the noSDC runs with evaporative cooling turned off (noSDC_noEVC).

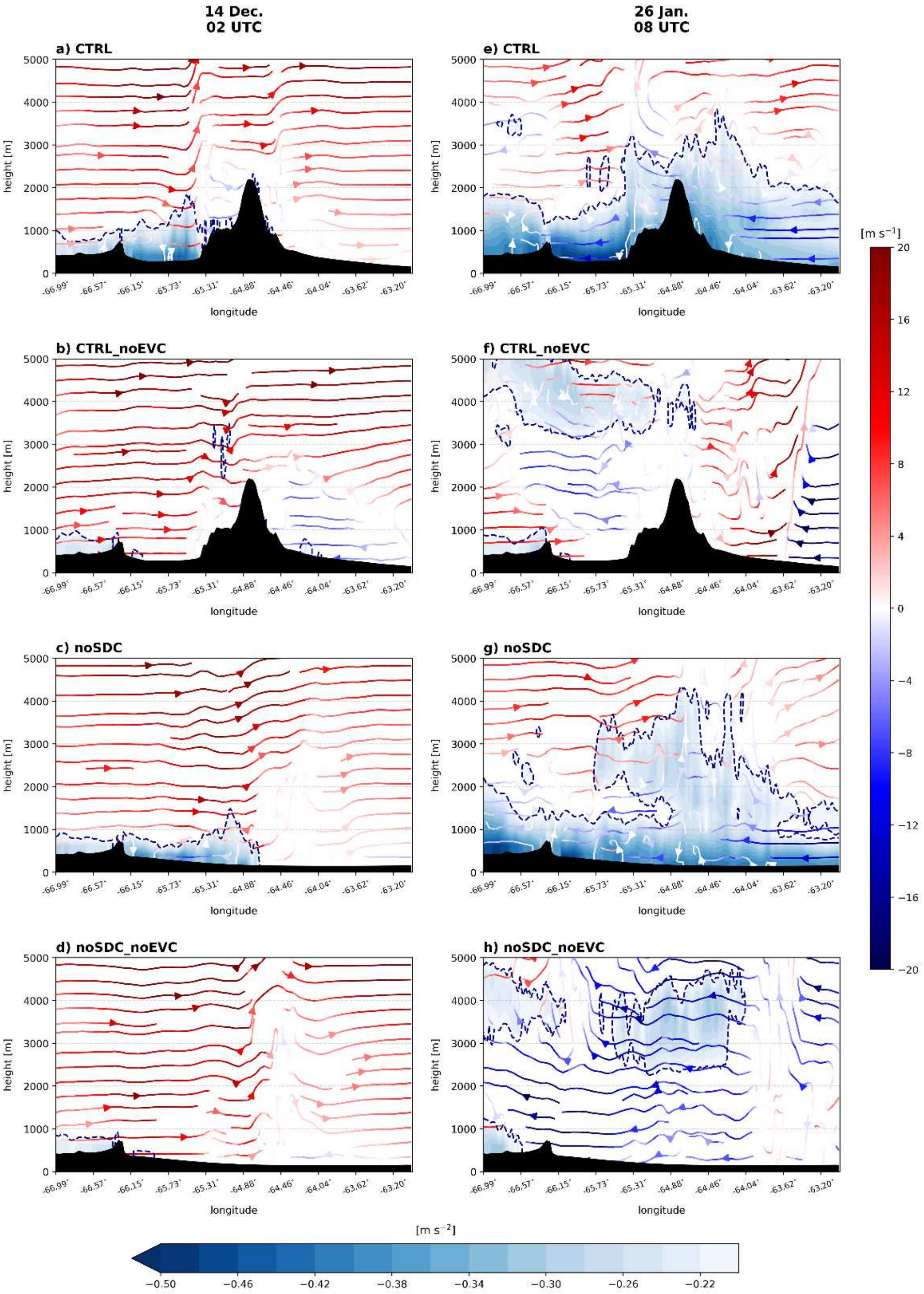

Figure 3.19: Cross sections of cold pools (shaded; $B < -0.2$ m s^{-2} and dashed; $B = -0.2$ m s^{-2}) and in-plane winds (streamlines shaded by magnitude; m s^{-1}). Panels on the left are shown at 0200 UTC on 14 December at 31.6°S from 67°W to 63°W, while panels on the right are shown at 0800 UTC on 26 January at 31.6°S from 67°W to 63°W. Panels (a) and (e) are from the CTRL runs, panels (b) and (f) are from the CTRL_noEVC runs, panels (c) and (g) are from the noSDC runs, and panels (d) and (h) are from the noSDC_noEVC.

2) For the weakly forced system, the convective environment is extremely favorable for convective development, and deep convection is continuously observed over the SDC. When the SDC are removed, cold pools become more disperse and there is little reinvigoration of convection along the terrain like there is when the SDC are present.
3) Cold pools play a critical role in the location, timing, and intensity of convection, especially under weak synoptic conditions.

Additional cases should be analyzed to determine if results here hold for other strong- vs. weak-synoptically-forced cases in the RELAMPAGO observations. Ensembles could also be run to determine the range of effects the SDC have on convection. Future work will continue to analyze the impacts of the SDC on mesoscale characteristics including updrafts, microphysics, and lightning using observations from the lightning mapping array (LMA), the geostationary lightning mapper (GLM) on board GOES-16, and other radars deployed during RELAMPAGO and the Cloud, Aerosol, and Complex Terrain Interactions (CACTI; Varble et al. 2021). Results from other model simulations may also be explored including large-eddy simulations run by ARM (Gustafson et al. 2020).

This analysis provides a better understanding of how terrain influences the growth of MCSs in SSA and may aid in the forecasting of severe weather under different synoptic conditions. Additionally, this research has shown that high resolution simulations in SSA can struggle to accurately resolve mesoscale details of severe MCSs. Data assimilation of observations is likely needed to more accurately represent local terrain influences and the mesoscale characteristics associated with MCSs in SSA near complex terrain.

CHAPTER 4

Lightning Characteristics Associated with Storm Modes Observed during RELAMPAGO

4.1 Introduction

A better understanding of global lightning distributions has been a subject of interest for the past several decades. Knowledge of current global lightning distributions and their variations by climate regime and storm type is important for understanding how these distributions may change in the future as a result of climate change. Several satellite studies have documented the global climatology of lightning and have attempted to estimate global flash rates. Using the Optical Transient Detector (OTD) onboard *MicroLab-1* (*OrbView-1*), which was one of the first instruments specifically designed to measure lightning, Christian et al. (2003) found hot spots in lightning flash rates along the coasts, in mountainous regions, and in the Congo basin. More recent studies such as from Zipser et al. (2006) and Albrecht et al. (2016) found maxima in lightning flash rates in the Congo basin and Lake Maracaibo in Venezuela, as well as downstream of mountain ranges, including the Andes in subtropical South America (SSA), using the Lightning Imager Sensor (LIS) onboard the Tropical Rainfall Measuring Mission (*TRMM*; Kummerow et al. 1998) satellite. In particular, storms in SSA have the highest lightning flashes per precipitation feature (PF) compared to any other location observed by TRMM (Zipser et al. 2006). More recently, Peterson et al. (2021) used OTD and LIS to analyze the global climatology of flash extent density, which includes the spatial extent of lightning. Their results agree with previous studies that have looked at global flash rates, naming coastal and mountainous regions as lightning hot spots. Furthermore, analysis of diurnal variations in flash extent densities show nocturnal to early morning moderate-to-high lightning activity in areas downstream of mountain ranges such as the central-southern U.S. Great Plains, northern Argentina, Southeast Asia, and West Africa (Albrecht et al. 2016).

Deep convection is also known to occur downstream of mountain ranges around the world (Zipser et al. 2006; Houze et al. 2015). This includes downstream of the Andes in SSA where convection often rapidly grows upscale into mesoscale convective systems (MCSs; Rasmussen and Houze 2011, 2016; Rasmussen et al. 2014, 2016). This convection is associated with extreme weather ranging from flash flooding to large hail to mega lightning flashes (Zipser et al. 2006; Cecil and Blankenship 2012; Rasmussen et al. 2014; Bruick et al. 2019; Peterson 2021). It is hypothesized that the Andes and the Sierras de Córdoba (SDC) support a favorable environment for deep convection and rapid upscale growth of MCSs in SSA (Romatschke and Houze 2010; Rasmussen and Houze 2011, 2016). Westerly flow over the Andes induces lee cyclogenesis, which strengthens the pressure gradient and enhances the South American Low-Level Jet (SALLJ; Vera et al. 2006), which transports moisture from the Amazon into the region. The SALLJ collides with the SDC, and convection rapidly develops, leading to extreme weather across the higher terrain as well as farther east across the La Plata Basin as MCSs propagate off the terrain.

The collocation of deep convection and high lightning flash rates in SSA was studied by Rasmussen et al. (2014) who analyzed the spatial and temporal patterns of lightning associated with different convective storm modes. They found lightning flash rates are highest in the deepest and widest convection, which occurs along the SDC in the late evening and early morning hours (20-02 LT). Unfortunately, satellite studies of deep convection in SSA were not able to capture the storm life cycles, given the polar-orbiting nature of *TRMM*. To collect higher spatial and temporal resolution data of intense deep convection in SSA, several instruments were deployed to

Córdoba, Argentina as part of the Remote sensing of Electrification, Lightning, And Mesoscale/microscale Processes with Adaptive Ground Observations (RELAMPAGO; Nesbitt et al. 2021) and Cloud, Aerosol, and Complex Terrain Interactions (CACTI; Varble et al. 2021) field campaigns. The intensive observing period of RELAMPAGO and CACTI occurred in November and December of 2018, but some instruments continued to operate through April 2019. This timing corresponds to the most intense lightning activity over the SDC (Rasmussen et al. 2014).

One of the key platforms deployed during RELAMPAGO was a very high frequency (VHF) Lightning Mapping Array (LMA; Rison et al. 1999) operated by National Aeronautics and Space Administration (NASA) George C. Marshall Space Flight Center (Lang et al. 2020). This was the first regional ground-based total (in-cloud and cloud-to-ground) lightning observing platform deployed in SSA that had very high lightning detection efficiency with the goal of validating satellite-based lightning observations, particularly from the Geostationary Lightning Mapper (GLM; Goodman et al. 2013; Rudlosky et al. 2019) onboard *GOES-16*. Lang et al. (2020) provided an initial overview of the data collected by the LMA network. They found flashes occur most frequently at 10 km in height, have areas of 0-50 km^2, and last for less than 0.5 s. Additionally, the diurnal cycle of flashes is bimodal with peaks at 17 and 00 LT. This diurnal cycle matches well with previous satellite studies (Rasmussen et al. 2014) but provides even higher temporal resolution.

This work aims to further analyze flash characteristics observed by the RELAMPAGO LMA as a function of storm mode based on ground-based radar observations, similar to the analysis done by Rasmussen et al. (2014) using LIS and OTD. These three-dimensional storm modes represent the most extreme vertical and horizontal components of storms and provide valuable information regarding the life cycle of convective events, including MCSs, in the region.

In addition to analyzing flash characteristics, microphysical characteristics derived from radar are examined to investigate processes related to electrification. Detailed analyses of lightning and microphysical characteristics for two cases from RELAMPAGO are presented: the 13-14 December 2018 MCS and the 25-26 January 2019 MCS. Several aspects of these cases have been studied in depth by Rocque and Rasmussen (2022) and Rocque et al. (2023; in review), including the impact of the Andes and SDC on the synoptic-scale environment and convective characteristics. Our goal is to extend this research by analyzing the electrical and microphysical properties of these storms to better understand why convection and associated lightning in this region are so intense.

4.2 Data and Methodology

4.2.1 Radars

The Colorado State University (CSU) C-band, dual-polarization radar (CHIVO) is used in this analysis to identify PFs and better understand the microphysical characteristics of storms in SSA. CHIVO was deployed near Córdoba, Argentina for the RELAMPAGO field campaign from 10 November 2018 through 31 January 2019 (Arias et al. 2019). The radar conducted 360° plan position indicators (PPIs), 135° sector scans (SEC), and range height indicators (RHIs), with update cycles every 5-10 minutes depending on precipitation events within the 150 km range. Due to its proximity to the SDC, CHIVO is blocked at low elevation angles to the west. There is also significant clutter to the north and east of CHIVO that is addressed in the quality-control (QC) process.

After data collection, a QC procedure was developed and applied to the CHIVO dataset. This procedure included azimuth, attenuation, and differential reflectivity corrections, and the application of normalized coherent power and correlation coefficient thresholds to remove non-meteorological data and clutter. An additional QC procedure was applied to two cases of interest to remove remaining clutter associated with the SDC. These cases were the 13-14 December 2018 strongly forced MCS, and the 25-26 January 2019 weakly forced MCS that were studied by Rocque and Rasmussen (2022) and Rocque et al. (2023; in review). The removal of clutter was achieved by running the National Center for Atmospheric Research (NCAR) particle identification (PID) algorithm (Vivekanandan et al. 1999). Soundings from the Atmospheric Radiation Measurement (ARM) Mobile Facility (AMF) near Villa Yacanto (about 75 km southwest of CHIVO) were matched with the closest radar time to retrieve the temperature profile needed for the PID calculation. Pixels that were identified as insects, second trip, or clutter were masked in all radar fields.

After QC was performed, the PPI and SEC data were interpolated to a 1 km horizontal resolution and 0.5 km vertical resolution grid. Then, a hydrometeor identification (HID) algorithm developed for C-band radar (Dolan et al. 2013) was applied to the interpolated dataset. As with the NCAR PID, soundings from AMF were matched with CHIVO to retrieve the temperature profile. The HID algorithm categorizes data into 10 groups, but this work is focused on bulk microphysical characteristics related to lightning. Thus, we classify the data into three groups: graupel and hail, snow, and ice. The graupel and hail category contains low density graupel, high density graupel, and hail, while the snow category contains wet snow and aggregates, and the ice category contains ice crystals and vertically aligned ice. After the data is categorized, Z-M relationships are applied to calculate hydrometeor masses. These relationships were first derived by Heymsfield and Palmer (1986) and Heymsfield and Miller (1988) and have been used in other lightning studies including Deierling et al. (2008):

$$\mathrm{M_{graupel}} = 0.0052 \times \mathrm{Z}^{0.5}$$

$$M_{\mathrm{hail}} = 0.000044 \times Z^{0.71}$$

$$M_{\mathrm{snow/ice}} = 0.017 \times Z^{0.529}$$

where M is in g m^{-3} and Z is in mm^6 m^{-3}.

To provide better radar coverage for the two cases of interest, data from the 2nd generation C-band Scanning ARM Precipitation Radar (CSAPR2) was also analyzed. CSAPR2 was located at the AMF site and conducted PPIs, RHIs, and hemispheric RHIs from 12 October 2018 through 30 April 2019 as part of the CACTI field campaign. The same QC procedure that was run for CHIVO was applied to the initial CSAPR2 data that was processed by ARM. Radar mosaics with CHIVO and CSAPR2 were created for the two cases of interest: 20-08 UTC on 13-14 December 2018 and 17-08 UTC on 25-26 January 2019. Data were interpolated to a 1.0 x 1.0 x 1.0 km grid using PyART (Helmus and Collis 2016), and the HID algorithm mentioned above was applied.

In addition to the HID, a convective/stratiform partitioning based on the Steiner et al. (1995) algorithm was applied to the CHIVO gridded dataset for the entire campaign, and the gridded radar mosaics for the cases of interest. This partitioning was applied from 3-5 km and is used to identify storm modes.

4.2.2 Storm mode identification

To better understand how lightning varies with different storm modes, a PF identification algorithm, developed by Rocque et al. (2023; in review), was employed. This algorithm is based on previous algorithms used in TRMM satellite studies (Nesbitt et al. 2000, 2006; Liu et al. 2008; Liu and Zipser 2013) and works by fitting an ellipse to the region of interest. In this work, PFs are identified where contiguous echoes of 3-5 km composite reflectivity are greater than 0 dBZ. Radar statistics associated with each PF are then calculated including echo top height and area. Radar parameters that are related to lightning are also calculated including graupel, hail, snow, and ice mass and volumes.

In addition to PFs, three-dimensional storm modes are also identified to more closely track storm characteristics in space and time. These storm modes have been used in TRMM satellite studies (Houze et al. 2007; Houze et al. 2015; Romatschke and Houze 2010; Rasmussen and Houze 2011, 2016) and ground-based studies (Zuluaga and Houze 2013; Rocque et al. 2023; in review) to evaluate the life cycle of MCS events. For this analysis, we use the strong-intensity storm thresholds defined in Houze et al. (2015). Deep convective cores (DCCs) have 40-dBZ convective echoes at least 10 km MSL, wide convective cores (WCCs) have contiguous 40-dBZ convective areas greater than 1,000 km^2, and broad stratiform regions (BSRs) have contiguous stratiform areas greater than 50,000 km^2. Additionally, if a feature satisfies both DCC and WCC criteria, it is considered a deep and wide convective core (DWCC). Radar statistics including feature area are also output for each storm mode. Given the size of the CHIVO radar domain, the size threshold associated with BSRs was modified to 10,000 km^2 for this study as was done in Rocque et al. (2023; in review). This PF identification algorithm was applied to the CHIVO gridded dataset and the two gridded mosaic datasets.

4.2.3 LMA

Ground-based observations of lightning were collected by a LMA (Rison et al. 1999) which was deployed near Córdoba, Argentina as part of the RELAMPAGO field campaign (Lang et al. 2020). The LMA consisted of 11 stations which were operating from November 2018 through April 2019 and it detects electromagnetic radiation emitted by lightning at VHF. LMA detected

VHF sources were mapped in three dimensions using a time-of-arrival technique (Proctor 1971), where at least 6 stations detected the source and the chi-square goodness of fit value (Thomas et al. 2004) was less than 5.0 (Lang et al. 2020). Within 100 km of the network, horizontal errors in location are estimated to be less than 100 m while vertical errors are less than 1 km. After sources were mapped, they were clustered into flashes if they were within 150 ms or 3 km of each other (Fuchs et al. 2016; Lang et al. 2020).

Flash characteristics including centroid location, area, duration, and total energy are analyzed for each PF identified by CHIVO. Flash rates are calculated by summing the number of flashes initialized within each PF over the time between the current and next radar scan, and dividing by the scan cycle, usually 10 minutes. Flash characteristics associated with three-dimensional storm modes were also analyzed. A flash was considered part of a storm mode if the centroid was within the storm mode bounds anytime during the radar scan. Flashes were also matched with PFs and storm modes identified in the radar mosaics for the 13-14 December and 25-26 January cases.

4.2.4 GLM

One purpose for the deployment of the LMA during RELAMPAGO was to provide ground-based validation of the Geostationary Lightning Mapper (GLM) onboard *GOES-16*. Thus, we briefly compare flash characteristics between LMA and GLM for the cases of interest. GLM detects lightning emissions at 777.4 nm through its 1372 × 1300 pixel Charge Coupled Device focal plane (Goodman et al. 2013). The footprint of GLM varies from 8 km at nadir to 14 km at the edges. Lightning pulses that occur within a footprint over 2 ms are called an event. The Lightning Cluster and Filter Algorithm (LCFA) then clusters simultaneous and adjacent events into groups. Groups are then clustered into flashes if they occur within 330 ms or 16.5 km from one another (Goodman et al. 2013). Due to the real-time nature of the LCFA, longer flashes (> 3 s) can sometimes be split up. To account for these mega flashes, we use the L2-CIERRA product which allows for longer flashes (Peterson 2019).

After comparing LMA flash centroid locations with GLM flash centroid locations for a few cases, it was determined an additional parallax correction needed to be applied to the GLM data. The level 2 cloud top height product from the GOES-16 Advanced Baseline Imager (ABI; Schmit et al. 2017) was used to calculate the median cloud height across the CHIVO-CSAPR2 radar domain. This height was then used to adjust the latitude and longitude of the flash centroids using equations described in Vicente et al. (2002). GLM flashes that were located within PFs identified by CHIVO and CSAPR2 in the mosaics were then analyzed.

4.3 Campaign-wide lightning statistics

4.3.1 Overview

A campaign-wide analysis of lightning characteristics associated with storm modes identified by CHIVO is presented first. Figure 4.1 shows a time series of LMA lightning flashes with at least 10 sources collocated with PFs identified by CHIVO during the RELAMPAGO time period. Several cases are easily identified, including the multi-day supercell-MCS event in early November (IOPs 4 and 5), the 13-14 December MCS (IOP17) and the 25-26 January MCS. In fact, the latter two cases have the highest lightning flash counts during the time frame, consistent with findings from Lang et al. (2020). In addition to flash counts, graupel and hail volumes identified by CHIVO are also shown. Graupel and hail volume tracks well with flash counts, particularly in December and January. However, graupel and hail volumes are much higher in the beginning of

November compared to the relative number of flashes observed. One reason for this lower number of flashes is that the number of operational LMA stations was lower until late November. The number of detection stations was particularly low on 11 November (Lang et al. 2020). When fewer stations are operational, there is a significant drop in the number of flashes detected. Thus, fewer flashes were detected by the LMA network in early November.

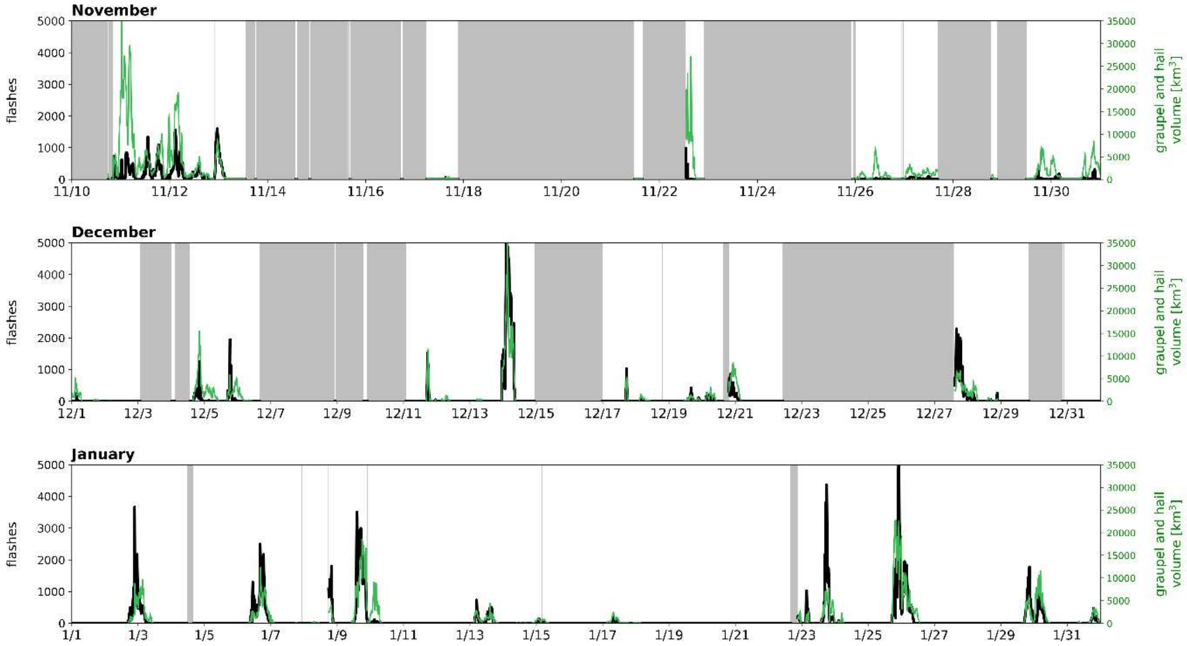

Figure 4.1: Time series of LMA flashes (≥ 10 sources; black) and graupel and hail volume (green; km^3) associated with CHIVO PFs.

4.3.2 Storm modes

The identification of storm modes, and the lightning flashes associated with them, provides insight into the life cycle of convective systems in the region. Previous analysis of lightning as a function of storm life cycle in central Argentina has shown that flashes associated with deep convection occur most frequently over the higher terrain, including the SDC, in the evening hours (Rasmussen et al. 2014). Using high spatial and temporal resolution data from the LMA network, the location and timing of lightning flashes with at least 10 sources associated with storm modes observed during RELAMPAGO are analyzed. We also analyzed lightning flashes with 3-10 sources and found similar results in the timing and location of these flashes. Figure 4.2 shows the frequency map of LMA flashes with at least 10 sources centered within a PF (Fig. 4.2a) or a storm mode (Figs. 4.2b-e). There is a strong concentration of flashes observed within PFs along and downstream of the highest terrain of the SDC (Fig. 4.2a). The frequency of flashes decreases as you approach the edges of the radar domain, especially towards the southwest. This region is also outside of the 100-km LMA radius, where detection decreases and errors associated with flash location increase. The frequency of DCC flashes is also maximized along the highest terrain of the SDC, matching well with those observed within PFs (Fig. 4.2b). Nearly 30% of all flashes identified within a PF are also identified within a DCC. Additionally, on average there are 71 flashes per DCC (Table 4.1). In contrast, fewer flashes are identified within WCCs (Fig. 4.2c). There are two maxima in WCC flash frequency that occur over the SDC to the northwest, and directly downstream of the SDC near the radar center. Very few WCCs were identified during RELAMPAGO (only 121; Table 4.1), but despite these low numbers, WCCs have the lowest flashes per storm mode on average compared to the other categories (27 flashes/WCC; Table 4.1). DWCCs, on the other hand, have the most flashes per feature at 722 flashes per DWCC (Table 4.1). The majority of flashes associated with DWCCs occur along the eastern edge of the SDC (Fig. 4.2d). These flashes are east of DCC flashes, consistent with the upscale growth of MCSs off the terrain with the highest flash rates along the topography (Rasmussen et al. 2014). About 17% of all flashes identified within a PF are also associated with a DWCC. Finally, flashes associated with BSRs tend to occur across the domain, with a maximum 50-100 km east of the SDC (Fig. 4.2e). On average, 68 flashes are identified per BSR (Table 4.1). Although this number is similar to flashes per DCC, BSRs are significantly larger than DCCs. One caveat with the identification of storm modes is that there are only two categories in the Steiner et al. (1995) algorithm, and stratiform is often overestimated. Some flashes occur along the edge of convection, which the algorithm will classify as stratiform and which could be incorporated into BSRs. A third classification between convective and stratiform such as “mixed” would likely reduce the number of stratiform flashes but is currently beyond the scope of this study.

Table 4.1: Number of features (DCCs, WCCs, DWCCs, and BSRs), number of flashes associated with each feature, and the average number of flashes per feature.

	DCC	**WCC**	**DWCC**	**BSR**
Number of features	3397	121	195	1400
Number of flashes	241643	3293	140737	94821
Average number of flashes per feature	71 fl/DCC	27 fl/WCC	722 fl/DWCC	68 fl/BSR

To analyze the diurnal cycle of flashes associated with storm modes, the timing of flashes and their location relative to the SDC are shown in the time-longitude plots in Figure 4.3. The main maximum in lightning flashes for all PFs occurs along the edge of the SDC in the afternoon hours (1400-1700 LT; Fig. 4.3a). This maximum extends along the SDC and to the east of the SDC. A secondary maximum occurs around midnight local time farther east. There is a minimum in lightning flashes that occurs in the morning hours from 0500-0900 LT. This diurnal cycle agrees with that found by Lang et al. (2020) using the full LMA dataset. DCCs are mostly found along the SDC in the afternoon hours as well (1400-1900 LT; Fig. 4.3b). The main peak in WCC flash frequency occurs around 0100 LT downstream of the SDC (Fig. 4.3c). Two maxima in DWCC flashes are identified, one maximum around 1800-2000 LT downstream of the SDC and a second wider maximum that extends from the highest terrain of the SDC to the eastern edge of the SDC around midnight local time (Fig. 4.3d). This again highlights the upscale growth and movement of

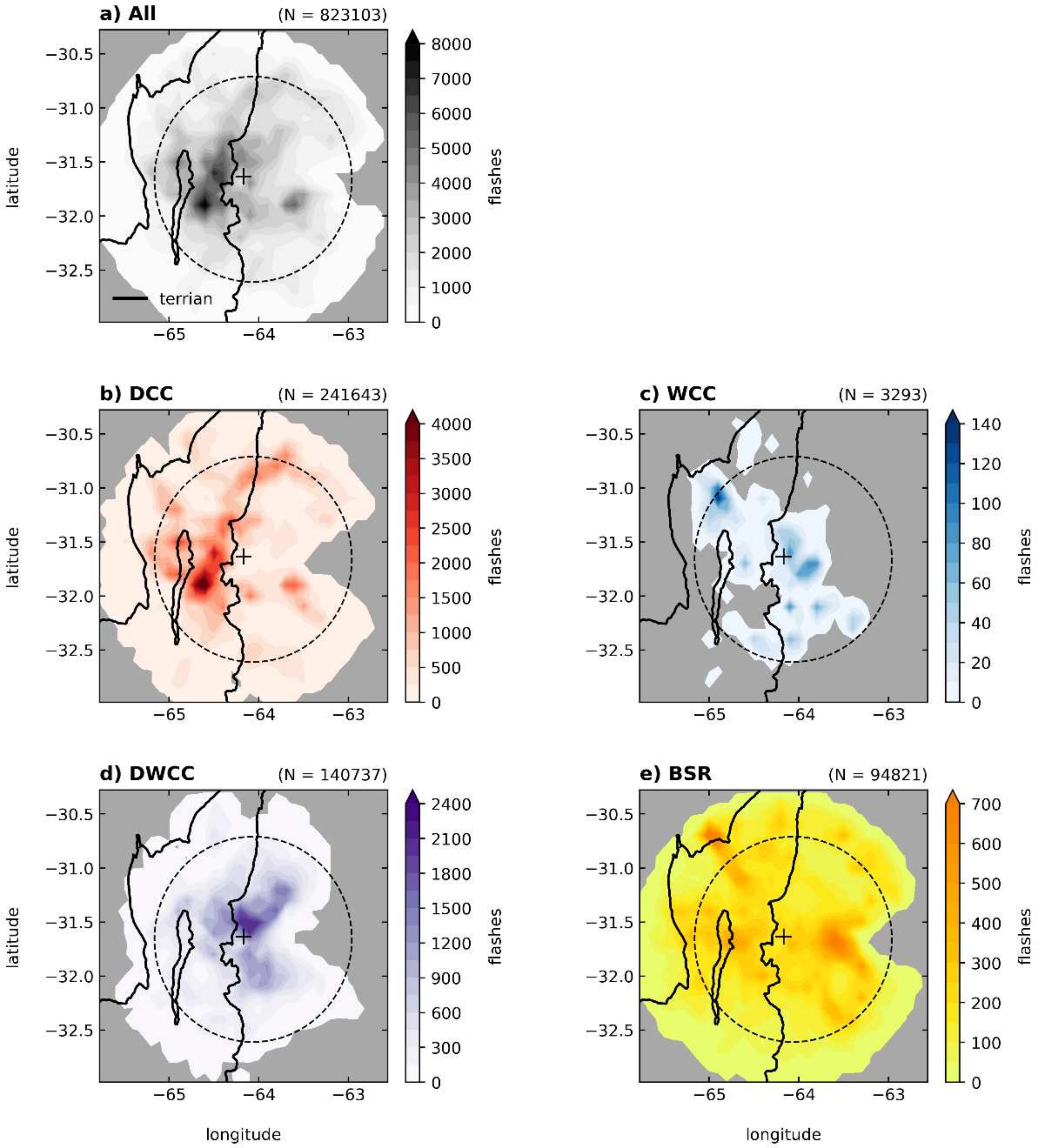

Figure 4.2: Location of LMA flashes with at least 10 sources centered within a) PFs, b) DCCs, c) WCCs, d) DWCCs, and e) BSRs for the CHIVO dataset. The total number of flashes is shown in the upper right of each plot. The 500 m and 2000 m terrain contours are shown in black, and the 100-km LMA range ring is shown as the dashed circle.

features off the terrain from deep convection to deep and wide convection to wide convection. Finally, stratiform flashes occur throughout most of the day but have two frequency maxima in the early afternoon hours and in the early morning hours (Fig. 4.3e). The first maximum in the afternoon begins west of the SDC around noon local time and extends to the eastern edge of the SDC around 1600 LT. This maximum is mainly associated with one case, 6 January 2019. The second maximum that occurs around midnight and extends through 0400 LT is associated with MCSs that have propagated eastward over the Plains. These results generally agree with Rasmussen et al. (2014), although the hotspot in DCC flashes is shifted later in the evening in their analysis.

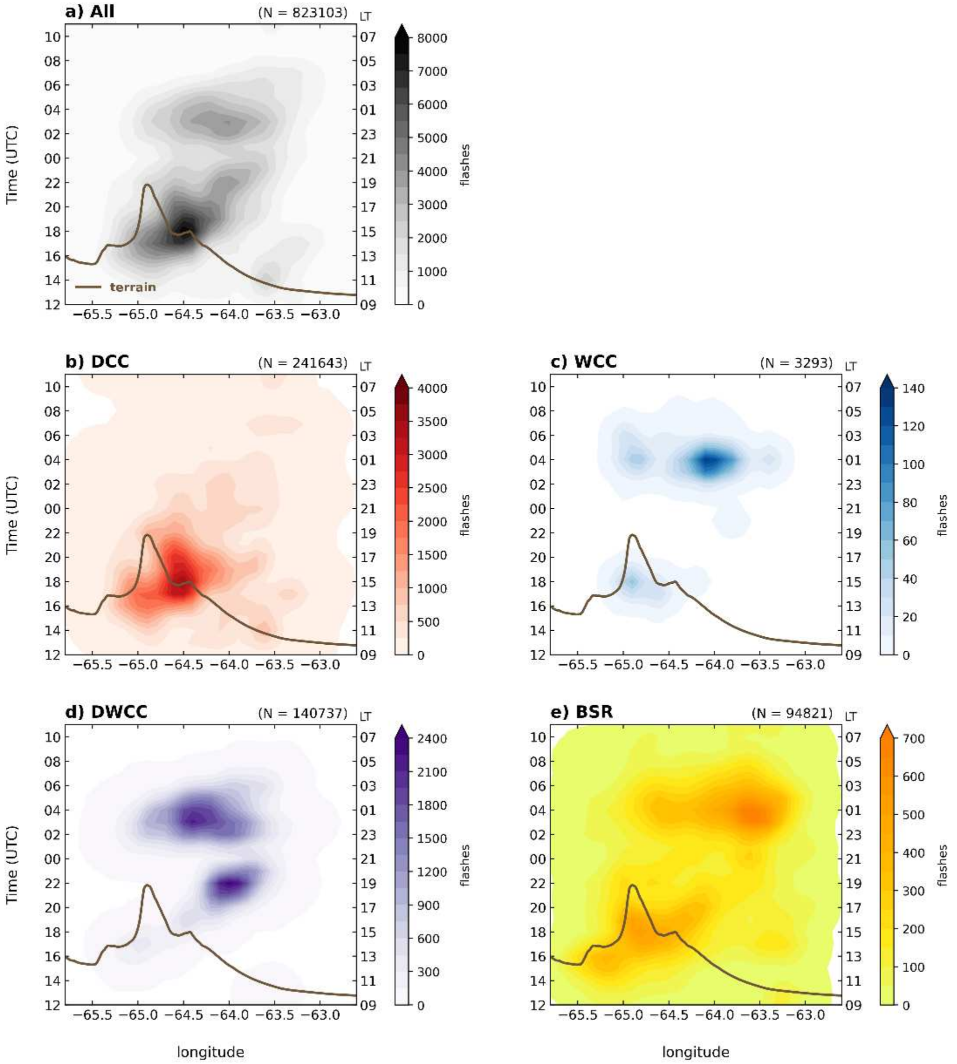

Figure 4.3: Time-longitude plots of LMA flashes with at least 10 sources centered within a) PFs, b) DCCs, c) WCCs, d) DWCCs, and e) BSRs for the CHIVO dataset. The number of flashes is shown in the upper right of each plot. The average terrain profile across the CHIVO latitude band is shown in dark brown. The local time (UTC -3) is shown on the right axis.

Distributions of flash area, flash duration, flash energy, and flash height are also examined to provide insight into the electrical characteristics of each storm mode (Fig. 4.4). In terms of flash area, the majority of all flashes identified with each storm mode occur within the first bin (0-100 km^2). This agrees well with Lang et al. (2020). Upon further investigation, we find that flashes associated with WCCs (Fig. 4.4b) and BSRs (Fig. 4.4d) have higher mean flash areas (42.8 and 70.9 km^2, respectively) compared to DCCs (Fig. 4.4a) and DWCCs (Fig. 4.4c; 14.8 and 15.7 km^2, respectively). The opposite is true when looking at flash durations. The most frequent flash duration is between 0.1 and 0.3 s, and the mean flash duration for DCCs (Fig. 4.4e) and DWCCs (Fig. 4.4g) are 0.265 and 0.284 s, respectively. The mean flash durations for WCCs (Fig. 4.4f) and BSRs (Fig. 4.4h) are 0.236 and 0.226 s, respectively. Although the average flash duration is lowest in BSRs, the maximum flash duration of 2.6 s was associated with a BSR flash. The distribution of flash energy is most similar to the distribution of flash area. This makes sense as the flash energy is proportional to flash area (Bruning and MacGorman 2013). The majority of flashes produce 1 GJ of energy, while the maximum energy produced was 662 GJ associated with a BSR flash. Mean flash energies are 6-11 GJ lower, on average, in DCCs (Fig. 4.4i) and DWCCs (Fig. 4.4k) compared to WCCs (Fig. 4.4j) and BSRs (Fig. 4.4l). Finally, the highest frequency of flash centroid heights occurs at 10-12 km, consistent with analysis from Lang et al. (2020). DCCs (Fig. 4.4m) and DWCCs (Fig. 4.4o) have higher mean flash heights compared to WCCs (Fig. 4.4n) and BSRs (Fig. 4.4p). Additionally, there is a secondary relative maximum in flash heights observed in WCCs and BSRs at around 6 km. This was also noted in Lang et al. (2020), who attributed this secondary maximum to anomalous polarity storms and stratiform flashes. Indeed, the flash height distribution associated with BSRs is shifted toward lower heights compared to distributions from convective storm modes.

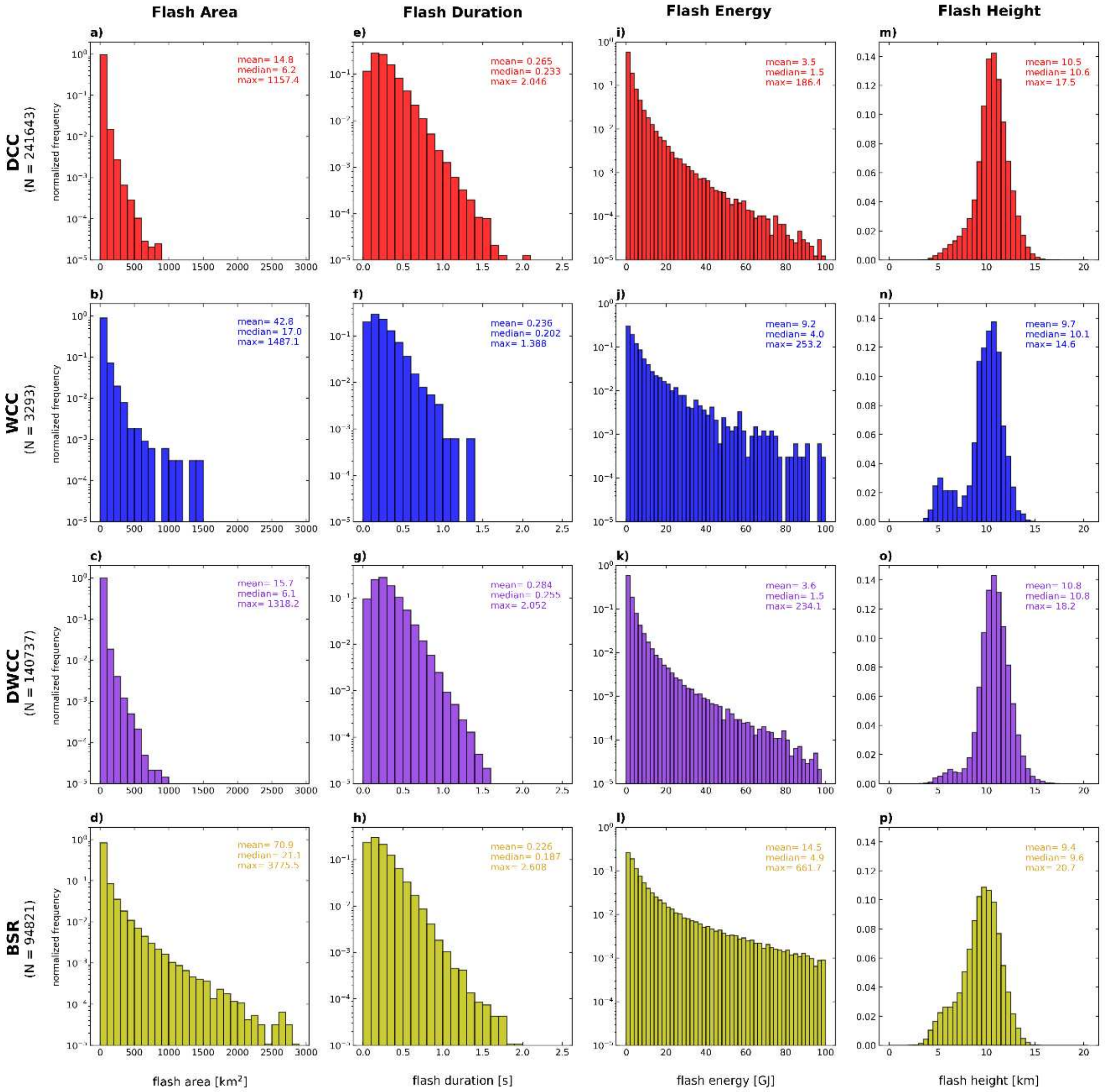

Figure 4.4: Histograms of (a-d) flash area (km^2), (e-h) flash duration (s), (i-l) flash energy (GJ), and (m-p) flash height (km) for flashes centered within DCCs (red; first column), WCCs (blue; second column), DWCCs (purple; third column), and BSRs (yellow; fourth column) for the CHIVO dataset. Mean, median, and maximum values are shown in the upper right of each panel and the number of flashes is shown at the top of each column.

4.3.3 RELAMPAGO lightning summary

Flashes associated with PFs and storm modes observed by CHIVO were analyzed for the RELAMPAGO time frame. The location and timing of flashes associated with storm modes agrees fairly well with previous research using satellite-based observations (Rasmussen et al. 2014). DCC flashes occur along the higher terrain of the SDC in the early afternoon and evening hours. They are typically smaller in size and occur higher in the convection. DWCC flashes occur along the eastern edge of the SDC and are most frequent overnight, consistent with the life cycle of MCSs. These flashes also tend to be smaller and occur higher in the convection. WCC flashes, although infrequent, occur farther east compared to deep convective flashes, and they tend to be larger in size, have larger energy associated with them, and occur lower in the storm. Finally, BSR flashes occur most frequently 50-100 km east of the SDC in the early morning hours. These flashes have large footprints, produce large amounts of energy, and occur more frequently at lower altitudes. These characteristics are consistent with previous studies based on U.S. storms (Bruning and MacGorman 2013; Mecikalski et al., 2015; Bruning et al. 2019).

Several IOPs and convective episodes with upscale growth stood out in the time series of flash counts, including the 13-14 December 2018 and the 25-26 January 2019 cases. About 30% of all flashes that were associated with CHIVO PFs came from these two cases (Table 4.2). The 13-14 December case also had 8.2% of the DCC flashes, 43.1% of the DWCC flashes, and 9.1% of the BSR flashes observed during the RELAMPAGO campaign (Table 4.2). The 25-26 January case only had 3.7% of all DCC flashes, but had nearly half of the WCC flashes, 41.2% of the DWCC flashes and 11.9% of the BSR flashes. This justifies examining these cases further to better understand the electrical characteristics of some of the most intense convection on Earth.

Table 4.2: Percent of all LMA flashes that occurred during the 13-14 December 2018 case and 25-26 January 2019 case, broken down by each feature type (all, DCC, WCC, DWCC, BSR).

	All flashes	**DCC flashes**	**WCC flashes**	**DWCC flashes**	**BSR flashes**
Dec. 13-14	16.3%	8.2%	0.0%	43.1%	9.1%
Jan. 25-26	14.2%	3.7%	49.9%	41.2%	11.9%

4.4 Case Study 1: 13-14 December 2018

4.4.1 Overview

The 13-14 December 2018 case featured a severe MCS that was associated with hail, flooding, and high lightning flash rates in the Córdoba region. Detailed analyses of the synoptic and mesoscale characteristics of this case can be found in Rocque and Rasmussen (2022) and Rocque et al. (2023; in review). This case occurred under strong synoptic flow, including a deep upper-level trough, a strong South American Low-Level Jet, and a strong cold front (Rocque and Rasmussen 2022). DCCs and DWCCs were prevalent across the case and volumetric rain rates were particularly high (Rocque et al. 2023; in review).

Spatial maps of reflectivity and graupel and hail mass summed for temperatures colder than -5°C are shown in Figure 4.5. At 0000 UTC on 14 December, a few isolated cells are visible off the southern SDC (Fig. 4.5a). These cells have 40-dBZ echoes that extend to 10 km and are associated with graupel and hail (Figs. 4.5a, b). Two hours later, the convective line develops just south of Córdoba (Fig. 4.5c). There is also a larger system to the southwest, and the graupel and hail mass is mostly concentrated over the SDC (Figs. 4.5c, d). At 0400 UTC, a large MCS has developed across the radar domains (Fig. 4.5e). There are pockets of higher graupel and hail mass that align well with the deepest convection (Figs. 4.5e, f). By 0600 UTC, the majority of the MCS has moved to the northeast out of the radar domains (Fig. 4.5g). There are still some intense lines of convection that remain tied to the SDC related to back-building characteristics that are also associated with enhanced graupel and hail (Figs. 4.5g, h).

The evolution of lightning flashes throughout the MCS is shown in Figure 4.6. At first glance, LMA and GLM flash locations and timing appear to agree well. There are some isolated cells that develop off the southern SDC on 13 December and move eastward out of the domain

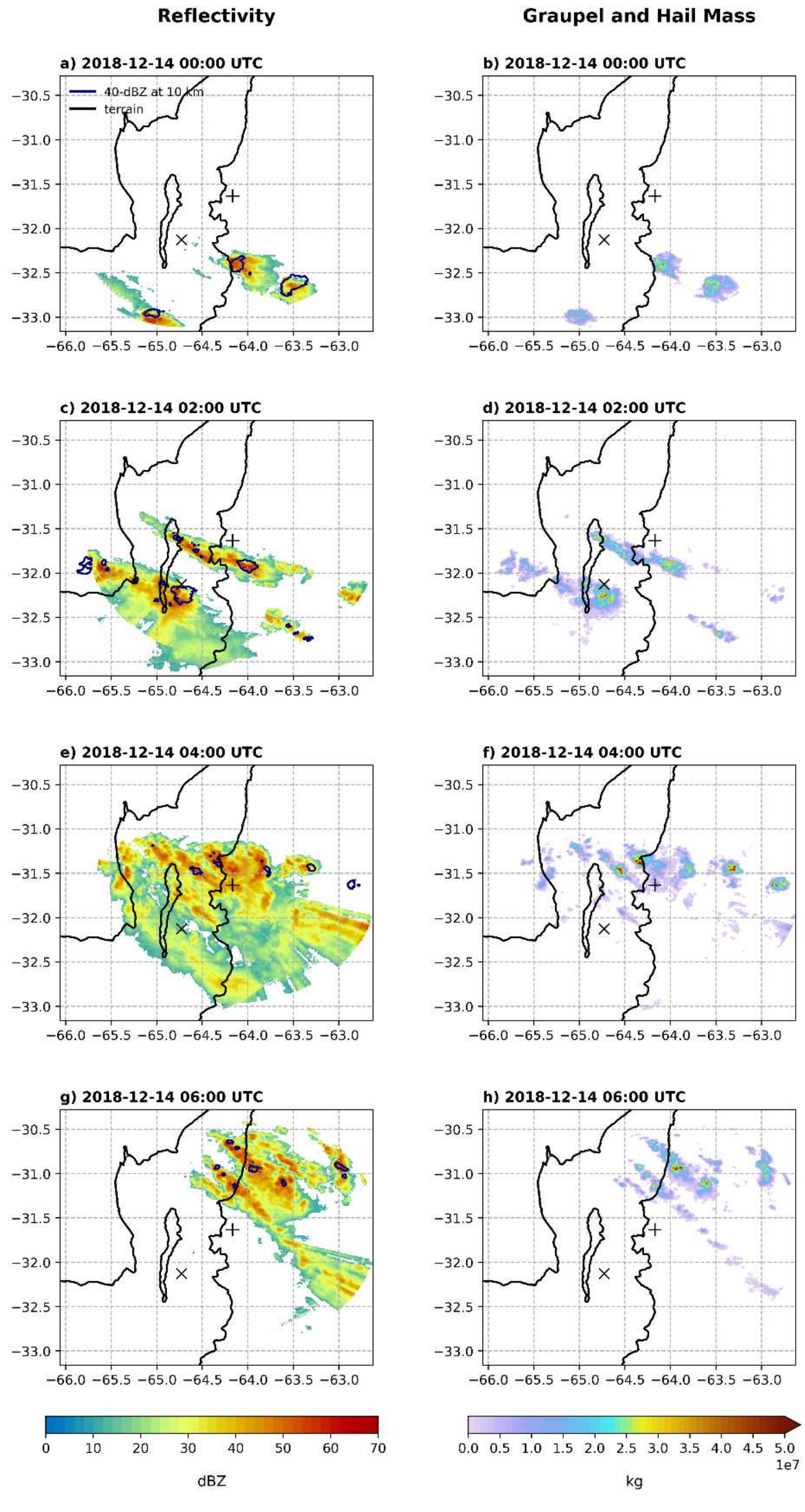

Figure 4.5: 3-5 km composite reflectivity (left) and graupel and hail mass summed above the -5°C level (right) every two hours starting at 0000 UTC on 14 December. 40-dBZ echoes at 10 km MSL are shown in the navy contours while the 500 m and 2000 m terrain contours are shown in black. The '+' indicates the location of CHIVO and the 'x' indicates the location of CSAPR2.

(Fig. 4.5a). The lightning associated with these cells is better captured with GLM as this region is outside of the 100-km LMA range ring and the loss in detection efficiency of the LMA starts being more noticeable in overall flash detections beyond this range. An intense line of convection rapidly develops around 0130 UTC south of Córdoba along the SDC (Fig. 4.5c). This convective line quickly grows upscale into a large MCS by 0230 UTC and continues to propagate to the northeast until it exits the radar domain around 0800 UTC.

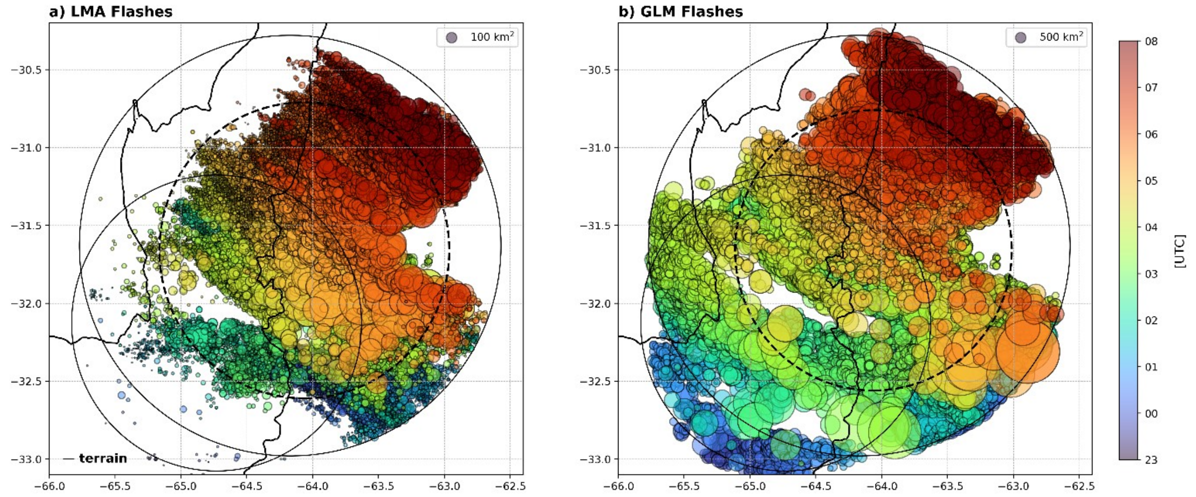

Figure 4.6: Location of a) LMA flash centroids and b) GLM flash centroids during the 13-14 December 2018 case. Markers are colored by time (UTC) and sized by flash area (km^2). The CHIVO 150-km range ring (solid; center), the CSAPR2 100-km range ring (solid; offset), the LMA 100-km range ring (dashed), and the 500-m terrain contour are plotted for context.

Flash characteristics are also analyzed for the LMA and GLM datasets throughout the MCS life cycle. Flash areas for LMA and GLM are low in the beginning of the event on the 13th and early 14th when isolated cells are present (Figs. 4.7a, b). After the convective line develops, the range of flash areas starts to increase in both LMA and GLM datasets. The mean and median flash areas also increase, especially after 0600 UTC. Flash durations follow a similar trend as flash areas (Figs. 4.7c, d). The LMA flash duration is low early in the MCS life cycle. It then increases slightly as the MCS develops and matures. The trend in GLM flash duration mean and median is more visible compared to LMA, with mean and median flash durations increasing as the MCS grows upscale (Fuchs 2017). Flash energies calculated from the LMA and GLM datasets similarly start off small but increase as the system grows upscale and stratiform precipitation is more prevalent (Figs. 4.7e, f). Optical energy observed by GLM particularly increases after 0600 UTC. Finally, the range in flash heights observed by LMA shows average flashes occur around 10 km (Fig. 4.7g). More flashes occur lower in the MCS later in the period though, especially after 0400 UTC. This agrees well with the presence of BSRs observed by CHIVO (Rocque et al. 2023; in review).

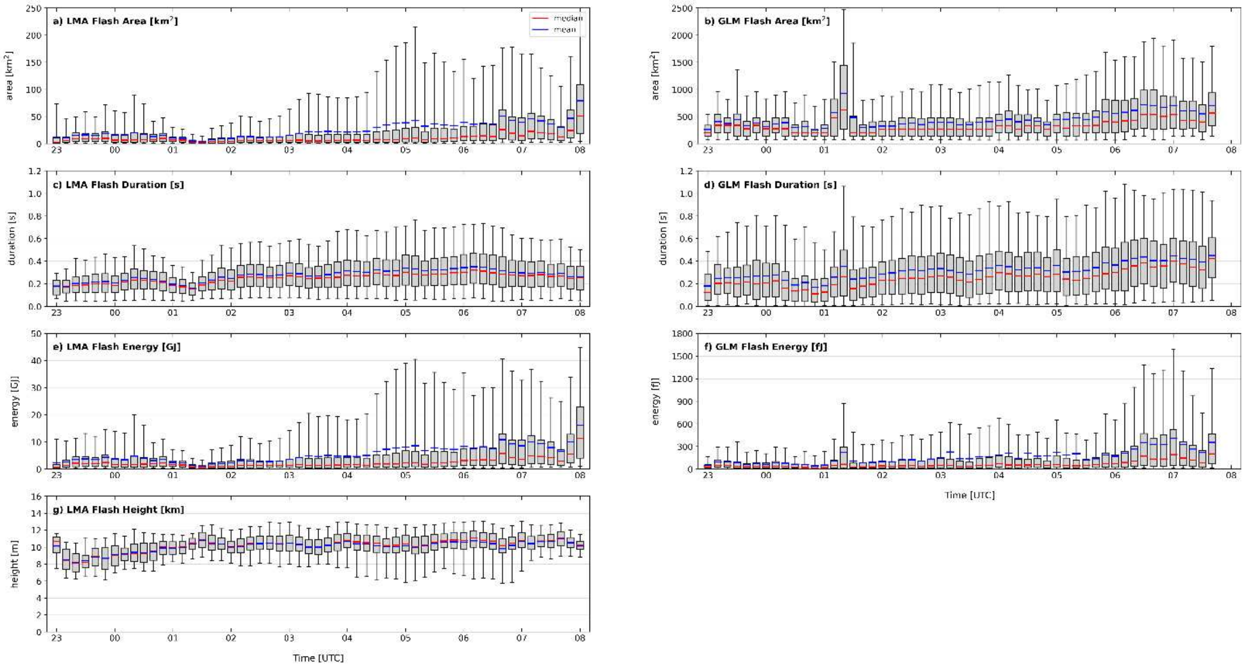

Figure 4.7: Time series of LMA and GLM flash characteristics during the 13-14 December 2018 case, represented by box plots. a) LMA flash area (km^2), b) GLM flash area (km^2), c) LMA flash duration (s), d) GLM flash duration (s), e) LMA total flash energy (GJ), f) GLM optical flash energy (fJ), and g) LMA flash height (km). The box spans the lower and upper quartiles of the data, the whiskers cover the 5 and 95 percentiles, and the red (blue) line represents the median (mean).

4.4.2 Microphysics

Lightning forms as a result of the separation of charged particles within the atmosphere. Hydrometeors such as graupel and ice crystals carry different charges depending on several different factors including temperature, liquid water content, and particle size (Reynolds et al. 1957; Takahashi 1978; Saunders and Peck 1998; Avila and Pereyra 2000). Knowing what type of hydrometeors are present in the mixed phase and where they occur is critical for better understanding the electrical characteristics of convective storms. Thus, microphysical parameters calculated above the -5°C level including 35-dBZ volume, ice water path, and graupel, hail, snow, and ice mass and volumes were derived from the CHIVO-CSAPR2 radar mosaic and compared with lightning observations. The evolution of storm total microphysical and electrical characteristics is shown in Figure 4.8. 35-dBZ volume, ice water path, graupel and hail volume and mass, and snow and ice mass increase from the start of the event to their maximum around 0230-0300 UTC on 14 December (Figs. 4.8a, b). This corresponds to increases in LMA flash rates, with a large jump occurring between 0130 and 0250 UTC, particularly for the smaller flashes (3-10 sources; Fig. 4.8d). GLM flash rate also increases during this period, but the rates are much lower than LMA flash rates (Fuchs 2017). The most rapid increase actually occurs with GLM event rates. After around 0300 UTC, flash rates start to decrease, along with 35-dBZ volume and graupel and hail mass and volume. Meanwhile, snow and ice volume peaks around 0330 UTC and then steadily declines afterwards (Fig. 4.8c). Ice water path also decreases, but not as steeply as the graupel and hail components, highlighting the presence of more snow and ice aloft. Storm total LMA flash areas reach maximum values after the peak in flash rates, around 0330-0530 UTC (Fig. 4.8e). This corresponds well with the increased range in flash areas and larger flash areas observed in Fig. 4.7a. LMA flash energy follows a similar trend as flash area (Fig. 4.8f). Interestingly, storm total GLM flash area and optical energy reach maximum values around 0230 UTC, consistent with the maximum in flash rates (Figs. 4.8d-f; Fuchs 2017).

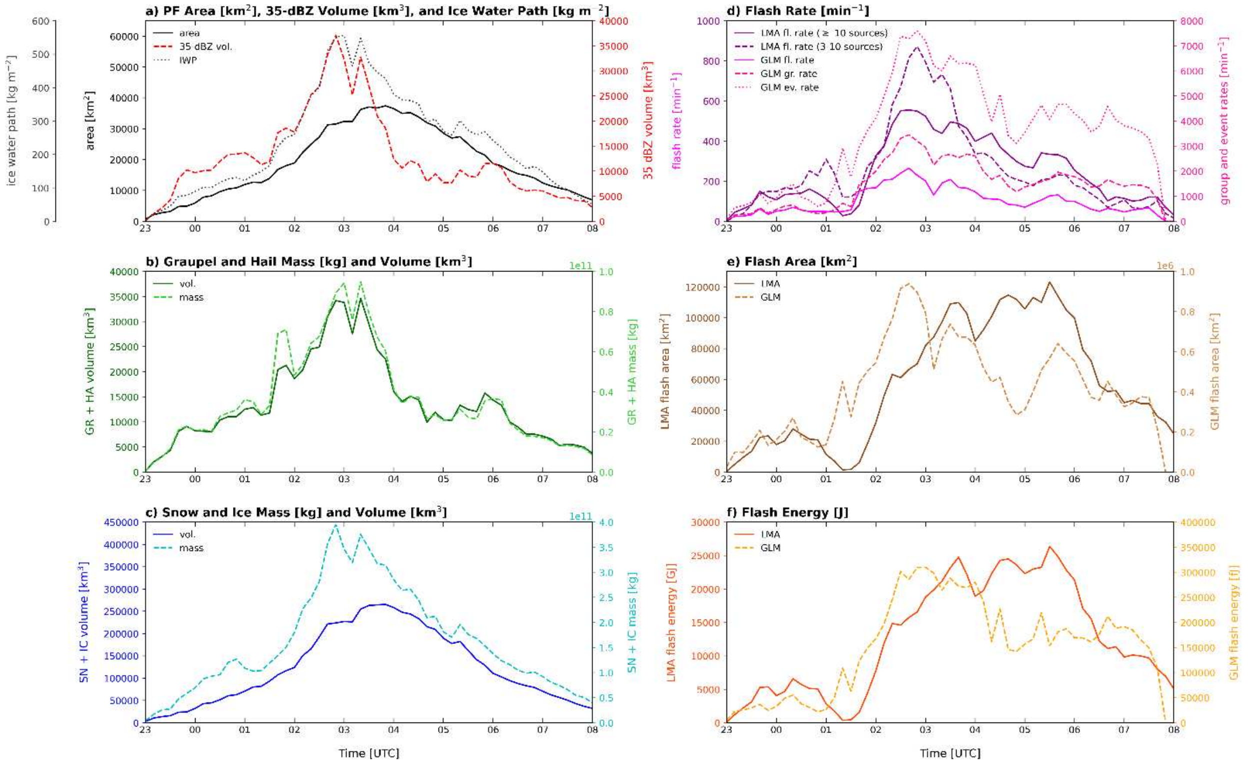
a) PF Area [km^2], 35-dBZ Volume [km^3], and Ice Water Path [kg m^{-2}]

b) Graupel and Hail Mass [kg] and Volume [km^3]

c) Snow and Ice Mass [kg] and Volume [km^3]

d) Flash Rate [min^{-1}]

e) Flash Area [km^2]

f) Flash Energy [J]

Figure 4.8: Time series of a) PF area (km^2; solid black), 35-dBZ volume (km^3; dashed red), and ice water path (kg m^{-2}; dotted grey), b) graupel and hail mass (kg; dashed light green) and volume (km^3; solid green), c) snow and ice mass (kg; dashed light blue) and volume (km^3; solid blue), d) LMA flash rates (≥ 10 sources, min^{-1}; solid purple, 3-10 sources, min^{-1}; dashed purple), GLM flash rates (min^{-1}; magenta), GLM group rates (min^{-1}; dashed pink) and GLM event rates (min^{-1}; dotted pink), e) LMA flash area (km^2; solid brown) and GLM flash area (km^2; dashed brown), and f) LMA flash energy (GJ; solid orange) and GLM flash energy (fJ; dashed orange) during the 13-14 December 2018 case.

The location of hydrometeors within the cloud can provide insight into the charge structure of the storm and lightning characteristics. Thus, the evolution of hydrometeors through the MCS life cycle by height is examined. Early in the time period when more isolated cells are developing, graupel, hail, snow, and ice masses are relatively low (Fig. 4.9). There is an increase in flash rates, particularly for LMA flashes, as well as an increase in the 0-dBZ and 40-dBZ echo top heights. As the convective line develops around 0130 UTC, flash rates start to increase considerably. Additionally, graupel and hail mass increases near the freezing level, with maximum values reaching to about 7 km (Fig. 4.9a). This coincides with LMA flash rates of 550 flashes min^{-1} at 0230 UTC. Ice mass also begins to increase at this time and has peak values just before 0300 UTC centered around 9-10 km (Fig. 4.9c). This is also where the mean and median height of flashes observed by the LMA occurs. Snow mass is highest around 0300-0500 UTC and extends from the melting level to around 10 km (Fig. 4.9b). After the peak in lightning flash rates occurs around 0230 UTC, flash rates decrease steadily, as do the 0-dBZ and 40-dBZ echo tops. GLM flash rates follow a similar trend as LMA flash rates but are much smaller. This could be due to optical attenuation caused by hydrometeors, especially ice, above the mean flash height (Fuchs 2017; Rutledge et al. 2020).

4.4.3 Storm modes

As mentioned earlier, three-dimensional storm structures that represent the most extreme components of the storm are analyzed to better understand the evolution of systems, particularly MCSs. To put this case into context with the entire campaign, the locations and timing of lightning flashes associated with storm modes observed by the CHIVO and CSAPR2 radars are shown in Figure 4.10. Flashes associated with DCCs occur throughout the entirety of the MCS (Fig. 4.10a). A large number of flashes occur within the isolated cells in the southern half of the domain early on the 14th (Figs. 4.10a, b). A hotspot in flashes south of the CHIVO radar corresponds to the location of the convective line around 0200-0300 UTC (Fig. 4.5c). Several flashes are also observed over the highest terrain of the SDC around 0400 UTC. Flashes then move with the

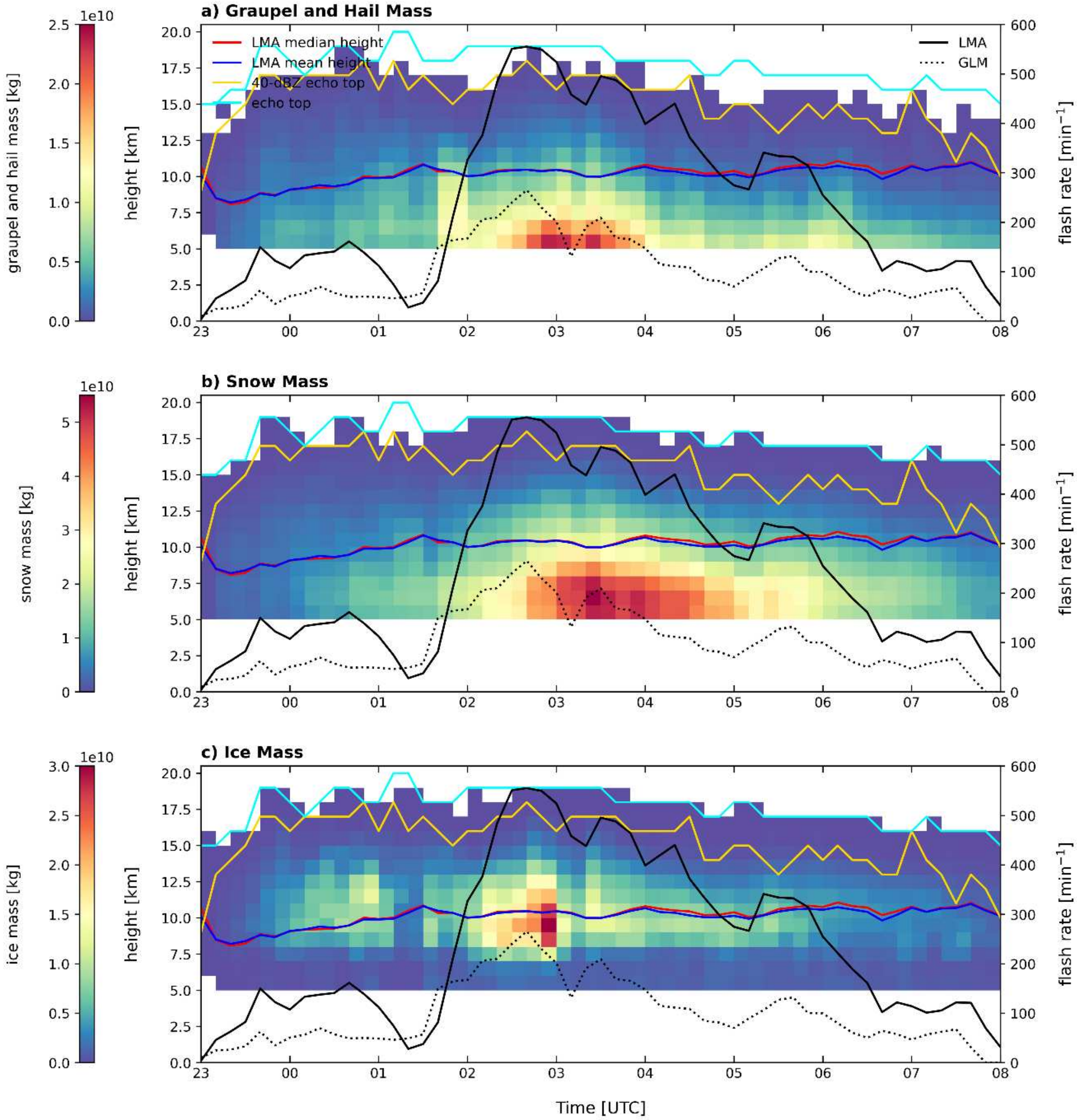

Figure 4.9: Time series of a) graupel and hail mass by height (kg; shaded), b) snow mass by height (kg; shaded), and c) ice mass by height (kg; shaded) for the 13-14 December 2018 case. Hydrometeor masses are summed above the -5°C level. Each plot also shows the median LMA flash height (km; red), mean LMA flash height (km; blue), 40-dBZ echo top height (km; gold), echo top height (km; cyan), LMA flash rate (min^{-1}; solid black), and GLM flash rate (min^{-1}; dashed black).

deepest convection to the northeast. Flashes that occur within DWCCs are observed from about 0200 UTC to 0800 UTC (Figs. 4.10c, d). These flashes are closely tied to the terrain and move to the northeast with the MCS. Additionally, 46% of all flashes observed during this event were associated with a DWCC. The highest concentration of DWCC flashes is directly north of CHIVO right along the edge of the SDC. BSR flashes occur across the domain from about 0230-0700 UTC (Figs. 4.10e, f). There are likely more stratiform flashes that occur through the end of the MCS, but the size threshold for BSRs is not met when the system exits the domain. The majority of BSR flashes occurs about 50-100 km east of the SDC, consistent with the movement of the MCS towards the east as it matures.

Flash characteristics associated with each storm mode are also analyzed for this case. To better understand how these flashes vary with MCS life cycle, three time periods are chosen to look at flash characteristics. The first time period is 2300-0130 UTC in which isolated cells develop off the southern SDC (Fig. 4.5a). This time period exhibits an increase in flash rates (Figs. 4.8d, 4.9a-c) and several DCCs are identified during this time (Rocque et al. 2023; in review). Flashes associated with these DCCs are small in size (Fig. 4.11a), short in duration (Fig. 4.11d), do not produce very high energies (Fig. 4.11g), and occur lower in the convection (Fig. 4.11j) compared to later time periods.

The second time period chosen is 0130-0400 UTC during which the convective line rapidly develops and grows upscale (Fig. 4.5c). Flash rates substantially increase during this time, as do graupel and hail mass (Figs. 4.8b, d, 4.9a-c). DCCs, DWCCs, and BSRs are all identified during this time. The majority of these flashes are also small in size (0-100 km^2; Figs. 4.11a-c). DWCCs tend to have larger flash areas compared to DCCs (12.4 vs 9.3 km^2), and BSR flashes are even larger on average compared to convective flashes (31.9 km^2). Similar to the campaign-wide flash statistics, DCC and DWCC flashes for this time period occur slightly longer than BSR flashes (Figs. 4.11d-f). Flash energies follow a similar pattern as flash areas in which BSR flashes are

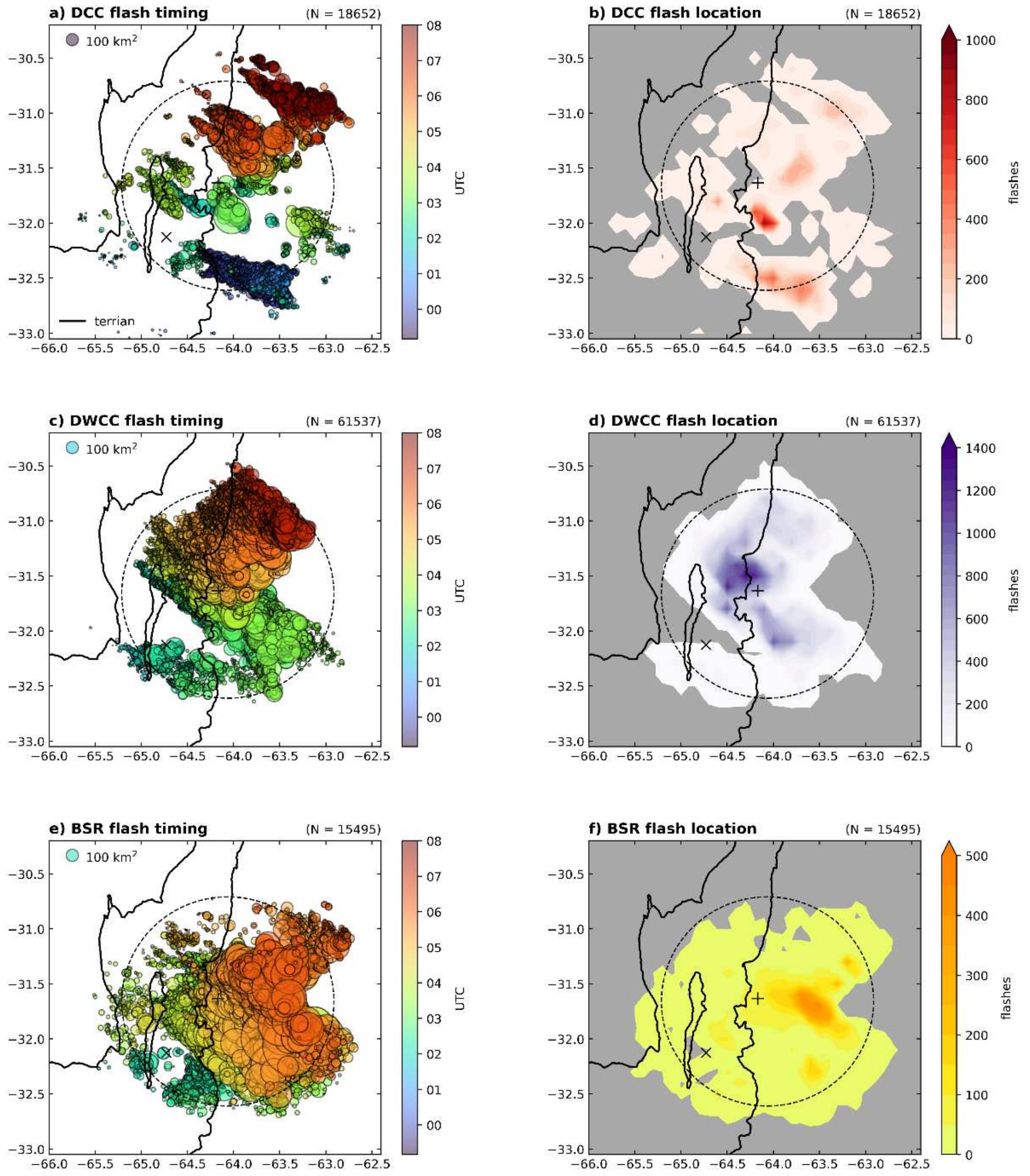

Figure 4.10: Location of LMA flashes centered within (a-b) DCCs, (c-d) DWCCs, and (e-f) BSRs for the 13-14 December 2018 case. Markers in the left panels are colored by time (UTC) and sized by flash area (km^2). Total number of flashes observed within a 0.1° x 0.1° pixel are shown in the right panels. The number of flashes is shown in the upper right of each plot. The 500 m and 2000 m terrain contours are shown in black, the 100-km LMA range ring is shown in the dashed circle, the '+' indicates the location of CHIVO and the 'x' indicates the location of CSAPR2. No WCCs were identified during this case.

most energetic (Figs. 4.11g-i). Flash heights during this time also more frequently occur around 10 km for each storm mode (Figs. 4.11j-l).

The final time period is 0400-0800 UTC and represents the mature phase of the MCS (Figs. 4.5e, g). Lightning flash rates decline during this period, as do graupel and hail mass, 35-dBZ volume, and ice water path (Figs. 4.8a, b, d, 4.9a-c). As in the previous time period, DCCs, DWCCs, and BSRs are all identified. For flash area, duration, and energy, there is a shift in the distribution for each storm mode to larger values (Figs. 4.11a-i). Average flash areas for DCC, DWCC, and BSR flashes increase from 9.3, 12.4, and 31.9 km^2 to 23.3, 22.1, and 83.9 km^2, respectively. The average flash duration for each storm mode is around 0.3 s, and the average flash energy ranges from 5 GJ for convective flashes to 17 GJ for stratiform flashes. Interestingly, the distribution of flash heights for DCC and DWCC flashes slightly increases (Figs. 4.11j, k). However, there is also a small secondary peak that occurs around 7 km. This secondary peak is more prominent in the BSR flash height distributions, and there is a clear shift toward lower heights for these stratiform flashes (Fig. 4.11l). These flash characteristics highlight the evolution of the MCS from convective initiation to mature stratiform.

4.4.4 Summary

The 13-14 December MCS case produced the most lightning of all cases observed by the LMA network and CHIVO. A deeper analysis into this case showed that the majority of these flashes were associated with the deepest, most intense components of the storm (DWCCs). These flashes were relatively small in size, generally lasted for 0.3 s, and occurred most frequently around 10 km. A rapid increase in lightning flash rates (lightning jump) was observed and was related to increases in the graupel and hail mass and volume, 35-dBZ volume, and ice water path. Flashes were also identified by GLM and correspond well in time and space compared to the LMA. However, flash rates observed by GLM were much lower than the LMA. This may be due to the

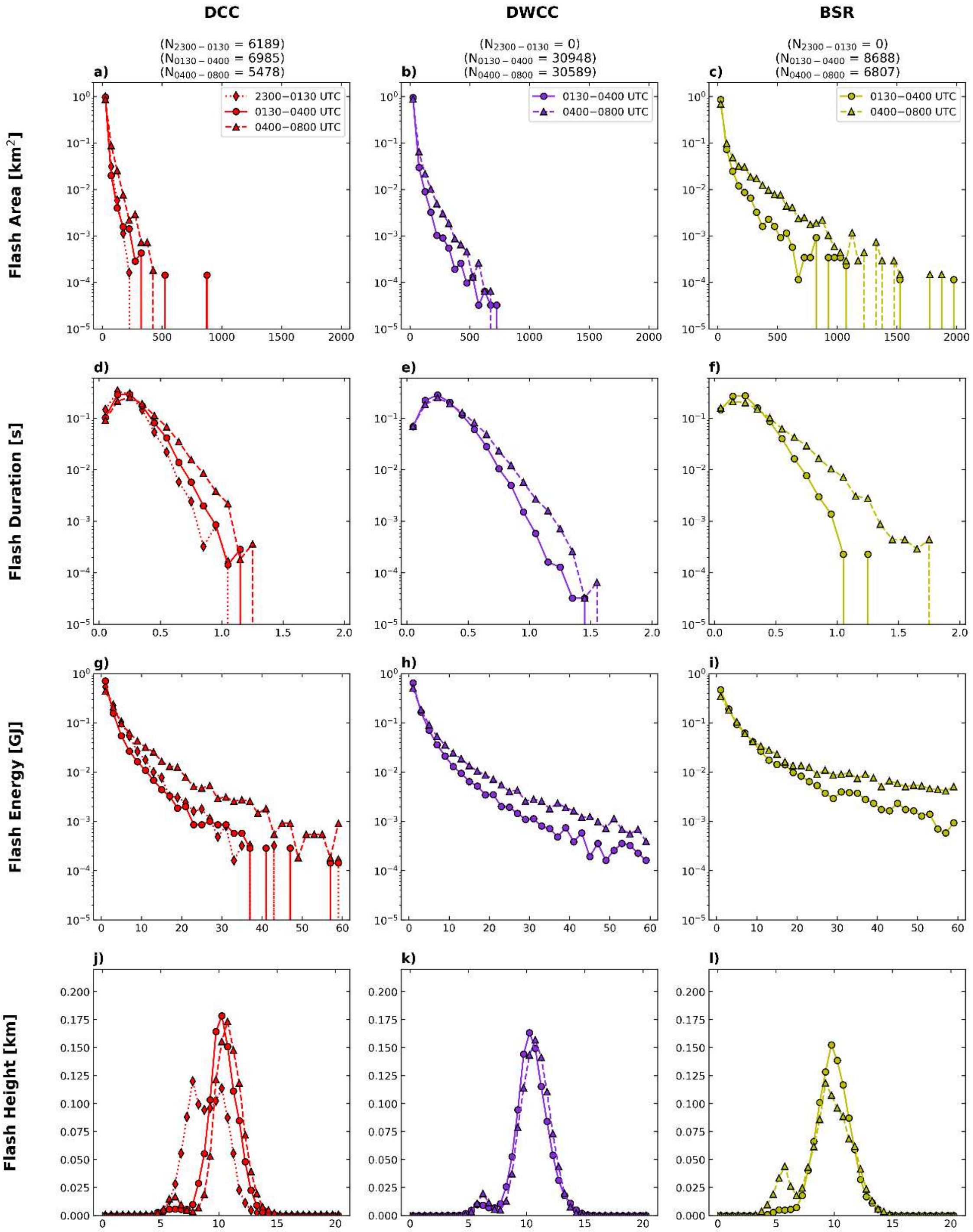

Figure 4.11: Histograms of (a-c) flash area (km^2), (d-f) flash duration (s), (g-i) flash energy (GJ), and (j-l) flash height (km) for LMA flashes centered within DCCs (red; first column), DWCCs (purple; second column), and BSRs (yellow; third column). Dotted lines with diamond markers indicate DCCs identified between 2300 and 0130 UTC on 13-14 December 2018. Solid lines with circle markers indicate storm modes identified between 0130 and 0400 UTC on 14 December 2018. Dashed lines with triangle markers indicate storm modes identified between 0400 and 0800 UTC on 14 December 2018. WCCs were not identified during this case.

small flash size or the occurrence of the flashes around 10 km. Although this storm is normal polarity, the echo top heights are still around 18 km, and thus optical attenuation through the upper part of the cloud is likely. More analysis is needed to better understand discrepancies in LMA and GLM flash detection efficiency in this region. Flash characteristics of the second most active lightning case are now analyzed in the context of the 13-14 December case and the RELAMPAGO campaign.

4.5 Case Study 2: 25-26 January 2019

4.5.1 Overview

The 25-26 January 2019 case featured two rounds of convection that moved over the RELAMPAGO radar domain. On 25 January, very intense, deep cells developed along the SDC and moved over the CHIVO radar (Figs. 4.12a-d). These cells were the deepest recorded by CHIVO, with 40-dBZ echo top heights reaching 20 km in height (Schumacher et al. 2021; Nesbitt et al. 2021, Feng et al. 2022; Rocque et al. 2023; in review). Large amounts of graupel and hail were also recorded in these cells. In the early morning hours on 26 January, a large MCS moved into the domain and remained relatively stationary over the SDC for more than 12 hours (Figs. 4.12e-h). Stratiform precipitation was dominant during this time and a few WCCs were observed (Rocque et al. 2023; in review). This case occurred under relatively weak synoptic flow compared to the 13-14 December case, and the SDC appeared to play a more important role in the development and evolution of the system (Rocque and Rasmussen 2022; Rocque et al. 2023; in review).

The evolution of lightning flashes for the 25th and 26th of January is shown in Figure 4.13. LMA flashes are first identified along the central and southern SDC around 17-18 UTC (Fig.

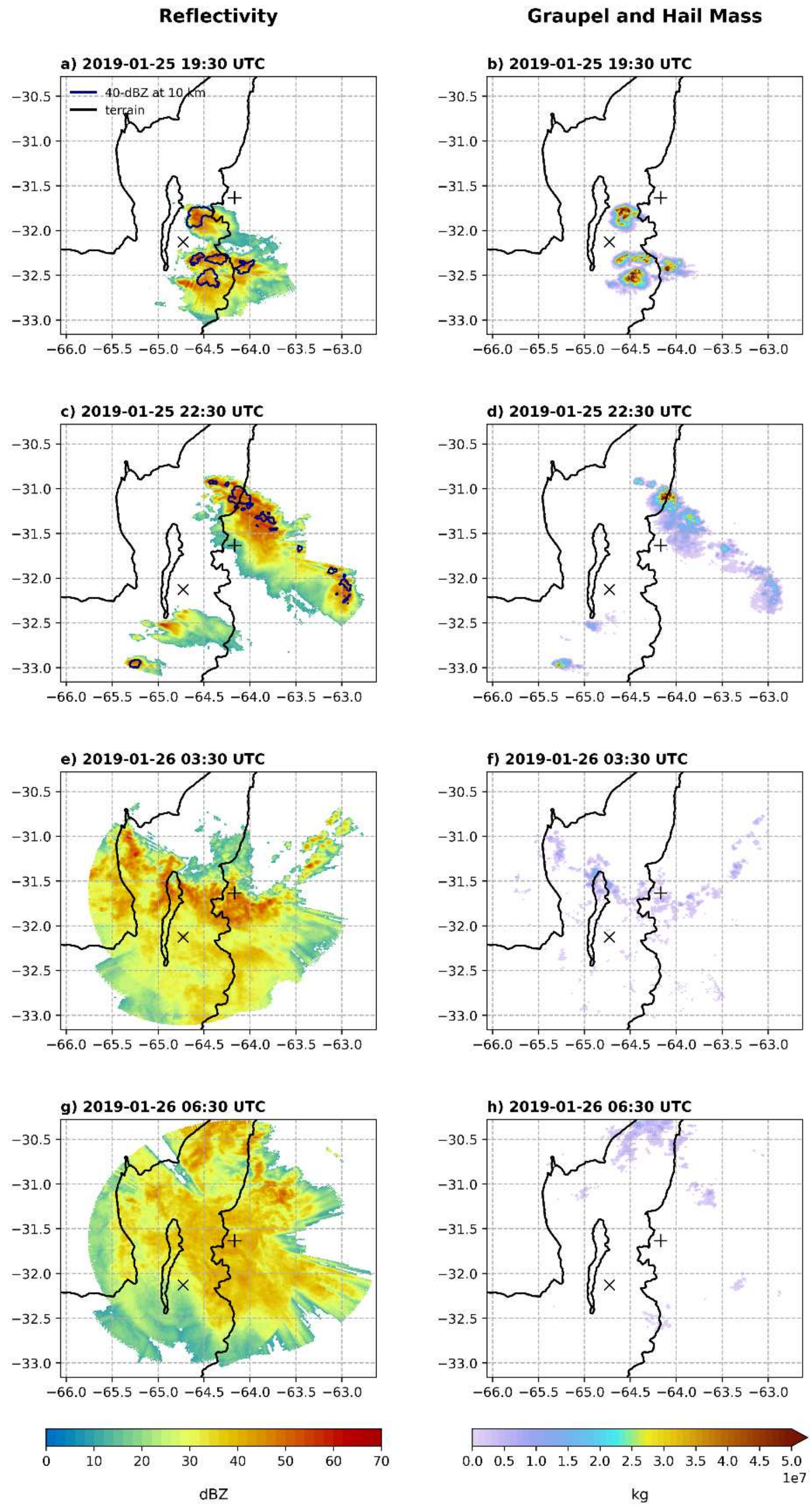

Figure 4.12: 3-5 km composite reflectivity (left) and graupel and hail mass summed above the -5°C level (right) at (a-b) 1930 UTC on 25 January, (c-d) 2230 UTC on 25 January, (e-f) 0330 UTC on 26 January, (g-h) 0630 UTC on 26 January. 40-dBZ echoes at 10 km MSL are shown in the navy contours while the 500 m and 2000 m terrain contours are shown in black. The '+' indicates the location of CHIVO and the 'x' indicates the location of CSAPR2.

4.13a). GLM flashes are also identified in similar locations during this time (Fig. 4.13b). LMA flashes then move to the east along the edge of the SDC around 1900-2000 UTC. GLM flashes are also identified here, but the concentration of flashes is much smaller than LMA flashes. There is a noticeable 'hole' in GLM lightning flashes slightly south of the center of CHIVO. Numerous LMA flashes occur here around 2100 UTC, though. LMA flashes continue to move towards the northeast with the convection, as do GLM flashes. Some additional GLM flashes are observed right before 0000 UTC along the highest terrain of the SDC. On 26 January, several very small LMA flashes are observed over the western SDC (Fig. 4.13c). These flashes are much more prevalent in the GLM dataset and highlight the usefulness of GLM beyond the LMA range (Fig. 4.13d). Flashes in both datasets then move toward the north over time with the MCS. GLM flashes are noticeably larger in size compared to LMA flashes (Fuchs 2017). Flash characteristics will be examined now for both datasets.

On 25 January, flash areas for LMA and GLM are small (Figs. 4.14a, b). These flashes occur within isolated, deep convective cells (Figs. 4.12a-d). The duration of these flashes is also low, with flashes averaging around 0.2 s in length (Figs. 4.14c, d). As with flash area, flash energy is also quite low on the 25th (Figs. 4.14e, f). This is especially true for GLM flashes, which have maximum optical energies less than 200 fJ, which is lower than the 13-14 December case. Average flash heights on the 25th vary between 9 and 12 km (Fig. 4.14g).

On 26 January, flash areas start to increase, consistent with the presence of the MCS and mature stratiform region (Figs. 4.12e-h; 4.14a, b). The range of LMA flash areas increases considerably after 0400 UTC, when the primary storm modes identified are BSRs (Rocque et al. 2023; in review). Interestingly, the mean and median LMA flash duration tends to decrease slightly during this time (Fig. 4.14c). GLM flash durations increase slightly, but the majority of flashes

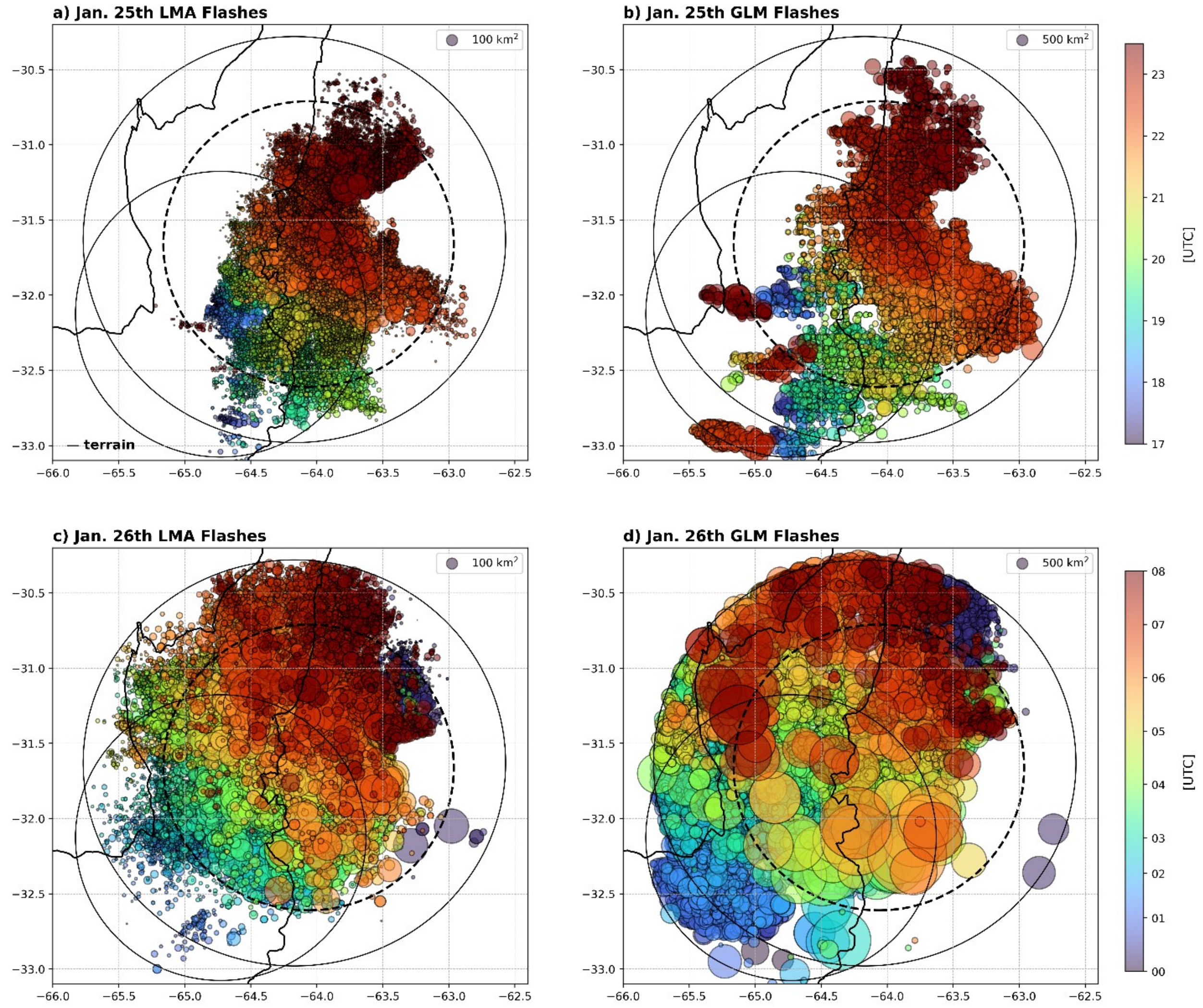

Figure 4.13: Location of a) LMA flash centroids and b) GLM flash centroids during the 25 January 2019 case. c) and d) as in a) and b) but for 26 January 2019. Markers are colored by time (UTC) and sized by flash area (km^2). The CHIVO 150-km range ring (solid; center), the CSAPR2 100-km range ring (solid; offset), the LMA 100-km range ring (dashed), and the 500-m terrain contour are plotted for context.

last for 0.2-0.5 s (Fig. 4.14d). The range in flash energy also increases toward the end of the event, consistent with increases in flash area (Figs. 4.14e, f), and similar to the 13-14 December 2018 case. Finally, more LMA flashes occur at lower heights towards the end of the event, coinciding with enhanced stratiform precipitation (Fig. 4.14g).

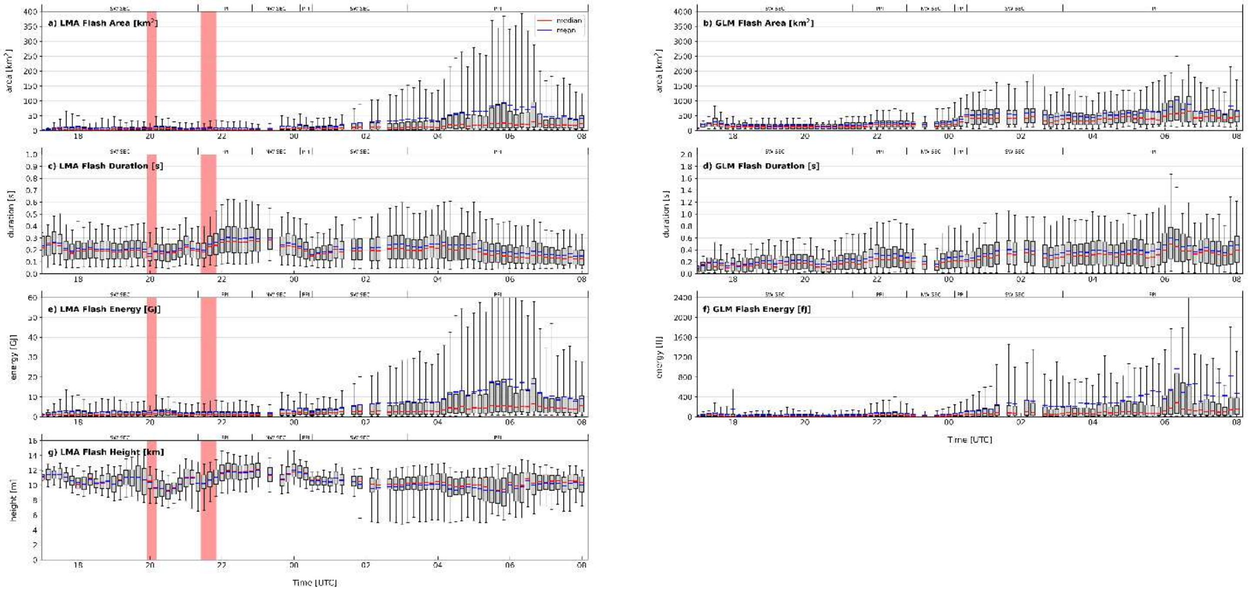

Figure 4.14: As in Fig. 4.7 but for the 25-26 January 2019 case. The red bar represents when the number of LMA stations dropped to 6, and the CHIVO scan strategy (PPI vs SEC) is shown on the top axis of each plot.

4.5.2 Microphysics

As mentioned earlier, the type, quantity, and location of hydrometeors within the cloud provide insights into the electrical characteristics of the storm. As in the 13-14 December case, microphysical parameters are identified in the radar mosaic and compared with flash characteristics. 35-dBZ volume, graupel and hail mass and volume, and ice water path all increase to maximum values around 2100 UTC on 25 January (Figs. 4.15a, b). This is also when LMA flash rates with 3-10 sources peak (Fig. 4.15d). There are a few instances when the number of LMA stations decreased to 6 during this time. This drop in stations significantly reduced the number of flashes identified, and we thus masked this time out. Interestingly, the peak in LMA flash rates with ≥10 sources (~600 fl min^{-1}) occurs later around 2230 UTC. GLM flash rates also peak during this time but are nearly 70% lower than LMA flash rates. These flash rates are similar to those observed in the 13-14 December 2018 case. Storm total flash area and flash energy also peak with flash rates around 2230 UTC (Figs. 4.15e, f). Flash rates then decrease after around 2300 UTC as isolated, deep convection moves out of the radar mosaic domain.

Microphysical quantities including 35-dBZ volume, graupel and hail mass and volume, and ice water path also decrease through 0000 UTC 26 January. As the MCS enters the domain, snow and ice mass and volume begin to increase, as does the PF area (Figs. 4.15a, c). Parameters associated with convective activity remain low, while ice water path increases again, consistent with the increase in snow and ice (Figs. 4.15a, b). LMA and GLM flash rates are lower (< 200 fl min^{-1}), but flash area and energy for both LMA and GLM flashes reach peak values around 04 UTC, consistent with the increase in stratiform precipitation (Figs. 4.15d-f; Rocque et al. 2023; in review).

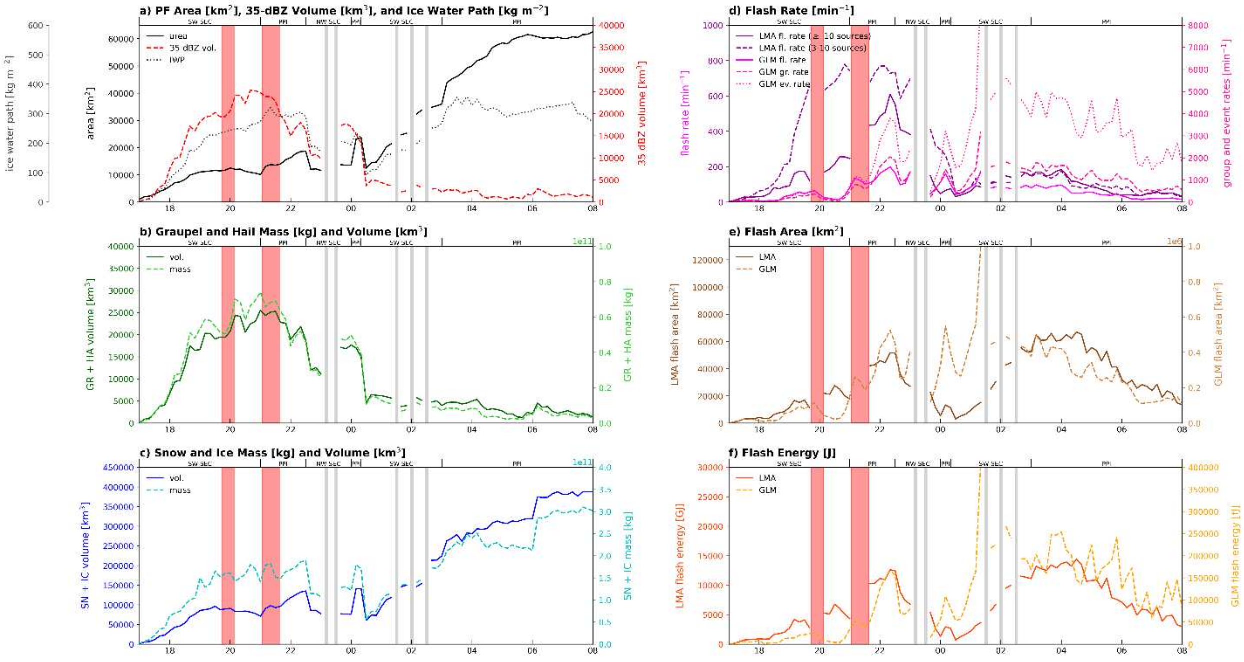

Figure 4.15: As in Fig. 4.8 but for the 25-26 January 2019 case. The grey bar represents missing radar data, the red bar represents when the number of LMA stations dropped to 6, and the CHIVO scan strategy (PPI vs SEC) is shown on the top axis of each plot.

The evolution of the vertical profile of hydrometeors identified during this case is quite different compared to the 13-14 December case. Graupel and hail mass increases to maximum values around 2030-2230 UTC (Fig. 4.16a). This maximum is concentrated around 6-9 km, which is below the average flash height around 10-12 km. LMA flash rates are rapidly increasing at this time and reach peak values around 600 fl min^{-1} near 2230 UTC. The trend in GLM flash rates is not as clear, but a maximum is achieved near 200 fl min^{-1} also around 2230 UTC. Echo top heights reach 20 km, and 40-dBZ echo tops also reach 20 km around 2030-2100 UTC. There is an enhancement in ice around 21 UTC around 12 km, but snow and ice mass is relatively low at this time compared to later in the event (Figs. 4.16b, c). After 0000 UTC, 40-dBZ echo tops decrease to around 10 km by 0200 UTC. 0-dBZ echo tops also decrease, as does the graupel and hail mass and lightning flash rates. Mean and median LMA flash heights decrease to 9-10 km, snow mass increases from about 5-8 km, and ice mass increases 9-12 km, all consistent with the maturing of the MCS and dominance of stratiform precipitation (Figs. 4.16b, c).

4.5.3 Storm modes

Once again, flashes associated with the most extreme components of the storm are analyzed to understand how electrical properties of the storm vary in time and space. Most DCC flashes occur just downstream of the highest terrain of the SDC (Figs. 4.17a, b). These flashes occur around 1900-2200 UTC and are associated with deep isolated cells (Fig. 4.12a). There are a few scattered DCC flashes across the domain associated with the isolated cells moving to the northeast, and the secondary MCS that enters the domain from the southwest. Flashes associated with WCCs most frequently occur in the northwest quadrant of the domain, over the SDC (Figs. 4.17c, d). These flashes occur around 0400-0800 UTC on 26 January and are associated with the mature MCS. There are not many of these flashes, but they are larger in area compared to DCC flashes. Two rounds of DWCC flashes are observed for this case (Figs. 4.17e, f). The first is associated with convection on the 25th, and most of these flashes occur along the edge of the SDC. The second

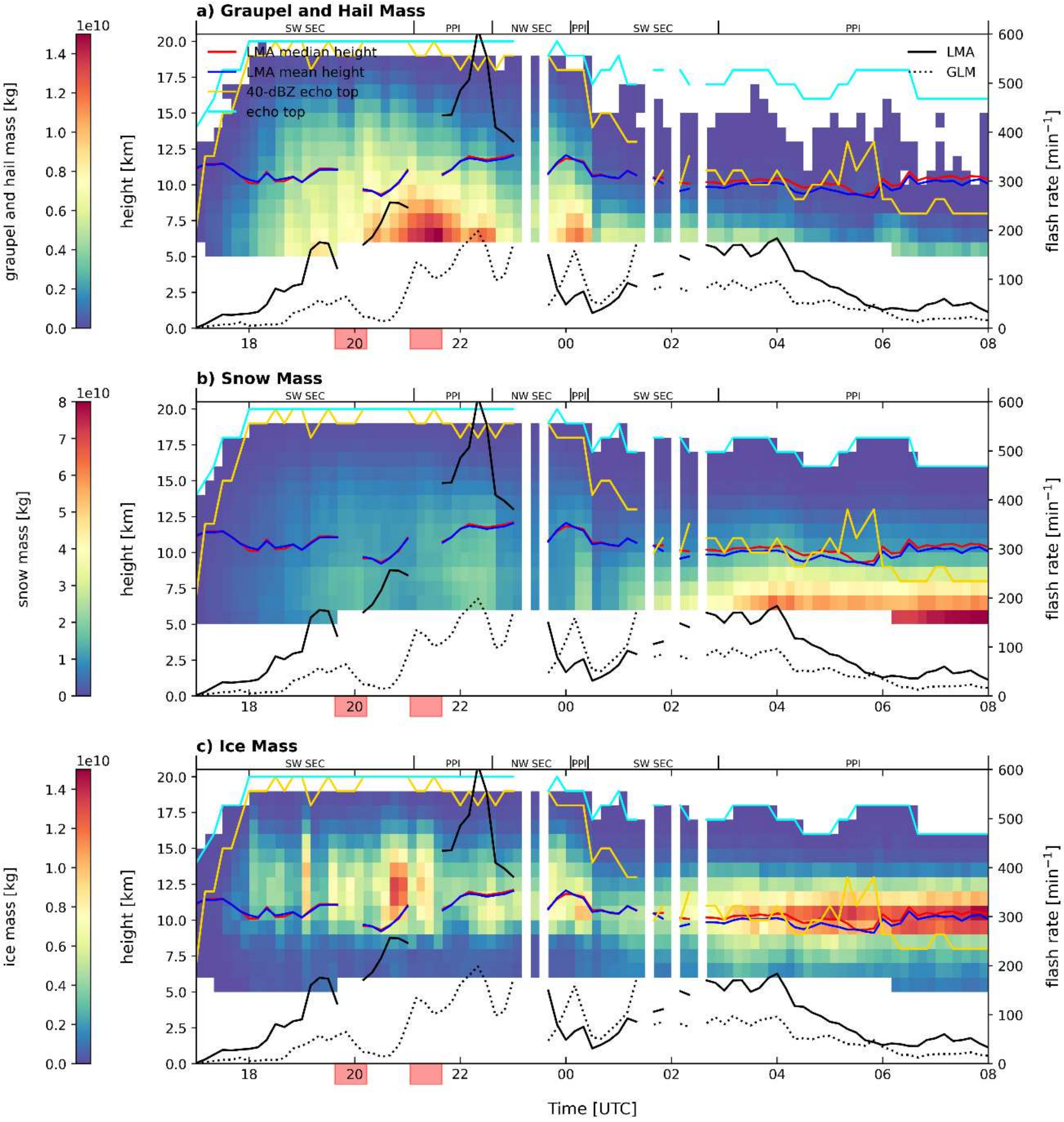

Figure 4.16: As in Fig. 4.9 but for the 25-26 January 2019 case. The red bar on the bottom axis represents when the number of LMA stations dropped to 6, and the CHIVO scan strategy (PPI vs SEC) is shown on the top axis of each plot.

set of DWCC flashes is associated with the MCS on the 26th, and these flashes appear to be larger in area and occur farther west over the SDC compared to the flashes on the 25th. Flashes associated with BSRs are only associated with the MCS around 0200-0800 UTC (Figs. 4.17g, h). These occur across the domain, but there is an enhanced area of BSR flashes southeast of the radars.

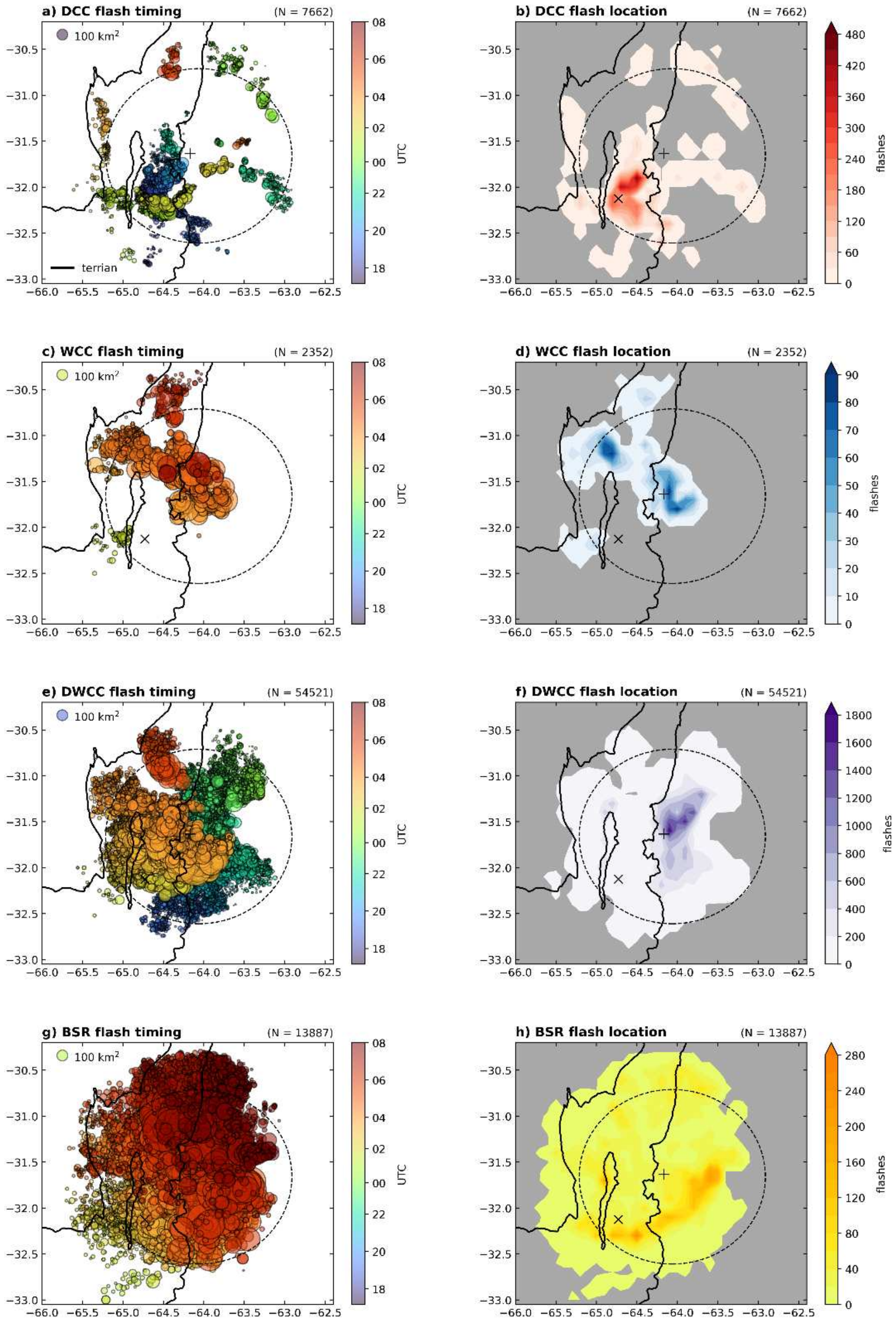

Figure 4.17: Location of LMA flashes centered within (a-b) DCCs, (c-d) WCCs, (e-f) DWCCs, and (g-h) BSRs for the 25-26 January 2019 case. Markers in the left panels are colored by time (UTC) and sized by flash area (km^2). Total number of flashes observed within a 0.1° x 0.1° pixel are shown in the right panels. The number of flashes is shown in the upper right of each plot. The 500 m and 2000 m terrain contours are shown in black, the 100-km LMA range ring is shown in the dashed circle, the '+' indicates the location of CHIVO and the 'x' indicates the location of CSAPR2.

Two time periods are chosen to analyze and compare flash characteristics. The first is 1700-0000 UTC on 25 January, when isolated cells produce very high lightning flash rates. During this time period, only DCCs and DWCCs are identified (Figs. 4.17a, e). The majority of both DCC and DWCC flashes are less than 50 km^2 in area (Figs. 4.18a, c). Additionally, most of these flashes last for 0.2-0.4 s, with more DWCC flashes lasting longer than DCC flashes (Figs. 4.18e, g). Flash energy follows a similar pattern as flash area (Figs. 4.18i, k), and flash heights peak at 10.4 and 11.4 km for DCCs and DWCCs, respectively (Figs. 4.18m, o).

The second time period analyzed is 0000-0800 UTC on 26 January, when the MCS moves into the region and stratiform rain dominates. DCCs and DWCCs are identified early on the 26th, whereas WCCs and BSRs tend to occur later (Figs. 4.17a, c, e, g). DCC and DWCC flash areas follow a similar pattern on 25 January but tend to be 5-15 km^2 larger on average (Figs. 4.18a, c). This increase in flash size as the MCS develops is similar to what was observed in the 13-14 December case. WCC flashes are next largest on average at 40 km^2 (Fig. 4.18b), and BSRs are much larger on average at 70 km^2 (Fig. 4.18d). Flash durations for DCC and DWCC flashes are similar to the 25th (Figs. 4.18e, g). WCC and BSR flashes have a larger range in durations, and the maximum flash duration of 1.84 s is associated with a BSR (Figs. 4.18f, h). However, on average, BSR flashes actually are the quickest, similar to the 13-14 December case. In terms of flash energy, WCC and BSR flashes similarly produce large amounts of energy on average compared to deep convective storm modes (Figs. 4.18i-l). Flash energy is particularly high for DWCCs on the 26th compared to the 25th, though (Fig. 4.18k). For flash heights, DCC flashes occur on average higher than flashes from other storm modes at 10.8 km. Flashes from other storm modes generally also peak around 10 km, but also have a smaller local maximum around 5-6 km, similar to the December case.

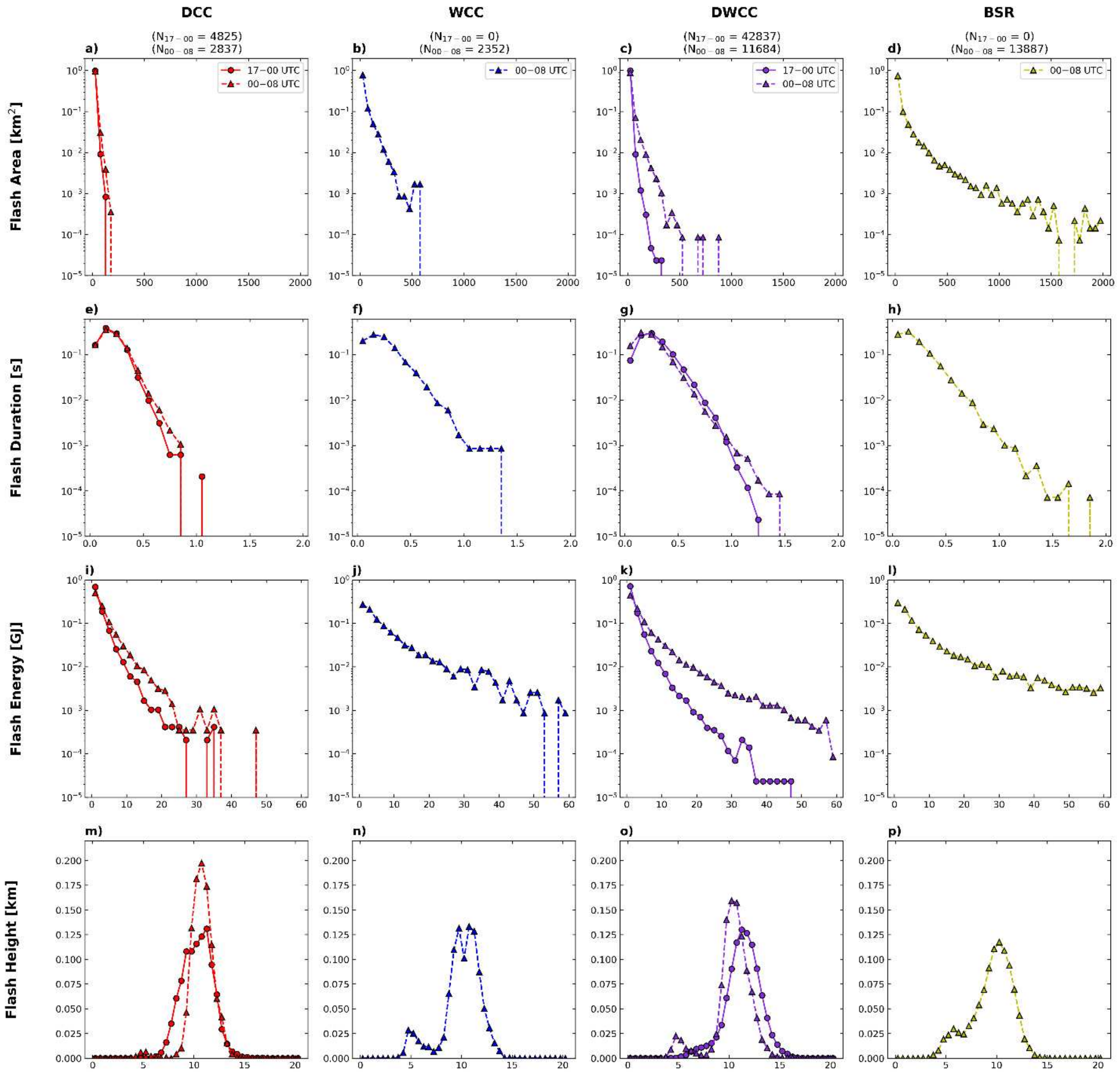

Figure 4.18: Histograms of (a-d) flash area (km^2), (e-h) flash duration (s), (i-l) flash energy (GJ), and (m-p) flash height (km) for LMA flashes centered within DCCs (red; first column), WCCs (blue; second column), DWCCs (purple; third column), and BSRs (yellow; fourth column). Solid lines with circle markers indicate DCCs and DWCCs identified between 1700 and 0000 UTC on 25 January 2019. Dashed lines with triangle markers indicate storm modes identified between 0000 and 0800 UTC on 26 January 2019.

4.5.4 Summary

The 25-26 January MCS case produced very high lightning flash rates of 600 fl min^{-1}. Similar to the December case, the majority of these intense lightning flashes were associated with

DWCCs. Flashes associated with deep convection tended to be smaller in size and produce less energy compared to flashes associated with wide convection and stratiform precipitation. The average flash height was around 10 km for this case as well. An increase in lightning flash rates on 25 January was associated with an increase in graupel and hail mass around 6-9 km, an increase in 35-dBZ volume, and an increase in ice water path. GLM flash rates were significantly lower than LMA flash rates, even though the timing and location of flashes between the two datasets matched okay. High lightning flash rates, the small nature of the flashes, and the location of flashes at 10 km within storms that topped 20 km are all potential reasons for decrease in GLM flash detection. After the deep, isolated convection exited the domain, a second system developed within radar range which was associated with more stratiform precipitation. Flashes were larger on the 26th and occurred at a lower height, consistent with stratiform conditions.

4.6 Conclusions

Ground-based lightning observations in central Argentina were combined with ground-based radar data to identify extreme three-dimensional storm structures and associated lightning characteristics in a variety of events observed during the RELAMPAGO and CACTI field campaigns. The use of these fixed platforms also allows for high temporal and spatial resolution analyses of individual storms. General lightning characteristics associated with each storm mode including location, timing, size, and duration are analyzed for all features identified during RELAMPAGO. Lightning flashes are most frequently associated with deep and wide convection (DWCCs). These flashes occur along the eastern edge of the SDC in the overnight hours. The location and timing of these flashes agrees well with previous studies that have used data from TRMM (Rasmussen et al. 2014). However, the use of the LMA and ground-based radar provides more details into the electrification of storms in the region and their evolution with respect to storm characteristics, microphysics, and detailed lightning flash characteristics. In particular, flashes in deep convective cores tend to be smaller in size and occur higher within the cloud compared to flashes within wide convective cores and stratiform areas, which are typically larger in extent and occur lower within the cloud. These flash characteristics have been documented in other storms, especially in the U.S., but not in SSA, to our knowledge.

In addition to a campaign-wide analysis, two case studies are analyzed in depth to better understand the relationship between the electrification and microphysics of MCSs in SSA. Both case studies recorded lightning flash rates > 600 fl min^{-1} and exhibited lightning jumps associated with storm intensification and the upscale growth of convection within the MCSs. These rapid increases in lightning corresponded to increases in graupel and hail mass and volume, 35-dBZ volume, and ice water path. Most of these flashes were associated with deep convection and were fairly small in size. The average height of these flashes was around 10 km. Flashes observed by GLM were also analyzed and compared with LMA flashes. The timing and location of flashes agreed fairly well between the two datasets. However, lightning flash rates were significantly lower from GLM compared to LMA. Although an in depth GLM detection efficiency analysis was not completed, we noted several likely reasons for a reduced flash rate including the nature of the flashes being small and the optical attenuation of flashes by hydrometeors above the flash height (~10 km).

This work has validated previous studies that have investigated the location and timing of lightning flashes associated with storm modes and demonstrates the unique nature of convection in SSA. This is the first analysis of how lightning characteristics such as flash heights, areas, and intensities vary throughout the storm life cycle in SSA. The use of high-resolution datasets deployed during RELAMPAGO has been useful in determining how convection and lightning are influenced by the terrain, particularly the SDC, in this region. Future work using Dual-Doppler analysis will provide more information on the updrafts associated with these storms and the relationship between kinematic, microphysics, and electrification of storms in SSA.

CHAPTER 5

Lightning Flash Rate Parameterizations based on Precipitation Features Identified in Subtropical South America

5.1 Introduction

Lightning influences the Earth system in many different ways, including maintaining the global electric circuit (Wilson 1921, 1929), producing nitrogen oxides in the upper troposphere that are precursors to ozone (Liu et al. 1987; Dye et al. 2000; DeCaria et al. 2005; Schumann and Huntrieser 2007; Barth et al. 2015), contributing to severe weather (Gatlin and Goodman 2010; Schultz et al. 2009, 2011, 2015, 2017), and posing a threat to people, infrastructure, and aviation (Holle 2016; Stano et al. 2019; Steiner et al. 2014). Parameterizations of lightning are often used in models to better understand and predict the impacts of lightning on these different sectors. Numerous studies have demonstrated strong relationships between lightning and different kinematic and microphysical parameters, some of which include cloud top height (Price and Rind 1992), updraft speed and volume (Price and Rind 1992; Deierling and Petersen 2008; Basarab et al. 2015; Carey et al. 2019), graupel mass and volume (Carey and Rutledge 1996; Deierling et al. 2008; Basarab et al. 2015; Bovalo et al. 2019; Carey et al. 2019), ice mass flux (Deierling et al. 2008; Basarab et al. 2015), volume of the 35-dBZ echo (Liu et al. 2012; Basarab et al. 2015; Carey et al. 2019), and ice water path (IWP; Petersen et al. 2005).

The majority of existing lightning parameterizations have been developed using data from U.S. storms, particularly in northern Alabama and the high plains of Colorado and Kansas (Deierling et al. 2008; Deierling and Petersen 2008; Basarab et al. 2015; Carey et al. 2019). Carey et al. (2019) compared parameterizations derived in Colorado (Basarab et al. 2015) to those derived in northern Alabama and found significant regional differences. Other studies have shown that storms vary regionally by warm cloud depth, convective available potential energy (CAPE), aerosol concentrations, and even charge structure, with a higher percentage of storms in Colorado exhibiting anomalous charge regions (Fuchs et al. 2015, 2018).

Despite most studies using data only from the U.S., there are other hot spots in lightning around the world. One of these is in subtropical South America, downstream of the Andes (Zipser et al. 2006). This region experiences some of the deepest convection on Earth and some of the highest flash rates per storm (Zipser et al. 2006; Romatschke and Houze 2010; Rasmussen and Houze 2011; Rasmussen et al. 2014; Houze et al. 2015; Albrecht et al. 2016). Prior to 2018, the majority of studies focused on this region used satellite data to investigate storm characteristics since there were limited ground-based instruments. However, in the austral spring and summer of 2018-2019, numerous ground-based instruments were deployed to central Argentina as part of the Remote sensing of Electrification, Lightning, And Mesoscale/microscale Processes with Adaptive Ground Observations (RELAMPAGO; Nesbitt et al. 2021) and the Cloud, Aerosol, and Complex Terrain Interactions (CACTI; Varble et al. 2021) field campaigns. These instruments included several research radars and a lightning mapping array (LMA; Rison et al. 1999; Lang et al. 2020). It was hypothesized that storms in subtropical South America are significantly different compared to the U.S. and other storms around the world (Romatschke and Houze 2010; Rasmussen et al. 2011, 2016; Rasmussen et al. 2014; Nesbitt et al. 2021). Given the extremely deep convection and intense lightning flash rates observed in this region, the goal of this study is to develop the first lightning parameterizations for convective storms in subtropical South America.

5.2 Data and Methodology

5.2.1 Radar and hydrometeor identification

The Colorado State University (CSU) dual-polarization C-band radar (CHIVO) was deployed to Córdoba, Argentina as part of the RELAMPAGO field campaign in November through January of 2018-2019 (Arias et al. 2019; Nesbitt et al. 2021). During RELAMPAGO, CHIVO conducted 360° plan position indicators (PPIs), 135° sector scans (SEC), and range height indicators (RHIs). The user-defined scan strategy was based on the proximity and intensity of convection, with update cycles ranging between 5 and 10 minutes.

After data was collected, several quality-control (QC) processes were applied. This included applying an azimuthal correction, an attenuation correction, and a differential reflectivity (ZDR) bias correction. Additionally, a second level of QC was developed that removed a significant amount of non-meteorological and second trip echoes. However, some clutter still remained below 3 km associated with the Sierras de Córdoba, a secondary terrain feature located downstream of the Andes. After the data was QCed, variables including reflectivity, ZDR, correlation coefficient, and differential phase were interpolated to a 1 km x 1 km x 0.5 km grid with vertical levels ranging from 0.5 km to 22 km.

The Dolan et al. (2013) hydrometeor identification (HID) algorithm for C-band was used to classify hydrometeors from the gridded dataset. The nearest sounding from the Atmospheric Radiation Measurement (ARM) Mobile Facility (AMF; about 75 km southwest of CHIVO) was used to retrieve the temperature profile. The HID algorithm has 10 categories ranging from big drops to vertically oriented ice crystals. For this analysis, we combine some of the categories into three main categories: graupel, snow, and ice. After the classification, Z-M relationships derived from Heymsfield and Miller (1988) are used to calculate graupel, snow, and ice mass. Since we are interested in how these variables are associated with lightning, these calculations are only applied above -5°C. Ice water content (IWC) was similarly calculated using a Z-M relationship with exponential size distribution (Carey and Rutledge 2000), and the bulk ice density was varied between 100-800 kg m^{-3} based on reflectivity (Petersen et al. 2005). IWC was then summed above the -5°C level and multiplied by the vertical resolution (500 m) to get IWP.

5.2.2 Lightning Mapping Array

Another platform that was deployed during RELAMPAGO was the LMA which was operated by the National Aeronautics and Space Administration (NASA) George C. Marshall Space Flight Center (Lang et al. 2020). The LMA consisted of 11 stations along the Sierras de Córdoba that measured very high frequency (VHF) sources of lightning. Sources were then clustered in space and time using a time-of-arrival technique (Proctor 1971; Lang et al. 2020). Horizontal and vertical errors in flash location are minimized within 100 km of the LMA network. For this analysis, only flashes with at least 10 sources are considered.

5.2.3 Precipitation feature identification

To identify precipitation features (PFs) in the radar, an algorithm was developed that is based on storm identification algorithms used by satellites including the Tropical Rainfall Measuring Mission (TRMM; Kummerow et al. 1998). These algorithms work by fitting an ellipse to PFs and calculating statistics including PF centroids, areas, and echo top heights (Nesbitt et al. 2000, 2006; Liu et al. 2008; Liu and Zipser 2013; Rocque and Rutledge 2021; Rocque et al. 2023; in review). PFs considered in this study have at least 0 dBZ composite reflectivity between 3-5 km MSL. Data below 3 km is not analyzed because of the additional clutter caused by the mountains, and CHIVO is significantly blocked to the west below this level. The upper limit of 5 km is the approximate height of the melting level.

5.2.4 Lightning parameterizations

LMA flashes are associated with a PF if the flash centroid is within the PF area during the radar volume scan time. Average flash rates are then calculated by dividing the total number of flashes within each PF by the scan time. Storm average flash rates are then related to parameters including 35-dBZ volume, graupel mass, graupel volume, and IWP. These parameters are summed across the storm volume. Other parameters including snow and ice mass and volume are also analyzed but are not as well correlated as graupel. Additionally, updraft magnitudes, updraft volumes, and ice mass flux have been shown to be well correlated to lightning in U.S. storms (Deierling et al. 2008; Deierling and Petersen 2008). Dual-Doppler analysis for the entire RELAMPAGO campaign was beyond the scope of this study but should be looked at in future studies.

Linear regressions with zero y-intercepts were calculated between the lightning parameters and flash rates for the entire RELAMPAGO dataset. This is to ensure that no negative flash rates are predicted, which is a potential problem with other parameterizations. The Pearson correlation coefficient (r) is calculated for each set of parameters to determine how correlated lightning flash rates are to lightning parameters. Additionally, the root mean square error (RMSE) and normalized root mean square error (NRMSE; RMSE divided by the range of observed flash rates) were also computed, as other studies have also done (Basarab et al. 2015; Carey et al. 2019).

5.2.5 Model design

To test how well these parameterizations work, a 1-km resolution Weather Research and Forecasting (WRF; Skamarock et al. 2008) simulation was run for the 13-14 December 2018 (IOP17) mesoscale convective system (MCS) observed during RELAMPAGO. Details on this simulation can be found in Rocque et al. (2023), but a brief description is included here. Four nested domains with 27-, 9-, 3-, and 1-km grid spacing were designed centered over Córdoba, Argentina. The outer three domains were forced with ERA5 reanalysis data every hour, while the inner 1-km domain was forced with the 3-km domain using NDOWN. The 1-km domain was initialized at 20 UTC 13 December and run until 08 UTC 14 December. The National Center for Atmospheric Research (NCAR) continental U.S. (CONUS) physics suite is used along with the Thompson aerosol-aware microphysics scheme (Thompson and Eidhammer 2014). These model parameterizations have been shown to best represent precipitation in subtropical South America (Casaretto et al. 2022).

To compare observations with simulations, C-band reflectivity was calculated from the model using a radar forward model operator called the Cloud Resolving Model Radar Simulator (CR-SIM; Oue et al. 2020). The PF identification algorithm is then applied using the new C-band reflectivity, and PFs within the CHIVO radar domain in the model are calculated. The graupel mixing ratio is used to calculate graupel mass. Additionally, the C-band reflectivity is used to identify 35-dBZ echoes within each PF and to calculate IWP. The lightning parameterizations derived from observations are then applied to the simulated storm total parameters and results are compared with observed lightning flash rates from the LMA.

5.3 Lightning parameterizations derived from observations

The relationship between lightning parameters and flash rates is first analyzed using all CHIVO data from RELAMPAGO. A total of 2,767 PFs were identified by the CHIVO radar that had at least one flash collocated within the PF. The maximum number of flashes associated with any PF was 5,998 flashes. This occurred at 2220 UTC on 25 January 2019, resulting in an average flash rate of 600 flashes per minute. The mean and median flash rates were very small, though, at 22 and 3 flashes per minute, respectively.

Figure 5.1 shows the distribution of flash rates related to different radar-derived parameters including 35-dBZ volume, graupel mass and volume, and IWP. Linear regressions are also shown for the dataset, and the Basarab et al. (2015) and Carey et al. (2019) linear regressions based on their datasets are also included for reference. At first glance, there is substantial scatter, especially at lower flash rates. This is due to the large number of PFs identified, and the large variability associated with each PF. In terms of the linear regressions, flash rates are most correlated to graupel volume (r = 0.67), followed by graupel mass (r = 0.66), 35-dBZ volume (r = 0.63), and IWP (r = 0.47). The RMSE for each regression is fairly high, ranging from 41.8-49.7 fl min^{-1} (Table 5.1). The RELAMPAGO linear regressions compare better with parameterizations of Colorado storms (Basarab et al. 2015) rather than Alabama storms that have lower RMSE values (Carey et al. 2019). However, if the flash range is taken into consideration, the NRMSE is actually fairly low for each parameter, ranging from 7.0-8.3% (Table 5.1).

Interestingly, the linear regressions derived for the RELAMPAGO dataset are shifted considerably to higher values compared to U.S. parameterizations. This suggests that there is more graupel and intense convective cores in subtropical South American storms compared to those in Colorado and Alabama for a given flash rate. It has been hypothesized that storms in subtropical

South America are fundamentally different than other storms from around the world (Zipser et al. 2006; Rasmussen et al. 2011, 2016; Cecil and Blankenship 2012; Nesbitt et al. 2021), and these results suggest that the microphysics may be key in explaining those differences. These results also show that parameterizations vary considerably by region, and employing U.S. based parameterizations in other regions of the world may overestimate or underestimate flash rates depending on the nature of the convective population.

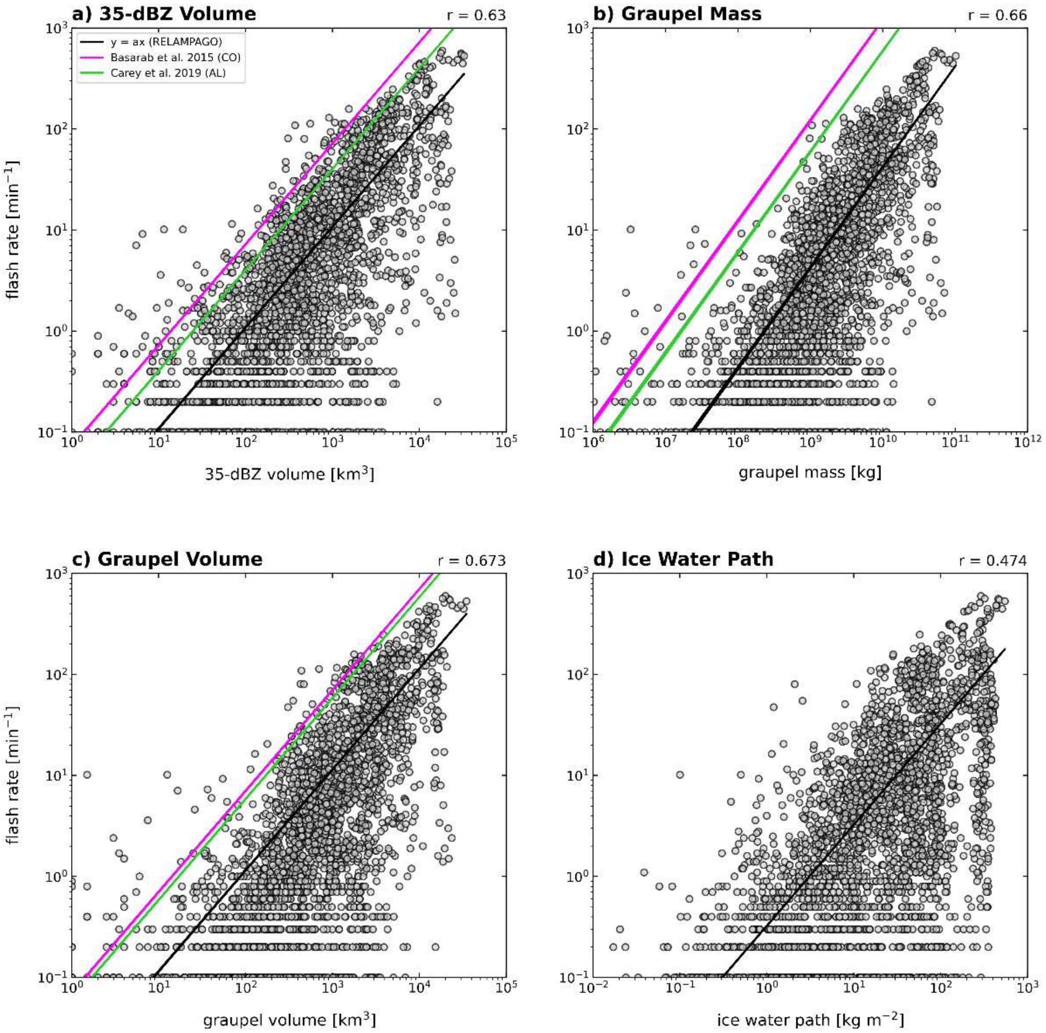

Figure 5.1: Scatter plots of storm averaged lightning flash rates vs. a) 35-dBZ volume (km^3), b) graupel mass (kg), c) graupel volume (km^3), and d) IWP (kg m^{-2}) for all PFs identified in the CHIVO radar during RELAMPAGO. Linear regressions for this dataset are shown in the black lines, and the correlation coefficients are shown in the upper right of each plot. The Basarab et al. (2015; light green) and Carey et al. (2019; magenta) regressions are also shown for context.

Table 5.1: Linear equations for estimated flash rate based on 35-dBZ volume (V35; km^3), graupel mass (GRM; kg), graupel volume (GRV; km^3), and ice water path (IWP; kg m^{-2}). The correlation coefficient (r), the root mean square error (RMSE; min^{-1}), and the normalized RMSE (NRMSE; %) are also shown for each regression.

parameter	flash rate equation	r	RMSE (min^{-1})	NRMSE (%)
V35 (km^3)	f = (1.08 x 10^{-2}) x V35	0.63	43.9	7.3
GRM (kg)	f = (4.18 x 10^{-9}) x GRM	0.66	42.4	7.1
GRV (km^3)	f = (1.14 x 10^{-2}) x GRV	0.673	41.8	7.0
IWP (kg m^{-2})	f = (3.24 x 10^{-1}) x IWP	0.474	49.7	8.3

As mentioned earlier, there is a considerable amount of spread in the data, given the large number of PFs identified. To highlight how the flash rates can vary even within a single storm, three cases are examined. The 5 December case was an isolated, anomalous polarity storm that developed along the terrain in the afternoon hours (Medina et al. 2022). The 13-14 December 2018 case was an MCS that rapidly grew upscale along the terrain overnight and was associated with very strong synoptic forcing and the passage of a cold front (Rocque and Rasmussen 2022; Rocque et al. 2023a, b). The 25-26 January 2019 case was also an MCS that developed along the terrain and remained nearly stationary for 12 hours. This case occurred under weak synoptic forcing and was also more stratiform in nature (Rocque and Rasmussen 2022; Rocque et al. 2023a, b).

Figure 5.2 shows the distribution of flash rates and parameters for each case of interest. PFs from each case have flash rates and convective parameters that generally fall along the linear regression. There is still a wide range of flash rates and parameters within each PF, though. The 5 December case stands out as having a wide range of flash rates, but a narrower range of other parameters. Whether or not other anomalous polarity storms exhibit a similar behavior is not clear. The two MCS cases have the highest flash rates and convective parameters. The 25-26 January

MCS was associated with the most stratiform precipitation and this is evident in the high IWP, but large range of flash rates.

These regressions show that storms in subtropical South America are fundamentally different from those observed in the U.S., including Colorado and Alabama. To determine if these new parameterizations can accurately represent lightning from a forecasting perspective, we investigate results from a high-resolution simulation of the 13-14 December 2018 MCS.

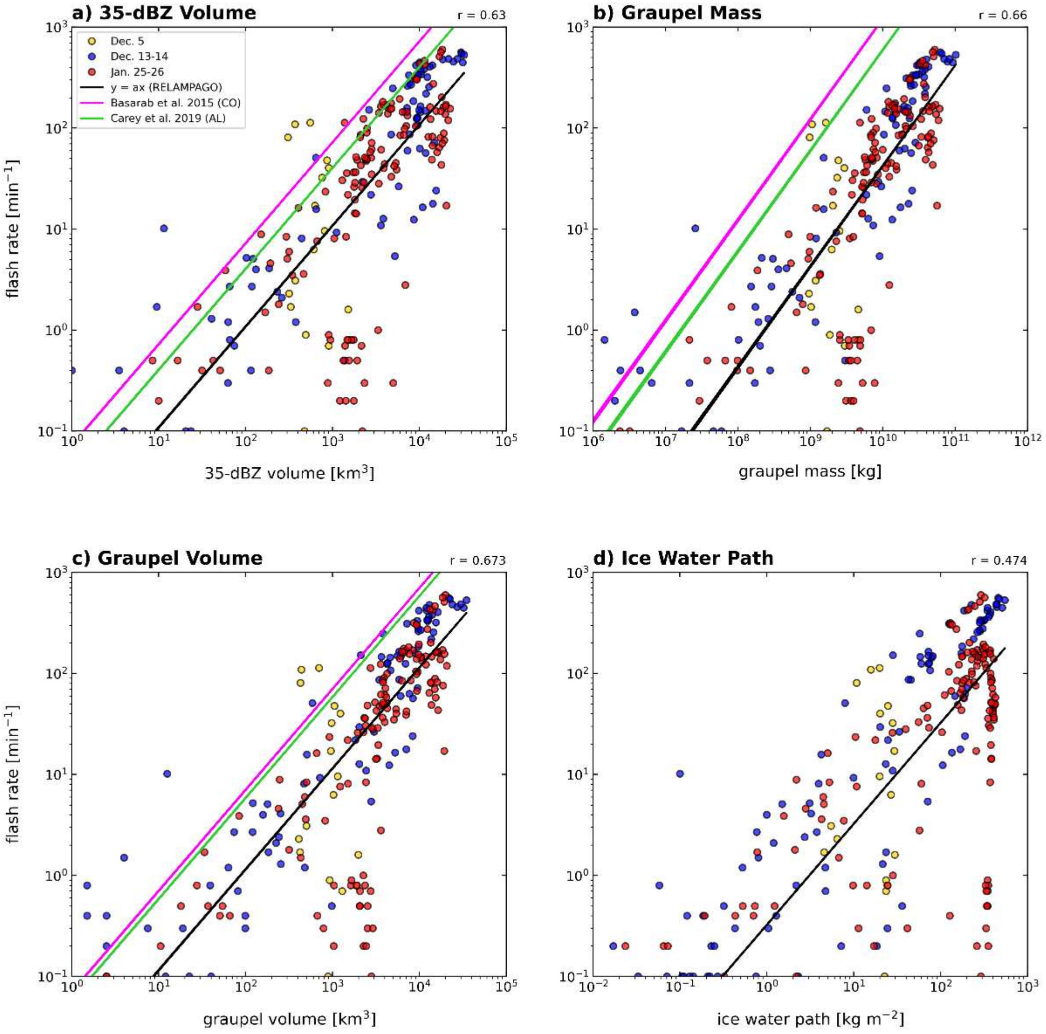

Figure 5.2: As in Fig. 5.1 but now only showing PFs from three cases: the 5 December 2018 anomalous polarity cell (yellow), the 13-14 December 2018 strongly forced MCS (blue), and the 25-26 January 2019 weakly forced MCS (red).

5.4 Case study: 13-14 December 2018

The RELAMPAGO lightning parameterizations are applied to a high-resolution simulation to test whether they are comparable to observed flash rates or not. Extensive model testing and validation has been done by Rocque et al. (2023a) to ensure the best representation of the storm is captured. Overall, the model captured the timing and location of convection well compared to observations in their study. However, deep convection was overestimated. With this in mind, lightning parameters were calculated from the model including 35-dBZ volume, graupel mass, and IWP. These variables were summed across the storm at each time (every 10 minutes), and a time series of the evolution of these parameters is shown in Figure 5.3a. 35-dBZ volume and graupel mass increase from 0000 UTC to their peak just before 0400 UTC. IWP similarly peaks around 0330-0400 UTC but does not increase as rapidly as the convective parameters. After 0400 UTC, convective parameters decrease more rapidly, while IWP decreases more slowly, consistent with the stratiform precipitation that is prevalent at this time (Rocque et al. 2023a).

Using the equations derived from observations and shown in Table 5.1, lightning flash rates from the simulated parameters are calculated and plotted as a function of time in Figure 5.3b. The observed flash rate is also shown for reference. Observed flash rates increase rapidly after 0130 UTC and peak around 0230 UTC at nearly 600 fl min^{-1}. The flash rate then steadily declines afterwards. In the simulation, flash rates derived from 35-dBZ volume and graupel mass have a similar trend, and peak just before 0400 UTC. Flash rates from the 35-dBZ volume parameterizations peak near 660 fl min^{-1}, while peak flash rates from the graupel mass parameterization are lower at 380 fl min^{-1}. The IWP parameterization does not capture the rapid increase in flash rates and underestimates the peak flash rate compared to other convective parameterizations and observations.

Even though the parameterized flash rates are not identical to the observed flash rates, the overall shape of the distribution and the range in values are not far off, especially for the 35-dBZ volume parameterization. Forecasters interested in lightning would still be able to warn for enhanced flash rates within a six hour time frame (from 0000-0600 UTC). If 35-dBZ volume parameterizations based on U.S. storms had been used, flash rates would have been overestimated by up to a factor of 8. These results emphasize the need for regional flash rate parameterizations and highlight just how different storms in subtropical South America are.

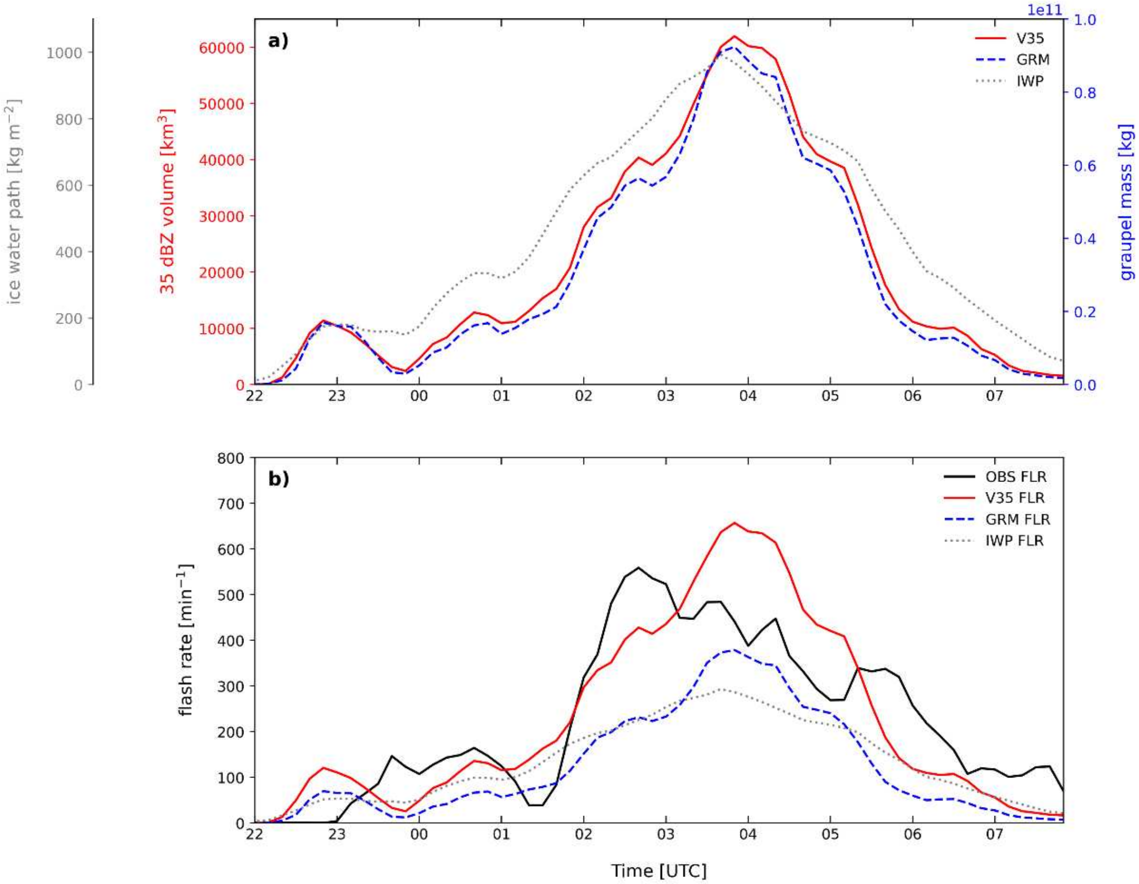

Figure 5.3: Time series of a) 35-dBZ volume (km^3; solid red), graupel mass (kg; dashed blue), and ice water path (kg m^{-2}; dotted grey) from the model simulation and b) observed flash rates (min^{-1}; solid black) and parameterized flash rates for 35-dBZ volume (solid red), graupel mass (dashed blue), and ice water path (dotted grey) for the 13-14 December MCS.

5.5 Conclusions

This study is the first to develop lightning parameterizations based on storms in subtropical South America. High resolution, ground-based observations from a C-band radar and high-quality lightning observations from a LMA, both of which were deployed during the RELAMPAGO field campaign in Córdoba Argentina, are compared for 2,767 PFs. Linear regressions are calculated between lightning flash rates and storm parameters including 35-dBZ volume, graupel mass, graupel volume, and IWP. The 35-dBZ volume, graupel mass, and IWP parameterizations are then tested with a 1-km simulation of an MCS that occurred during RELAMPAGO. Results from this study are as follows:

1. Lightning flash rates in subtropical South America are most correlated with graupel volume and the average percent error between the regression and observations is only 7%.
2. Flash rate parameterizations using simulated 35-dBZ volume and graupel mass do a reasonable job of predicting the high flash rates and the evolution of lightning flash rates that were observed during an MCS.
3. If parameterizations developed based on U.S. storms had been used to predict lightning flash rates for this MCS, they would have overestimated lightning by up to a factor of 8.

These findings show there are significant differences in the microphysics of storms identified in subtropical South America compared to storms in the U.S. Past studies have shown there to be regional differences in storm characteristics and lightning, and results from this study further support these findings. Regional parameterizations of lightning flash rates need to be considered when estimating lightning in model simulations, whether the end user is interested in atmospheric chemistry or severe weather forecasting. Future studies to evaluate lightning parameterizations using ground-based lightning observations in other regions of the world should also be considered.

CHAPTER 6

Conclusions

Convective storms, including MCSs, in SSA are some of the deepest, most intense systems on Earth. With data collected during the RELAMPAGO and CACTI field campaigns, details on the mesoscale and microscale processes that contribute to the development and evolution of these deep storms can be analyzed in depth. Studies in this dissertation combine data from radars, soundings, and the LMA with high-resolution, convection-permitting simulations to determine the role of the terrain, including the Andes and the SDC, on the synoptic environment, mesoscale and storm-scale features, and electrical and microphysical characteristics of two MCSs observed during RELAMPAGO. Prior to these studies, little work had been done investigating the differences between MCSs that occur under strong vs. weak synoptic forcing in SSA. In addition, results from analyses of the lightning and microphysical characteristics of convective storms in SSA during their life cycle evolution are among the first efforts to compare these characteristics with storms in other regions of the world. Thus, results from the studies included in this dissertation provide important insights into the unique nature of storms in SSA and could be used as a guide by forecasters interested in the evolution of MCSs, severe weather prediction, and lightning in this region. Summaries of each study are presented here.

In Chapter 2, the main goal of the study is to determine how the Andes and SDC modify the large-scale environment under strong vs. weak synoptic forcing. WRF simulations are run on two case studies, each that produce a severe MCS within the RELAMPAGO-CACTI domain but occur under very different environmental conditions. The terrain is modified in the simulations to determine if the Andes or SDC play a significant role in the development of each MCS. Under strong synoptic forcing, the Andes play the largest role in the development of convection. Reducing the height of the Andes by 50% results in a weaker lee cyclone, a weaker and shallower SALLJ, quicker intrusion of dry air from the west, and a weaker MCS that quickly moves off the terrain to the east. Under weak synoptic forcing, there are fewer differences in the environments when the Andes are modified or when the SDC are removed. However, differences in the resulting MCS are still evident. From this, it is hypothesized that mesoscale processes and how they are influenced by the SDC are more important in the development of the weakly forced MCS.

In Chapter 3, observations of the two MCS cases are compared with results from high-resolution model simulations. An algorithm is developed to identify three-dimensional storm structures in the radar observations and simulations, and the location, timing, and intensity of these storm modes are compared across datasets. During the strongly forced case, deep convection rapidly develops into an MCS along the SDC. Deep convection is scattered across the domain, but there is a clear back-building signature over the SDC toward the end of the event. When the SDC are removed in the simulation, deep convection does not continue to develop toward the west. Upon further analysis, it is determined that cold pools are significantly blocked between the SDC and the Andean foothills, which allows for secondary generation of convection. This signature is not as prominent when the SDC are removed. During the weakly forced case, intense isolated cells develop along the SDC in the afternoon. A second round of convection is then observed overnight and is associated with more stratiform precipitation. The model fails to capture the isolated cells in the afternoon, possibly because the low-to-mid levels are considerably drier than observations. However, the timing and location of the second MCS is well captured. When the SDC are removed, the system is delayed in entering the domain. Cold pool analyses from this case similarly show that cold pools are blocked by the SDC to the west, which allows for reinvigoration of convection near the foothills.

In Chapter 4, ground-based lightning observations are matched with storm modes to evaluate how electrical characteristics vary within different parts of the convective storms observed during RELAMPAGO. This analysis is first completed for the entire RELAMPAGO dataset. Two additional case-study analyses are conducted that compare ground-based and satellite-based lightning characteristics, and further evaluate electrical and microphysical relationships. Flashes associated with deep convection are located along the SDC and occur most frequently in the afternoon and early evening hours. Flashes associated with wide convection most frequently occur overnight along the eastern edge of the SDC. Stratiform flashes most frequently occur 50-100 km downstream of the SDC, consistent with the upscale growth of MCSs. These flashes are generally larger in area and occur lower in the cloud compared to convective flashes. For the case studies, LMA and GLM flashes generally match well in space and time. However, GLM significantly underestimates flash rates, likely due to measurement differences between the two datasets. These results suggest GLM is missing many flashes that are most likely very small and short duration. Mean flash height for both of these cases is 10 km, which is still 6-8 km within the storm. Optical attenuation by hydrometeors above the mean flash height also likely contributes to GLM’s lower detection efficiency. In terms of microphysics, graupel and hail increase most rapidly with lightning flashes, and snow and ice generally peak later in the MCS life cycle when flashes are larger and stratiform is more prevalent.

In Chapter 5, lightning parameterizations for storms in SSA are developed using radar observations and LMA flash information from RELAMPAGO. This is the first set of lightning parameterizations developed in this region, and the differences between other parameterizations developed based on U.S. storms are clear. Parameters including storm total graupel volume, graupel mass, 35-dBZ volume, and ice water path are the most correlated with flash rates. A new set of equations is developed based on these correlations, and these parameterizations are tested using the 1-km WRF simulation of the strongly forced MCS. Parameterized flash rates match fairly well with observed flash rates for this case. If the parameterizations developed based on U.S. storms had been used instead, flash rates for this case would have been overestimated by up to a factor of 8.

In conclusion, the four studies in this dissertation are the first of their kind to compare large-scale, storm-scale, electrical, and microphysical characteristics of strongly vs. weakly forced MCSs in SSA using high-resolution, ground-based data and simulations. Additionally, the first analysis of how lightning and its characteristics vary throughout the convective life cycle in SSA, and the first set of parameterizations that relate lightning flash rates to microphysical properties in SSA provide valuable insights into how storms in SSA are different compared to other regions of the world. Terrain, in particular, plays a major role in the development and evolution of convection in SSA. The Andes act to modify the large-scale environment, especially under strong synoptic forcing. Deep convection often initiates along the SDC, and the SDC block cold pools generated by convection, which allows for repeated development along the terrain. Convection in SSA is also associated with more graupel and lightning flash rates are much larger in these storms compared to storms in the U.S. Results from this dissertation provide insights into the nature of convection in SSA that were not previously possible given the lack of ground-based observations in the region. Results from this dissertation highlight the important need for ground-based observations in other regions of the world where intense, severe convection is observed by satellites, including downstream of the Himalayas in Asia and over the Congo basin in Africa.

REFERENCES

Albrecht, R. I., S. J. Goodman, D. E. Buechler, R. J. Blakeslee, and H. J. Christian, 2016: Where are the lightning hotspots on Earth? *Bull. Amer. Meteor. Soc.*, **97**, 2051–2068, doi: 10.1175/BAMS-D-14-00193.1.

Arias, I., V. Chandrasekar, and S. S. Joshil, 2019: Cross-validation of CSU-CHIVO radar and GPM during RELAMPAGO. *Int. Geoscience Remote Sensing Symp.*, Yokohama, Japan, IEEE, 7586–7589, doi:10.1109/IGARSS.2019.8898835.

Avila, E. E., and R. G. Pereyra, 2000: Charge transfer during crystal-graupel collisions for two different cloud droplet size distributions. *Geophys. Res. Lett.*, **27**, 3837–3840, doi:10.1029/2000GL012302.

Barth, M. C., and Coauthors, 2015: The Deep Convective Clouds and Chemistry (DC3) field campaign. *Bull. Amer. Meteor. Soc.*, **96**, 1281–1309, doi:10.1175/BAMS-D-13-00290.1.

Basarab, B. M., S. A. Rutledge, and B. R. Fuchs, 2015: An improved lightning flash rate parameterization developed from Colorado DC3 thunderstorm data for use in cloud-resolving chemical transport models. *J. Geophys. Res. Atmos.*, **120**, 9481–9499, doi:10.1002/2015JD023470.

Blackadar, A. K., 1957: Boundary layer wind maxima and their significance for the growth of nocturnal inversions. *Bull. Amer. Meteor. Soc.*, **38**, 283–290, doi:10.1175/1520-0477-38.5.283.

Bovalo, C., C. Barthe, and J. Pinty, 2019: Examining relationships between cloud-resolving model parameters and total flash rates to generate lightning density maps. *Q. J. R. Meteorol. Soc.*, **145**, 1250–1266, doi:10.1002/qj.3494.

Bruick, Z. S., K. L. Rasmussen, and D. J. Cecil, 2019: Subtropical South American hailstorm characteristics and environments. *Mon. Wea. Rev.*, **147**, 4289–4304, doi:10.1175/MWRD-19-0011.1.

Bruning, E. C., and Coauthors, 2019: Meteorological imagery for the Geostationary Lightning Mapper. *J. Geophys. Res. Atmos.*, **124**, 14285–14309, doi:10.1029/2019JD030874.

Bruning, E. C., and D. R. MacGorman, 2013: Theory and observations of controls on lightning flash size spectra. *J. Atmos. Sci.*, **70**, 4012–4029, doi:10.1175/JAS-D-12-0289.1.

Carey, L. D., and S. A. Rutledge, 1996: A multiparameter radar case study of the microphysical and kinematic evolution of a lightning producing storm. *Meteorol. Atmos. Phys.*, **59**, 33–64, doi:10.1007/BF01032000.

Carey, L. D., and S. A. Rutledge, 2000: The relationship between precipitation and lightning in tropical island convection: A C-Band polarimetric radar study. *Mon. Wea. Rev*., **128**, 2687–2710, doi:10.1175/1520-0493(2000)128<2687:TRBPAL>2.0.CO;2.

Carey, L. D., E. V. Schultz, C. J. Schultz, W. Deierling, W. A. Petersen, A. L. Bain, and K. E. Pickering, 2019: Parameters and lightning flash rates in Alabama storms. *J. Atmos.*, **10**, 796, doi:10.3390/atmos10120796.

Casaretto, G., M. E. Dillon, P. Salio, Y. G. Skabar, S. W. Nesbitt, R. S. Schumacher, C. M Garcia, and C. Catalini, 2022: High-resolution NWP forecast precipitation comparison over complex terrain of the Sierras de Córdoba during RELAMPAGO-CACTI. *Weather Forecast*, **37**, 241–266, doi:10.1175/WAF-D-21-0006.1.

Cecil, D. J., and C. B. Blankenship, 2012: Toward a global climatology of severe hailstorms as estimated by satellite passive microwave imagers. *J. Climate*, **25**, 687–703, doi:10.1175/JCLID-11-00130.1.

Chen, F., and J. Dudhia, 2001: Coupling an advanced land- surface/hydrology model with the Penn State/NCAR MM5 modeling system. Part I: Model description and implementation. *Mon. Wea. Rev*., **129**, 569–585, doi:10.1175/1520-0493(2001)129,0569:CAALSH.2.0.CO;2.

Chen, H., V. Chandrasekar, and R. Bechini, 2017: An improved dual-polarization radar rainfall algorithm (DROPS2.0): Application in NASA IFloodS field campaign. *J. Hydrometeorol.*, **18**, 917–937, doi:10.1175/JHM-D-16-0124.1.

Christian, H. J., and Coauthors, 2003: Global frequency and distribution of lightning as observed from space by the Optical Transient Detector. *J. Geophys. Res*., **108**, 4005, doi:10.1029/2002JD002347.

Copernicus Climate Change Service, 2017: ERA5: Fifth generation of ECMWF atmospheric reanalyses of the global climate. Copernicus Climate Change Service Climate Data Store, accessed 26 July 2021, https://cds.climate.copernicus.eu/cdsapp#!/home.

DeCaria, A. J., K. E., Pickering, G. L. Stenchikov, and L. E. Ott, 2005: Lightning generated NOx and its impact on tropospheric ozone production: A three-dimensional modeling study of a Stratosphere-Troposphere Experiment: Radiation, Aerosols, and Ozone (STERAO-A) thunderstorm. *J. Geophys. Res*., **110**, D14303, doi:10.1029/2004JD005556.

Deierling, W., and W. A. Petersen, 2008: Total lightning activity as an indicator of updraft characteristics. *J. Geophys. Res.,* **113**, D16210, doi:10.1029/2007JD009598.

Deierling, W., W. A. Petersen, J. Latham, S. Ellis, and H. J. Christian, 2008: The relationship between lightning activity and ice fluxes in thunderstorms. *J. Geophys. Res.*, **113**, D15210, doi:10.1029/2007JD009700.

Dolan, B., S. A. Rutledge, S. Lim, V. Chandrasekar, and M. Thurai, 2013: A robust C-band hydrometeor identification algorithm and application to a long-term polarimetric radar dataset. *J. Appl. Meteorol. Climatol.*, **52**, 2162–2186, doi:10.1175/JAMC-D-12-0275.1.

Du, Y. and R. Rotunno, 2014: A simple analytical model of the nocturnal low-level jet over the Great Plains of the United States. *J. Atmos. Sci*., **71**, 3674–3683, doi:10.1175/JAS-D-14-0060.1.

Dudhia, J., 1989: Numerical study of convection observed during the winter monsoon experiment using a mesoscale two- dimensional model. *J. Atmos. Sci*., **46**, 3077–3107, doi:10.1175/1520-0469(1989)046,3077:NSOCOD.2.0.CO;2.

Dye, J. E., and Coauthors, 2000: An overview of the Stratospheric-Tropospheric Experiment: Radiation, Aerosols, and Ozone (STERAO)-Deep Convection experiment with results for the July 10, 1996 storm. *J. Geophys. Res*., **105**, 10,023–10,045, doi:10.1029/1999JD901116.

Ervens, B., 2015: Modeling the processing of aerosol and trace gases in clouds and fogs. *Chem. Rev*., **115**, 4157–4198, doi:10.1021/cr5005887.

Feng, Z., A. Varble, J. Hardin, J. Marquis, A. Hunzinger, Z. Zhang, and M. Thieman, 2022: Deep convection initiation, growth, and environments in the complex terrain of central Argentina during CACTI. *Mon. Wea. Rev*., **150**, 1135–1155, doi:10.1175/MWR-D-21-0237.1.

Frame, J., and P. Markowski, 2006: The interaction of simulated squall lines with idealized mountain ridges. *Mon. Wea. Rev*., **134**, 1919–1941, doi:10.1175/MWR3157.1.

Fritsch, J. M., R. J. Kane, and C. R. Chelius, 1986: The contribution of mesoscale convective weather systems to the warm-season precipitation in the United States. *J. Appl. Meteorol. Climatol*., **25**, 1333 – 1345, doi:10.1175/1520-0450(1986)025<1333:TCOMCW>2.0.CO;2.

Fuchs, B. R., 2017: Microphysical, dynamical, and lightning processes associated with anomalous charge structures in isolated convection. Ph.D. dissertation. Department of Atmospheric Science, Colorado State University, Fort Collins, Colorado.

Fuchs, B. R., and Coauthors, 2015: Environmental controls on storm intensity and charge structure in multiple regions of the continental United States, *J. Geophys. Res. Atmos.,* **120**, 6575–6596, doi:10.1002/2015JD023271.

Fuchs, B. R., E. C. Bruning, S.A. Rutledge, L.D. Carey, P. R. Krehbiel, and W. Rison, 2016: Climatological analyses of LMA data with an open-source lightning clustering algorithm. *J. Geophys. Res. Atmos*., **121**, 8625–8648, doi:10.1002/2015JD024663.

Fuchs, B. R., S. A. Rutledge, B. Dolan, L. D. Carey, and C. Schultz, 2018: Microphysical and kinematic processes associated with anomalous charge structures in isolated convection. *J. Geophys. Res. Atmos.,* **123**, doi:10.1029/2017JD027540.

Gatlin, P. N., and S. J. Goodman, 2010: A total lightning trending algorithm to identify severe thunderstorms. *J. Atmos. Ocean. Technol.* **27**, 3–22, doi:10.1175/2009JTECHA1286.1.

GOES-R Algorithm Working Group, and GOES-R Series Program Office (2018): NOAA GOES-R Series Advanced Baseline Imager (ABI) Level 2 Cloud Top Height (ACHA). [cloud top height] NOAA National Centers for Environmental Information. doi:10.7289/V5HX19ZQ. [18 Jan. 2023].

Goodman, S. J., and Coauthors, 2013: The GOES-R Geostationary Lightning Mapper (GLM). *Atmos. Res*., **125–126**, 34–49, doi:10.1016/j.atmosres.2013.01.006.

Gustafson, W. I., A. M. Vogelmann, Z. Li, X. Cheng, K. K. Dumas, S. Endo, K. L. Johnson, B. Krishna, T. Fairless, and H. Xiao, 2020: The Large-Eddy Simulation (LES) Atmospheric Radiation Measurement (ARM) Symbiotic Simulation and Observation (LASSO) activity for continental shallow convection. *Bull. Amer. Meteor. Soc*., **101**, E462–E479, doi:10.1175/bams-d-19-0065.1.

Han, B., J. Fan, A. Varble, H. Morrison, C. R. Williams, B. Chen, X. Dong, S. E. Giangrande, A. Khain, E. Mansell, J. A. Milbrandt, J. Shpund, and G. Thompson, 2019: Cloud-resolving model intercomparison of an MC3E squall line case: part II. Stratiform precipitation properties. *J. Geophys. Res. Atmos.*, **124**, 1090–1117, doi:10.1029/2018JD029596.

Hartmann, D. L., L. A. Moy, and Q. Fu, 2001: Tropical convection and the energy balance at the top of the atmosphere. *J. Climate*, **14**, 4495–4511, doi:10.1175/1520-0442(2001)014<4495:TCATEB>2.0.CO;2.

Helmus, J.J. and S. M. Collis, 2016: The Python ARM Radar Toolkit (Py-ART), a Library for Working with Weather Radar Data in the Python Programming Language. *J. Open Res. Softw*. **4**, e25, doi:10.5334/jors.119.

Heymsfield, A. J., and A. G. Palmer, 1986: Relations for deriving thunderstorm anvil mass of CCOPE storm water budget estimates, *J. Clim. Appl. Meteorol*., **25**, 691–702. doi:10.1175/1520-0450(1986)025<0691:RFDTAI>2.0.CO;2.

Heymsfield, A. J., and K. M. Miller, 1988: Water vapor and ice mass transported into the anvils of CCOPE thunderstorms: Comparison with storm influx and rainout. *J. Atmos. Sci*., **45**, 3501–3514, doi:10.1175/1520-0469(1988)045<3501:WVAIMT>2.0.CO;2.

Holle, R. L., 2016: A summary of recent national-scale lightning fatality studies. *Weather Clim. Soc.,* **8**, 35–42, doi:10.1175/WCAS-D-15-0032.1.

Holton, J. R., 1967: The diurnal boundary layer wind oscillation above sloping terrain. *Tellus*, **19**, 199–205, doi:10.1111/j.2153-3490.1967.tb01473.x.

Hong, S.-Y., Y. Noh, and J. Dudhia, 2006: A new vertical diffusion package with an explicit treatment of entrainment processes. *Mon. Wea. Rev.*, **134**, 2318–2341, doi:10.1175/MWR3199.1.

Houze, R. A. Jr., 1973: A climatological study of vertical transports by cumulus-scale convection. *J. Atmos. Sci.*, **30**, 1112–1123, doi:10.1175/1520-0469(1973)030<1112:ACSOVT>2.0.CO;2.

Houze, R. A. Jr., K. L. Rasmussen, M. D. Zuluaga, and S. R. Brodzik, 2015: The variable nature of convection in the tropics and subtropics: A legacy of 16 years of the Tropical Rainfall Measuring Mission satellite. *Rev. Geophys.*, **53**, 994–1021, doi:10.1002/2015RG000488.

Houze, R. A., Jr., 2004: Mesoscale convective systems. *Rev. Geophys.*, **42**, RG4003, doi:10.1029/2004RG000150.

Houze, R. A., Jr., D. C. Wilton, and B. F. Smull, 2007: Monsoon convection in the Himalayan region as seen by the TRMM Precipitation Radar. *Quart. J. Roy. Meteor. Soc.*, **133**, 1389–1411, doi:10.1002/qj.106.

Insel, N., C. J. Poulsen, and T. A. Ehlers, 2010: Influence of the Andes mountains on South American moisture transport, convection, and precipitation. *Climate Dyn.*, **35**, 1477–1492, doi:10.1007/s00382-009-0637-1.

Kain, J. S., and J. M. Fritsch, 1993: Convective parameterization for mesoscale models: The Kain-Fritsch scheme. *The Representation of Cumulus Convection in Numerical Models*, *Meteor. Monogr.*, No. 46, Amer. Meteor. Soc., 165–170.

Kelly, N., 2022: Rain and RELAMPAGO: Analysis of the Deep Convective Storms of Central Argentina. Ph.D. dissertation. Department of Atmospheric Science, Colorado State University, Fort Collins, Colorado.

Kummerow, C., W. Barnes, T. Kozu, J. Shiue, and J. Simpson, 1998: The Tropical Rainfall Measuring Mission (TRMM) sensor package. *J. Atmos. Oceanic Technol.*, **15**, 809–817, doi:10.1175/1520-0426(1998)015,0809:TTRMMT.2.0.CO;2.

Ladwig, W. (2017). wrf-python (Version 1.3.2) [Software]. Boulder, Colorado: UCAR/NCAR. doi:10.5065/D6W094P1.

Lang, T. J., and Coauthors, 2020: The RELAMPAGO Lightning Mapping Array: Overview and initial comparison with the Geostationary Lightning Mapper. *J. Atmos. Oceanic Technol.*, **37**, 1457–1475, doi:10.1175/JTECHD-20-0005.1.

Liu, C., and E. Zipser, 2013: Regional variation of morphology of organized convection in the tropics and subtropics. *J. Geophys. Res. Atmos*., **118**, 453–466, doi:10.1029/2012JD018409.

Liu, C., D. J. Cecil, E. J. Zipser, K. Fronfeld, and R. Robertson, 2012: Relationships between lightning flash rates and radar reflectivity vertical structures in thunderstorms over the tropics and subtropics. *J. Geophys. Res*., **117**, D06212, doi:10.1029/2011JD017123.

Liu, C., E. Zipser, D. J. Cecil, S. W. Nesbitt, and S. Sherwood, 2008: A cloud and precipitation feature database from nine years of TRMM observations. *J. Appl. Meteor. Climatol*., **47**, 2712–2728, doi:10.1175/2008JAMC1890.1.

Liu, S. C., M. Trainer, F. C. Fehsenfeld, D. D. Parrish, E. J. Williams, D. W. Fahey, G. Hubler, and P. C. Murphy, 1987: Ozone production in the rural troposphere and the implications for regional and global ozone distributions. *J. Geophys. Res.,* **92**, 4191–4207, doi:10.1029/JD092iD04p04191.

Marengo, J. A., W. R. Soares, C. Saulo, and M. Nicolini, 2004: Climatology of the low-level jet east of the Andes as derived from the NCEP-NCAR reanalyses: Characteristics and temporal variability. *J. Climate.*, **17**, 2261–2280, doi:10.1175/1520-0442(2004)017<2261:COTLJE>2.0.CO;2.

Martinez, J. A., and F. Dominguez, 2014: Sources of atmospheric moisture for the La Plata River Basin. *J. Climate*, **27**, 6737–6753, doi:10.1175/JCLI-D-14-00022.1.

May, R. M., S. C. Arms, P. March, E. Bruning, J. R. Leeman, K. Goebbert, J. E. Thielen, Z. Bruick, and M. D. Camron, 2022: MetPy: A python package for meteorological data. Unidata, https://github.com/Unidata/Metpy, doi:10.5065/D6WW7G29.

Mecikalski, R. M., A. L. Bain, and L. D. Carey, 2015: Radar and lightning observations of deep moist convection across Northern Alabama during DC3: 21 May 2012. *Mon. Wea. Rev*., **143**, 2774–2794, doi:10.1175/MWR-D-14-00250.1.

Medina, B. L., L. D. Carey, P. M. Bitzer, T. J. Lang, and W. Deierling, 2022: The relation of environmental conditions with charge structure in central Argentina thunderstorms. *Earth Space Sci*., **9**, e2021EA002193, doi:10.1029/2021EA002193.

Medina, B. L., L. D. Carey, W. Deierling, and T. J. Lang, 2022: Microphysical and kinematic characteristics of anomalous charge structure thunderstorms in Córdoba, Argentina. *Atmosphere*, **13**, 1329, doi:10.3390/atmos13081329.

Mlawer, E. J., S. J. Taubnam, P. D. Brown, M. J. Iacono, and S. A. Clough, 1997: Radiative transfer for inhomogeneous atmospheres: RRTM, a validated correlated-k model for the longwave. *J. Geophys. Res*., **102**, 16 663–16 682, doi:10.1029/97JD00237.

Morrison, H., G. Thompson, and V. Tatarskii, 2009: Impact of cloud microphysics on the development of trailing stratiform precipitation in a simulated squall line: comparison of one- and two-moment schemes. *Mon. Wea. Rev.*, **137**, 991–1007, doi:10.1175/2008MWR2556.1.

Mulholland, J. P., S. W. Nesbitt, and R. J. Trapp, 2019: A case study of terrain influences on upscale convective growth of a supercell. *Mon. Wea. Rev.*, **147**, 4305–4324, doi:10.1175/MWR-D-19-0099.1.

Mulholland, J. P., S. W. Nesbitt, R. J. Trapp, and J. M. Peters, 2020: The influence of terrain on the convective environment and associated convective morphology from an idealized modeling perspective. *J. Atmos. Sci.*, **77**, 3929–3949, doi:10.1175/JAS-D-19-0190.1.

Mulholland, J. P., S.W. Nesbitt, R. J. Trapp, K. L. Rasmussen, and P. V. Salio, 2018: Convective Storm Life Cycle and Environments near the Sierras de Córdoba, Argentina. *Mon. Wea. Rev.*, **146**, 2541–2557, doi:10.1175/MWR-D-18-0081.1.

Nelson, T. C., J. Marquis, A. Varble, and K. Friedrich, 2021: Radiosonde observations of environments supporting deep moist convection initiation during RELAMPAGO-CACTI. *Mon. Wea. Rev.*, **149**, 289–309, doi:10.1175/MWR-D-20-0148.1.

Nesbitt, S. W., and Coauthors, 2021: A storm safari in subtropical South America. *Bull. Amer. Meteor. Soc.*, **102**, 1621–1644, doi:10.1175/BAMS-D-20-0029.1.

Nesbitt, S. W., E. J. Zipser, and D. J. Cecil, 2000: A census of precipitation features in the tropics using TRMM: Radar, ice scattering, and lightning observations. *J. Climate*, **13**, 4087–4106, doi:10.1175/1520-0442(2000)013,4087:ACOPFI.2.0.CO;2.

Nesbitt, S. W., R. Cifelli, and S. A. Rutledge, 2006: Storm morphology and rainfall characteristics of TRMM precipitation features. *Mon. Wea. Rev.*, **134**, 2702–2721, doi: 10.1175/MWR3200.1.

Oue, M., A. Tatarevic, P. Kollias, D. Wang, K. Yu, and A. M. Vogelmann, 2020: The Cloud-resolving model Radar SIMulator (CR-SIM) Version 3.3: description and applications of a virtual observatory. *Geosci. Model Dev.*, **13**, 1975–1998, doi:10.5194/gmd-13-1975-2020.

Parker, M. D., 2021: Self-Organization and Maintenance of Simulated Nocturnal Convective Systems from PECAN, *Mon. Wea. Rev.*, **149**, 999–1022, doi:10.1175/MWR-D-20-0263.1.

Petersen, W. A., H. J. Christian, and S. A. Rutledge, 2005: TRMM observations of the global relationship between ice water content and lightning. *Geophys. Res. Lett.*, **32**, L14819, doi:10.1029/2005GL023236.

Peterson, M., 2019: Research applications for the Geostationary Lightning Mapper operational lightning flash data product. *J. Geophys. Res. Atmos.*, **124**, 10,205–10,231, doi:10.1029/2019JD031054.

Peterson, M., 2021: Where are the most extraordinary lightning megaflashes in the Americas? *Bull. Amer. Meteor. Soc.*, **102**, E660–E671, doi:10.1175/BAMS-D-20-0178.1.

Peterson, M., D. Mach, and D. Buechler, 2021: A global LIS/OTD climatology of lightning Flash Extent Density. *J. Geophys. Res. Atmos*., **126**, e2020JD033885, doi:10.1029/2020JD033885.

Phadtare, J., 2018: Role of Eastern Ghats orography and cold pool in an extreme rainfall event over Chennai on 1 December 2015. *Mon. Wea. Rev*., **146**, 943–965, doi:10.1175/MWR-D-16-0473.1.

Piersante, J. O., K. L. Rasmussen, R. S. Schumacher, A. K. Rowe, and L. A. McMurdie, 2021: A synoptic evolution comparison of the smallest and largest MCSs in subtropical South America between spring and summer. *Mon. Wea. Rev*., **149**, 1943–1966, doi:10.1175/MWR-D-20-0208.1.

Price, C., and D. Rind, 1992: A simple lightning parameterization for calculating global lightning distributions. *J. Geophys. Res.,* **97**, 9919–9933, doi:10.1029/92JD00719.

Proctor, D. E., 1971: A hyperbolic system for obtaining VHF radio pictures of lightning. *J. Geophys. Res*., **76**, 1478–1489, doi:10.1029/JC076i006p01478.

Rasmussen, K. L., 2014: On the nature of severe orographic thunderstorms near the Andes in subtropical South America. Ph.D. dissertation, 227 pp., Department of Atmospheric Sciences, University of Washington, Seattle, Washington.

Rasmussen, K. L., and R. A. Houze Jr., 2011: Orogenic convection in subtropical South America as seen by the TRMM satellite. *Mon. Wea. Rev*., **139**, 2399–2420, doi:10.1175/MWR-D-10-05006.1.

Rasmussen, K. L., and R. A. Houze Jr., 2016: Convective initiation near the Andes in subtropical South America. *Mon. Wea. Rev*., **144**, 2351–2374, doi:10.1175/MWR-D-15-0058.1.

Rasmussen, K. L., M. D. Zuluaga, and R. A. Houze Jr., 2014: Severe convection and lightning in subtropical South America. *Geophys. Res. Lett*., **41**, 7359–7366, doi:10.1002/2014GL061767.

Rasmussen, K. L., M. M. Chaplin, M. D. Zuluaga, and R. A. Houze Jr., 2016: Contribution of extreme convective storms to rainfall in South America. *J. Hydrometeor*., **17**, 353–367, doi:10.1175/JHM-D-15-0067.1.

Reynolds, S. E., M. Brook, and M. F. Gourley, 1957: Thunderstorm charge separation. *J. Atmos. Sci.*, **14**, 426–436, doi:10.1175/1520-0469(1957)014<0426:TCS>2.0.CO;2.

Rison, W., R. Thomas, P. Krehbiel, T. Hamlin, and J. Harlin, 1999: A GPS-based three-dimensional lightning mapping system: Initial observations in central New Mexico. *Geophys. Res. Lett.*, **26**, 3573–3576, doi:10.1029/1999GL010856.

Rocque, M. N., and S. A. Rutledge, 2021: Diurnal cycle of precipitation features observed during DYNAMO. *J. Atmos. Sci.*, **78**, 2287–2306, doi:10.1175/JAS-D-20-0215.1.

Romatschke, U., and R. A. Houze Jr., 2010: Extreme summer convection in South America. *J. Climate*, **23**, 3761–3791, doi:10.1175/2010JCLI3465.1.

Romatschke, U., and R. A. Houze Jr., 2013: Characteristics of precipitating convective systems accounting for the summer rainfall of tropical and subtropical South America. *J. Hydrometeor.*, **14**, 25–46, doi:10.1175/JHM-D-12-060.1.

Rudlosky, S.D., S. J. Goodman, K. S. Virts, and E. C. Bruning, 2019: Initial Geostationary Lightning Mapper observations. *Geophys. Res. Lett.*, **46**, 1097–1104, doi:10.1029/2018GL081052.

Sasaki, C. R. S., A. K. Rowe, L. A. McMurdie, and K. L. Rasmussen, 2022: New insights into the South America Low-Level Jet from RELAMPAGO observations. *Mon. Wea. Rev.*, **150**, 1247 – 1271, doi:10.1175/MWR-D-21-0161.1.

Saunders, C. P. R., and S. L. Peck, 1998: Laboratory studies of the influence of the rime accretion rate on charge transfer during graupel/crystal collisions. *J. Geophys. Res.*, **103**, 13949–13956, doi:10.1029/97JD02644.

Schmidt, T. J., P. Griffith, M. W. Gunshor, J. M. Daniels, S. J. Goodman, and W. J. Lebair, 2017: A closer look at the ABI on the GOES-R series. *Bull. Amer. Meteor. Soc.*, **98**, 681–698, doi:10.1175/BAMS-D-15-00230.1.

Schmidt, T. J., P. Griffith, M. W. Gunshor, J. M. Daniels, S. J. Goodman, and W. J. Lebair, 2017: A closer look at the ABI on the GOES-R series. *Bull. Amer. Meteor. Soc.*, **98**, 681–698, doi:10.1175/BAMS-D-15-00230.1.

Schultz, C. J., L. D. Carey, E. V. Schultz, and R. J. Blakeslee, 2015: Insight into the kinematic and microphysical processes that control lightning jumps. *Weather Forecast.,* **30**, 1591–1621, doi:10.1175/WAF-D-14-00147.1.

Schultz, C. J., L. D. Carey, E. V. Schultz, and R. J. Blakeslee, 2017: Kinematic and microphysical significance of lightning jumps versus nonjump increases in total flash rate. *Weather Forecast.,* **32**, 275–288, doi:10.1175/WAF-D-15-0175.1.

Schultz, C. J., W. A. Petersen, and L. D. Carey, 2009: Preliminary development and evaluation of lightning jump algorithms for the real-time detection of severe weather. *J. Appl. Meteorol. Climatol*., **48**, 2543–2563, doi:10.1175/2009JAMC2237.1.

Schultz, C. J., W. A. Petersen, and L. D. Carey, 2011: Lightning and severe weather: A comparison between total and cloud-to-ground lightning trends. *Weather Forecast.,* **26**, 744–755, doi:10.1175/WAF-D-10-05026.1.

Schumacher, R. S., and Coauthors, 2021: Convective-storm environments in subtropical South America from high-frequency soundings during RELAMPAGO-CACTI. *Mon. Wea. Rev*., **149**, 1439–1458, doi:10.1175/MWR-D-20-0293.1.

Schumann, U., and H. Huntrieser, 2007: The global lightning-induced nitrogen oxides source. *Atmos. Chem. Phys.,* **7**, 3823–3907, doi:10.5194/acp-7-3823-2007.

Shapiro, A., E. Fedorovich, and S. Rahimi, 2016: A unified theory for the Great Plains nocturnal low-level jet. *J. Atmos. Sci*., **73**, 3037–3057, doi:10.1175/JAS-D-15-0307.1.

Singh, I., S. W. Nesbitt, and C. A. Davis, 2022: Quasi-idealized numerical simulations of processes involved in orogenic convection initiation over the Sierras de Córdoba. *J. Atmos. Sci*., **79**, 1127–1149, doi:10.1175/JAS-D-21-0007.1.

Skamarock, W. C., and Coauthors, 2008: A description of the Advanced Research WRF version 3. NCAR Tech. Note NCAR/TN-475+STR, 113 pp., doi:10.5065/D68S4MVH.

Stano, G. T., M. R. Smith, and C. J. Schultz, 2019: Development and evaluation of the GLM stoplight product for lightning safety. *J. Oper. Meteorol*., **7**, 92–104, doi:10.15191/nwajom.2019.0707.

Steiner, M., R. A. Houze Jr., and S. E. Yuter, 1995: Climatological characterization of three-dimensional storm structure from operational radar and rain gauge data. *J. Appl. Meteor*., **34**, 1978–2007, doi:10.1175/1520-0450(1995)034,1978:CCOTDS.2.0.CO;2.

Steiner, M., W. Deierling, K. Ikeda, E. Nelson, and R. Bass, 2014: Airline and airport operations under lightning threats—Safety risks, impacts, uncertainties, and how to deal with them all. In Proceedings of the 6th AIAA Atmospheric and Space Environments Conference; American Institute of Aeronautics and Astronautics: Atlanta, GA, USA, 2014.

Takahashi, T., 1978: Riming electrification as a charge generation mechanism in thunderstorms. *J. Atmos. Sci*., **35**, 1536–1548, doi:10.1175/1520-0469(1978)035<1536:REAACG>2.0.CO;2.

Thomas, R. J., P. R. Krehbiel, W. Rison, S. J. Hunyady, W. P. Winn, T. Hamlin, and J. Harlin, 2004: Accuracy of the Lightning Mapping Array. *J. Geophys. Res*., **109**, D14207, doi:10.1029/2004JD004549.

Thompson, G., and T. Eidhammer, 2014: A study of aerosol impacts on clouds and precipitation development in a large winter cyclone. *J. Atmos. Sci.*, **71**, 3636–3658, doi:10.1175/JAS-D-13-0305.1.

Trenberth, K. E., J. T. Fasullo, and J. Kiehl, 2009: Earth's global energy budget. *Bull. Amer. Meteor. Soc.*, **90**, 311–324, doi:10.1175/2008BAMS2634.1.

Varble, A. C. and Coauthors, 2021: Utilizing a storm-generating hotspot to study convective cloud transitions. *Bull. Amer. Meteor. Soc.*, **102**, E1597–E1620, doi:10.1175/BAMS-D-20-0030.1.

Vera, C., and Coauthors, 2006: The South American Low-Level Jet Experiment. *Bull. Amer. Meteor. Soc.*, **87**, 63–77, doi:10.1175/BAMS-87-1-63.

Vicente, G. A., J. C. Davenport, and R. A. Scofield, 2002: The role of orographic and parallax corrections on real time high resolution satellite rainfall rate distribution. *Int. J. Remote Sens*., **23**, 221–230, doi:10.1080/01431160010006935.

Vivekanandan, J., D. S. Zrnic, S. M. Ellis, R. Oye, A. V. Ryzhkov, and J. Straka, 1999: Cloud microphysics retrieval using S-band dual-polarization radar measurements. *Bull. Amer. Meteor. Soc*., **80**, 381–388, doi:10.1175/1520-0477(1999)080<0381:CMRUSB>2.0.CO;2.

Wilson, C. T. R., 1921: Investigations on lightning discharges and on the electric field of thunderstorms. *Philos. Trans. R. Soc. Lond*., **A221**, 73–115.

Wilson, C. T. R., 1929: Some thundercloud problems. *J. Frankl. Inst.,* **208**, 1–12.

Xu, W., E. J. Zipser, Y.-L. Chen, C. Liu, Y.-C. Liou, W.-C. H. Lee, and B. J.-D. Jou, 2012: An orography-associated extreme rainfall event during TiMREX: Initiation, storm evolution, and maintenance. *Mon. Wea. Rev*., **140**, 2555–2574, doi:10.1175/MWR-D-11-00208.1.

Zhang, Z., A. Varble, Z. Feng, J. Hardin, and E. Zipser, 2021: Growth of mesoscale convective systems in observations and seasonal convection-permitting simulation over Argentina. *Mon. Wea. Rev.*, **149**, 3469–3490, doi:10.1175/MWR-D-20-0411.1.

Zhang, M., K. L. Rasmussen, Z. Meng, and Y. Huang, 2022: Impacts of the coastal terrain on the warm-sector heavy-rain-producing MCSs in Southern China. *Mon. Wea. Rev*., **150**, 603 – 624, doi:10.1175/MWR-D-21-0190.1.

Zhou, C. M. D. Zelinka, and S. A. Klein, 2016: Impact of decadal cloud variations on the Earth's energy budget. *Nat. Geosci.*, **9**, 871–875, doi:10.1038/NGEO2828.

Zipser, E. J., D. J. Cecil, C. Liu, S. W. Nesbitt, and D. P. Yorty, 2006: Where are the most intense thunderstorms on Earth? *Bull. Amer. Meteor. Soc*., **87**, 1057–1071, doi:10.1175/BAMS-87-8-1057.

Zuluaga, M. D., and R. A. Houze Jr., 2013: Evolution of the population of precipitating convective systems over the equatorial Indian Ocean in active phases of the Madden–Julian oscillation. *J. Atmos. Sci.*, **70**, 2713–2725, doi:10.1175/JAS-D-12-0311.1.